8-13-2019

Characterizing Bars in Low Surface Brightness Galaxies

Wesley C. Peters

CHARACTERIZING BARS IN LOW SURFACE BRIGHTNESS GALAXIES

by

WESLEY C. PETERS

Under the Direction of Rachel Kuzio de Naray, PhD

ABSTRACT

Bars in low surface brightness galaxies (LSBs) are relatively understudied despite being important tools for our understanding of galaxy formation and evolution. Drawing from various LSB surveys, we obtained B- and I-band images from the ARCTIC imager on the 3.5m telescope at Apache Point Observatory of 15 barred LSBs in order to measure the three bar properties: length ($R_{\rm bar}$), strength ($S_{\rm b}$), and corotation radius ($R_{\rm CR}$). For 11 of these galaxies, we present new B- and I-band surface brightness profiles, magnitudes, and colors and find that barred LSBs are slightly brighter than the general LSB population, but have similar blue colors. In order to characterize the pattern speed of the bars in LSBs, we use phase crossings of the B- and I-band images to measure the corotation radius and a new bar length measure using azimuthal light profiles to calculate the relative bar pattern speed $\mathcal{R} \equiv R_{\rm CR}/R_{\rm bar}$. We also assembled a sample of 26 barred high surface brightness galaxies (HSBs) to explore how bar properties correlate with various galaxy properties. We find that $R_{\rm bar}$ and $S_{\rm b}$ correlate with galaxy morphology, stellar mass, surface brightness, and gas

fraction, but that $\mathcal{R}$ does not correlate with any galaxy properties. While previous works have shown bars are fast across morphology and redshift, we have extended this to surface brightness and present the currently largest sample of $\mathcal{R}$ measurements for barred LSBs. As LSBs are expected to form in high spin dark matter halos, we estimated the underlying halo spin λ and indeed found high spins of $\lambda > 0.03$ for the majority of our barred LSBs. This work sheds light on a relatively understudied galaxy population, and future work will help to put our results into context with our current understanding of galaxy formation and evolution.

INDEX WORDS: galaxies:structure — galaxies:photometry

CHARACTERIZING BARS IN LOW SURFACE BRIGHTNESS GALAXIES

by

WESLEY C. PETERS

A Dissertation Submitted in Partial Fulfillment of the Requirements of

Doctor of Philosophy

in the College of Arts and Sciences

Georgia State University

2019

CHARACTERIZING BARS IN LOW SURFACE BRIGHTNESS GALAXIES

by

WESLEY C. PETERS

Committee Chair:	Rachel Kuzio de Naray
Committee:	Misty C. Bentz
	D. Michael Crenshaw
	Meghan Connors
	Stacy S. McGaugh

Electronic Version Approved:

Office of Graduate Studies

College of Arts and Sciences

Georgia State University

August 2019

DEDICATION

To my parents, without whom I could never have pursued this dream.

ACKNOWLEDGEMENTS

None of this work would have been possible without the advice and guidance of my advisor, Dr. Rachel Kuzio de Naray, to whom I am forever grateful.

I would like to thank Dr. Marc Seigar and Dr. Amber Sierra for their very helpful discussions regarding azimuthal light profiles. I would like to thank Russet McMillan for her help in creating a master I-band fringe pattern for the ARCTIC imager, including allowing me multiple nights of observing. Finally, I would like to thank Dr. Stacy McGaugh for extensive discussions on LSB photometry, especially morphological classifications. Stacy also provided me with invaluable scientific mentoring as an undergraduate at Case Western Reserve University.

This research has made use of the NASA/ IPAC Infrared Science Archive, which is operated by the Jet Propulsion Laboratory, California Institute of Technology, under contract with the National Aeronautics and Space Administration. This research made use of Astropy, a community-developed core Python package for Astronomy (Astropy Collaboration et al. 2013; The Astropy Collaboration et al. 2018). We acknowledge the usage of the HyperLeda database (http://leda.univ-lyon1.fr).

Sections of this work, Chapters 2 and 3, were previously published in the Monthly Notices of the Royal Astronomical Society (MNRAS) by myself and Dr. Rachel Kuzio de Naray. MNRAS is published by Oxford University Press (OUP). Under the standard OUP license, authors retain the right to include articles in full in a dissertation. We acknowledge that Chapter 2 was published in Peters & Kuzio de Naray (2018), and that Chapter 3 was published in Peters & Kuzio de Naray (2019).

Table of Contents

List of Tables

List of Figures

Chapter 1

Introduction

1.1 Low Surface Brightness Galaxies

As has been pointed out for a long time, our view of the Universe is heavily biased towards what we are able to see (Zwicky 1957; Disney 1976). While this may seem an obvious and innocuous statement, it has significant implications for the picture we form of the Universe. More specifically, galaxies we observe are determined by both their brightness, as well as the brightness of the sky itself. One of the consequences of this fact was an observation that almost all galaxies tended to have central surface brightnesses $\mu_0(B) = 21.65 \pm 0.30$ mag arcsec^{-2} (Freeman 1970). As μ_0 approached the level of the sky (typically ~ 22.8 mag arcsec^{-2} in B, e.g. Pedani 2009), however, the number of observed galaxies declined sharply. This implied that either the Universe was aware of our observational sky-level, or that we were actually missing galaxies with central surface brightnesses fainter than this observational limit.

In the 1980s and 1990s, it began to become clear that the second scenario was the case and that we were missing a significant portion of the galaxy population due to limitations in our instruments. In fact, the bias was so severe that we were probably missing more than half of the true galaxy population in the Universe (McGaugh et al. 1995b; McGaugh 1996; Bothun et al. 1997; O'Neil & Bothun 2000; Trachternach et al. 2006). Thankfully, our understanding of these low surface brightness galaxies (LSBs) has greatly increased over the past three decades, with significant numbers being discovered and studied, from early visual and machine based searches of images and sky surveys (e.g. Schombert et al. 1992; Impey et

al. 1996), to recent large scale surveys (e.g. Zhong et al. 2008; Greco et al. 2018; Du et al. 2019). While there is not a set definition for these galaxies, there is a general consensus on $\mu_0(B) = 22.5$ mag arcsec^{-2} separating high surface brightness galaxies (HSBs) and LSBs.

Presently, we know that LSBs are on a different end of the galaxy spectrum from the familiar galaxy population of HSBs in more than just their luminosities. Specifically, they appear to be relatively unevolved systems with low metallicity (McGaugh & Bothun 1994; van Zee et al. 1997a; de Blok & van der Hulst 1998; Kuzio de Naray et al. 2004), low star formation rates (van der Hulst et al. 1993; van Zee et al. 1997a; Bell et al. 2000; van den Hoek et al. 2000), high gas fractions (de Blok et al. 1996; McGaugh & de Blok 1997; Burkholder et al. 2001), and, most interestingly, are dominated by dark matter at nearly all radii (de Blok & McGaugh 1996; de Blok et al. 1996; McGaugh et al. 2000; Swaters et al. 2003). While historically LSBs tended to be bluer (McGaugh & Bothun 1994; de Blok et al. 1995; Impey et al. 1996), this ended up being a result of photometric plates being biased towards bluer colors. Now, a significant red LSB population is known to exist (O'Neil et al. 1997; Greco et al. 2018), suggesting that there exists a range of ongoing star formation within LSBs. These red LSBs show similar low surface densities to blue LSBs, but appear to have had a more accelerated evolutionary history, possibly due to interactions with neighboring galaxies (O'Neil et al. 1997), and generally have earlier Hubble types.

A comparison between an LSB (NGC 4395, top panel) and HSB (M63, bottom panel) is shown in Fig. 1.1 with SDSS *gri* composite images. Here, both galaxies subtend roughly $\sim 12'$ on the sky, but M63 is twice the distance of NGC 4395, $\sim$8 kpc vs $\sim$4 kpc. Other than the clear difference in brightnesses, we can see that NGC 4395 is much bluer than M63 and has a more diffuse structure.

1.2 Bars in LSBs

We now know that we have been missing a significant fraction of the galaxy population, and that our current view of the Universe is biased towards the very brightest galaxies. However,

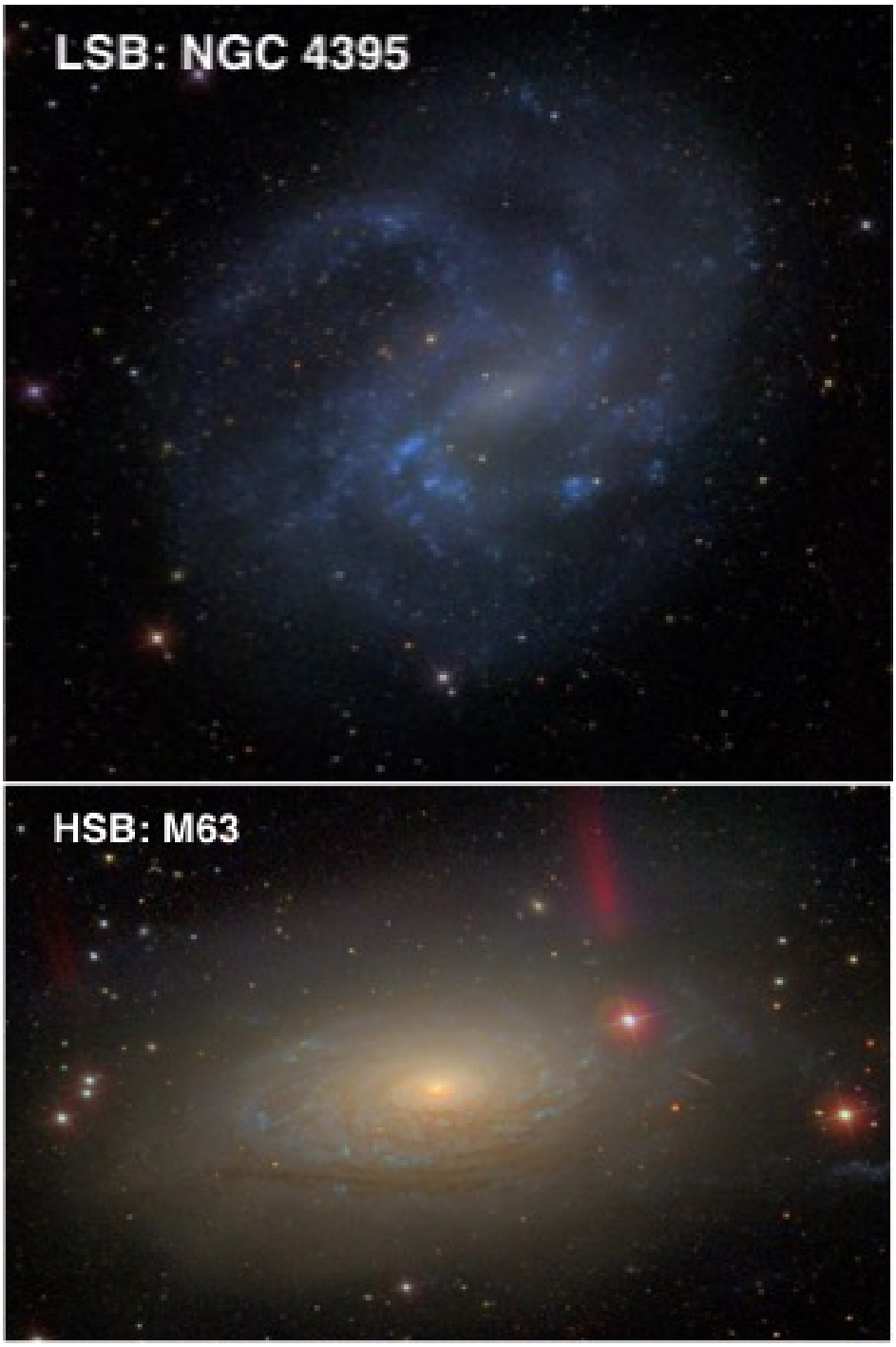

Figure 1.1: A comparison between an LSB (NGC 4395, top panel) and HSB (M63, bottom panel). Both galaxies subtend $\sim 12'$ on the sky, but M63 is twice the distance of NGC 4395.

we have further classified the known galaxy population into a number of groupings, namely ellipticals and spirals. Therefore, a logical question would be: are also missing various types of LSBs, and if so, what can these relatively unknown galaxies tell us about galaxy evolution?

Figure 1.2: The strongly barred HSB galaxy NGC 1300. Image credit: HST/NASA/ESA.

For example, the spiral galaxy population is further broken up into two subcategories: barred and unbarred. A bar is a component of stars in the center of a galaxy disk where stars are mostly locked in radially oscillating orbits (when viewed from the rotational reference frame). When examining HSBs, nearly 60% of spirals are hosts to bars (Eskridge et al. 2000; Marinova & Jogee 2007; Menéndez-Delmestre et al. 2007). However, this fraction strongly depends on wavelength, with bluer bands showing a lower bar fraction. As bars are mostly stellar features, they are most prominent in near infrared bands, where the above 60% fraction is derived from. An example of the strongly barred HSB NGC 1300 is shown in Fig. 1.2 (Image credit: HST/NASA/ESA). Note the presence of dust lanes within the bar, as well as how the spiral arms begin at the ends of the bar. That bars can affect the structure of a galaxy disk is well known.

Given that bars are found in the majority of HSB galaxies, they are important in our understanding of galaxy evolution (such as the feeding of active galactic nuclei and angular momentum transfer between the disk and dark matter halo) and are a major focus of study. In

the literature, bars are usually classified by three properties: length, strength, and corotation radius. The bar length, $R_{\rm bar}$, is simply the extent of the bar in the galaxy disk. However, measuring this is not as straightforward as it seems, and there are many definitions. The bar length is generally necessary for determining the other two parameters, so it is vital that this parameter is determined as accurately as possible.

The strength of a bar generally measures the non-axisymmetric forces from the bar potential (Laurikainen & Salo 2002), but there is no universally agreed upon definition or measure of it. For example, Abraham & Merrifield (2000) define a quantity based on the ellipticity of the bar that ranges from 0 (unbarred) to 1 (infinitely strong), Combes & Sanders (1981) defined a parameter based on the ratio of tangential to radial forces, and many other definitions are based on Fourier decompositions and ellipticities (e.g. Wozniak et al. 1995; Aguerri et al. 1998). Bar length and strength show general trends with galaxy properties, with longer and stronger bars found in earlier Hubble types and red, gas-poor galaxies.

The corotation radius, $R_{\rm CR}$, is the radius at which orbits in the disk are equal to the pattern speed of the bar (Ω_b), or where the net forces cancel out in the rotating reference frame. With this parameter, one can characterize the pattern speed of a bar as 'fast' or 'slow' by the relative bar pattern speed $\mathcal{R} \equiv R_{\rm CR}/R_{\rm bar}$. This is useful as it can be used to see if bars have been slowed down by dynamical friction with the dark matter halo. When examining HSBs, bars are fast across the Hubble sequence (Aguerri et al. 2015) as well as redshift (Pérez et al. 2012), implying that there has not been significant angular momentum transfer between the bar and dark matter halo. $\mathcal{R}$ is an easier parameter to measure than Ω_b due to the only direct measurement of the bar pattern speed (TW method, Tremaine & Weinberg 1984) being quite observationally expensive (luminosity weighted spectroscopy is required), as well as quite sensitive to uncertainties in disk position angle and inclination (Debattista 2003; Corsini 2011).

While the majority of HSBs appear to be hosts to bars ($\sim 60\%$), the bar fraction is much lower when examining LSBs, ranging from a few percent in the optical catalogs of Schombert

et al. (1992) and Impey et al. (1996), 8% in Mihos et al. (1997), and, most recently, $\sim 20\%$ in Cervantes Sodi & Sánchez García (2017). This is attributed to a number of causes, namely that LSBs are likely stable against local and global instabilities (Mihos et al. 1997), that high gas fractions in galaxies can prevent bar growth (e.g. Masters et al. 2012), and that LSBs are expected to form in high spin dark matter halos (Dalcanton et al. 1997; Jimenez et al. 1998; Boissier et al. 2003; Kim & Lee 2013; Long et al. 2014) which can also prevent bar growth (Cervantes Sodi & Sánchez García 2017; Collier et al. 2018). Finally, as previously stated, bars are most prominent in near infrared bands, which could also be a reason for the lower bar fraction in these LSB surveys. There is only one LSB with a pattern speed measurement (UGC 628, Chemin & Hernandez 2009; Chequers et al. 2016), and many recent studies focus on galaxies with LSB disks rather than true LSB galaxies (e.g. Honey et al. 2016). As such, bars in LSBs are not as well understood when compared with those in HSBs.

Recent work has shown that bars in LSBs are generally weaker and shorter than those in HSBs (e.g Cervantes Sodi & Sánchez García 2017), but there exists a lack of data with regard to bar pattern speed measurements for LSBs. This is due to both the expensive nature of spectroscopically observing LSBs, as well as complications in obtaining rotation curves from velocity fields when bars are present (Spekkens & Sellwood 2007; Sellwood & Sánchez 2010). However, if the corotation radius is measured with photometry, it is then possible to characterize all three parameters of bars in LSBs, and put them into context with those in HSBs.

1.3 Goals

LSBs are vital to our understanding of the galaxy population as a whole, but are generally biased against in surveys. In addition, barred galaxies are important tools for understanding the evolutionary processes in galaxies, but barred LSBs are also avoided in studies for various reasons. While some recent work has begun to shed light on bars in LSBs, they are not as well understood as those in HSBs. In addition, the dynamical properties of bars in LSBs

(namely the corotation radius and pattern speed) are all but unknown due to there being only a single LSB with a direct measurement. With this in mind, we set out to accomplish the following:

1. **Characterize the three bar properties for a sample of barred LSBs.** We will accomplish this by first identifying well studied LSBs in the literature that are also hosts to bars for which we will develop and apply methods to measure the bar properties. We will then extend these methods to a larger sample of barred LSBs with almost no available data by obtaining new photometric measurements. Most importantly, we will obtain the currently largest number of relative bar pattern speed measurements for LSBs. We will use these measurements to determine if barred LSBs show evidence of dynamical slow down due to dark matter halos.

2. **Obtain surface brightness profiles, magnitudes, and colors for barred LSBs.** It is important to place these LSBs into context with unbarred LSBs. We will use these measurements to investigate whether barred LSBs are brighter or fainter, have different colors, or have different disk scale lengths than unbarred LSBs.

3. **Obtain stellar and gas mass estimates for barred LSBs.** As bar growth is thought to be hampered by high gas fractions, it is important to see how the gas fractions of barred LSBs compare to the general LSB population. We will use these data to determine whether barred LSBs have different gas fractions than unbarred LSBs.

4. **Compare our results for barred LSBs with those of barred HSBs.** We will compare the two samples to determine if there are trends with bar properties across surface brightness.

1.4 Layout of Dissertation

In Chapter 2 we measure the bar properties of four well studied low surface brightness galaxies that are hosts to bars. In Chapter 3 we expand our sample, measuring the bar properties in 11 additional LSBs that have not been studied at all. We also generate mock galaxy images in order to quantify how accurate our bar length measures are, and we present full B- and I-band photometry, and gas fractions for a portion of the sample. In Chapter 4 we explore bar properties across stellar and gas mass by comparing LSBs to a sample of high surface brightness galaxies. We place the results from these chapters into context with each other in Chapter 5, as well as pose future work that is necessary to answer any outstanding questions. Finally, we summarize each chapter and present our conclusions from this dissertation in Chapter 6.

Chapter 2

Pilot Study of Four Low Surface Brightness Galaxies

Peters, W. & Kuzio de Naray, R., "Characterising bars in low surface brightness disc galaxies", 2018, MNRAS, 476, 2938

2.1 Introduction

Low surface brightness galaxies (LSBs) are incredibly faint galaxies, typically defined as having central surface brightnesses $\mu_0(B) \geq 22.0$ mag arcsec^{-2}. Due to this, LSBs are very hard to detect, and have been biased against in large-scale surveys, even though they may make up more than half of all galaxies (McGaugh et al. 1995b; Bothun et al. 1997). Although they are faint, LSBs are not simply just small and featureless galaxies, but come in a whole suite of morphologies comparable to 'normal' high surface brightness galaxies (HSBs) (McGaugh et al. 1995a). As LSBs have bluer colors, lower star formation rates, and lower metallicities than HSBs but similar total masses, they must have taken a different evolutionary path (van der Hulst et al. 1993; van Zee et al. 1997a; van den Hoek et al. 2000; Kuzio de Naray et al. 2004). Finally, LSBs are thought to be dark matter dominated at all radii (de Blok & McGaugh 1996; de Blok et al. 1996; McGaugh et al. 2000; Swaters et al. 2003), making these galaxies vital to our understanding of galaxy formation and evolution.

Although LSBs are comparatively not as well understood as HSBs, their dark matter domination is very well studied. Traditionally, understanding the nature of dark matter in LSBs has been approached with the examination of HI/Hα rotation curves and decomposition

of baryonic and dark matter mass profiles (e.g. Swaters et al. 2000; de Blok et al. 2001b; McGaugh et al. 2001; de Blok & Bosma 2002; Kuzio de Naray et al. 2006, 2008). In addition, mock observations of simulated LSBs have also been used to test predictions from cold dark matter simulations (de Blok et al. 2003; Kuzio de Naray et al. 2009; Kuzio de Naray & Kaufmann 2011; Pineda et al. 2017).

While there has historically been disagreement over the reliability of observations, such as concerns over HI beam smearing (e.g. van den Bosch et al. 2000; van den Bosch & Swaters 2001; Blais-Ouellette et al. 2004), Hα long-slit rotation curve resolution (e.g. Swaters et al. 2003), or, more recently, unaccounted for gas dynamics (e.g. Pineda et al. 2017), these have largely been accounted for. The result is that we are now left with observations that conflict with expectations from cold dark matter simulations (e.g. McGaugh et al. 2001; de Blok & Bosma 2002; Spekkens et al. 2005; Kuzio de Naray et al. 2006). Despite this, pseudoisothermal dark matter halos still match observations rather well, suggesting LSBs are embedded in massive dark matter halos.

A subset of LSBs have been historically avoided, however, in these kinematic studies: those with bars. This is unfortunate as these galaxies may allow for a different approach to exploring dark matter. Barred LSBs have been avoided for two major reasons. Firstly, non-circular motions due to bars are not very well modeled or constrained, with both minimal (van Eymeren et al. 2009) and significant (Spekkens & Sellwood 2007; Sellwood & Sánchez 2010) effects on rotation curves being detected. Secondly, as a consequence of their implied dark matter domination, LSBs should be stable against bar formation, making these features very rare.

Through visual classifications, Mihos et al. (1997) placed the bar fraction at $\sim$4% for LSBs. They also used numerical simulations to show that global instabilities are unlikely to form in LSB disks unless perturbed. This bar fraction was recently updated to $\sim$8% by Honey et al. (2016) using optical SDSS images of LSB galaxies compiled from various catalogs. Cervantes Sodi & Sánchez García (2017) used a large sample of SDSS LSB galaxies classified

from Galaxy Zoo 2 and found the bar fraction to be near 20%. Each of these fractions are far lower than the ∼60% found in HSBs when using NIR imaging (Eskridge et al. 2000; Marinova & Jogee 2007; Menéndez-Delmestre et al. 2007). This lower bar fraction likely stems from the higher gas content of LSBs (Cervantes Sodi 2017).

There has been recent work on exploring bars in LSBs, mostly with numerical simulations, to probe any correlations between bar morphology and host galaxy. Mayer & Wadsley (2004) used high resolution simulations of gas dominated disks and found that bars could form if the dark matter halo had a low concentration and the stellar component was higher than typically observed in LSBs. Chequers et al. (2016) used hydrodynamical numerical simulations of UGC 628 to estimate the bar pattern speed and found it to suggest the galaxy was not dark matter dominated in the inner bar region. Cervantes Sodi & Sánchez García (2017) observationally found a strong dependance on bar length with disk surface brightness, as well as finding weaker bars in comparison to HSBs.

Given the current lack of data for barred LSBs, our goal is to quantify bars in LSBs. We hope to place these into morphological context with bars in HSBs, as well as infer properties of the dark matter halos barred LSBs are embedded in. To accomplish this, we use optical B and I-band images of four barred LSB galaxies and use these new data in combination with archival Spitzer 3.6 μm data to quantify bar length and strength beyond a visual classification or description. In addition, we use a photometric technique from Puerari & Dottori (1997) to characterize the relative bar pattern speeds of our sample.

This chapter is organized as follows. In Sec. 2.2 we discuss our sample selection, observations, and data reduction. In Sec. 2.3 we detail how we construct our azimuthal light profiles and how we measure the bar length, strength, and speed. In Sec. 2.4 we present the results for each individual galaxy. In Sec. 2.5 we place our results into context with results from the literature as well as into context with previous dark matter studies. Finally, in Sec. 2.6 we list our conclusions from this work.

2.2 Sample and Data

In this section we detail how we constructed our sample of barred LSB galaxies. We also discuss our acquisition of new broadband B and I-band images of our targets, and the retrieval of Spitzer 3.6 μm archival data. Finally, we detail our data reduction process, including how we deproject our galaxy images.

2.2.1 Sample

As no single catalog of barred LSBs exists currently, we have begun assembling one from multiple sources. We have examined the catalogs of Schombert et al. (1992) and Impey et al. (1996) to visually identify barred LSBs. Schombert et al. (1992) and Impey et al. (1996) both list large numbers of LSBs that give us a starting point for a sample selection: Schombert et al. (1992) lists 198 LSBs identified visually from the Second Palomar Sky Survery (Reid et al. 1991), whereas Impey et al. (1996) lists 693 LSBs identified from a combination of visual and machine scan searches. A few galaxies from Schombert et al. (1992) have Spitzer 3.6 μm images (Schombert & McGaugh 2014), giving total stellar masses for these galaxies. The galaxies found in Impey et al. (1996), however, have very rarely been observed again. Because we are interested in the traditional LSB (i.e. dark matter dominated at all radii) from these catalogs, we avoid selecting bulge-dominated galaxies (e.g. Beijersbergen et al. 1999) and those that only have LSB outer disks.

We also search the samples of Swaters et al. (2000), de Blok et al. (2001b), McGaugh et al. (2001), de Blok & Bosma (2002), Kuzio de Naray et al. (2006), and Kuzio de Naray et al. (2008). These studies provide rotation curves and mass models for numerous LSBs. Some of these galaxies overlap with the sample of Schombert et al. (1992).

Finally, we also have selected UGC 628, which has had its bar pattern speed measured via Fabry-Perot kinematics (Chemin & Hernandez 2009) and numerical modeling (Chequers et al. 2016).

Table 2.1: Barred LSBs used in this study. Disk inclinations and P.A.s are derived from our data using `ELLIPSE`, except for F563-V2 where we take the disk parameters from de Blok et al. (2001b). The distance for UGC 628 was taken from de Blok & Bosma (2002), with the rest taken from de Blok et al. (2001b).

Galaxy	R.A. (J2000)	Dec. (J2000)	Inc. (°)	P.A. (°)	D (Mpc)
UGC 628	01:00:51.9	+19:28:33	58.2±0.7	-42.8±0.9	65
F563-V2	08:53:03.8	+18:26:09	29	-32	61
F568-1	10:26:06.3	+22:26:01	24.9±3.8	-86.0±7.9	85
F568-3	10:27:20.2	+22:14:24	39.6±1.8	-11.4±2.2	77

For this chapter, we have selected four LSBs of varied morphology and that have previous kinematic mass modeling: UGC 628, F568-1, F568-3, and F563-V2. UGC 628 and F568-1 display clear grand-design structure. However, these types of LSBs are rather rare. The other two, F568-3 and F563-V2, are more indicative of typical LSB structure, with F568-3 having a clear disk but very messy spiral structure, and F563-V2 having rather tenuous disk and arm structure.

Properties of our sample are listed in Table 2.1. The disk inclinations and position angles (P.A.) listed here are derived from our data (with F563-V2 an exception) and discussed later in the text. The distance for UGC 628 is taken from de Blok & Bosma (2002), with the remaining distances taken from de Blok et al. (2001b).

2.2.2 Data

We have obtained broadband B and I-band images of our targets using the ARCTIC imager on the 3.5-m telescope at Apache Point Observatory[1]. ARCTIC has a field of view of $7.5' \times 7.5'$. We used ARCTIC in single read out mode with 2×2 binning, giving a plate scale of 0.228 arcsec/pix.

ARCTIC observations for UGC 628 were taken on 2016 August 7. ARCTIC observations of F568-1 and F563-V2 were obtained on 2017 February 24. Observations for F568-3 were

[1]Based on observations obtained with the Apache Point Observatory 3.5-meter telescope, which is owned and operated by the Astrophysical Research Consortium.

taken on 2017 February 28, along with additional observations for F568-1 and F563-V2. We observed UGC 628, F568-1, and F563-V2 with 3×600 sec exposures in both B and I. We observed F568-3 with 2×600 sec exposures in both bands. We dithered 15 arcsec between each exposure in both bands to correct for bad pixels and cosmic rays.

We also obtained fully reduced 3.6 μm images of our sample from the Infrared Science Archive (IRSA) published in Schombert & McGaugh (2014). Observations had a maximum exposure time of 100 sec, and the final images have a pixel scale of 0.60 arcsec/pix.

2.2.3 Data Reduction

The Spitzer 3.6 μm images are fully reduced and flux calibrated. We converted the units of the image from MJy/sr to counts/pix using data from the header files in order to be compared with our optical images. The sky-background was determined by using the average value of six 50×50 pixel star-free boxes on each image to determine a mean sky which was then subtracted from the image (see Schombert & McGaugh 2014).

The ARCTIC data were reduced in `IRAF`[2] using standard packages and routines. The images were bias subtracted, dark subtracted, flat-fielded, and fringe corrected (see Appendix A for a description of this process). The sky-subtraction was performed using the method outlined above, with six 100×100 pixels boxes. The I-band images were corrected for the fringe pattern present in each image. Our final, reduced and sky-subtracted B and I-band images are shown in Fig. 2.1.

After the data were reduced, we deprojected all the data (including the Spitzer 3.6 μm images) so that the galaxies appear face-on. We have made the assumption that our disk galaxies are intrinsically circular. With this assumption, we used the `ELLIPSE` task in `IRAF` to fit elliptical isophotes to our galaxy images to determine the eccentricity ($\epsilon = 1 - b/a$) and position angle (P.A.) of the outer disk of our galaxies. We first ran `ELLIPSE` with all

[2]IRAF is distributed by the National Optical Astronomy Observatory, which is operated by the Association of Universities for Research in Astronomy (AURA) under a cooperative agreement with the National Science Foundation.

parameters free in order to determine the galaxy center. We then re-ran ELLIPSE with the center fixed to derive ϵ and P.A. for the outer disk. We also confirmed that the centers found by ELLIPSE were the same location in the galaxy for all three bands. Finally, we used GEOTRAN to rotate the image by the disk position angle so that the major axis of the galaxy is aligned with the y-axis, and then 'stretch' the minor axis (now aligned with the x-axis) by the axis ratio (b/a). If done properly, the deprojected galaxy images should have roughly circular outer isophotes.

In order to ensure our images are deprojected in the same manner for each band, we derive inclinations and P.A. in the three bands for each galaxy and use the average as the final value. We use these final values to deproject each image. We list our derived inclinations and P.A. for our sample in Table 2.1, with the exception of F563-V2 where we took the disk parameters from de Blok et al. (2001b). The reason for this is as follows: the sharp change in the light profile between the bright bar and faint disk, as well as the rather tenuous disk structure, causes IRAF's ELLIPSE task to fail when attempting to fit elliptical isophotes to the images. Due to this, we adopted literature values for our deprojection for this galaxy. Because F568-1 is nearly face on ($i \sim 25°$), the errors on the P.A. are relatively large. But because it is so face-on, the rotation angle does not affect the deprojection to a large degree.

2.3 Measurements

For our four galaxies, we want to measure the bar lengths, strengths, and corotation radii. In this section we discuss the techniques that we use for measuring each of these bar properties.

2.3.1 Bar Length

The length of a bar is rather straightforward, simply how far it extends from the center of the galaxy. And yet, there are many ways of measuring the bar radius, since defining the end of a bar is more complex than expected. We use three in this work: the behaviour of azimuthal light profiles, Fourier analysis, and the behaviour of elliptical isophotes. These techniques

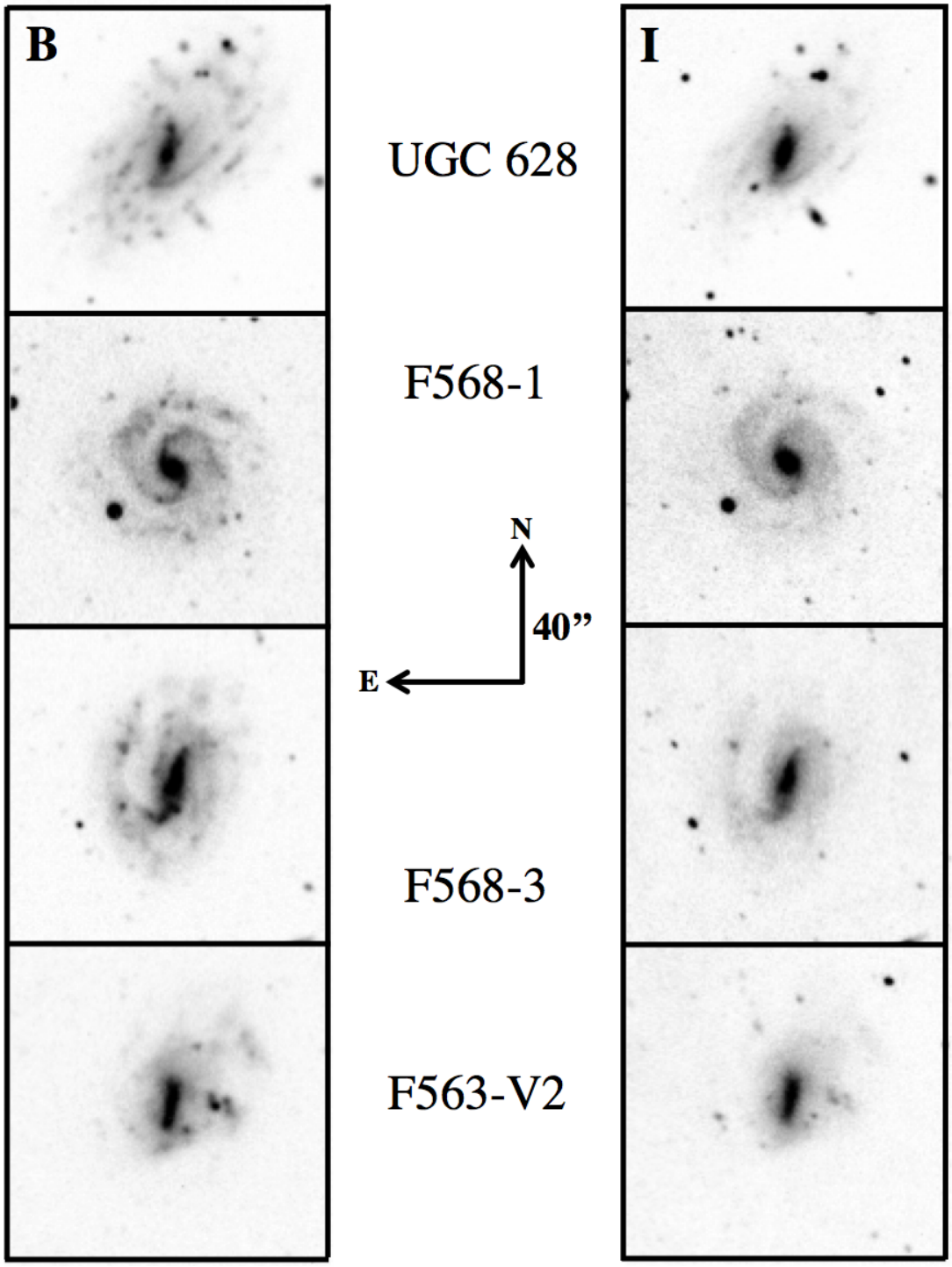

Figure 2.1: On-sky images of our target galaxies. B-band images are in the left column and I-band images are in the right column, all were taken with ARCTIC on the APO 3.5m. Directional arrows in the center are both $40''$ long and apply to each image. Images are all scaled linearily in order to show the best contrast between the bar, spiral arms, and disk.

each provide an objective (and quantitative) measure of the bar length. Each technique is described in detail below. Because bars are stellar features, we only use the I-band and 3.6 μm images to measure the bar length. We compare the results of each technique to confirm that each is physically meaningful (i.e. does not include a significant portion of a spiral arm).

2.3.1.1 Azimuthal Light Profiles

Determining how light is distributed in a galaxy is very useful for studying properties of galaxies, including bars. For example, we can examine how the light behaves as a function of azimuthal angle and radius (i.e. an azimuthal light profile).

Ohta et al. (1990) describe how azimuthal light profiles appear for different morphological features. In the very inner radii, the light profiles should be fairly constant due to the nucleus or a bulge. If a bar is in the galaxy, then there should be two 'humps' present in the light profiles, separated by 180 degrees in azimuthal angle. These humps should also remain roughly constant in angle for all radii within the bar. Once outside the bar region, these humps should change depending on the morphology of the galaxy. If there are two spiral arms present, these humps should roughly remain 180 degrees out of phase but begin moving to different angles, as the arms are not at constant azimuthal angle. Because spiral arms and disks are typically fainter than bars, the peak intensities of these humps will also decrease dramatically outside the bar region. Using these changes in the humps, it should be possible to measure the radius of the bar.

For consistency, we construct the azimuthal light profiles in the same manner for all of our galaxies. We use 120 azimuthal divisions for the B and I-bands and 60 divisions for 3.6 μm (i.e. 3° and 6° wide, respectively). We use a radial spacing of every 2 pixels for the B and I bands and every 1 pixel for 3.6 μm (i.e. a spacing of 0.46″ and 0.6″ respectively). We begin our profiles at 3″ for each galaxy, as starting too far in results in some bins containing no pixels. We then sum up the intensity of all pixels within each radial and azimuthal bin

and divide by the number of pixels to return intensity per pix^2. In order to account for local variations that may be present, we use a nearest-neighbor smoothing at the end.

To measure the bar radius, we fit Gaussians to each hump in order to measure the azimuthal angle and peak intensity. By examining both the location and height of a hump at each radial slice relative to the other hump in a given radius, which should be 180 degrees out of phase and of similar intensity, we can track its behaviour across all radii. Where we find changes similar to what was described above and in Ohta et al. (1990) we call the bar radius.

2.3.1.2 Fourier Analysis

An alternative method for measuring the bar length is through a Fourier analysis (e.g. Ohta et al. 1990; Aguerri et al. 1998, 2000a, 2009; Puerari & Dottori 1997). This involves decomposing our azimuthal light profiles via a Fourier transform, given as:

$$\mathcal{F}(r) = \int_{-\pi}^{\pi} I_r(\theta) \exp(-2i\theta) d\theta \tag{2.1}$$

where $I_r(\theta)$ are the azimuthal light profiles, and θ is the azimuthal angle.

The Fourier coefficients are:

$$A_m(r) = \frac{1}{\pi} \int_0^{2\pi} I_r(\theta) \cos(m\theta) d\theta \tag{2.2}$$

$$B_m(r) = \frac{1}{\pi} \int_0^{2\pi} I_r(\theta) \sin(m\theta) d\theta \tag{2.3}$$

and the amplitudes are:

$$I_0(r) = \frac{A_0(r)}{2} \tag{2.4}$$

$$I_m(r) = \sqrt{A_m^2(r) + B_m^2(r)} \tag{2.5}$$

These amplitudes can be used both to confirm the presence of a bar, as well as measure the bar length. Within the bar region, the $m = 2$ and $m = 4$ amplitudes are strong compared

with the odd modes (Ohta et al. 1990). In order to measure the bar length, Ohta et al. (1990) and Aguerri et al. (2000a) use the bar and interbar Fourier intensities (I_b and I_{ib} respectively), defined as:

$$I_b = I_0 + I_2 + I_4 + I_6 \tag{2.6}$$

$$I_{ib} = I_0 - I_2 + I_4 - I_6 \tag{2.7}$$

From Aguerri et al. (2000a), the bar region is defined as:

$$\frac{I_b}{I_{ib}} > \frac{1}{2}\left[\left(\frac{I_b}{I_{ib}}\right)_{max} - \left(\frac{I_b}{I_{ib}}\right)_{min}\right] + \left(\frac{I_b}{I_{ib}}\right)_{min} \tag{2.8}$$

and the last radius at which this is satisfied (within the bar region) is taken as the bar radius. More simply, Ohta et al. (1990) define the bar region as $(I_b/I_{ib}) > 2$. Because Aguerri et al. (2000a) claim Equation 2.8 takes the behaviour of the Fourier intensity profiles better into account than simply $(I_b/I_{ib}) > 2$, we use their definition as the bar radius from the Fourier intensities.

2.3.1.3 Elliptical Isophotes

Perhaps a more familiar means of finding the bar radius is to fit elliptical isophotes to the light distribution of a galaxy disk and use either the radius of maximum ellipticty or the radius where the ellipticity changes discontinuously as an indication that the end of the bar has been reached (e.g., Wozniak et al. 1995; Aguerri et al. 2000a). Because Aguerri et al. (2000a) find that choosing the radius of discontinuity often leads to overestimating the bar length, we use the radius at which the ellipticity reaches its maximum value as the bar length.

2.3.2 Bar Strength

The second bar parameter we want to measure is the strength. The strength of a bar can be thought of as a tracer of the underlying gravitational potential of the bar, best traced by NIR imaging since bars are stellar features. While originally only a visual classification based

on how bright or large the bar appeared (de Vaucouleurs 1959), with strong bars simply classified as SB and weaker bars as SAB, bar strength is now a quantifiable parameter. This parameter can be measured via multiple methods, such as the torques present in the galaxy (Buta & Block 2001; Laurikainen & Salo 2002), or the ellipticity of isophotes (Martin 1995). Here, we will follow Aguerri et al. (2000a) and define the bar strength as

$$S_b = \frac{1}{r_{bar}} \int_0^{r_{bar}} \frac{I_2}{I_0} dr \tag{2.9}$$

where r_{bar} is the radius of the bar, and I_2 and I_0 are the $m = 2$ and $m = 0$ Fourier amplitudes shown in Equation 2.5. However, as we begin our azimuthal light profiles at $3''$ and *not* the very center, we can only report a lower limit on the bar strengths for our galaxies. We will use the behaviour of our relative Fourier amplitudes as an indicator of how well our lower limits approximate the true strength. Similar to our bar radius measurements, we obtain bar strengths in only the I band and 3.6 μm. In order to get a more accurate indicator of the bar strength, we also remake our azimuthal light profiles starting at $1.5''$ and increase the azimuthal spacing from 3° to 6° for I and from 6° to 12° for 3.6 μm. We do this to probe down closer to the centers of our galaxies to see if this increases the bar strength significantly. These new profiles are not used further in the analysis.

2.3.3 Corotation Radius

Finally, the third parameter we want to measure is the corotation radius. The corotation radius (R_{CR}) of the bar is where orbital speeds are equal to the pattern speed of the bar. As will be discussed in Sec. 2.5.3, R_{CR} is useful for determining relative bar pattern speeds and in turn inferring properties of the dark matter halo. There are numerous ways of measuring or inferring R_{CR}, including: identifying R_{CR} with photometric rings (i.e. Buta 1986; Pérez et al. 2012), modeling galaxies based on their luminosity distributions or velocity fields (i.e. Salo et al. 1999; Rautiainen et al. 2004, 2008), phase intersections of multi-band photometry (Puerari & Dottori 1997), and many others.

For this work, we will use the Puerari & Dottori (1997, hereafter PD97) method to measure R_{CR}. PD97 expanded upon the results of Beckman & Cepa (1990), by showing how phase crossings of B and I-band images can be used as an indicator of R_{CR}. Based on spiral density wave theory (Lin & Shu 1964), spiral arms act as density waves that trigger star formation by compressing gas. As orbits are faster within corotation and slower outside, this means that the shock front triggering star formation is present on different sides of the arm on either side of R_{CR}. Since the shock can be traced by newer O and B stars and the underlying density wave can be traced by the older stellar population, the phase intersection between the B and I bands will occur at corotation.

This method has been used to determine the corotation radii for HSBs, and has found consistent results with both direct measurements of the pattern speed and numerical simulations of real galaxies (Aguerri et al. 1998; Vera-Villamizar et al. 2001; Sierra et al. 2015). In addition, Martínez-García & Puerari (2014) expanded the use of this method to HI, CO, 24 μm, and FUV with success.

We calculate the phase as:

$$\Theta(r) = \arctan\left(\frac{\mathrm{Re}(\mathcal{F}(r))}{\mathrm{Im}(\mathcal{F}(r))}\right) \tag{2.10}$$

where $\mathrm{Re}(\mathcal{F}(r))$ and $\mathrm{Im}(\mathcal{F}(r))$ are the real and imaginary parts of the Fourier transform shown in Eq. 2.1 respectively. In order to use the PD97 method, we require images in photometric bands separated by a large wavelength range, specifically one band for the newer stellar population and one for the older. We use the B band to trace the newer stars, and the I band and 3.6 μm to trace the older stars.

R_{CR} is the intersection between the B band phase profile and either the I band or 3.6 μm phase profile. We take the first intersection after the bar radius to be R_{CR}. Since we are using the I band and 3.6 μm as tracers of the older stellar populations, both phase profiles should intersect the B band at roughly the same radius. This is because even though the I band and 3.6 μm are separated by a large wavelength range, they both trace the older stars.

Table 2.2: Bar radii (R_{bar}), corotation radii (R_{CR}), relative bar pattern speeds ($\mathcal{R}$), and lower limits on bar strengths (S_b) for our sample. Radii are in arcsec. Relative bar pattern speeds and bar strengths are dimensionless. Bar radii are those derived from our azimuthal light profile method (see Sec. 2.3.1.1).

	I				3.6 μm			
Galaxy	R_{bar}	R_{CR}	$\mathcal{R}$	S_b	R_{bar}	R_{CR}	$\mathcal{R}$	S_b
UGC 628	11.21±0.92	13.96±0.46	1.25±0.11	0.26	11.40±1.20	13.96±0.60	1.22±0.14	0.22
F568-1	4.37±0.46	5.86±0.46	1.34±0.18	0.13	4.80±0.60	7.06±0.60	1.47±0.22	0.14
F568-3	8.93±0.92	10.06±0.46	1.13±0.13	0.19	9.60±1.20	13.86±0.60	1.44±0.19	0.19
F563-V2	6.65±0.46	15.86±0.46	2.38±0.18	0.29	7.20±0.60	15.86±0.60	2.20±0.20	0.26

2.4 Results

In this section we detail the results for each galaxy individually. Final bar lengths, strengths, and corotation radii are shown in Table 2.2. In general, we find that all four of our galaxies show very strong $m = 2$ amplitudes, and some show strong $m = 4$ and $m = 6$ amplitudes. This leaves little doubt that our galaxies are barred (see Sec. 2.3.1.2). In fact, the strength of our $m = 2$ and $m = 4$ amplitudes are comparable to those of HSBs from Elmegreen & Elmegreen (1985).

2.4.1 UGC 628

As seen in Fig. 2.1, UGC 628 displays a clear bar and dual spiral arm morphology. We also can see that there is a clear difference in appearance between the B and I-band images. We see the spiral arms more clearly in the B-band image, as well as numerous HII regions that appear along the arms. In the I-band image we can see the bar is both visually larger and fatter.

2.4.1.1 Bar Radii

Our azimuthal light profiles for UGC 628 are shown in Fig. 2.2. Here, the profiles are plotted only every 1.2″ for the B and I bands and every 1.8″ for 3.6 μm in order to more clearly see the behaviour of the profiles. The profiles are plotted in a rainbow continuum with the red

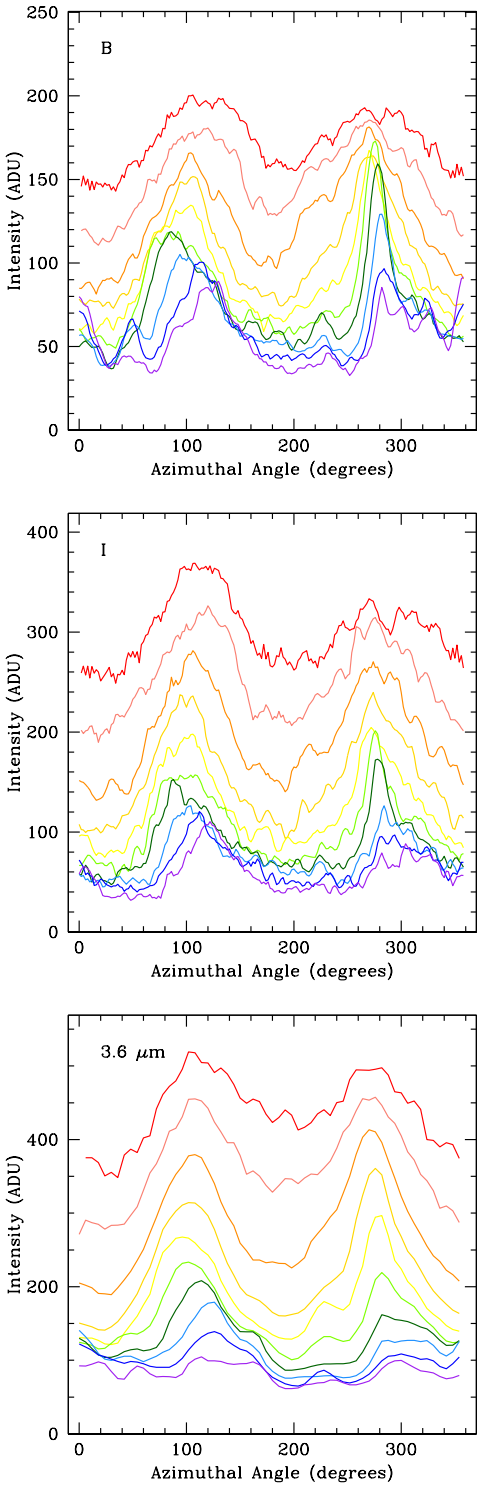

Figure 2.2: Azimuthal light profiles for UGC 628 in B (top), I (middle), and 3.6 μm (bottom). For clarity, profiles are plotted every 1.2″ (every 6 pixels) for the B and I-bands and 1.8″ (every 3 pixels) for 3.6 μm. All three bands begin at 3″. Profiles are plotted in a rainbow continuum, with red as the inner radius and purple the outermost.

profile (top line) showing the inner radius and the purple profile (bottom line) the outermost. This galaxy displays strong humps in its light profiles at inner radii, confirming the presence of a bar. In order to quantitatively track the motion of the humps, we fit Gaussians to the light profiles to obtain azimuthal centroids and intensities (Sec. 2.3.1.1), seen in Fig. 2.3.

In this figure, the brown and orange circles denote the I-band humps, and the purple and pink triangles denote the 3.6 μm humps. We only show the region around the bar, ending around 14″. The top left panel shows the azimuthal position of the two humps seen in Fig. 2.2. The top right panel shows the azimuthal difference between the two humps (ϕ_1 and ϕ_2), with the horizontal black line denoting 180 degrees. Humps due to a bar should remain at this value (Ohta et al. 1990). We can see that between roughly 7″ to 12″ the humps are close to 180 degrees out of phase. We therefore take the angle of each hump at the beginning of this region to be the angle of the bar, or bar centroid. The bottom left panel shows the angle of the humps relative to the bar centroid, remaining roughly constant until ∼11.5″, where both humps in both bands begin moving towards larger azimuthal angle. We find that the humps remain roughly constant in angle before moving together towards larger azimuthal angle, where they begin tracing the path of the spiral arms. We find that there is still quite significant structure within the bar, as the centroids do not remain exactly constant in the bar region. In fact, the very inner regions ($< 8''$) do not appear constant at all, possibly indicating the presence of a bulge of some sort (see the large movement in the top right and bottom left panels of Fig. 2.3). In the bottom right panel we show the peak intensity of the humps above the galaxy light, measured as the height of the hump above the 'continuum' at each radius seen in the azimuthal light profiles. Here, we see that the intensity drops off significantly after the bar region, most pronounced in the open symbols. This is a reflection of the somewhat non-symmetric nature of the bar, where the northern part of the bar (open symbols) has a more intense decrease in intensity than the southern part (closed symbols). This trend is seen in both bands.

We determine the bar length from the azimuthal light profiles via the bottom left panel of Fig. 2.3. We take the radius where the centroids begin moving together towards larger azimuthal angle (the start of the spiral arms) as an indication that the bar has ended, shown as the vertical dashed lines, short-dashed for the I band and long-dashed for 3.6 μm. The bar lengths from this method are $11.21'' \pm 0.92''$ in I and $11.40'' \pm 1.2''$ in 3.6 μm. Since the radius at which the behaviour given in Ohta et al. (1990) (see Sec. 2.3.1.1) could be assigned to a few of the points in Fig. 2.3, we assign the error to be four pixels (equivalent to $0.92''$) in the I-band and two pixels (equivalent to $1.2''$) in 3.6 μm.

Our second bar length measure comes from our Fourier analysis. In Figures 2.4 and 2.5 we show the relative Fourier amplitudes and bar/interbar Fourier intensities for UGC 628. All three bands show strong $m = 2$ and $m = 4$ modes within the inner regions, strongly supporting the presence of a bar. Using the Fourier Bar/Interbar method from Aguerri et al. (2000a), we find a bar length of $16.96'' \pm 0.46''$ for the I band and $15.86'' \pm 0.60''$ for 3.6 μm. As this measure for the bar length is simply where the Fourier intensities cross the value given by Equation 2.8, the error comes from the radii spacing of our azimuthal light profiles: two pixels (equivalent to $0.46''$) for the I-band and one pixel (equivalent to $0.60''$) for 3.6 μm.

Our third bar length measure is the radius of maximum ellipticity. We show the radial plot of deprojected ellipticity for UGC 628 for all three bands in Fig. 2.6. Here, we use only the I band and 3.6 μm to obtain bar radii, but also show the B band to check how successful our deprojection was. In the outer radii, we can see the isophotes are roughly circular in all three bands, indicating our deprojection was successful. Using the radius of maximum ellipticity of elliptical isophotes, we find the I-band bar radius to be $11.63'' \pm 0.68''$ and a 3.6 μm bar radius of $8.40'' \pm 0.60''$. However, we note that both the I-band and 3.6 μm ellipticity profiles appear quite flat within the bar radius, making the reliability of choosing the radius of maximum ellipticity uncertain for this galaxy. In order to confirm our results, we began our starting radius for `ELLIPSE` at various radii to see what effect this had on the bar radius chosen. We found that this did not affect our bar lengths from this method.

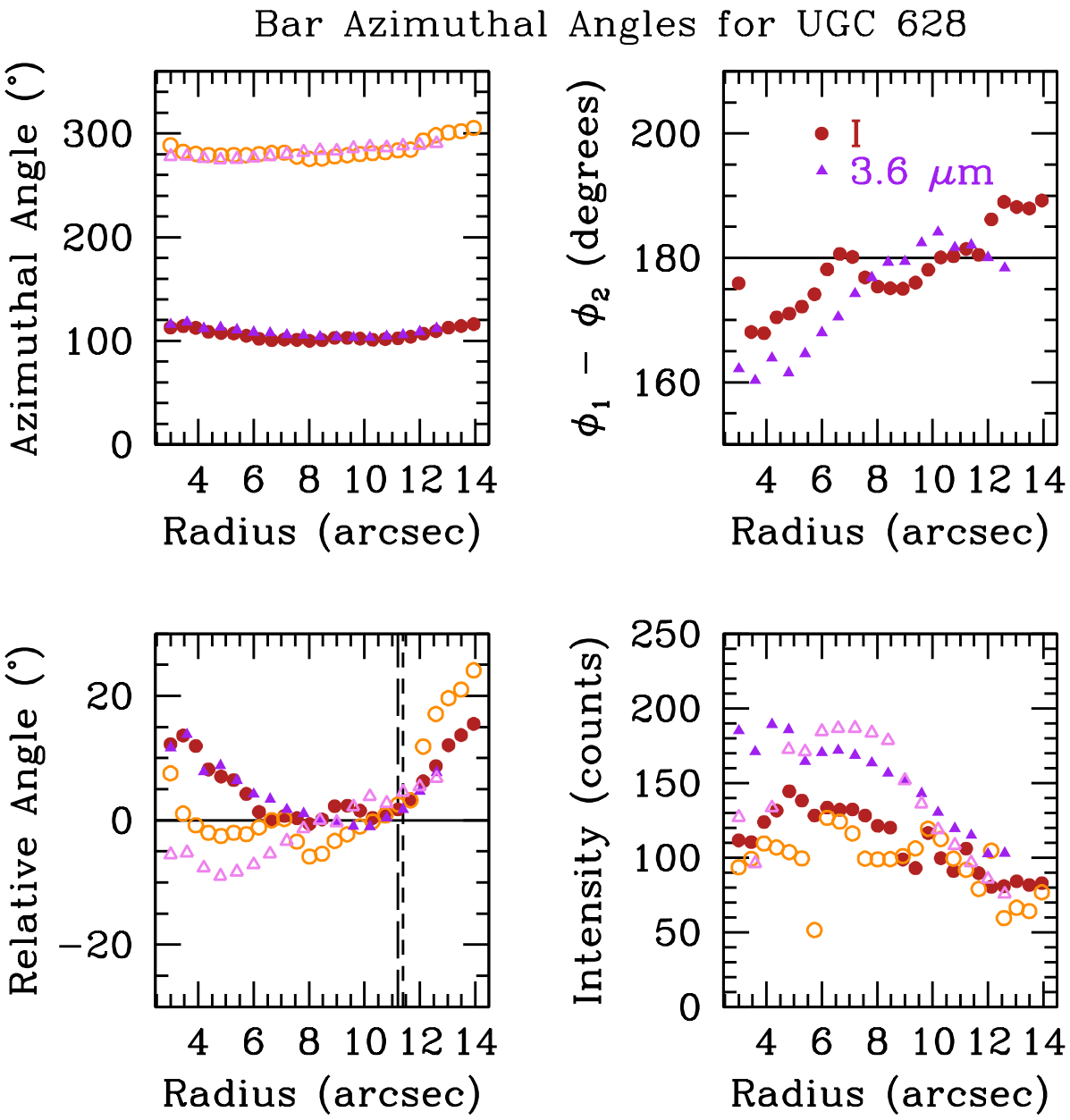

Figure 2.3: Bar azimuthal angle centroid positions for UGC 628. The brown and orange circles denote the location of the I-band humps in Fig. 2.2, and the purple and pink triangles denote the location of the 3.6 μm humps. The top left panel shows the angular positions of the two humps, derived from fits with Gaussians. The top right panel shows the angular difference between the centroids of the two humps, with the horizontal line showing 180 degrees difference. The bottom left panel shows the relative motion from the bar centroid of the humps. The vertical dashed lines indicate the radius of the bar. The bottom right panel shows the intensity of the humps above the galaxy light.

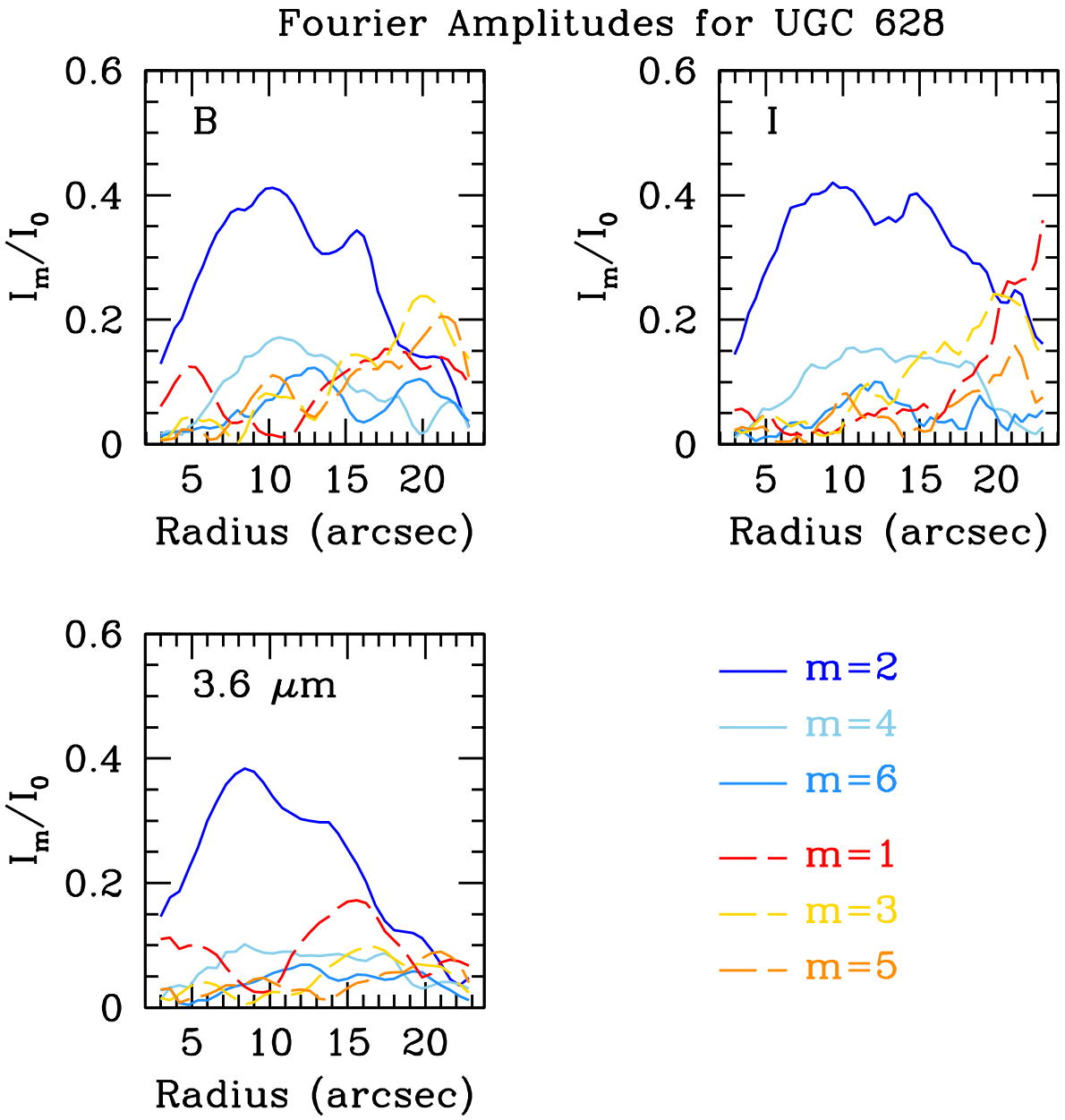

Figure 2.4: Fourier amplitudes for UGC 628. Bluer colors show the even modes, with the dark blue being $m = 2$. Redder colors show the odd modes, with the dark red being $m = 1$. All three bands show strong $m = 2$ and $m = 4$ modes within the inner regions, strongly supporting the presence of a bar.

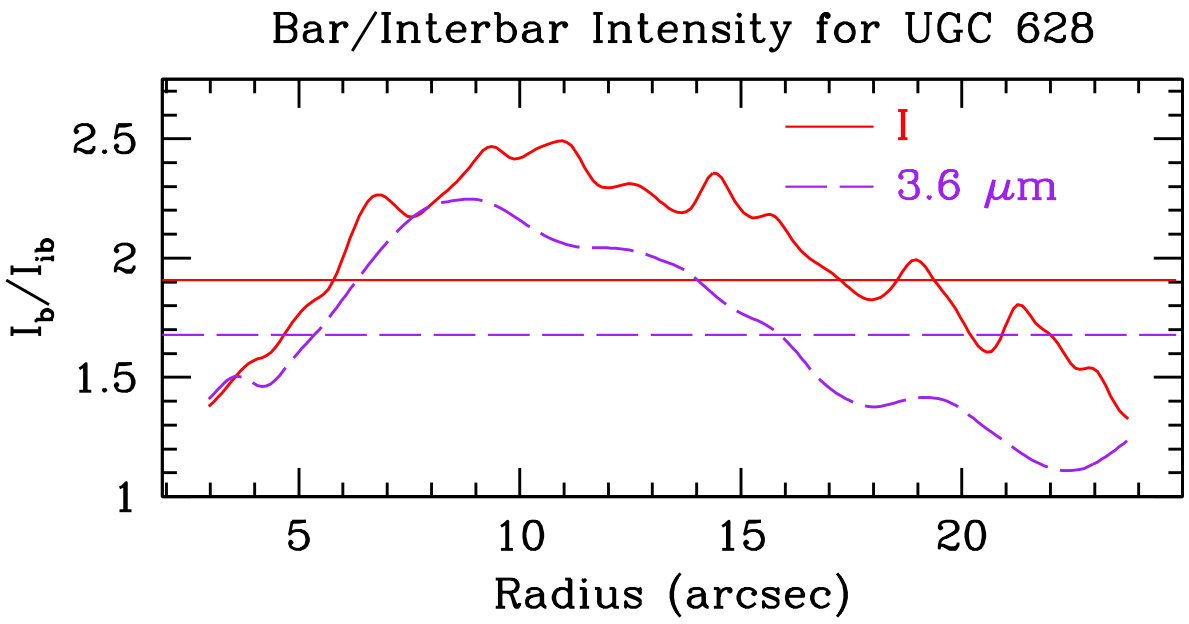

Figure 2.5: Bar/Interbar Fourier intensities for the I band (solid red) and 3.6 μm (dashed purple) for UGC 628. The horizontal lines show equation 2.7.

Therefore, the error on the bar length from this method is equivalent to the radial spacing from ELLIPSE.

These three techniques give us a bar radius that ranges from $\sim$8.5″ to $\sim$16.8″. At first glance, we are left with values that span a factor of two, but this is due to outliers. To compare the results visually, the bar radii are plotted over the deprojected I band and 3.6 μm images of UGC 628 in Fig. 2.7. From this figure, it is clear that the Fourier method overshoots the bar radius in both bands rather significantly, as the red circle extends beyond the fat, bright bar and even includes a rather large portion of the spiral arms. Therefore, we can safely assume the Fourier bar radii are not accurate. The azimuthal and elliptical isophote bar radii agree for the I-band, but the elliptical isophote bar radius for 3.6 μm appears to be too short, with the bar visually extending past the pink circle. Given the agreement between the results for both bands, we use the bar length derived using the azimuthal light profile method as the bar radius for UGC 628 in both I and 3.6 μm, listed in Table 2.2.

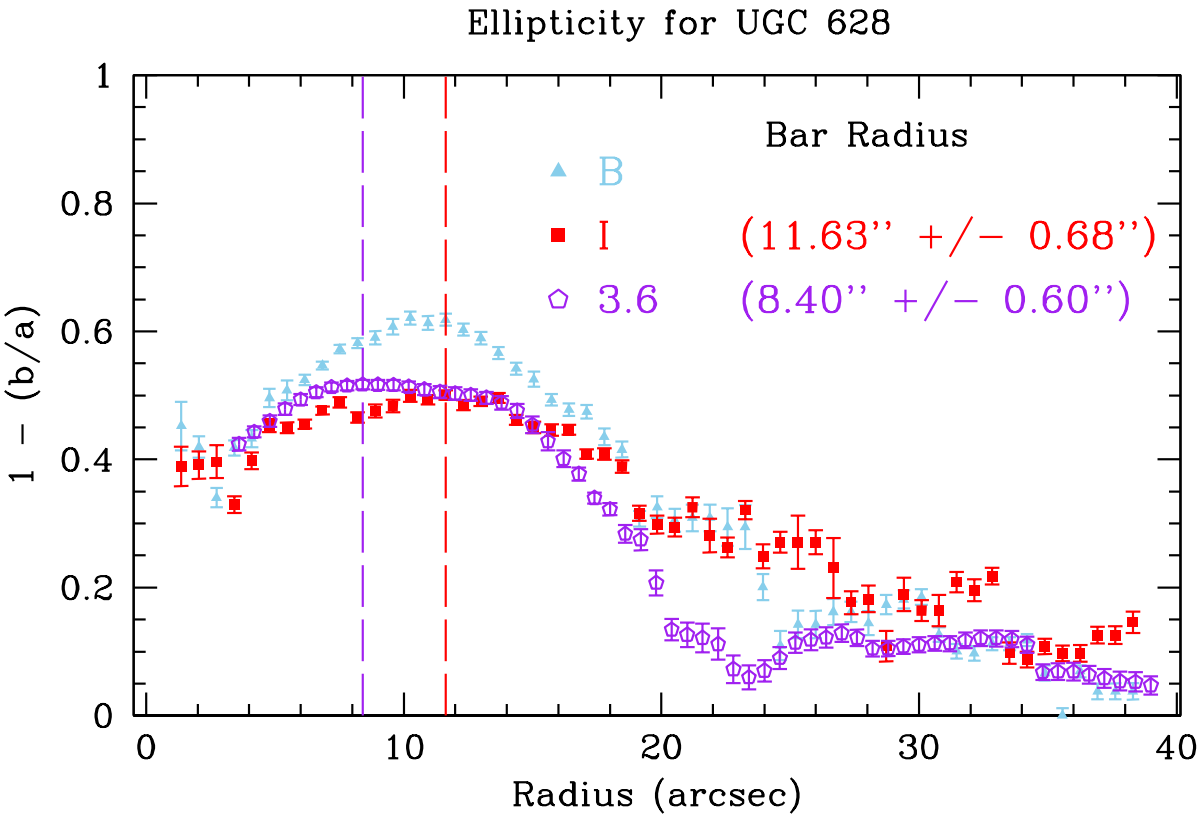

Figure 2.6: Ellipticity as a function of radius of elliptical isophotes for the deprojected images of UGC 628. The roughly zero ellipticity in all three bands at large radii shows our deprojection was successful. The vertical dashed lines indicate the radius of maximum ellipticity in I and 3.6 μm, which we take as the isophotal bar radius. The B band is shown by the blue triangles, I band by the red squares, and 3.6 μm by the open purple pentagons.

2.4.1.2 Bar Strength

The next parameter that we have measured is the bar strength. Using Equation 2.9, we measure bar strengths to be 0.26 and 0.22 in the I and 3.6 μm respectively (see Table 2.2). As described in Sec. 2.3.1.2, these are lower limits on the bar strength. However, based on the relative Fourier amplitudes in Fig. 2.4, it is most likely that these values are close to the true strength, as the $m = 2$ mode appears to be trending towards zero near the center. In addition, when decreasing the starting radius from 3″ to 1.5″ when constructing the azimuthal light profiles (see Sec. 2.3.2) our values remained the same, suggesting our lower limits are accurate.

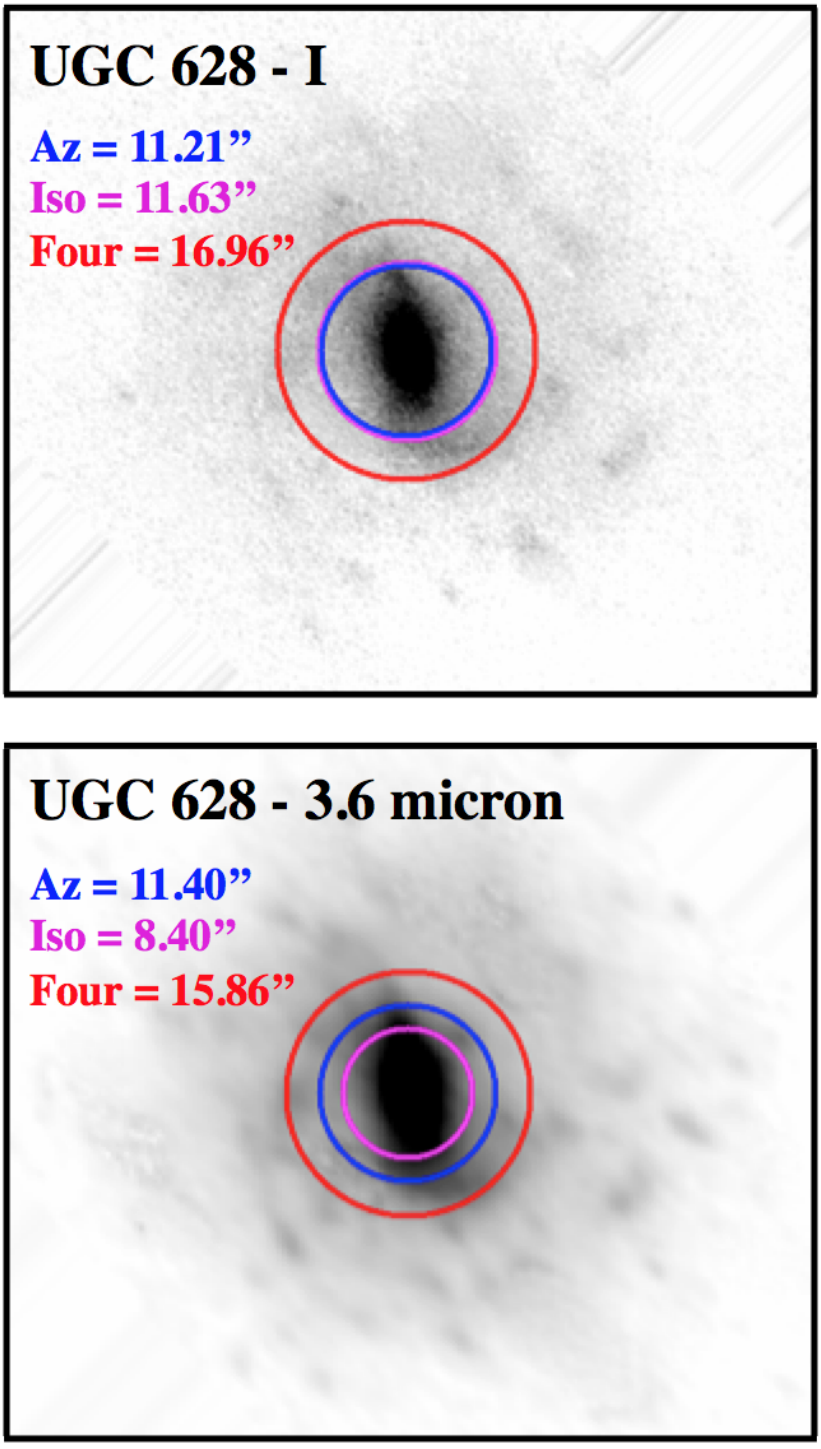

Figure 2.7: Bar radii for the I band (top) and 3.6 μm (bottom) for UGC 628 overplotted on the deprojected images. In both panels, blue circles are derived from the azimuthal light profile method, pink circles are derived from the elliptical isophote method, and red circles are derived from the Fourier bar/interbar intensities. Radii are in arcsec.

2.4.1.3 Corotation Radii

In Fig. 2.8 we show the phase profiles, calculated with Equation 2.10, for all three bands for UGC 628. We find a B,I phase crossing at $13.96'' \pm 0.46''$ and a B,3.6 μm phase crossing at $13.96'' \pm 0.60''$. We also find a second B,3.6 μm phase crossing at $30.36'' \pm 0.60''$, but no second phase crossing between B and I. This second B,3.6 μm phase crossing is beyond the range plotted in Fig. 2.8. Given the clear phase reversal present in both the B,I profiles and B,3.6 μm profiles, we are confident in placing the corotation radius at $13.96'' \pm 0.46''$ for the I-band and $13.96'' \pm 0.60''$ for 3.6 μm, listed in Table 2.2. The error on the corotation radius is equivalent to the radial spacing of the azimuthal light profiles.

As an interesting aside, we can also use the phase profiles to determine if the spiral arms are leading or trailing (Fig. 1 in PD97). Based on the observed phase profiles (Fig. 2.8), we find the shock front (B-band) begins below the density wave (I-band), intersects, and remains at greater phase for all radii. This is indicative of a Z-leading spiral pattern, consistent with our images of this galaxy.

2.4.2 F568-1

F568-1 shows clear dual spiral arm structure, with a small bar and bulge in the center of the galaxy (Fig. 2.1). As with UGC 628, we see that the spiral arms are stronger in the B-band image. We see that the arms in the I-band image are quite diffuse and less extensive than in B. In both bands we see that the arms somewhat vanish before returning at a much fainter level (the south-western arm for instance). We also see that the bar in both bands is quite small angularly.

2.4.2.1 Bar Radii

Our azimuthal light profiles for F568-1 are shown in Fig. 2.9. We find that F568-1 displays a dual humped pattern in its azimuthal light profiles, indicating the presence of a bar. Curiously, we find that while the humps remain at a constant azimuthal separation in the I band with

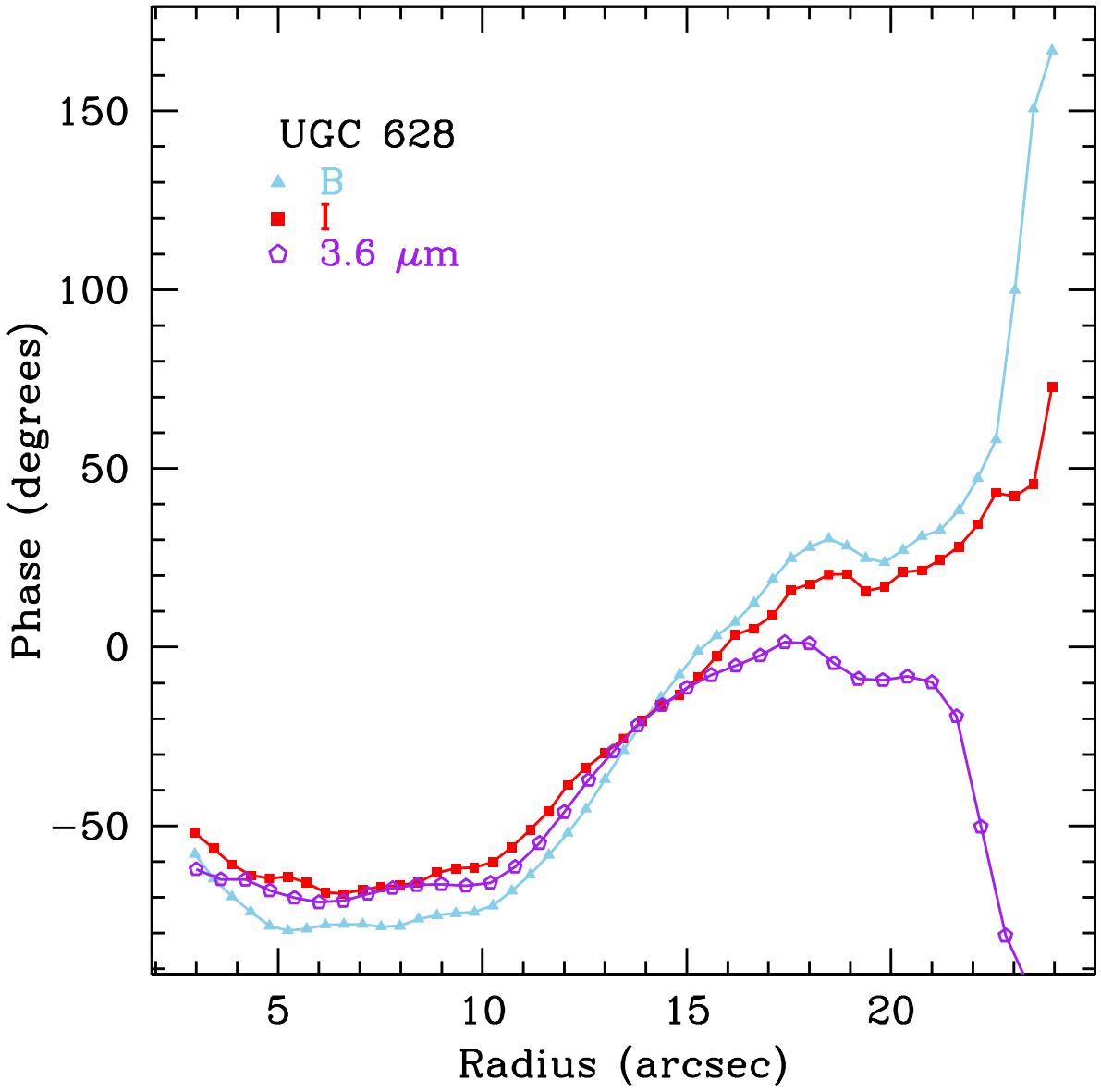

Figure 2.8: Phase profiles for UGC 628: B band (blue triangles), I band (red squares), and 3.6 μm (open purple pentagons).

one another, they do so at 190 degrees as opposed to 180 degrees (top right panel of Fig. 2.10). In addition to the bar, our azimuthal light profiles also clearly show the presence of a dual spiral arm pattern, seen in the path of the humps after the bar radius in the lower left panel of Fig. 2.10. The spiral arms also appear to be 190 degrees out of phase with each other in

the I band as well (top right panel). We do not find significant inner structure in this galaxy, with the humps remaining at quite constant angle within the bar (bottom left panel).

Using our azimuthal light profile method, we find a bar length of $4.37'' \pm 0.46''$ in the I band and $4.80'' \pm 0.60''$ in 3.6 μm for F568-1, shown in Fig. 2.10. After the bar, there is a clear dual armed spiral pattern in this galaxy, seen in the bottom left panel where all four humps begin moving away from the centroid at the same rate. We find the intensity of the humps drops off rather significantly after the bar radius (bottom right panel). We do note that the few points within the bar region indicate that we are pushing the limits of this method. However, given the very clear behaviour of the spiral arms seen in Fig. 2.10, the error on this bar radius measurement is two pixels in the I-band (equivalent to $0.46''$) and one pixel in 3.6 μm (equivalent to $0.60''$).

For our second technique, we show the relative Fourier amplitudes for F568-1 in Fig. 2.11, and the Fourier bar/interbar intensities in Fig. 2.12. We find strong $m = 2$ and $m = 4$ modes in the inner region of the galaxy, supporting the presence of a bar. We also find strong $m = 2$ modes past $\sim 10''$, an indicator of the grand-design spiral arms. Using the bar/interbar Fourier intensities, we find an I-band bar radius of $7.76'' \pm 0.46''$ and a 3.6 μm bar radius of $7.56'' \pm 0.60''$. Values have been trimmed past $13''$ in Fig. 2.12 as the strong even modes due to the spiral arms result in additional crossings far beyond the bar region. As with UGC 628, the errors on this bar radius are equivalent to the radial spacing of the azimuthal light profiles.

For our third technique, we show the radial plots of deprojected ellipticity for F568-1 in Fig. 2.13. After $\sim 26''$, the average ellipticity of the isophotes is roughly zero in the three bands, indicating our deprojection was successful. The ellipticity values in the I-band oscillate between 0 and 0.2, likely due to the very faint outer disk. However, the average ellipticity is quite similar to the other two bands. Using the radius of maximum ellipticity for elliptical isophotes, we find an I band bar radius of $8.44'' \pm 0.91''$ and a 3.6 μm bar radius of $6.60'' \pm 1.20''$. As with UGC 628, the radius of maximum ellipticity is hard to measure for

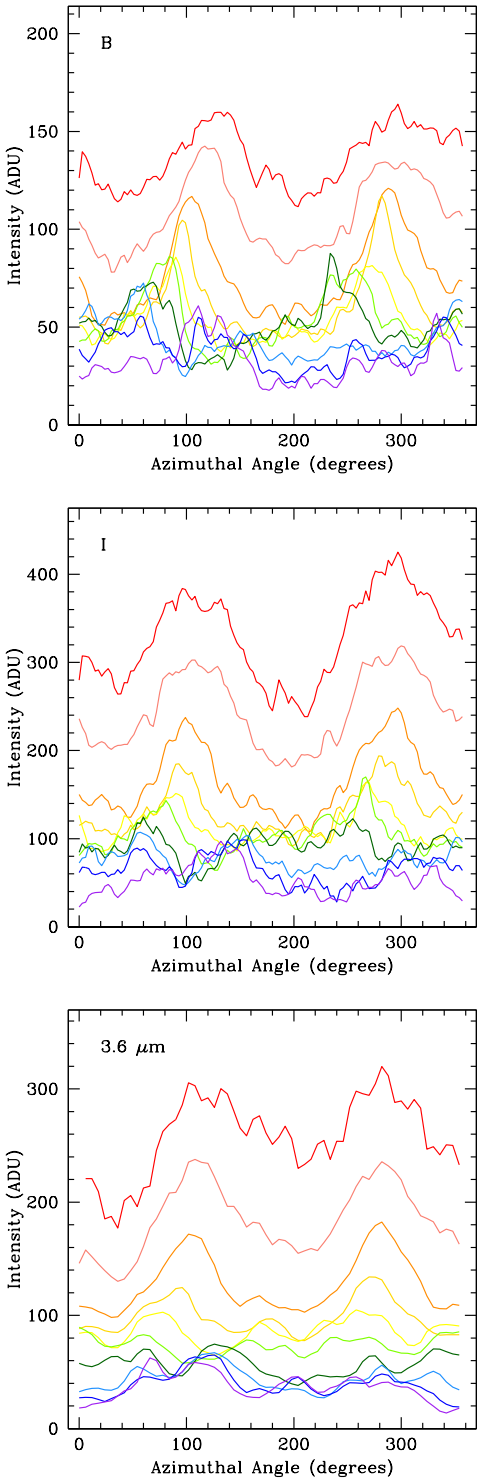

Figure 2.9: Same as Fig. 2.2, but for F568-1.

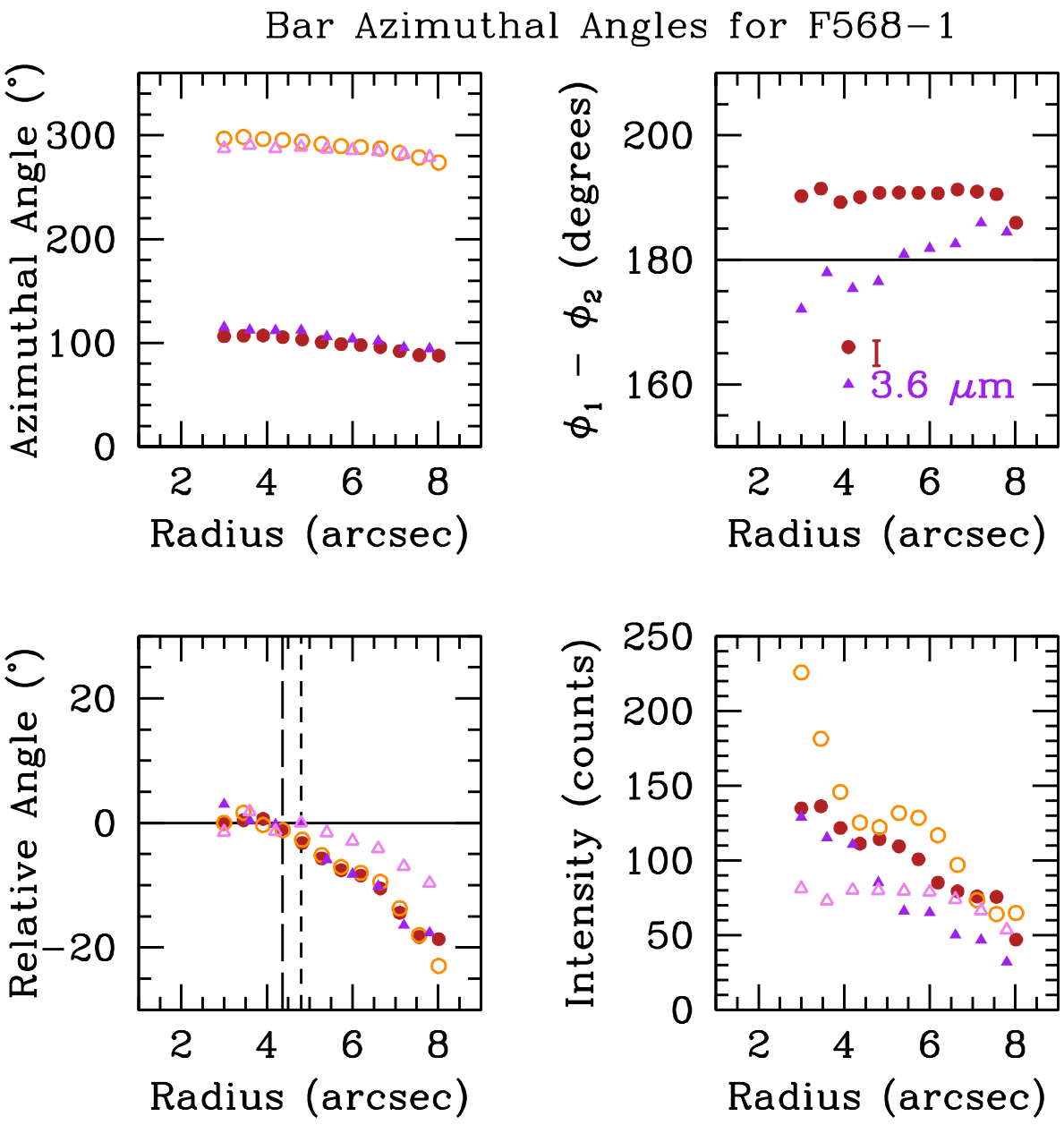

Figure 2.10: Same as Fig. 2.3, but for F568-1.

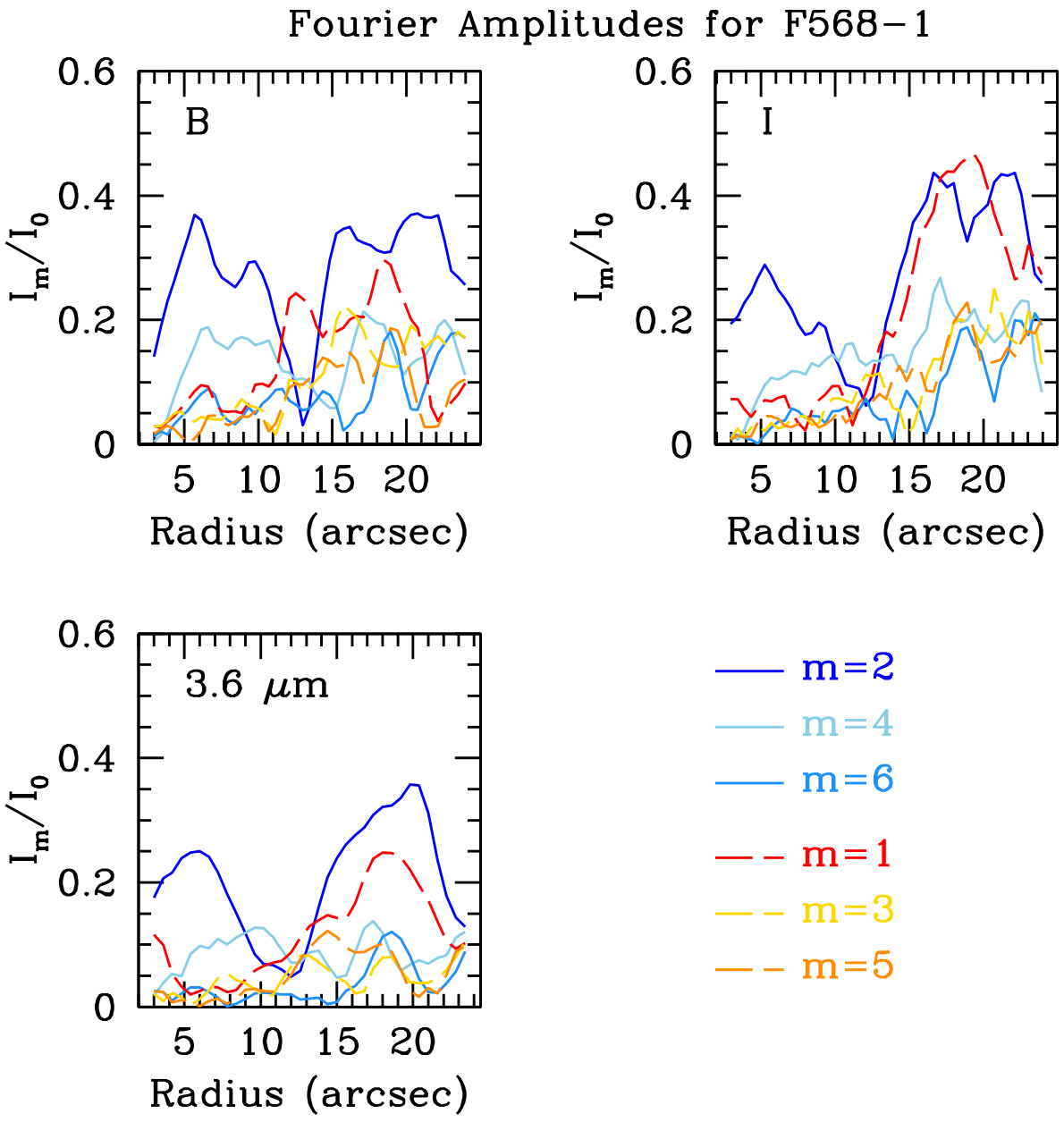

Figure 2.11: Same as Fig. 2.4, but for F568-1.

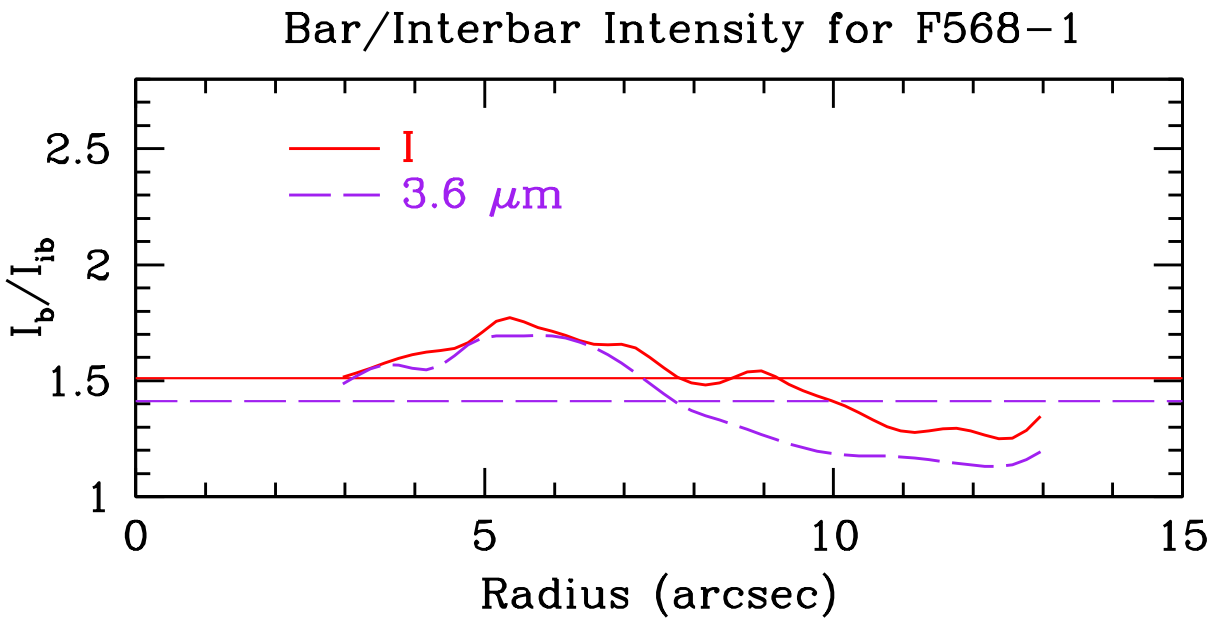

Figure 2.12: Same as Fig. 2.5, but for F568-1.

this galaxy due to the somewhat flat behaviour within the bar radius and beginning of the spiral arms. The error is set to the radial spacing of `ELLIPSE`.

These three techniques give us bar radii that range from ∼4.4″ to ∼8.4″. As with UGC 628 these values span a factor of two due to outliers. The bar radii are visually plotted over the deprojected I-band and 3.6 μm images in Fig. 2.14. Here, the azimuthal light profile bar radius is consistent between the two bands, but the radius of maximum ellipticity differs between the two bands. The Fourier method gives consistent results between both bands, but like with UGC 628 it overshoots the bar radius and contains part of the spiral arms. Therefore, we take the bar radius derived from our azimuthal light profile method to be the bar radius in both I and 3.6 μm, listed in Table 2.2.

2.4.2.2 Bar Strength

We find lower limits on the bar strength to be 0.09 and 0.10 in I and 3.6 μm, respectively. However, when decreasing the starting the starting radius from 3″ to 1.5″ we find our bar strengths increase to 0.13 and 0.14 in I and 3.6 μm respectively (Table 2.2). Due to the

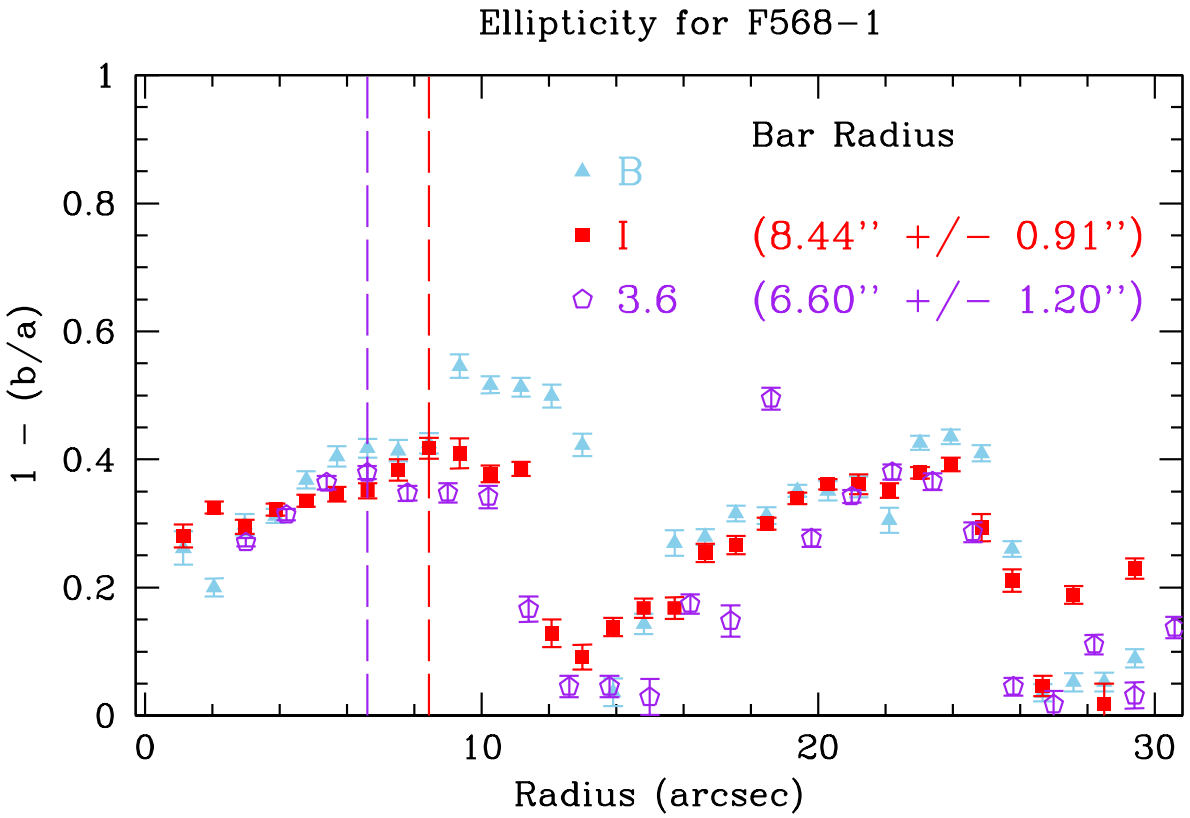

Figure 2.13: Same as Fig. 2.6, but for F568-1.

small angular size of the bar, we are not as confident that these are representative of the true strength as we were with UGC 628.

2.4.2.3 Corotation Radii

We show the phase profiles for F568-1 in Fig. 2.15. We find three sets of clear phase crossings for F568-1. The first B,I phase crossing occurs at 5.86″±0.46″ and the first B,3.6 μm at 7.06″±0.60″. The second B,I phase crossing occurs at 9.66″±0.46″ and the second B,3.6 μm phase crossing occurs at 9.66″±0.60″. The third occurs at 13.26″±0.46″ for B and I and at 13.46″±0.60″ for B and 3.6 μm. Although the B and I-band phase profiles are quite close in value near the first phase crossing, this is simply due to the wide range of angles plotted (-150° to 350°) causing the lines to appear close together and is similar to what is seen in PD97. In addition, the 3.6 μm profile exhibits clear phase reversal as well, leading us to

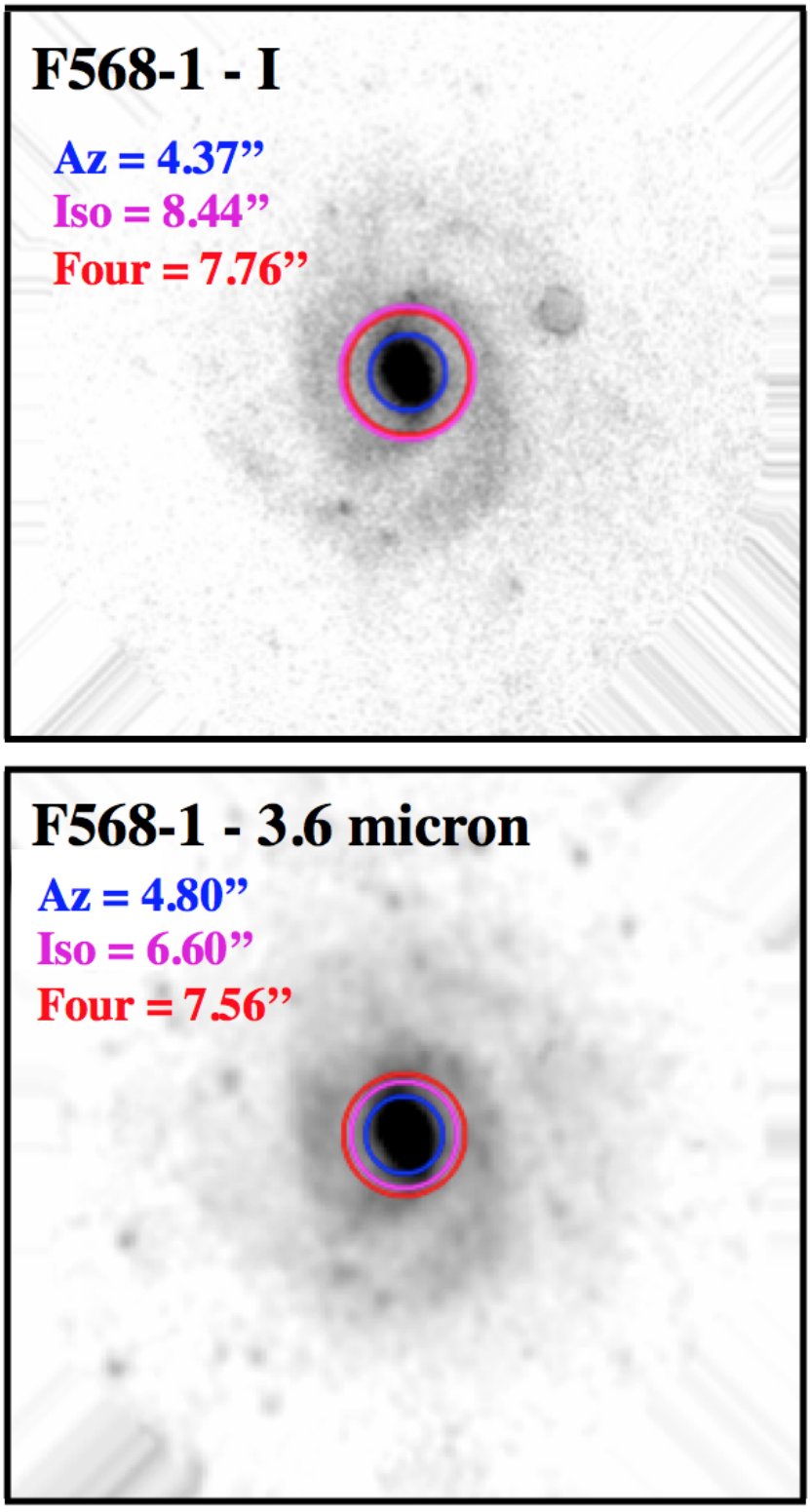

Figure 2.14: Same as Fig. 2.7, but for F568-1.

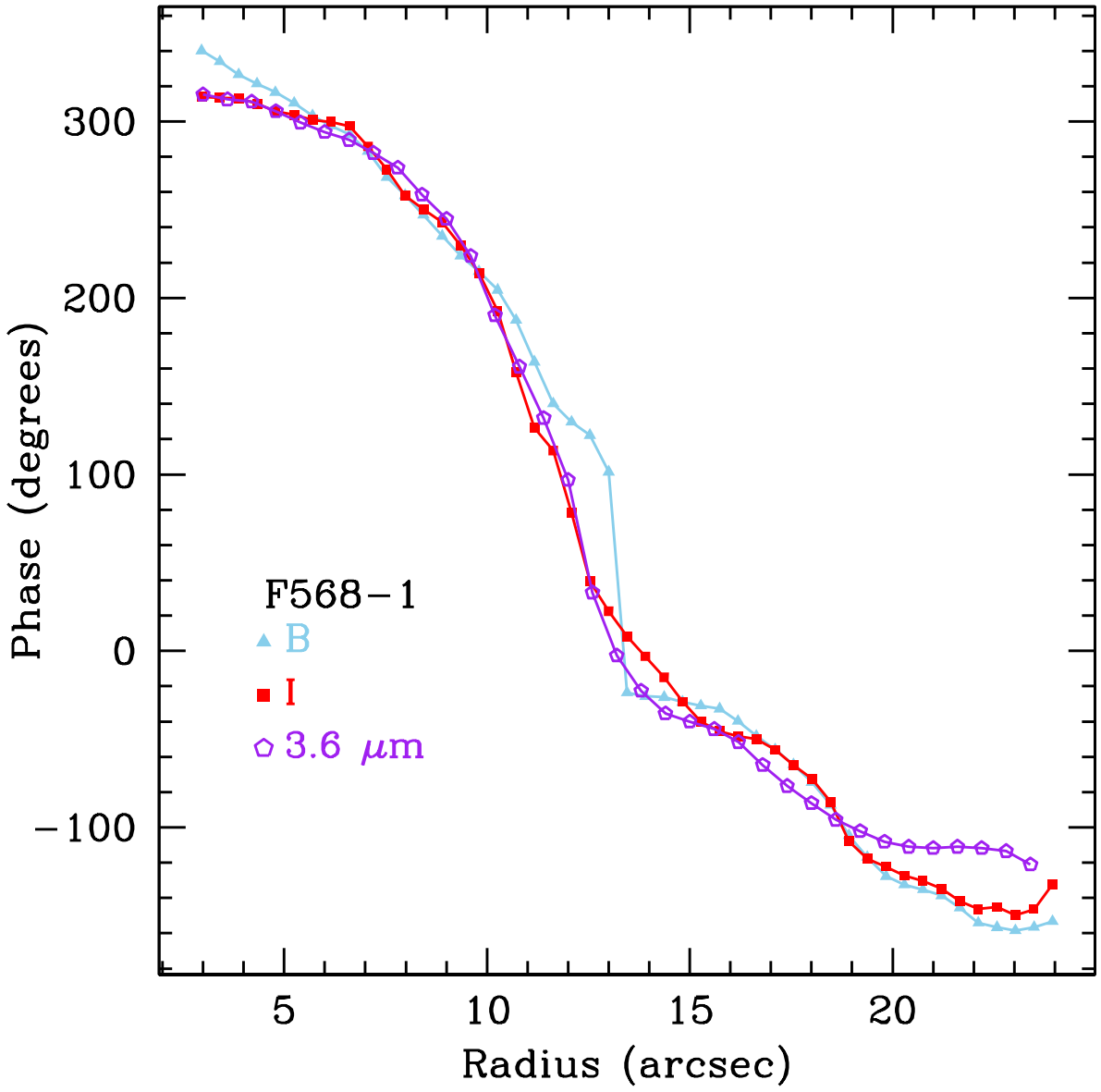

Figure 2.15: Same as Fig. 2.8, but for F568-1.

conclude that the first phase crossing is the radius of corotation for both bands, listed in Table 2.2. As with UGC 628, the error on the corotation radius is equivalent to the radial spacing of the azimuthal light profiles.

We also used these phase profiles to characterize the spiral pattern in F568-1. We find the phase profiles of the shock front and density wave to follow that of an S-leading spiral pattern. This is consistent with our images of this galaxy.

2.4.3 F568-3

F568-3 poses a few complications when examining its morphology. Firstly, when looking at Fig. 2.1 we see that there is a very rough dual arm structure, with one clear, strong arm on the southern side of the galaxy and a weaker arm on the northern side. In addition, it also appears as though there may be a third weaker arm that begins on the eastern side of the bar. Whether this is a true third arm or whether it connects to the northern arm is unclear. Secondly, the bar structure is not as straightforward as it may appear when Fig. 2.1 is scaled differently. As shown in Fig. 2.16, there appears to be either a second bar or an inner spiral structure resembling a lightning bolt. This inner structure is quite small, contained within the inner $3''$ and thus not probed by our azimuthal light profiles. What this means is that the main bar is not exactly symmetric, as it begins at the end of the inner bar. The white lines in Fig. 2.16 are drawn to better show this asymmetric nature of the bar. Finally, the southern arm appears to be quite a bit brighter than the northern arm, which may possibly influence our determination of the bar radius.

2.4.3.1 Bar Radii

The complicated morphology described above can be seen in our azimuthal light profiles for this galaxy in Fig. 2.17. Here, the left hump is the southern arm of the bar/galaxy and shows the rather non-Gaussian shape of the arm, as well as how the two humps are not symmetric. We can see the two humps are not roughly 180 degrees out of phase (top right panel of Fig. 2.18), but closer to 170 degrees. The southern hump also does not appear Gaussian at all, preventing us from obtaining accurate centroids for this hump. However, the northern hump is well behaved, seen in the bottom left and right panels of Fig. 2.18. Here, we see that the northern humps remain quite stationary for the duration of the bar before dramatically moving. We also find that the intensity within the bar region is rather constant, and drops off significantly outside.

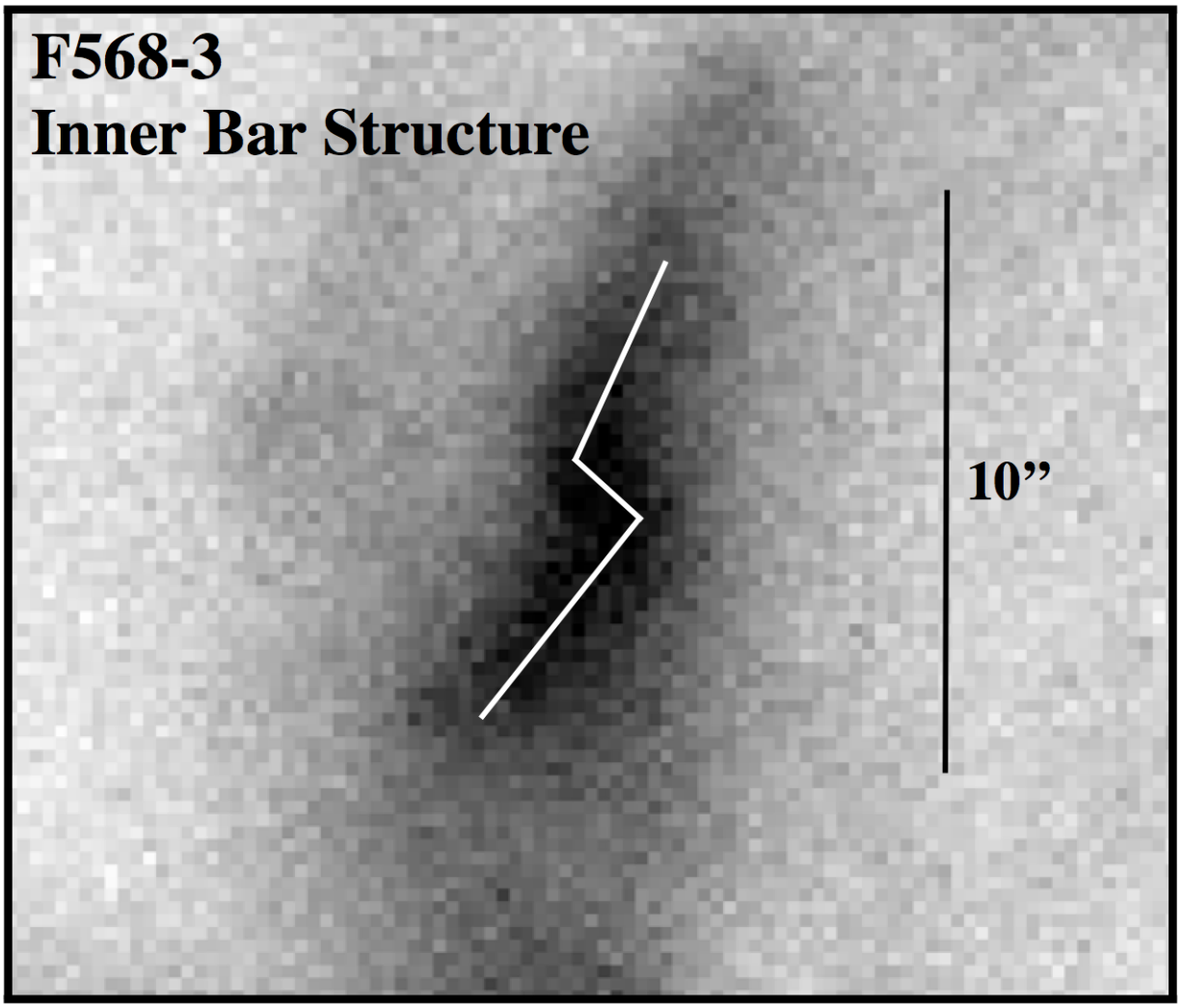

Figure 2.16: Re-scaled B-band image of F568-3 showing the inner bar structure. White lines have been drawn to show the asymmetric nature of the bar.

Using our azimuthal light profile method, we find a bar length of $8.93'' \pm 0.92''$ in the I band and $9.60'' \pm 1.2''$ in 3.6 μm for F568-3, shown in Fig. 2.18. Here we see that there is at least one clear spiral arm, noticeable as the movement away from the centroid after the denoted bar radii. The humps at smaller azimuthal angle appear to remain roughly constant after the bar radius, likely indicating the bright spiral arm seen in Fig. 2.1. Given that only one of the spiral arms is well behaved in Fig. 2.18, we assign an error of four pixels (equivalent to $0.92''$) in the I band and two pixels (equivalent to $1.2''$) in 3.6 μm.

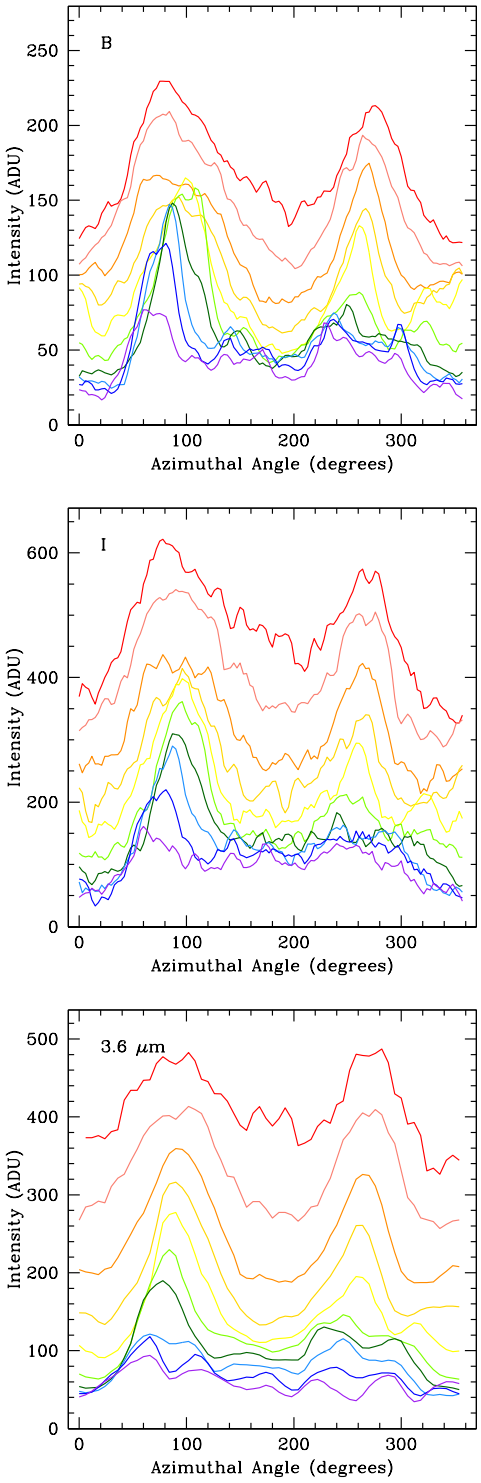

Figure 2.17: Same as Fig. 2.2, but for F568-3.

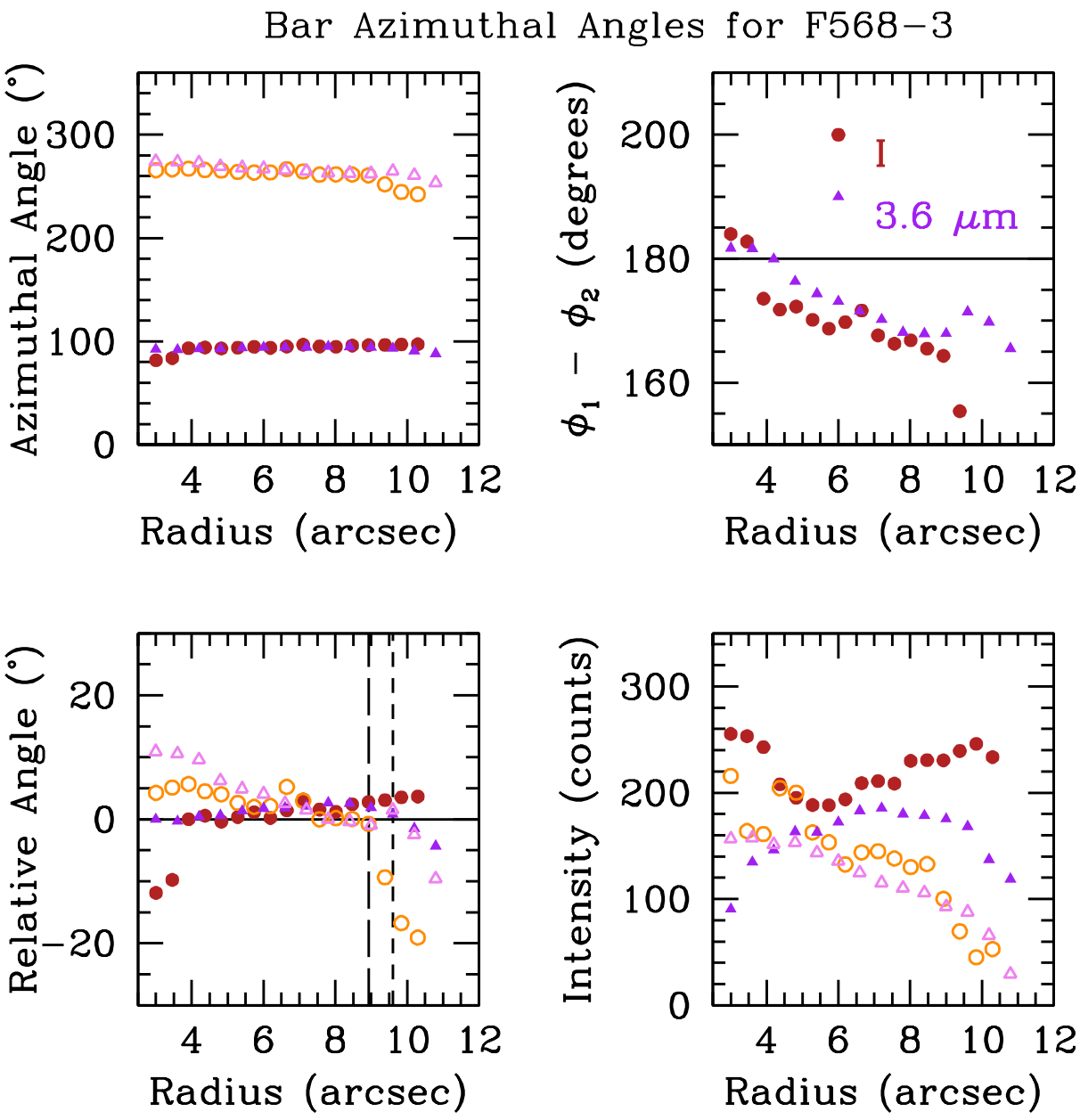

Figure 2.18: Same as Fig. 2.3, but for F568-3.

We show the relative Fourier amplitudes for F568-3 in Fig. 2.19, and the Fourier bar/interbar intensities in Fig. 2.20. We find strong $m = 2$ and $m = 4$ modes in the inner region, but also quite strong $m = 1$ modes. This is likely due to the complicated morphology, and the very bright, southern arm of the galaxy, reinforced by the increase in the $m = 1$ mode past $\sim$15″. Using the bar/interbar fourier intensities we find an I-band bar radius of 13.96″$\pm$0.46″ and a 3.6 μm bar radius of 18.16″$\pm$0.60″. Again, the errors on the bar length from this method are equivalent to the radial spacing of our azimuthal light profiles.

We show the radial plots of deprojected ellipticity for F568-3 in Fig. 2.21. We find the outer radii are consistent with ellipticities of zero, albeit with a large amount of scatter. Using the radius of maximum ellipticity for elliptical isophotes, we find an I-band bar radius of 7.75″$\pm$0.68″ and a 3.6 μm bar radius of 9.00″$\pm$1.20″. The errors on this measurement are equivalent to the radial spacing from `ELLIPSE`.

For F568-3, we have bar radii that range from $\sim$7.8″ to $\sim$18.2″, shown visually in Fig. 2.22. Once again, this large discrepancy can be attributed to the Fourier method. We find agreement between the azimuthal light profile and ellipticity methods, around $\sim$8″ in I and $\sim$9″ in 3.6 μm, with the ellipticity method finding a slightly shorter bar in both bands. Again, we find the Fourier method to overshoot the bar radius, quite significantly in 3.6 μm. Here it almost entirely encompasses the bright portion of the southern arm. We take the bar radius from our azimuthal light profile method to be the bar radius for both bands, listed in Table 2.2.

2.4.3.2 Bar Strength

We find bar strength lower limits of 0.18 in both I and 3.6 μm. When decreasing the starting radius from 3″ to 1.5″ when constructing the azimuthal light profiles we find the bar strength increases only by 0.01 in both bands to 0.19 (Table 2.2). Based on the behaviour of the relative Fourier amplitudes, we find these bar strengths are indicative of the true bar strength for F568-3.

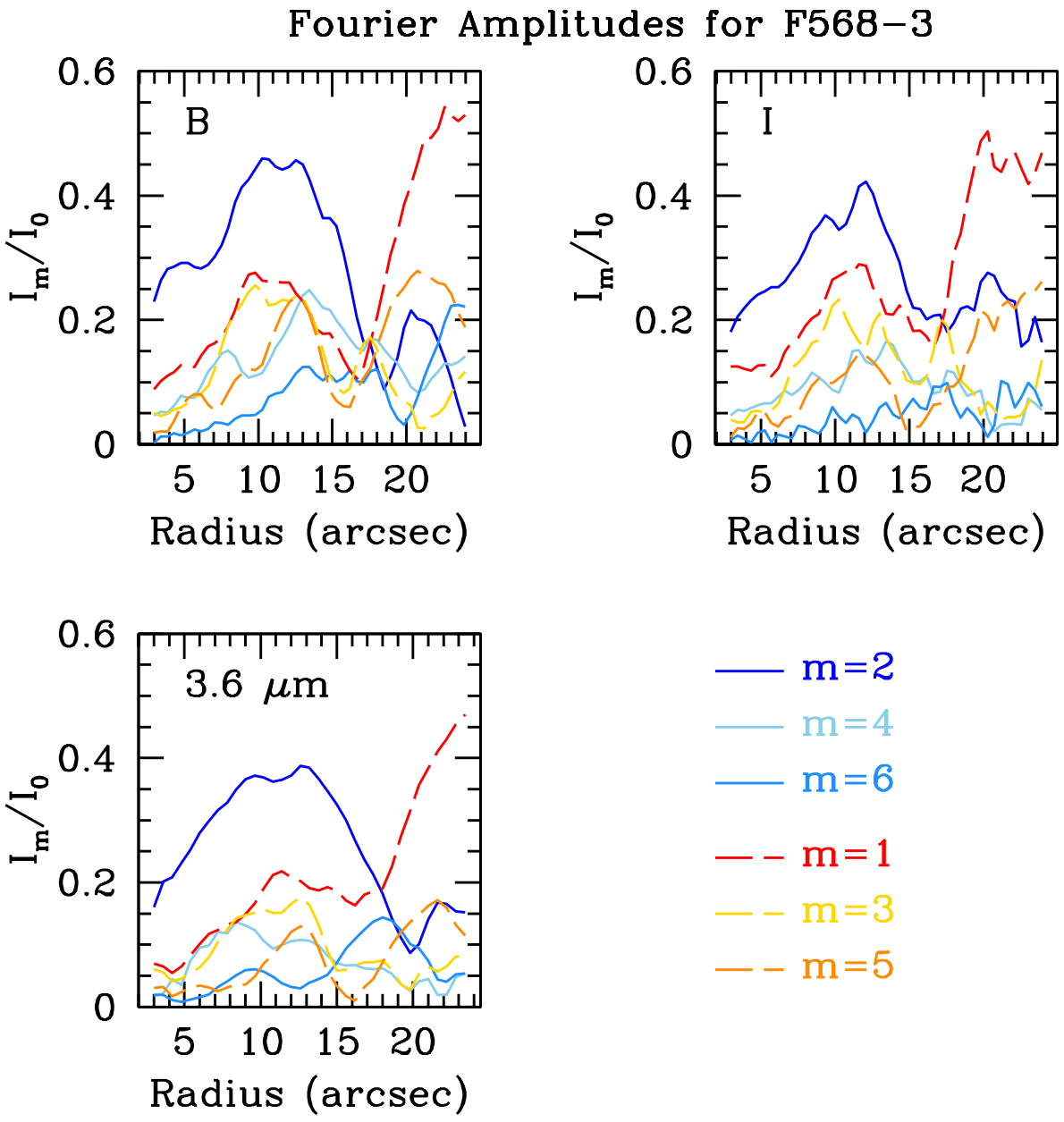

Figure 2.19: Same as Fig. 2.4, but for F568-3.

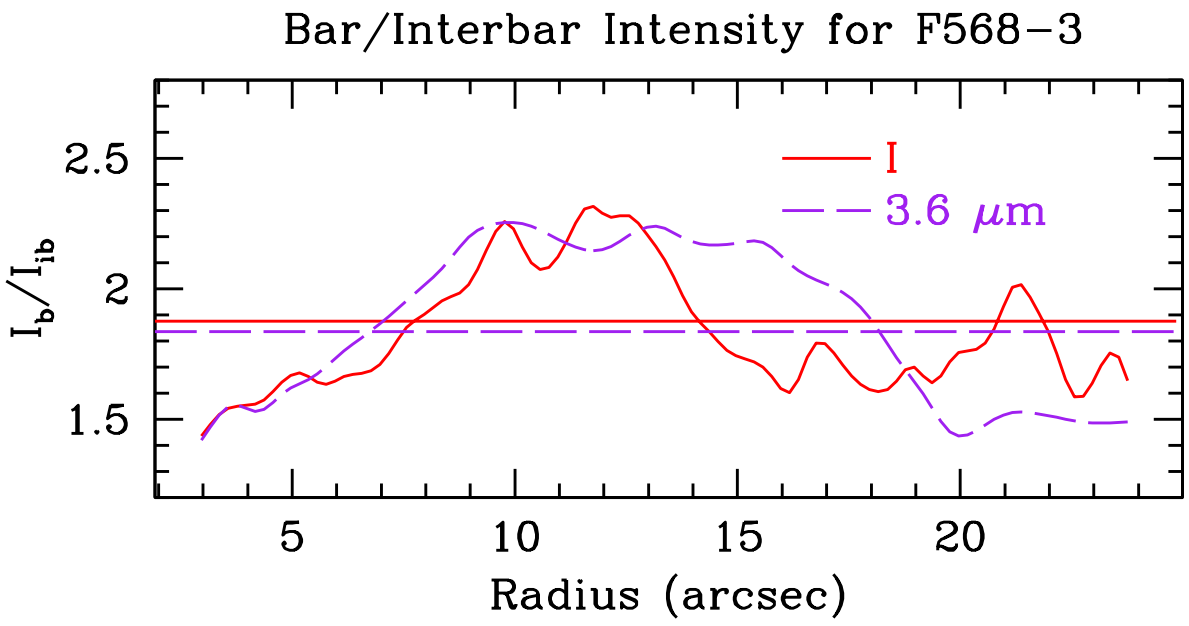

Figure 2.20: Same as Fig. 2.5, but for F568-3.

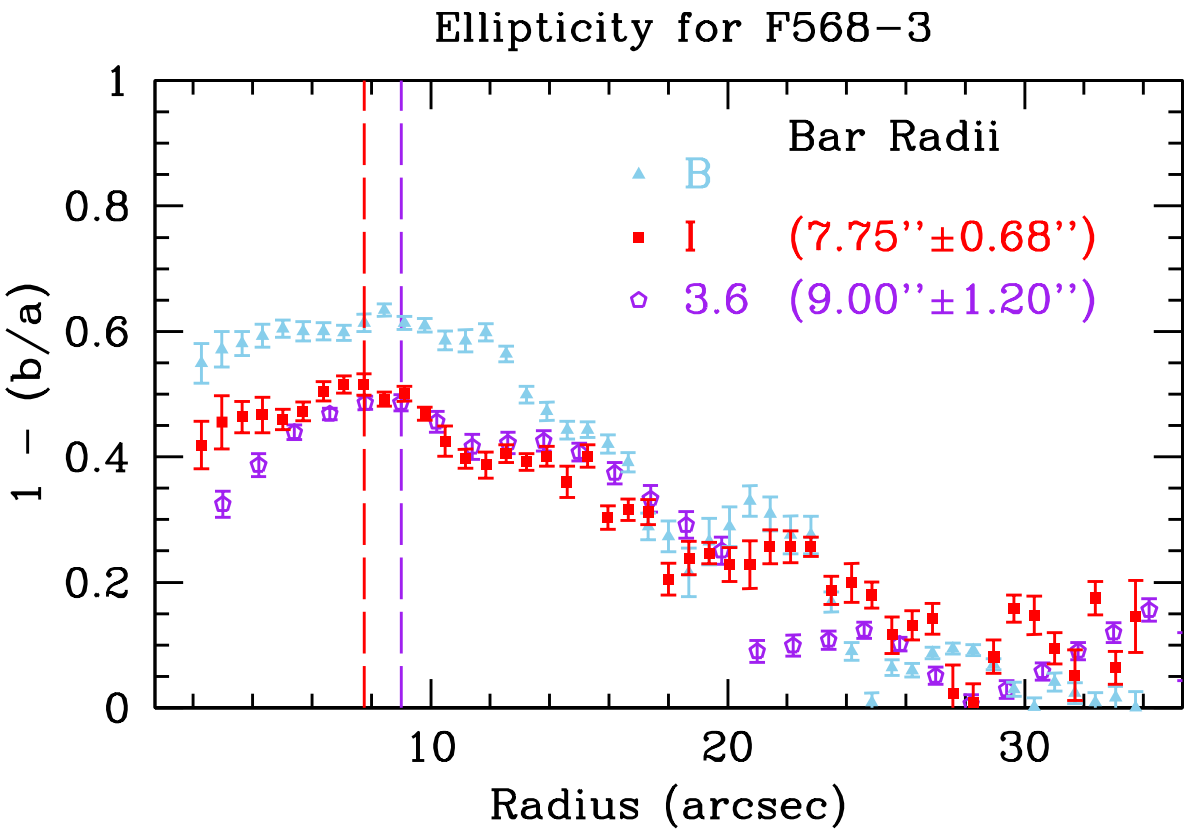

Figure 2.21: Same as Fig. 2.6, but for F568-3.

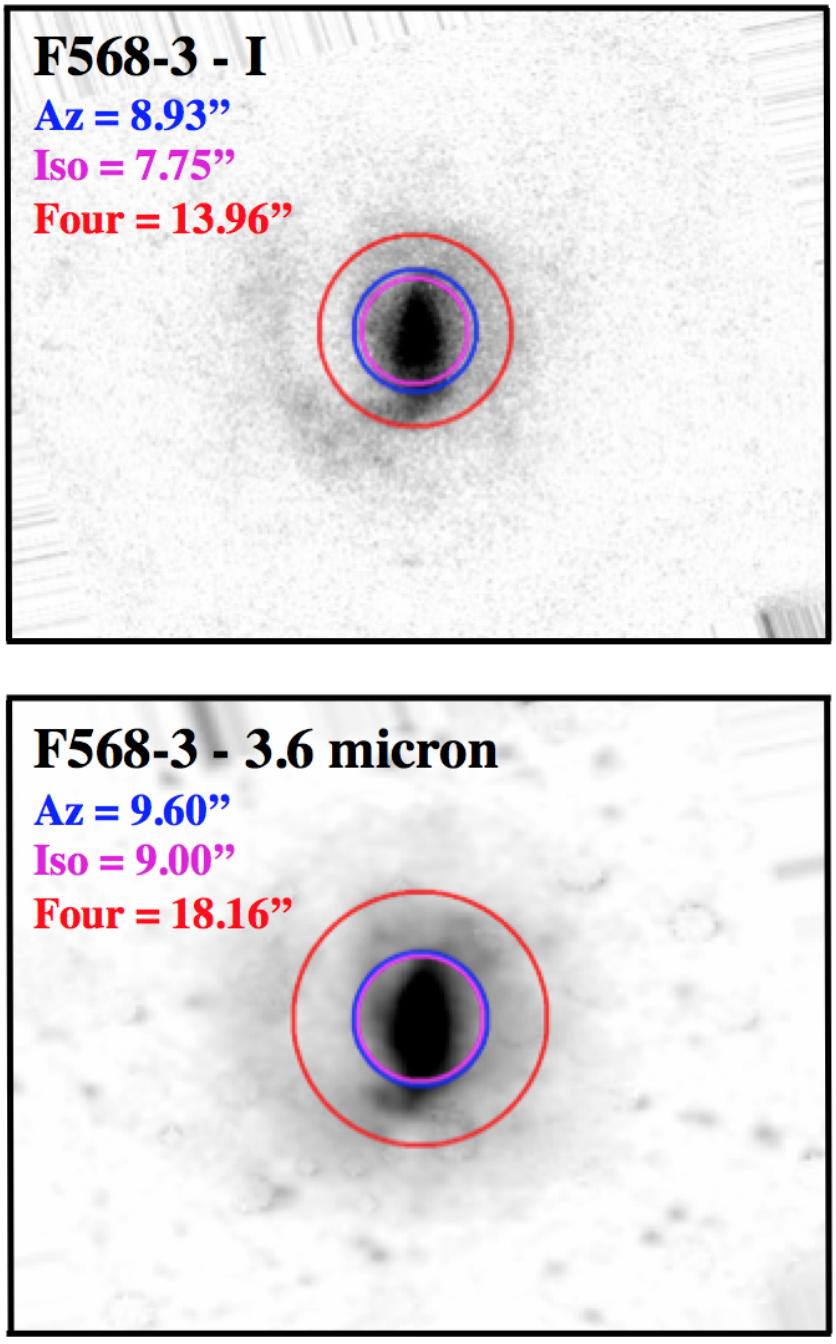

Figure 2.22: Same as Fig. 2.7, but for F568-3.

2.4.3.3 Corotation Radii

Our phase profiles for F568-3 are shown in Fig. 2.23. We find a first B,I phase crossing at $10.06'' \pm 0.46''$, and a second at $13.86'' \pm 0.46''$. We find only one B,3.6 μm phase crossing at $13.86'' \pm 0.60''$. While we do not find a phase crossing near $10''$ between B and 3.6 μm, it is a clear phase reversal for the B and I bands, and cannot be ignored. A possible reason this phase crossing does not appear for the 3.6 μm is due to the large pixel scale. Regardless, if we only had the B and I bands, the phase profile behaviour would be clear enough to trust the intersections. This gives a bar corotation radius of $10.06'' \pm 0.46''$ for the I-band. Because we do not see the phase crossing in 3.6 μm near $10''$, we must report the corotation radius in 3.6 μm as $13.86'' \pm 0.60''$. Again, the errors on the corotation radius are equivalent to the radial spacing of the azimuthal light profiles.

While there is only one *clear* arm present in this galaxy, we also attempted to characterize the spiral pattern in F568-3. We find the phase profiles of the shock front and density wave to follow that of an S-trailing spiral pattern. This is consistent with our images of this galaxy.

2.4.4 F563-V2

F563-V2 shows a very clear bar in its morphology, but not clear spiral arms. There appears to possibly be one arm on the southern edge of the galaxy, however (see Fig. 2.1). The structure in the I-band image is quite diffuse, with not much of the disk visible outside of the bar. There may possibly be a second arm visible on the northern edge of the galaxy in the B-band image. This lack of well-defined arm/disk structure complicates the analysis of this galaxy, particularly the deprojection, as discussed in Sec. 2.2.3.

2.4.4.1 Bar Radii

Our azimuthal light profiles for this galaxy are shown in Fig. 2.24, showing the very bright bar. We find significant deviation from 180 degree separation between the two humps (top right panel of Fig. 2.25). This is due to the northern hump in both bands, which remains at

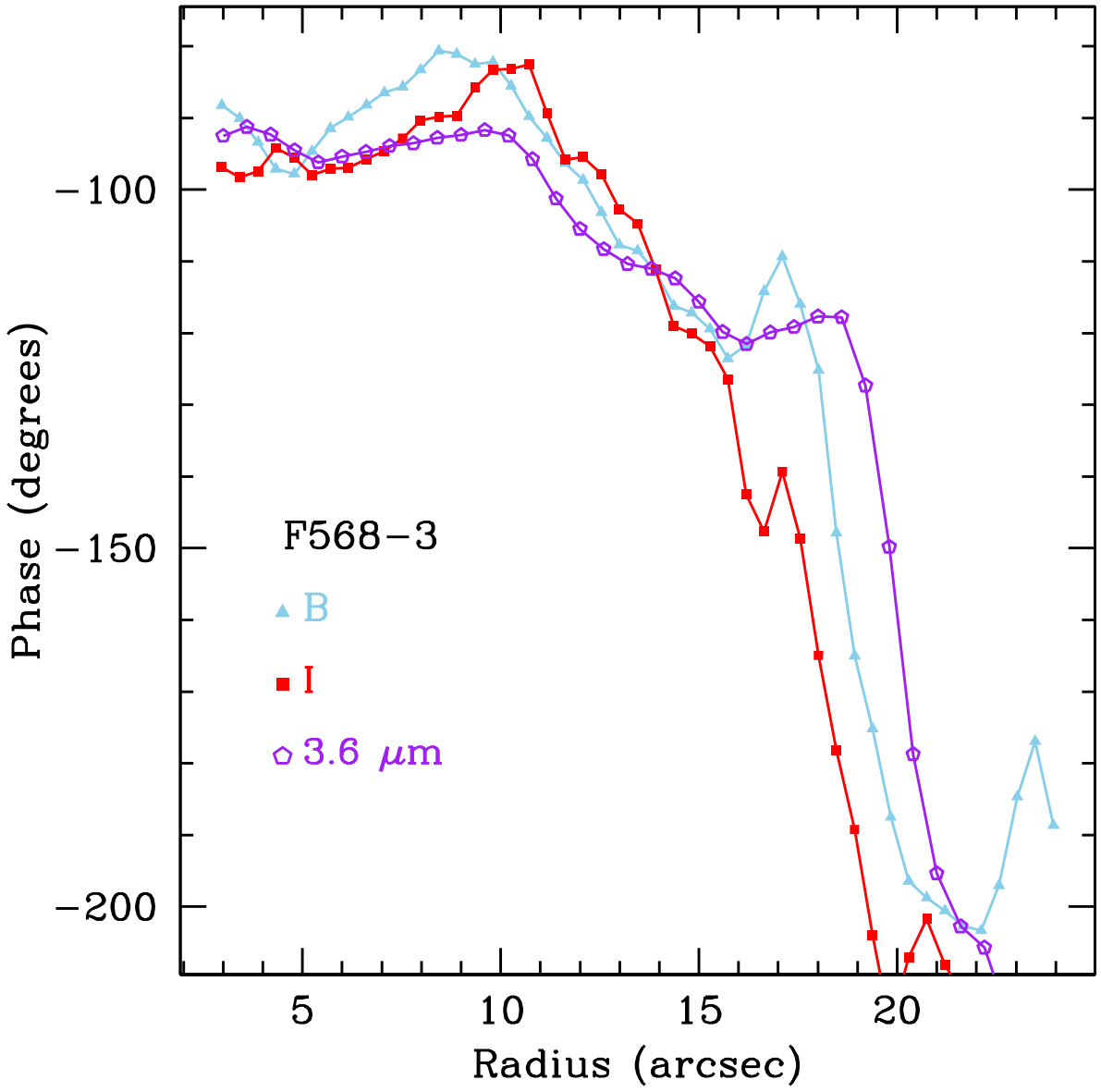

Figure 2.23: Same as Fig. 2.8, but for F568-3.

a constant angle for the range plotted. We therefore only show the movement of the southern hump, seen in the bottom left panel of Fig. 2.25. Here, we can see the movement of the azimuthal centroids in both bands away from the bar, showing the path of the single arm in this galaxy. We also see the dramatic decrease in intensity after the bar radius (bottom right panel).

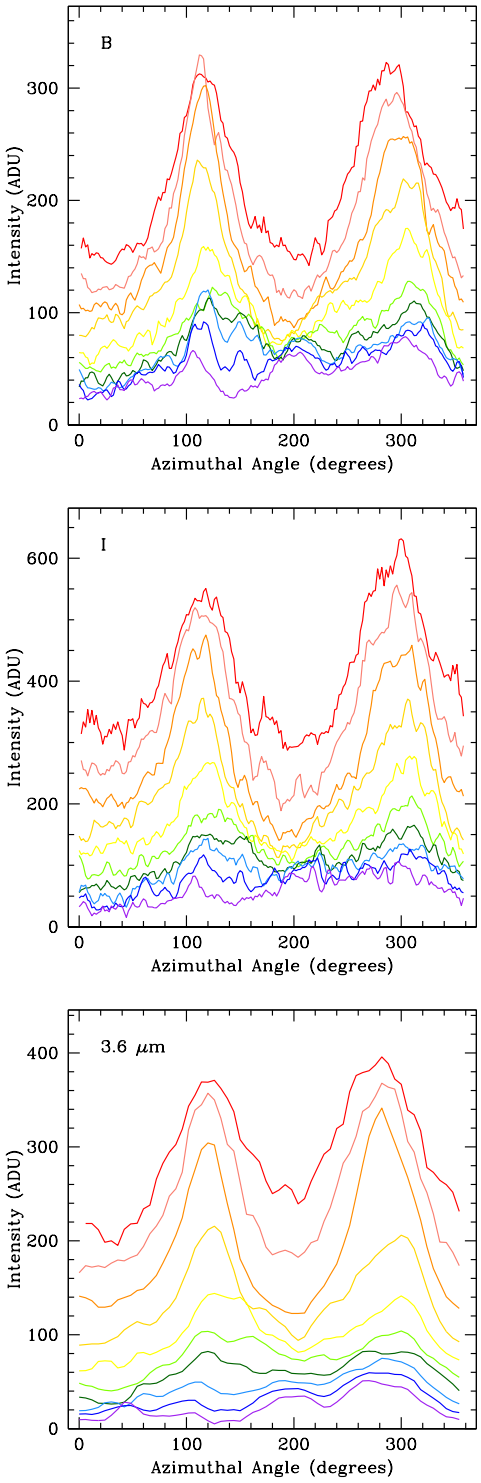

Figure 2.24: Same as Fig. 2.2, but for F563-V2.

Using our azimuthal light profile method, we find a bar length of $6.65'' \pm 0.46''$ in the I-band and $7.20'' \pm 0.60''$ in 3.6 μm for F563-V2. Even though we are only examining the azimuthal behaviour of one spiral arm, the very well behaved nature of the arm gives an error of two pixels in the I band (equivalent to $0.46''$) and one pixel in 3.6 μm (equivalent to $0.60''$).

We show the relative Fourier amplitudes for F563-V2 in Fig. 2.26, and the Fourier bar/interbar intensities in Fig. 2.27. We find strong $m = 2$ and $m = 4$ modes in the inner regions, reinforcing the presence of a bar. Outside the bar, we see a dramatic increase in the strength of the odd modes, reinforcing the single arm in this galaxy. Using the bar/interbar Fourier intensities, we find a bar radius in the I band of $7.96'' \pm 0.46''$ and a 3.6 μm bar radius of $8.56'' \pm 0.60''$. As with the other three galaxies, the error on this bar length is equivalent to the radial spacing of our azimuthal light profiles.

We show the radial plots of deprojected ellipticity for F563-V2 in Fig. 2.28. Using the radius of maximum ellipticity of elliptical isophotes, we find an I-band bar radius of $5.02'' \pm 0.91''$ and a 3.6 μm bar radius of $9.60'' \pm 2.40''$. The errors on these measurements is equivalent to the radial spacing from `ELLIPSE`.

We find bar lengths that range from $\sim 5''$ to $\sim 9.6''$ for F563-V2, shown in Fig. 2.29. The wide range of values is due to the bar length from the elliptical isophote method. We find the azimuthal light profile to provide consistent bar radii between the two bands, $6.7''$ and $7.2''$. The ellipticity method does not provide consistent results, with the 3.6 μm bar radius much longer than the I-band radius, $5''$ vs. $9.6''$. The Fourier method provides consistent results, both between bands, and roughly with our azimuthal light profile method, $8''$ and $8.5''$. This is the sole exception for our sample, likely due to the lack of clear spiral arms in this galaxy. Again, we take the azimuthal light profile method bar radius to be the bar length for both bands, listed in Table 2.2.

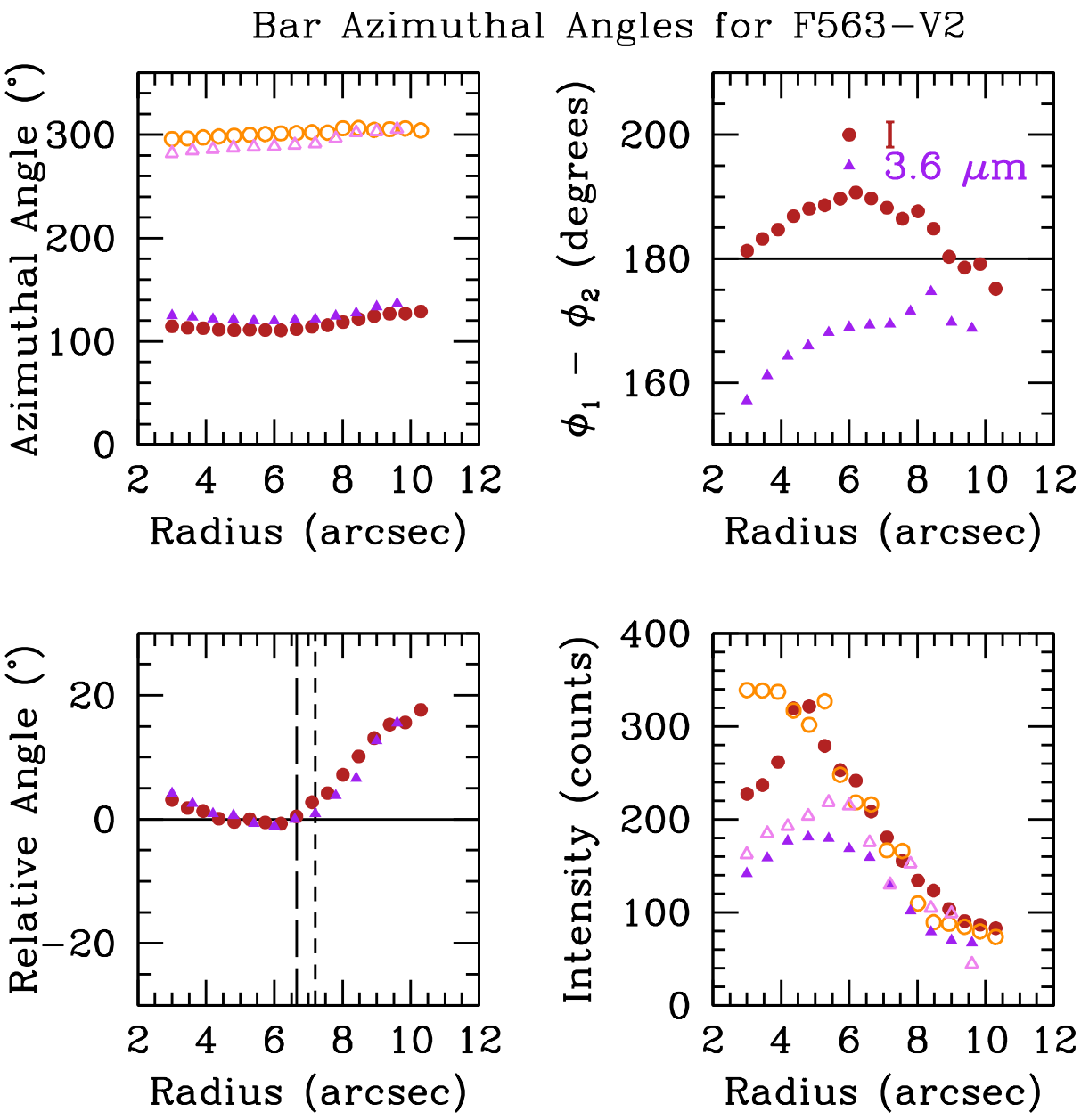

Figure 2.25: Same as Fig. 2.3, but for F563-V2.

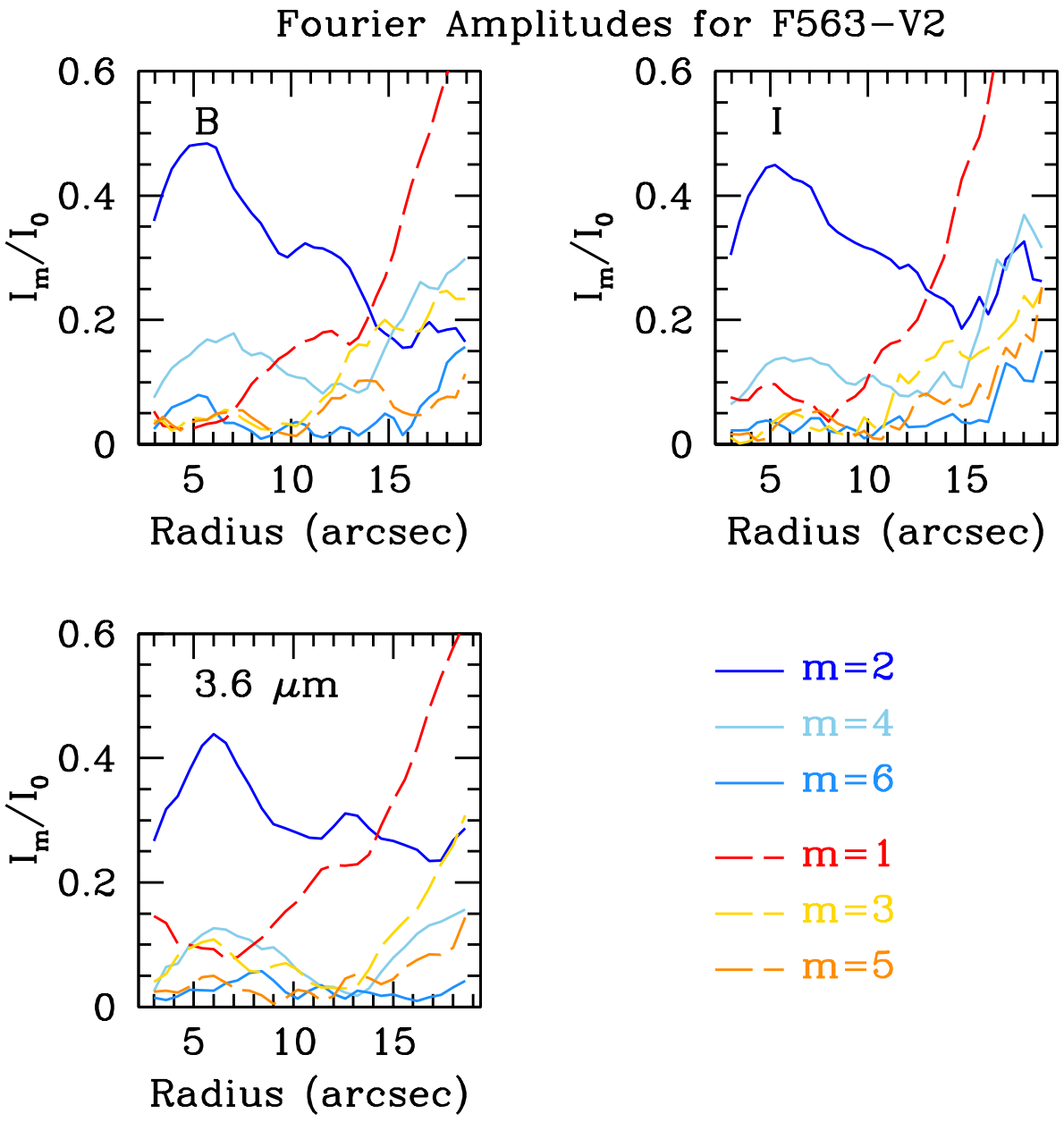

Figure 2.26: Same as Fig. 2.4, but for F563-V2.

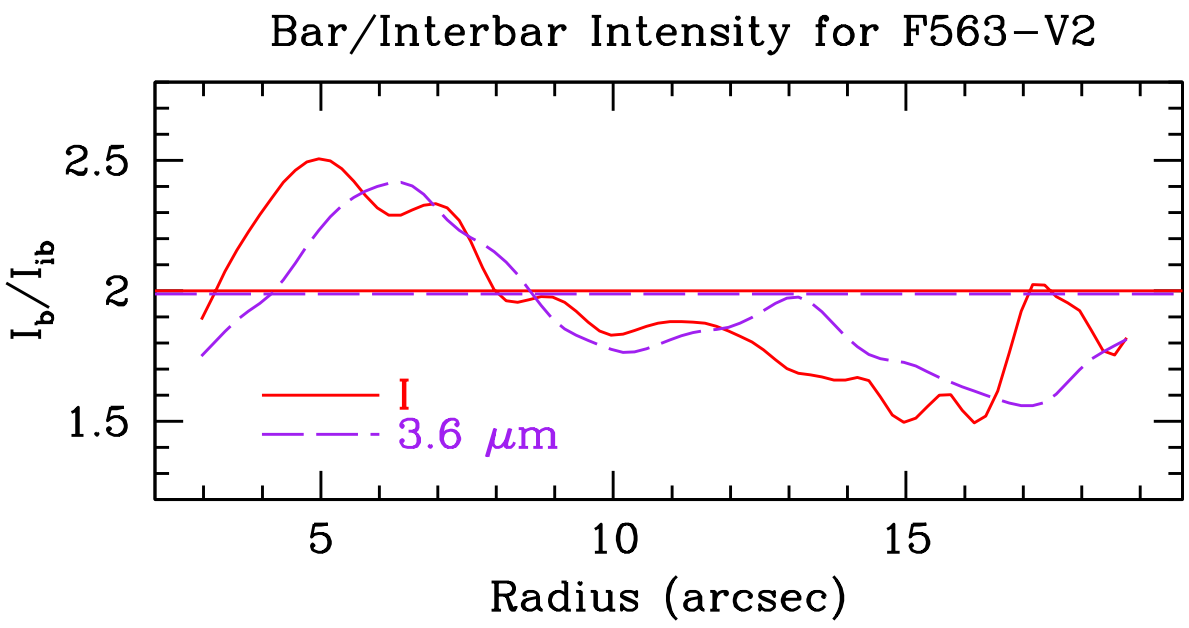

Figure 2.27: Same as Fig. 2.5, but for F563-V2.

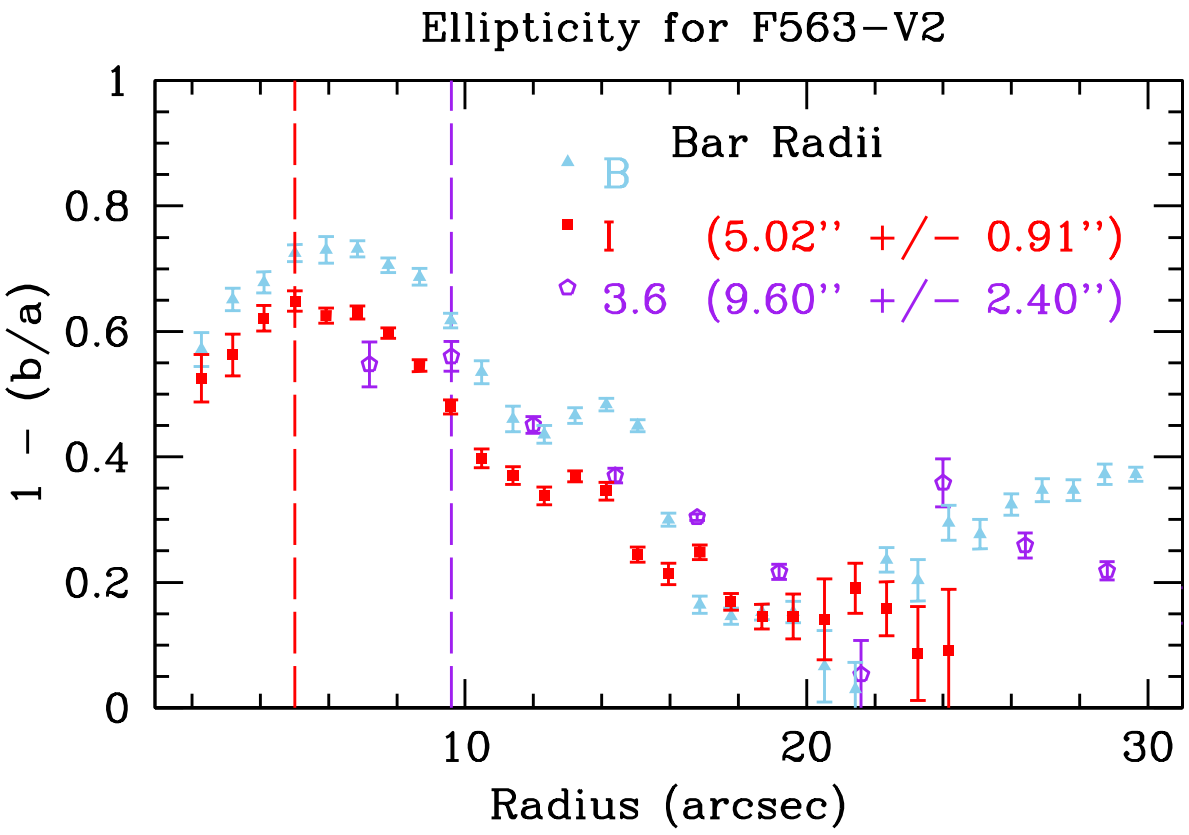

Figure 2.28: Same as Fig. 2.6, but for F563-V2.

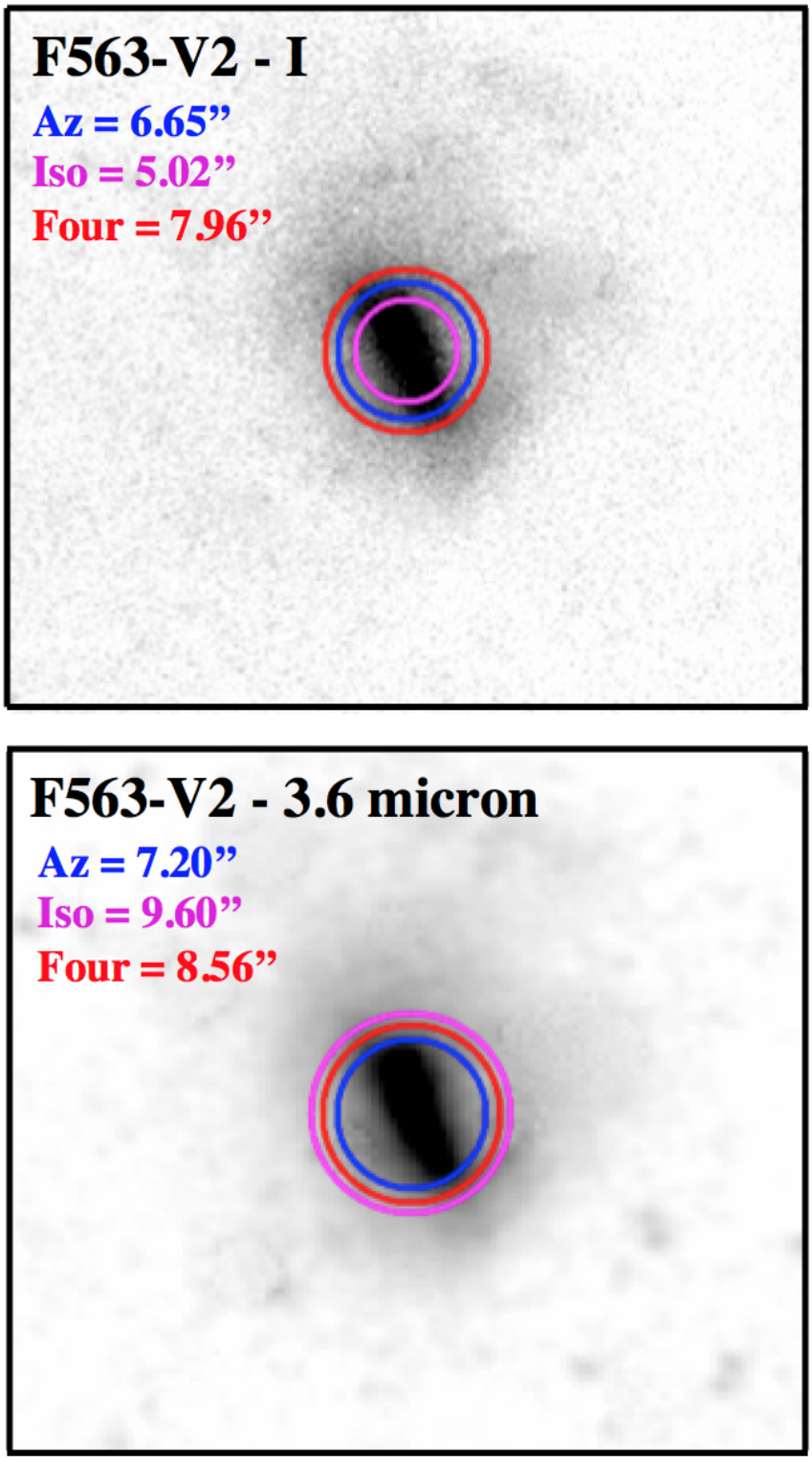

Figure 2.29: Same as Fig. 2.7, but for F563-V2.

2.4.4.2 Bar Strength

We find lower limits on the bar strengths to be 0.26 in I and 0.23 in 3.6 μm. When decreasing the starting radius from 3″ to 1.5″ we find the bar strengths increased by 0.03 in both bands to 0.29 and 0.26 in I and 3.6 μm respectively (Table 2.2). Based on this and the behaviour of the relative Fourier amplitudes, we are confident that our lower limits are accurate.

2.4.4.3 Corotation Radii

We show the phase profiles for F563-V2 in Fig. 2.30. We find a B,I phase crossing at 15.86″±0.46″ and a B,3.6 μm phase crossing at 15.86″±0.60″. Due to the complicated morphology of this galaxy, the phase crossings are not as well defined as the previous galaxies. We report the bar corotation radius to be at 15.86″±0.46″ for the I-band and at 15.86″±0.60″ for 3.6 μm. Again, the errors on the corotation radius are equivalent to the radial spacing of the azimuthal light profiles.

As F563-V2 displays very tenuous spiral structure, we did not attempt to characterize the spiral pattern in this galaxy.

2.5 Discussion

Here we discuss the results for our bar lengths and strengths for our galaxies, as well as describing how R_{CR} can be used to obtain relative bar pattern speeds. We discuss our bar lengths in context of our three techniques, as well as between the two photometric bands used (Sec. 2.5.1). We discuss the accuracy of the lower limit on our bar strengths using the relative Fourier amplitudes (Sec. 2.5.2). Finally, we go into detail about the relative bar pattern speeds of our galaxies in context with their dark matter halos (Sec. 2.5.3). We compare our results to those of HSBs throughout as well.

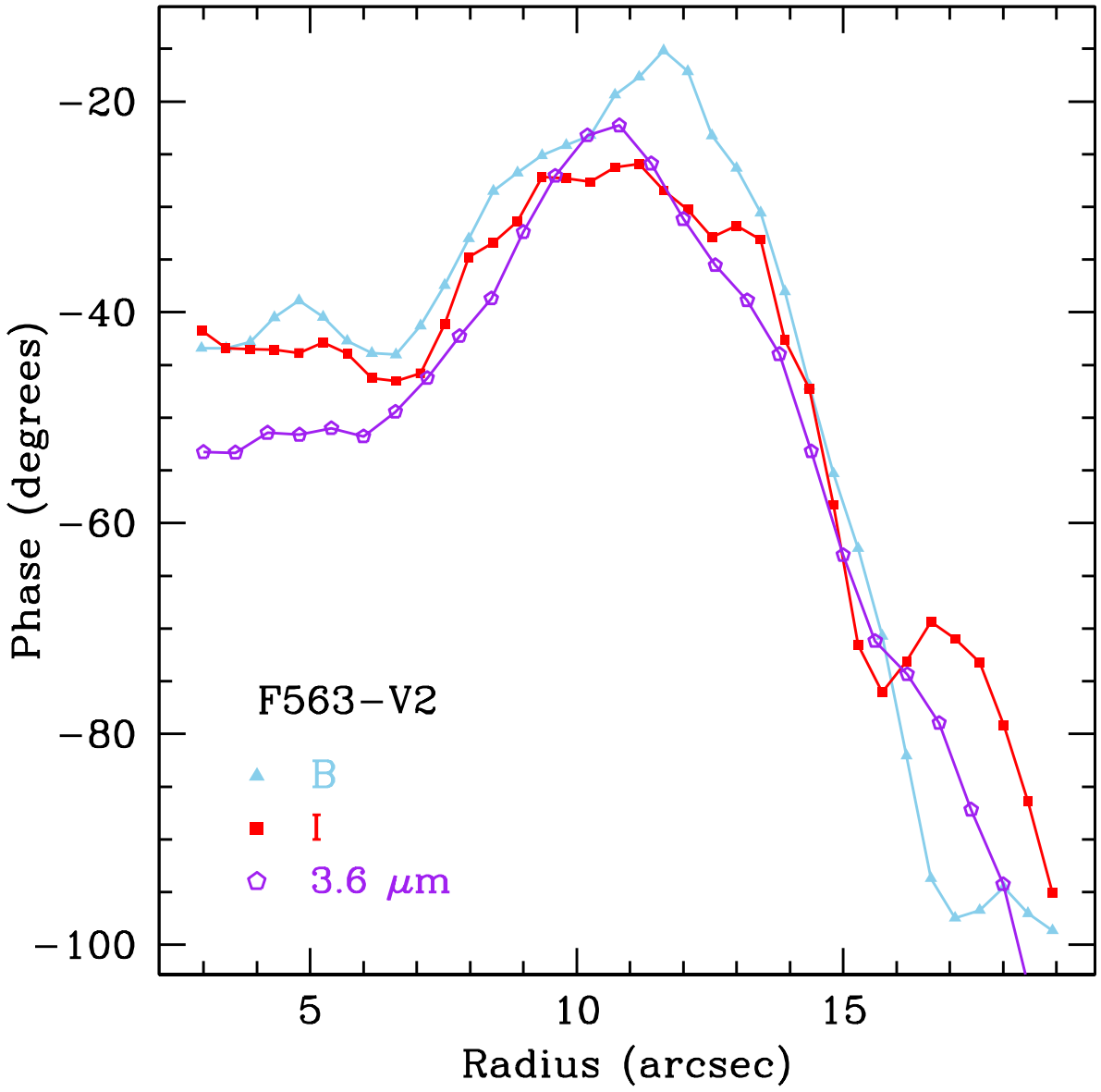

Figure 2.30: Same as Fig. 2.8, but for F563-V2.

2.5.1 Bar Lengths

We have applied three different techniques for measuring the lengths of bars in our four galaxies. We find agreement between our azimuthal light profile bar radii measurements between the I band and 3.6 μm for all four galaxies. We also find that the bar length from the radius of maximum ellipticity mostly agrees with our azimuthal bar radius, although for

F568-1 this is not the case. Finally, we find that the Fourier method consistently overshoots the bar radius when compared with the other two methods, sometimes quite significantly. For UGC 628, for example, the Fourier bar radius is larger than our first corotation radius. In general, it appears that the Fourier method includes spiral arms as well as the bar, biasing the result to larger radii.

We visually show how the bar length measurements compare for the whole sample in Fig. 2.31. Here, the x-axis is the bar length measured from our azimuthal light profile method and the y-axis is the difference from the other two techniques (ΔR_{bar}), the radius of maximum ellipticity and the Fourier bar/interbar intensities (i.e. $R_{bar,Four} - R_{bar,az}$). Triangle points are values from the elliptical isophote method and squares are from the Fourier method. The horizontal dashed line shows zero, and the vertical lines connect bar radii measurements for a given band. Red, closed points are I-band values and purple, open points are 3.6 μm values.

We find that 3.6 μm (purple) azimuthal light profile bar radius measurements are consistently larger than the I-band values (red) for each galaxy, while not differing too extremely. We expect them to be similar, as bars are stellar features and both our photometric bands trace this galaxy component. This could also be due to the poorer spatial resolution at 3.6 μm. We also find that the elliptical isophotal bar measurements are equally smaller and larger than the azimuthal light profile method, and that the Fourier bar radius measurements are consistently larger. Aguerri et al. (2009) also found the Fourier method to overshoot the bar radius.

When looking at the bar radii overplotted on the deprojected images (Fig. 2.7 for instance), we find that our azimuthal light profile method provides the best measure of the bar radius for each galaxy in both bands. Based off of these figures, the elliptical isophote method provides a good measure for the bar radius as well, with F568-1 being the exception. We believe the reason for this is due to transition from bar to spiral arms in this galaxy biasing the isophotes towards the bright arms.

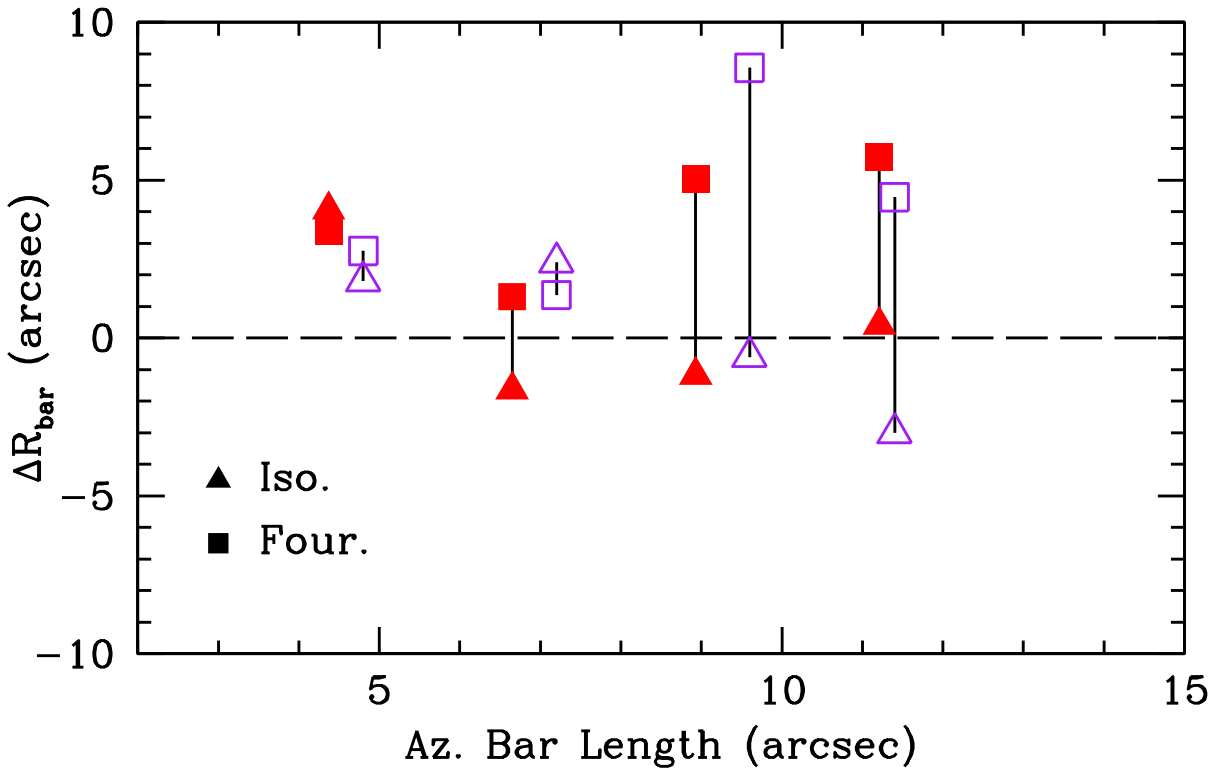

Figure 2.31: Bar radii measurement comparison between the three techniques for the entire sample. The x-axis is the bar radius from the azimuthal light profile method, and the y-axis is the difference from the other two techniques (ΔR_{bar}), the radius of maximum ellipticity and the Fourier bar/interbar intensities (i.e. Fourier - azimuthal). Triangle points are values from the elliptical isophote method and squares are from the Fourier method. Red, closed points are from the I-band and purple, open points are from 3.6 μm. Vertical lines connect points for the same galaxy in each band.

As only F563-V2 has comparable bar radii between the azimuthal light profile method and the Fourier method and has only one arm, we think that the dual spiral arms of the other three galaxies are biasing the bar radius measurement to larger values. Thus, it is possible given either angularly larger targets or better angular resolution that our bar radius measurements from the Fourier method would be more accurate for UGC 628, F568-1, and F568-3. We feel justified in saying this, as the Fourier method has been used to find accurate bar lengths in the literature, albeit for angularly large HSBs (see Aguerri et al. 2000a, for instance).

We also find that the bar lengths in physical units (kpc) for our sample are on the lower end of those found by Honey et al. (2016) (2.5 - 14.3 kpc), shown in Fig. 2.32. Here we show histograms of the bar lengths (kpc) for Honey et al. (2016) (solid black) and our I-band and 3.6 μm values (dashed red). Compared to HSB galaxies, however, we find that our bar lengths are of comparable size. For example, the majority of the bars in the HSB samples of Erwin (2005), Marinova & Jogee (2007), and Aguerri et al. (1998, 2009) are $\leq$3.5 kpc, $\leq$5 kpc, and $\leq$5 kpc, respectively. In Fig. 2.33 we plot our bar lengths with the bar lengths of the HSBs in Aguerri et al. (1998).

2.5.2 Bar Strengths

We have found lower limits on the strengths of our bars and find that they range from $\sim$0.13 to $\sim$0.29. We find that our lower limit of bar strengths for our sample, while on the weaker side, are consistent with bar strengths found for HSBs. Aguerri et al. (2000a) and Laurikainen & Salo (2002) list bar strengths that range from $\sim$0.1 to $\sim$0.6 for example. This is also consistent with Honey et al. (2016) who found that bar lengths and strengths for LSBs are similar to those in HSBs, although a different measure of bar strength was used than in our work. We show this visually in Fig. 2.33 where we compare our I-band (red triangles) and 3.6 μm (purple squares) bar lengths and strengths with those from HSBs in Aguerri et al. (1998) (open black circles). We find that our bar strength values form a continuum with the Aguerri et al. (1998) HSB galaxies (the outlier at $R_{bar} \approx 10$ kpc is not addressed).

Our bar strength values found for UGC 628, 0.26 and 0.22, are roughly consistent with those found by Chequers et al. (2016) at late simulation time, $\sim$0.30, although our values are somewhat weaker. Based on the behaviour of the relative Fourier amplitudes, our bar strengths are likely indicative of the true strength.

F568-1 has the lowest bar strengths of our sample, 0.13 and 0.14. Looking at Fig. 2.1, this is not surprising, as the bar is quite small, and quickly turns into spiral arms. As previously mentioned in Sec 2.3.2, bar strength was originally a visual classification based on

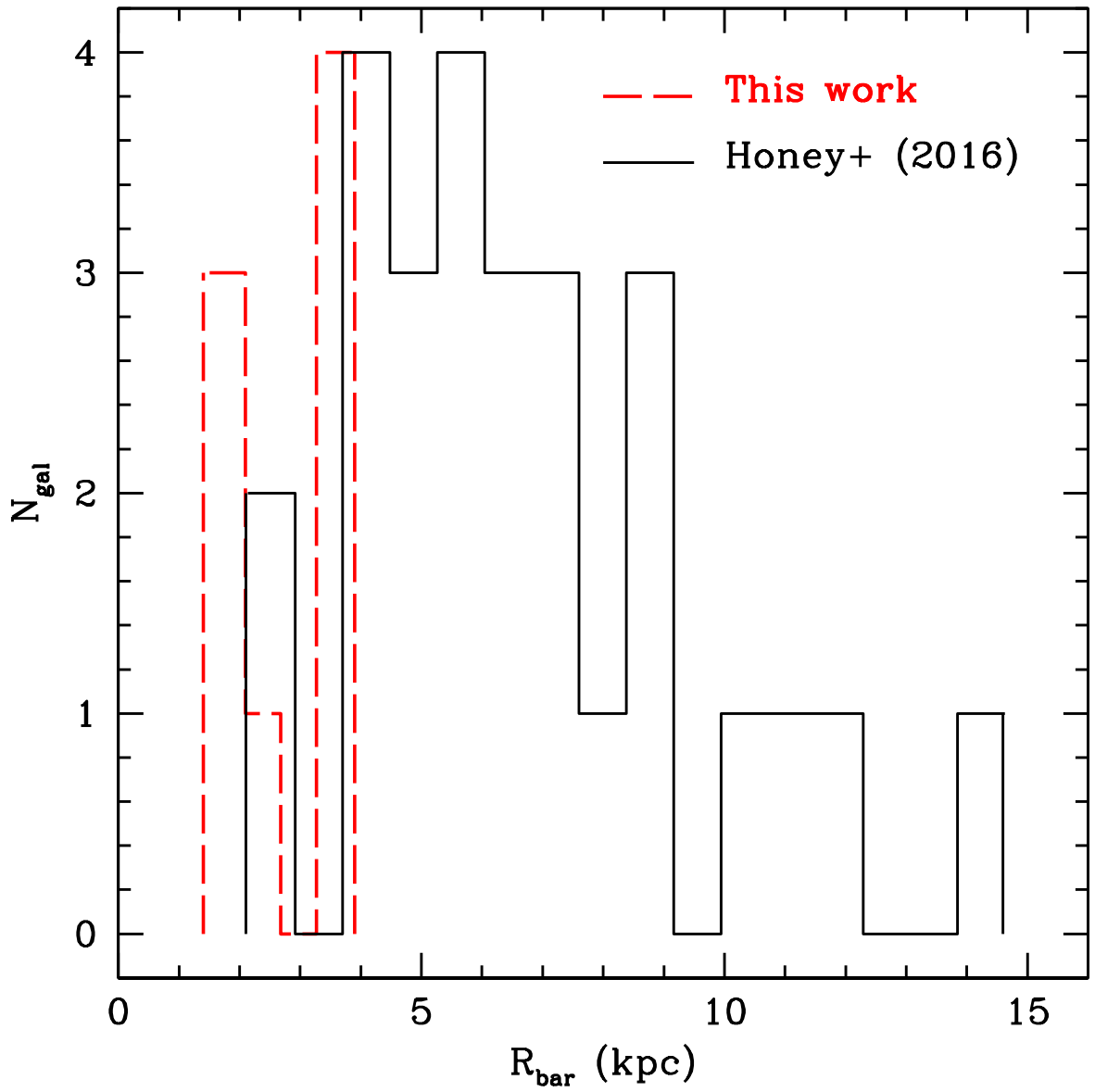

Figure 2.32: Histogram of bar lengths from Honey et al. (2016) (solid black) and this work (dashed red). Here we include both our I-band and 3.6 μm bar lengths. Our bar lengths clearly fall on the shorter side compared with the LSBs in Honey et al. (2016).

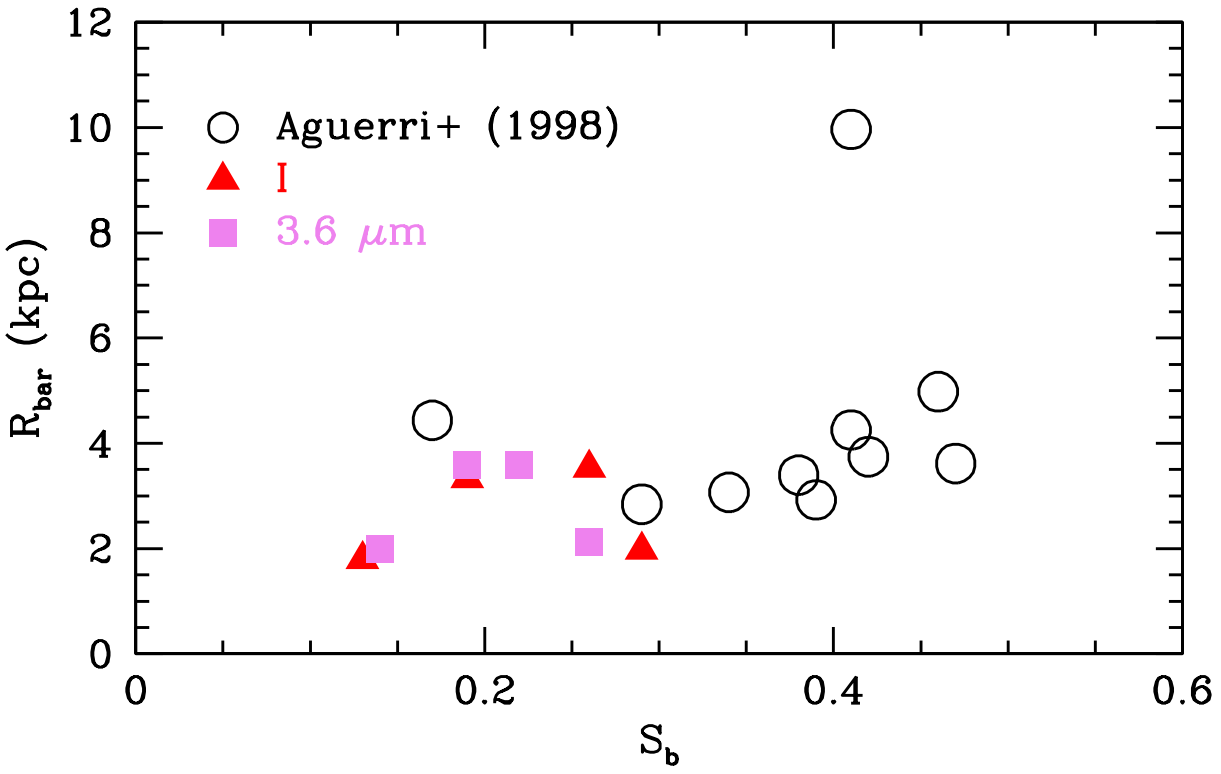

Figure 2.33: Comparison of bar strengths and bar lengths (kpc) between our I-band (red triangles) and 3.6 μm (purple squares) values and those from HSBs in Aguerri et al. (1998) (open black circles).

how bright/pronounced the bar was. However, we are unable to probe down to small enough radii to be confident that our strengths are representative for this galaxy.

Our bar strengths found for F568-3, 0.19 in both bands, are likely indicative of the true bar strength, as the bar is long enough for the missing, inner portion of the relative Fourier amplitudes to not be a large factor. It may seem surprising that the bar strength for this galaxy is as low as it is given the bar in Fig. 2.1. However, F568-3 seems to possess either a double bar, or inner spiral structure within the bar, which may be the cause of the lower strength.

As we are not missing a significant portion of the bar, our bar strengths for F563-V2 are likely indicative of the true value, 0.29 and 0.26. However, we do note that when decreasing the starting radius of the azimuthal light profiles we found an increase of 0.03 in both bands.

This leaves us with a relatively strong bar, which is not surprising given the I-band image in Fig. 2.1.

2.5.3 Relative Bar Pattern Speeds

The third bar parameter we measured was the radius of corotation (R_{CR}). This parameter can be used to characterize the pattern speed of the bar, Ω_p, which can give important information about the mass distribution within the host galaxy. Ω_p is simply the rotational frequency of the bar itself (Binney & Tremaine 2008). The only method of directly measuring the bar pattern speed was introduced in Tremaine & Weinberg (1984, hereafter the TW method). The TW method requires spectroscopy to map the velocity of orbits in the disk, either with multiple long-slit observations across the galaxy or with integral field unit (IFU) spectroscopy to create a velocity field. In addition, these velocity maps must be weighted by the underlying light distribution, measured either with the stellar continuum in the spectroscopy or with NIR imaging. This method has usually been applied to one, bright, grand-design spiral at a time (i.e Kent 1987b; Merrifield & Kuijken 1995; Gerssen et al. 1999), although applications to dwarf galaxies exist as well (Bureau et al. 1999; Banerjee et al. 2013). However, Aguerri et al. (2015) recently applied this method to 15 bright and strongly barred galaxies from the CALIFA (Sánchez et al. 2012) IFU survey.

While it is very desirable to obtain actual pattern speed measurements, the current number of LSBs with bar pattern speed measurements is only one: UGC 628. The bar pattern speed of this galaxy was measured by applying the TW method to an Hα velocity field (Chemin & Hernandez 2009) as well as with numerical simulations (Chequers et al. 2016). The lack of pattern speed measurements for LSBs is due to the large observing time required to obtain high signal to noise spectroscopy for LSBs. As a result, LSBs are largely absent from IFU surveys, such as the aforementioned CALIFA survey. However, large numbers of galaxies can be characterized by measuring the dimensionless parameter $\mathcal{R} = R_{CR}/R_{bar}$, or the 'relative bar pattern speed', allowing us to probe LSBs in a more general context. Both the corotation

radius (R_{CR}) and bar radius (R_{bar}) have been measured for our sample using photometry alone.

$\mathcal{R}$ can be measured simply with photometry (Sec. 2.3), and can be used to infer properties of the host galaxy. Bars are classified as 'fast' if $\mathcal{R} < 1.4$ or 'slow' if $\mathcal{R} > 1.4$ (Athanassoula 1992; Elmegreen et al. 1996; Debattista & Sellwood 2000). This designation arises from the prediction that galaxies dominated by baryons (as opposed to dark matter) in their central regions should have $\mathcal{R} = 1.2 \pm 0.2$ (Athanassoula 1992). In other words, corotation should occur very close to the end of the bar. Based on studies of HSBs, there seems to be little dependence on $\mathcal{R}$ with either morphology (Aguerri et al. 1998, 2015) or redshift (Pérez et al. 2012), although none of these studies go to Hubble types later than SBbc. For those galaxies that have had $\mathcal{R}$ measured, the almost unanimous result are 'fast' bars, confirming the prediction of $\mathcal{R} = 1.2 \pm 0.2$.

Due to the relative lack of studies of barred LSBs, it is uncertain what values of $\mathcal{R}$ are/will be observed for LSBs. However, we have a few insights based on simulations and theory as to what to expect. While there is debate about the likelihood of bars forming and surviving in very centrally dense halos, the general consensus is that only slow, weak bars can form and that they will exist as transient features (Mihos et al. 1997; El-Zant & Shlosman 2002; Mayer & Wadsley 2004, but see Valenzuela & Klypin 2003). It is expected that centrally dense dark matter halos should be hosts to slow bars ($\mathcal{R} > 1.4$) because the bar should be dynamically slowed down by the dense halo (Weinberg 1985; Debattista & Sellwood 2000).

As previously introduced in Sec. 2.1, the kinematics of LSB galaxies are well-studied and have been used to measure the overall density and the density profile of the dark matter halos in which they are embedded. In general, two types of density profiles for the halos are considered in these studies: cuspy profiles and cored profiles. The most common form of a cuspy halo is the NFW profile (Navarro et al. 1996a). It is characterized by a density power law $\rho \sim r^{\alpha}$ and dark matter concentration c. Halos in cold dark matter simulations generally have a slope of $\alpha = -1$, or steeper (i.e. 'cusp'). These halos are very centrally dense. For

cored halos, the pseudo-isothermal density profile is the most commonly used. These have a constant density center, $\rho \sim r^0$ (i.e. 'core'). The central density of cored halos is much lower than cuspy halos. Cored halos are motivated by observations rather than coming from simulations or theory.

Observations of LSBs are typically better fit by cored halos rather than cuspy halos (e.g., de Blok & McGaugh 1996; de Blok et al. 1996; McGaugh et al. 2000; Swaters et al. 2003). In addition, the overall halo density for LSBs is also lower than expected from simulations (see Fig. 1b in Kuzio de Naray & Spekkens 2011, for example). The conflict between kinematic observations being better fit by cores and simulations creating cusps is referred to as the 'cusp-core' problem and is well documented in the literature (see the review, de Blok 2010).

All four of our galaxies have kinematic data in the form of rotation curves, and have had mass models that confirm their dark matter domination down to small radii (de Blok et al. 2001a; McGaugh et al. 2001; Kuzio de Naray et al. 2006, 2008). Rotation curves of LSBs are better explained by pseudo-isothermal halos rather than NFW halos, suggesting the density profile of the dark matter is 'cored'. These studies find the data to be better explained by cored halos rather than very centrally dense cuspy halos. Now that we have measured the length and corotation radius of the bar, we can use the ratio of these two parameters to determine the relative bar pattern speed ($\mathcal{R}$) and probe the dark matter halo in a new way.

Using the azimuthal bar radius and *first* phase crossing after the bar radius using the PD97 method, our relative bar pattern speeds ($\mathcal{R}$) are shown in Table 2.2. Here we have propagated the bar length and corotation radius errors through to determine the error on $\mathcal{R}$. The relative bar pattern speeds for our sample are shown in Fig. 2.34. With the exception of F568-3, we find excellent agreement between the relative bar pattern speeds of both photometric bands. We note that we are comparing two different corotation radii for F568-3 between the I-band and 3.6 μm. Excluding F563-V2, our relative bar pattern speeds span values from 1.13 to 1.47, suggesting that these galaxies are not embedded in dark matter halos with high central densities. While a few values straddle the line between fast and

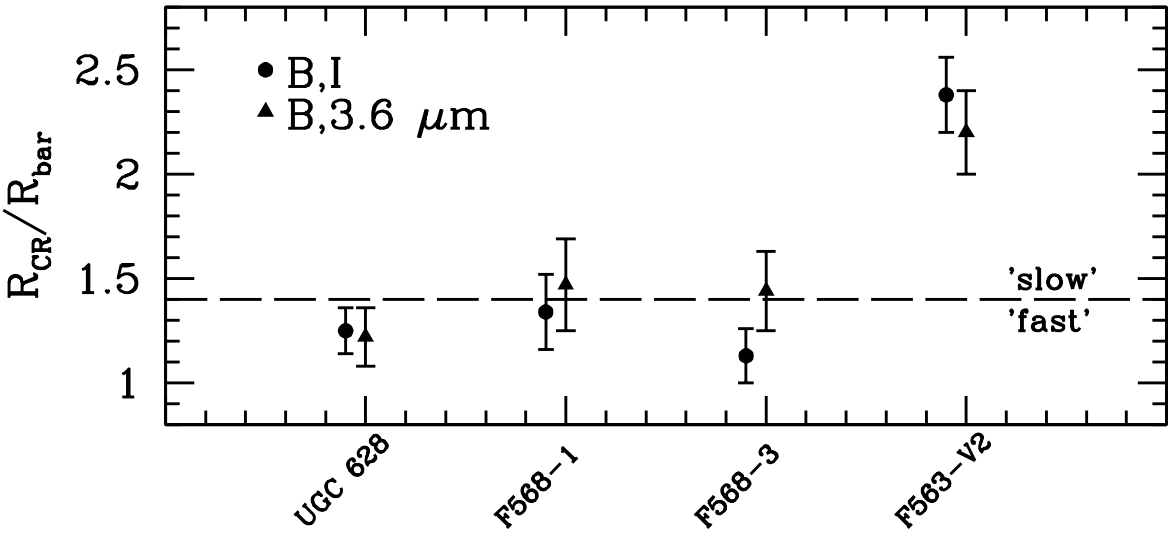

Figure 2.34: Relative bar pattern speeds for our sample. From left to right: UGC 628, F568-1, F568-3, F563-V2. Filled circles show the B,I values and filled triangles show the B,3.6 μm values. Horizontal dashed line indicates the distinction between 'fast' and 'slow' bars. If LSBs reside in centrally dense (i.e. cuspy) halos as expected, they should reside in the upper portion of this plot. 'Normal' HSBs almost exclusively live in the bottom portion of the figure, as they are baryon dominated in their inner regions.

slow with large errors, the values are still comparable to those found for HSBs (i.e. fast) with F563-V2 being the clear exception. Since we find such a slow bar in F563-V2, we are confident that we are able to differentiate between fast and slow bars.

As previously mentioned in Sec. 2.2.1, our four galaxies have kinematic data in the literature and were part of dark matter halo studies. In Fig. 2.35 we show the relative bar pattern speeds versus the NFW concentration c and pseudo-isothermal central density ρ_0. Red triangles in Fig. 2.35 are UGC 628, green squares are F568-1, blue pentagons are F568-3, and purple hexagons are F563-V2. Halo parameters for UGC 628 are taken from de Blok & Bosma (2002), parameters for F568-1 are from de Blok et al. (2001b), and parameters for F568-3 and F563-V2 are from Kuzio de Naray et al. (2008). The NFW fits to F568-3 (Kuzio de Naray et al. 2008) were held fixed unlike the other three galaxies, because a fit to the data could not be made. In each of these studies, R-band photometry from de Blok et al. (1995)

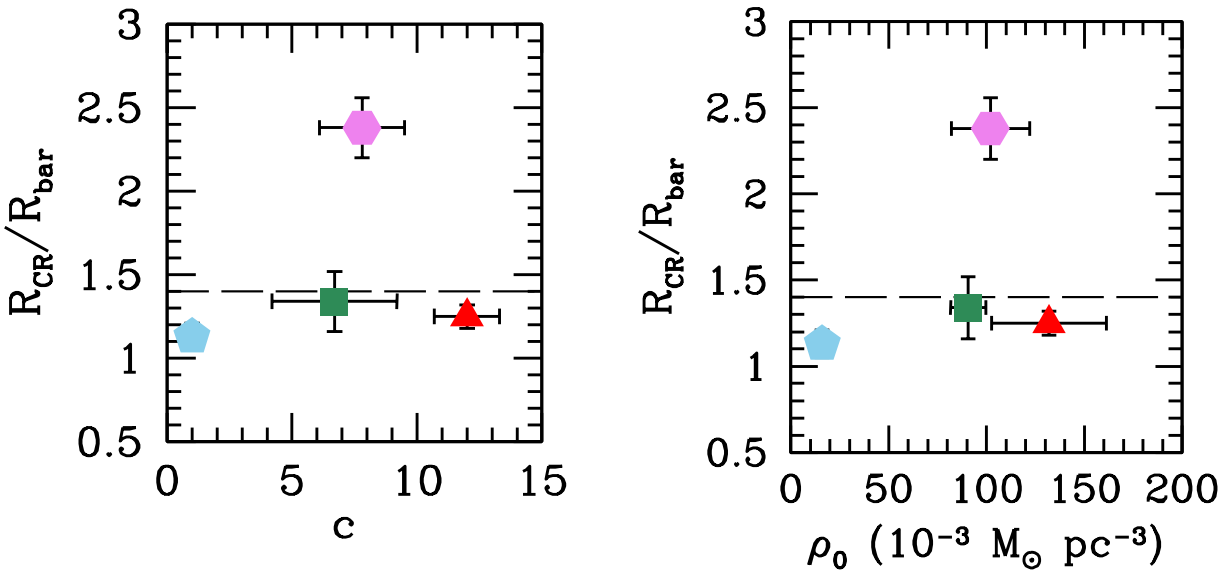

Figure 2.35: Relative bar pattern speed plotted versus NFW concentration c (left) and pseudo-isothermal central density ρ_0 (right), both halo fits from population synthesis models. Red triangles are UGC 628, green squares are F568-1, blue pentagons are F568-3, and purple hexagons are F563-V2. Halo parameters for UGC 628 are taken from de Blok & Bosma (2002); parameters for F568-1 are from de Blok et al. (2001b); parameters for F568-3 and F563-V2 are from Kuzio de Naray et al. (2008). NFW parameters for F568-3 are not fits, but held fixed. The horizontal dashed line shows $\mathcal{R} = 1.4$, the deliminator between fast and slow bars.

and Swaters (1999) and stellar M/L ratios from population synthesis models have been used to determine the contribution of the stars to the total mass of each system. The horizontal dashed line shows $\mathcal{R} = 1.4$. In our small sample we do not find any correlation between the dark matter halo parameters and the relative bar pattern speeds.

We show our relative bar pattern speeds versus strength compared with the HSB galaxies from Aguerri et al. (1998) in Fig. 2.36. The black line indicates the fit from Aguerri et al. (1998), $\mathcal{R} = 0.82 + 1.12S_b$. We find that our galaxies all fall above this relation. Excluding F563-V2, the two points far above the rest, it appears as though there is no correlation with relative bar pattern speed and bar strength for both LSBs and HSBs. In fact, were it not for the HSB at $S_B \approx 0.18$, the Aguerri et al. (1998) sample would be roughly flat as well. To test

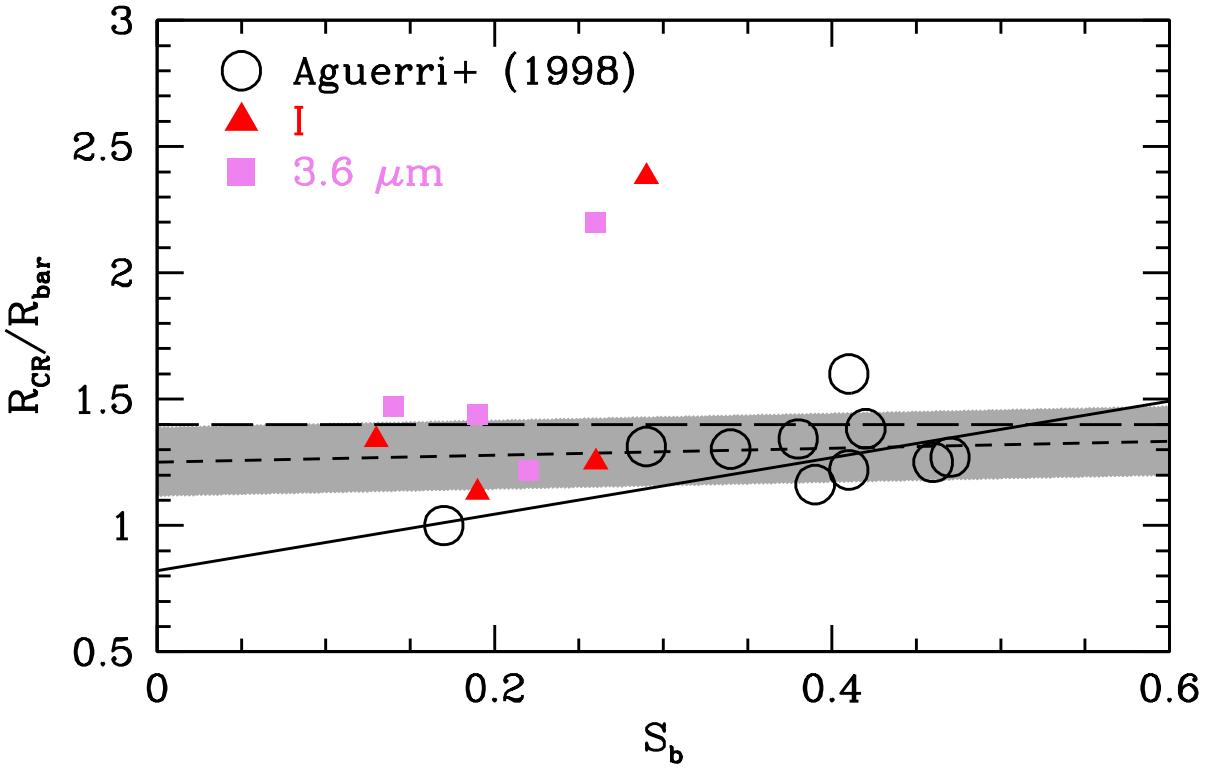

Figure 2.36: Same as Fig. 2.33, but with relative bar pattern speed instead of length. The solid line is the fit to the HSBs, found by Aguerri et al. (1998), and the horizontal long dashed line shows the deliminator between fast and slow bars. The short dashed line is a fit to the HSBs and LSBs, excluding F563-V2 (the two points above the rest): $\mathcal{R} = 1.25 + 0.14S_b$. The shaded gray region denotes the scatter about the fit: $\sigma = 0.137$.

this, we fit both the LSB and HSB datasets (excluding F563-V2) and found $\mathcal{R} = 1.25 + 0.14S_b$ with a scatter $\sigma = 0.137$ shown as the short dashed line and gray shaded band in Fig. 2.36.

In the following sections we discuss the relative bar pattern speeds, $\mathcal{R}$, for each galaxy individually in context with any previous work, as well as with previous dark matter studies.

2.5.3.1 Comments on UGC 628

Our relative bar pattern speeds for UGC 628 are $\mathcal{R}_I = 1.25 \pm 0.11$ and $\mathcal{R}_{3.6} = 1.22 \pm 0.14$, clearly indicating a fast bar, suggesting the dark matter halo is not as centrally dense as would be expected for a cuspy halo. de Blok & Bosma (2002) find that both NFW halo and pseudo-isothermal fits to the Hα rotation curve of UGC 628 provide similar results. In

addition, they find that UGC 628 has a steep, cuspy inner slope ($\alpha \sim$ -1.3). However, de Blok (2005) show how cuspy halos do not provide realistic or physically meaningful fits to the data for UGC 628 (and many other LSBs).

Our relative pattern speeds are in conflict with Chemin & Hernandez (2009) and Chequers et al. (2016), who both find a slow bar ($\mathcal{R} \sim 2$). As previously mentioned, Chemin & Hernandez (2009) applied the TW method to an Hα velocity field to measure the bar pattern speed, and Chequers et al. (2016) used an N-body simulation to model the bar pattern speed. We think this conflict ultimately stems from the measure of the bar radius. Both of these previous works place the bar radius at $\sim$14.5$''$ in the R-band, far longer than our value of $\sim$11.5$''$. Looking at Fig. 2.7, a bar radius of $\sim$14.5$''$ would be more similar to the bar radii from the Fourier intensities method and would contain a portion of the spiral arms. In addition, our radius of corotation is $\sim$14$''$, falling *inside* the bar for these other two works. However, corotation cannot occur within the bar, since these orbits would be unstable and eventually cause the bar to be destroyed (Contopoulos 1980). We also note that we do find the radius of corotation reported by Chemin & Hernandez (2009) in 3.6 μm, $\sim$30$''$. If we use this value for R_{CR}, we find $\mathcal{R} > 2$, which brings us into agreement with Chemin & Hernandez (2009) and Chequers et al. (2016).

We also emphasize that the result from the Chequers et al. (2016) modeling *assumes* a centrally-dense, cuspy NFW dark matter halo for their simulation, so it is not unexpected that a slow bar was found. This assumption is contrary to previous works that found UGC 628 to not be well fit by an NFW halo (e.g. poor fits in de Blok et al. 2001a; de Blok 2005). Based on our results, we reclassify UGC 628 as having a fast bar. Chequers et al. (2016) find that despite the slow pattern speed, their model of UGC 628 implies that the galaxy is not dark matter dominated in the inner radii, as found by Chemin & Hernandez (2009). This would be consistent with our finding of a fast bar in this galaxy.

2.5.3.2 Comments on F568-1

Because we are confident that the first phase crossing for both I and 3.6 μm are real, we have relative bar pattern speeds of $\mathcal{R}_I = 1.34 \pm 0.18$ and $\mathcal{R}_{3.6} = 1.47 \pm 0.22$, respectively. This leaves us with results that span both the fast and slow regimes for F568-1. This is likely due to the large errors found for this galaxy, resulting from the angularly small bar radius.

In terms of mass profiles for this galaxy, de Blok et al. (2001a) find that the pseudo-isothermal halo profile is the best fit to the rotation curve for F568-1, and that the NFW profiles all over predict the rotation curve in the inner and outer regions. Swaters et al. (2000) also found a relatively flat inner density slope, $\alpha \sim 0.3$, suggesting a cored halo. According to de Blok et al. (2001a), the maximum disk profile is the best scenario for the NFW fits, albeit still worse than the pseudo-isothermal halos. In addition, Fuchs (2003) showed that the maximum disk hypothesis holds for dual-armed spiral LSBs; F568-1 was included in this work. Lee et al. (2004) find that a bottom heavy IMF in combination with very recent star formation can explain the results from Fuchs (2003), lowering the required mass of the dark matter halo significantly.

When considering the errors, the relative bar pattern speeds calculated for F568-1 span the range of 1.15 to 1.69, bracketing the $\mathcal{R} = 1.4$ dividing line between the fast and slow regimes. The only way for us to obtain unambiguously high relative bar pattern speeds would be to ignore the first phase crossing for both I and 3.6 μm and take the second intersection of 9.66″ in both bands to be the corotation radius. This would give relative bar pattern speeds of $\mathcal{R}_I = 2.21 \pm 0.11$ and $\mathcal{R}_{3.6} = 2.01 \pm 0.28$. Finding pattern speeds that are not clearly slow or clearly fast is not uncommon for the PD97 method; Sierra et al. (2015) for instance find roughly ten of the 57 galaxies in their sample have relative bar pattern speeds that span both fast and slow within their errors. All galaxies in Sierra et al. (2015), however, are baryon-dominated HSBs that display little need for dark matter until large radii (the flat part of their rotation curves). In contrast, LSBs require dark matter to become a significant mass component much farther in. That the bars in UGC 628, F568-1, and F568-3 (see below)

do not reside well inside the slow regime is perhaps suggestive that these galaxies do not contain as much dark matter near their centers as would be expected for systems inside centrally dense cuspy dark matter halos.

2.5.3.3 Comments on F568-3

For F568-3, we are left with two very different results, both of which depend on the corotation radius that is used. If we take the first phase intersection between the B and I bands, then we find that $\mathcal{R}_I = 1.13 \pm 0.13$, clearly indicating a fast bar. However, this phase intersection is not seen in 3.6 μm. If we take the corotation radius as the second phase intersection between B and I, which is in agreement with the B,3.6 μm phase crossing, then we have $\mathcal{R}_I = 1.55 \pm 0.17$, or a slow bar. To further complicate things, the phase intersection between B and 3.6 μm gives $\mathcal{R}_{3.6} = 1.44 \pm 0.19$, spanning both fast and slow.

Because the phase reversal between the B and I bands is quite clear, it is very likely real, as justified in Sec. 2.4.3.3. We therefore trust that our results for the B and I phase crossing are more certain than the B and 3.6 μm phase crossings. Thus we conclude that F568-3 is more likely to have a fast bar, suggesting the dark matter halo is not centrally dense. F568-3 is also present in the Fuchs (2003) and Lee et al. (2004) samples, whose findings suggest that the stellar component in this galaxy may be more massive than previously thought. This is also supported by the complex morphology that is present in the inner radii for this galaxy. If the dark matter halo for F568-3 were centrally dense, then it would be very unlikely to find the inner spiral structure and bar as these *global* features would be smoothed out by the dark matter halo (Mihos et al. 1997).

The NFW profile rotation curve fitting from de Blok et al. (2001a) and Kuzio de Naray et al. (2008) for this galaxy were unable to converge, forcing the authors to hold best guess values fixed by hand. In addition, Swaters et al. (2000) found a flat inner density slope, $\alpha \sim 0.2$, inconsistent with a cuspy halo.

2.5.3.4 Comments on F563-V2

Based off of the bar radii and corotation radii from both bands, F563-V2 clearly has a slow bar. For the I band we have $\mathcal{R}_I = 2.38 \pm 0.18$, and $\mathcal{R}_{3.6} = 2.20 \pm 0.20$ for 3.6 μm. Our azimuthal light profiles reveal there to be only one strong arm, with possibly a fainter arm as well. As described in Sec. 2.2.3, this prevented us from being able to use ELLIPSE to determine the deprojection and we relied instead on values from the literature. In addition, the sole-arm could pose issues for the PD97 method, which selects the $m = 2$ mode for the Fourier transform. This likely explains the large errors on our $\mathcal{R}$ values. Due to this, the phase profiles for this galaxy are not as clear as the rest of our sample. Somewhat supporting this, F563-V2 is a clear outlier when looking at Fig. 2.36, seen as the two points above the rest. This figure suggests that there is no real correlation between bar strength and pattern speed.

Based off of the rotation curve fitting from de Blok et al. (2001a), the NFW profile does much worse than the pseudo-isothermal profile. This is supported both by the overestimating of the inner portions of the rotation curve as well as the relatively flat inner slope of the density profile, $\alpha \sim 0$, from Swaters et al. (2000), suggestive of a cored halo. However, our relative bar pattern speed for F563-V2 would be in agreement with a very centrally dense dark matter density profile.

2.6 Conclusions

We have used multi-band photometry to characterize bars in four low surface brightness galaxies. In general, we find that techniques used for high surface brightness galaxies can be successfully applied to LSBs. We list our conclusions here.

1. Bar morphology in LSBs is quite complicated, allowing for structures such as double bars or inner spirals within the bar region, as well as being generally lopsided features.

2. We find measuring bar properties in LSBs with poorly-defined spiral arms is more difficult than in those with a clear dual-arm structure because of the uncertainties associated with the disk deprojection.

3. The bars in our sample have comparable lengths to those found in late-type HSB galaxies. We require a larger sample to know if this holds for LSBs in general or not.

4. The bars in our LSBs appear to have weaker bars than HSBs on average, but not drastically so.

5. Excluding F563-V2, our barred LSBs appear to have relative bar pattern speeds that are comparable to HSBs, with the majority of our measurements consistent with fast bars. This implies that the dark matter halos of our LSBs are unlikely to be centrally dense (i.e. cuspy). Since we find such a slow bar in F563-V2, however, we are confident in differentiating between fast and slow bars for our sample.

6. We reclassify UGC 628 as having a fast bar due to both our clear phase intersections and shorter bar radius than previous works.

7. We find no correlation between bar strength and relative bar pattern speed when including measurements from HSBs.

Our initial findings that LSB bars are fast is intriguing, but we require a much larger sample before we can say anything about the general population as a whole. Observations of nearly two-dozen more barred LSBs are currently underway and the results from those studies will be combined with our findings here to give a more clear and wide-ranging picture of LSB galaxies.

Chapter 3

Expanding the Sample

Peters, W. & Kuzio de Naray, R., "Bar properties and photometry of barred low surface brightness disc galaxies", 2019, MNRAS, 484, 850

3.1 Introduction

Low surface brightness galaxies (LSBs) are disk galaxies typically defined as having central surface brightness $\mu_0(B) > 22.0$ mag arcsec^{-2} (e.g. McGaugh et al. 1995b) or $\mu_0(B) > 23.0$ mag arcsec^{-2} (e.g. Impey & Bothun 1997). Although LSBs occupy a large portion of the galaxy population, they are often biased against in large surveys due to their faint nature (McGaugh et al. 1995b; O'Neil & Bothun 2000; Trachternach et al. 2006). LSBs are not exclusively low-mass galaxies, but instead span all mass ranges (McGaugh et al. 1995a; O'Neil & Bothun 2000). LSBs are also HI rich (i.e. $M_{\rm HI}/M_* > 1$) when compared with HSBs (de Blok et al. 1996; Pahwa & Saha 2018), suggesting they may be relatively unevolved systems.

LSBs are vital to our galaxy formation and evolution theories. In particular, LSBs serve as ideal dark matter laboratories, as analysis of their rotation curves have indicated they are dominated by dark matter at nearly all radii (e.g. de Blok et al. 1996; de Blok & McGaugh 1997; McGaugh et al. 2000; Swaters et al. 2003; Haghi et al. 2018). As such, the dynamics of unbarred LSBs are particularly well understood. However, given the inherent noncircular motions of *barred* LSBs, these galaxies and their bars are less well studied. Nonetheless, these systems could shed further light on the nature of dark matter.

Due to their gas rich nature (e.g. McGaugh & de Blok 1997; Cervantes Sodi & Sánchez García 2017), dark matter domination (e.g. de Blok & McGaugh 1997; Bothun et al. 1997), and isolated environments (e.g Bothun et al. 1993; Mo et al. 1994; Rosenbaum & Bomans 2004; Du et al. 2015; Honey et al. 2018), LSBs are expected to be quite stable against bar formation. Indeed, the bar fraction for LSBs has historically been quite low, ∼8%, (Mihos et al. 1997; Honey et al. 2016) when compared with the HSB bar fraction, ∼60% (e.g. Eskridge et al. 2000; Marinova & Jogee 2007). However, large-scale LSB studies have begun increasing this bar fraction to ∼20% (see Cervantes Sodi 2017; Pahwa & Saha 2018). Finally, while LSBs are relatively isolated, there is recent work to suggest that galaxy isolation has less of an effect on bar formation than previously thought (Casteels et al. 2013; Lin et al. 2014; Zana et al. 2018).

In the previous chapter, Chapter 2, we measured the photometric bar properties of four well-studied LSBs: UGC 628, F563-V2, F568-1, and F568-3. We found that the bars in these galaxies had comparable lengths and relative bar pattern speeds to those in HSBs, albeit weaker. Most interestingly, we found that three of the four galaxies were hosts to 'fast' bars, contrary to expectations for objects in non-rotating dark matter halos.

Here, we use the same methods as in Chapter 2 for 11 new targets that are comparably less well studied, i.e. no existing surface brightness profiles, mass modeling, or rotation curves. We have used the same measurement techniques as those in Chapter 2, with an additional bar length measure used here. Finally, we have created mock galaxy images in order to fully test our various bar length measurements, specifically to quantify how accurately we can determine the other two parameters we are interested in: strength and corotation radius.

We have also obtained broadband B- and I-band photometry of our full sample, and derived surface brightness profiles, magnitudes, and colors. In addition, we have used published HI fluxes to obtain HI mass estimates, and population synthesis models to obtain stellar mass estimates in order to examine the gas fractions of a subset of our sample.

The organization of this chapter is as follows. We detail our sample, data acquisition and reduction in Sec. 3.2. Our methods and results for the bar properties of our sample are presented in Sec. 3.3, and we describe and show results of our mock galaxy image procedure in Sec. 3.4. We outline our methods for measuring photometry and present the results in Sec. 3.5. We use published HI fluxes and obtain stellar mass estimates for a subset of our sample in Sec. 3.6 to examine gas fractions. Finally, our discussion and conclusions are in Sec. 3.7.

3.2 Sample and Data

In this section we briefly outline our sample selection and observations of barred LSBs. We also detail our data reduction.

3.2.1 Sample

As discussed in Chapter 2, we have assembled a sample of 15 barred LSBs drawn from the catalogs of Schombert et al. (1992) and Impey et al. (1996). Not much is known about the 11 new targets in this sample, with few of the galaxies being observed since appearing in Impey et al. (1996). We show the entire observed sample in Table 3.1. Here, we list the R.A. (col. 1) and Dec. (col. 2) coordinates, date of observation (col. 3), photometric bands observed (col. 4), average seeing for observations (col. 5), derived position angles (col. 6) and inclinations (col. 7).

Table 3.1: Sample of observed barred LSBs. The R.A. (col. 1) and Dec. (col. 2) coordinates, date of observation (col. 3), photometric bands observed (col. 4), average seeing for observations, B then I, (col. 5), derived photometric disk position angles (col. 6) and inclinations (col. 7), distances (col. 8), and morphologies (col. 9). Position angles and inclinations for UGC 628, F563-V2, F568-1, and F568-3 are taken from Chapter 2, with the remainder derived in this work (Sec. 3.2.2). The Tully-Fisher distance for UGC 628 is taken from Tully et al. (2016); the remaining distances are derived using available spectroscopic distances from NED.

Galaxy	R.A. (J2000)	Dec. (J2000)	Date	Bands	Seeing ($''$)	P.A. ($^\circ$)	i ($^\circ$)	D (Mpc)	Morph.
UGC 628	01:00:51.9	+19:28:33	7 August 2016	B, I	1.74, 1.50	-42.80	58.20	86	SBc
LEDA 135682	03:39:34.2	-00:30:43	29 October 2017	B, I	1.06, 0.92	42.66	32.75	104	SBbc
LEDA 135684	03:41:44.5	-02:00:09	29 October 2017	B, I	1.12, 0.91	30.07	44.35	46	SBd
LEDA 135693	03:53:26.3	+00:50:32	29 October 2017	B, I	0.88, 0.87	37.84	22.12	154	SB(r)b
UGC 2925	04:01:02.5	-00:43:03	29 October 2017	B, I	1.00, 0.79	-36.64	31.79	57	SB(r)c
F563-V2	08:53:03.8	+18:26:09	24, 28 February 2017	B, I	1.50, 1.54	-32.00	29	60	Irr
F568-1	10:26:06.3	+22:26:01	24, 28 February 2017	B, I	1.43, 1.08	-86.00	24.90	92	SBbc
F568-3	10:27:20.2	+22:14:24	24, 28 February 2017	B, I	1.59, 1.15	-11.40	39.60	83	SBcd
LEDA 135782	11:28:29.6	+00:08:40	13 May 2018	B, I	1.27, 1.21	5.27	35.91	208	SBc
UGC 8066	12:57:00.3	+01:01:43	13 May 2018	B, I	1.11, 0.91	-8.46	50.90	40	SB(r)d
LEDA 135867	14:48:56.4	-00:43:38	13 May 2018	B, I	1.32, 1.25	73.40	38.30	119	SBd
F602-1	22:34:46.0	+22:33:48	25 August 2017	B, V, R, I	0.84, 0.97	-6.00	28.58	105	SBc
PGC 70352	23:03:21.5	+01:53:12	25 August 2017	B, R, I	1.11, 1.10	60.90	31.09	73	SBd
ASK 25131	23:12:21.0	-01:05:42	25 August 2017	B, V, R, I	1.04, 0.83	-2.96	38.00	107	SBcd
[ISI96] 2329-0204	23:31:40.8	-01:48:01	25 August 2017	B, V, R, I	0.87, 0.74	20.28	31.43	...	SBcd

In col. 8 we list distances (Mpc). Only one of our galaxies, UGC 628, has a redshift independent distance (Tully et al. 2016). We estimated the distances for the remainder of the galaxies by averaging the derived spectroscopic redshift distances on the NASA Extragalactic Database (NED)[1], assuming $H_0 = 73$ km s^{-1} Mpc^{-1}. There are no available spectra or distance measurements for [ISI96] 2329-0204. For those galaxies with distances less than $\sim$100 Mpc, these distance estimates likely have large errors. However, we use the distances here to obtain estimates of physical bar lengths and disk-scale lengths from our arcsec measurements, allowing the physical values to be scaled later on if a redshift independent distance is determined at a later time.

In col. 9 we list the morphologies of the sample, following the same method as for HSBs (i.e. de Vaucouleurs 1959). As with LSBs in general, our targets are all late- to very late-type galaxies. With the exception of F563-V2, all our galaxies have a spiral structure, some much more pronounced than others.

3.2.2 Observations and Reduction

To observe our targets, we used the ARCTIC imager on the 3.5-m telescope at Apache Point Observatory[2]. ARCTIC has a field of view of $7.5' \times 7.5'$. We used ARCTIC in single read out mode with 2×2 binning, giving a plate scale of 0.228 arcsec pix^{-1}. We obtained B- and I-band images of 13 new galaxies. In addition, we obtained V- and R-band images for a subset of four galaxies.

We observed each galaxy in all bands with 3×600 sec. exposures, with $15''$ dithering between each image. In addition, we used a circular dithering pattern for the I-band images in order to create a master fringe pattern for reduction (see Appendix A for a description of

[1]The NASA/IPAC Extragalactic Database (NED) is operated by the Jet Propulsion Laboratory, California Institute of Technology, under contract with the National Aeronautics and Space Administration.

[2]Based on observations obtained with the Apache Point Observatory 3.5-meter telescope, which is owned and operated by the Astrophysical Research Consortium.

this process). We reduced the data using standard packages and routines in IRAF[3]: CCDPROC, IMCOMBINE, etc.. For photometric calibration, stars near our targets from Landolt (1992) were observed to obtain photometric zero points. These zero points were found to be accurate to 0.2 mags by checking with stars in the field from Pan-STARRS1 (Chambers et al. 2016) and TASS Mark III (Richmond et al. 2000). Sky values were determined by subtracting the average value of six 50×50 pixel star-free boxes in each image (see Chapter 2 and Schombert & McGaugh 2014).

As with Chapter 2, we deproject our galaxy images for our analysis. To do this, we use the IRAF task ELLIPSE to determine the disk position angle and inclination of each galaxy in each photometric band. We then take the average value between all available bands to be the P.A. and inclination of the galaxy, with the largest deviation from the average assigned as the error. Errors in P.A. and inclination are typically $\sim \pm 5^{\circ}$ and $\sim \pm 2^{\circ}$, respectively. The deprojection is then performed using GEOTRAN to rotate and 'stretch' the image. Our derived P.A. and inclinations are listed in Table 3.1.

Our final, reduced, on-sky B- and I-band images for our new galaxies are presented in Fig. 3.1. Here, images of the same photometric band have been scaled the same way for easy comparison (except for the I-band image of UGC 2925 which has a larger scaling range), and every image uses asinh scaling to best show the structure in each galaxy. Each image is 400×400 pixels, or $1.52' \times 1.52'$.

3.3 Bar Properties

Here we describe the methods used to characterize each of the bar properties for the full sample. In addition, we present and discuss the results in relation to previous LSB and HSB results.

[3]IRAF is distributed by the National Optical Astronomy Observatory, which is operated by the Association of Universities for Research in Astronomy (AURA) under a cooperative agreement with the National Science Foundation

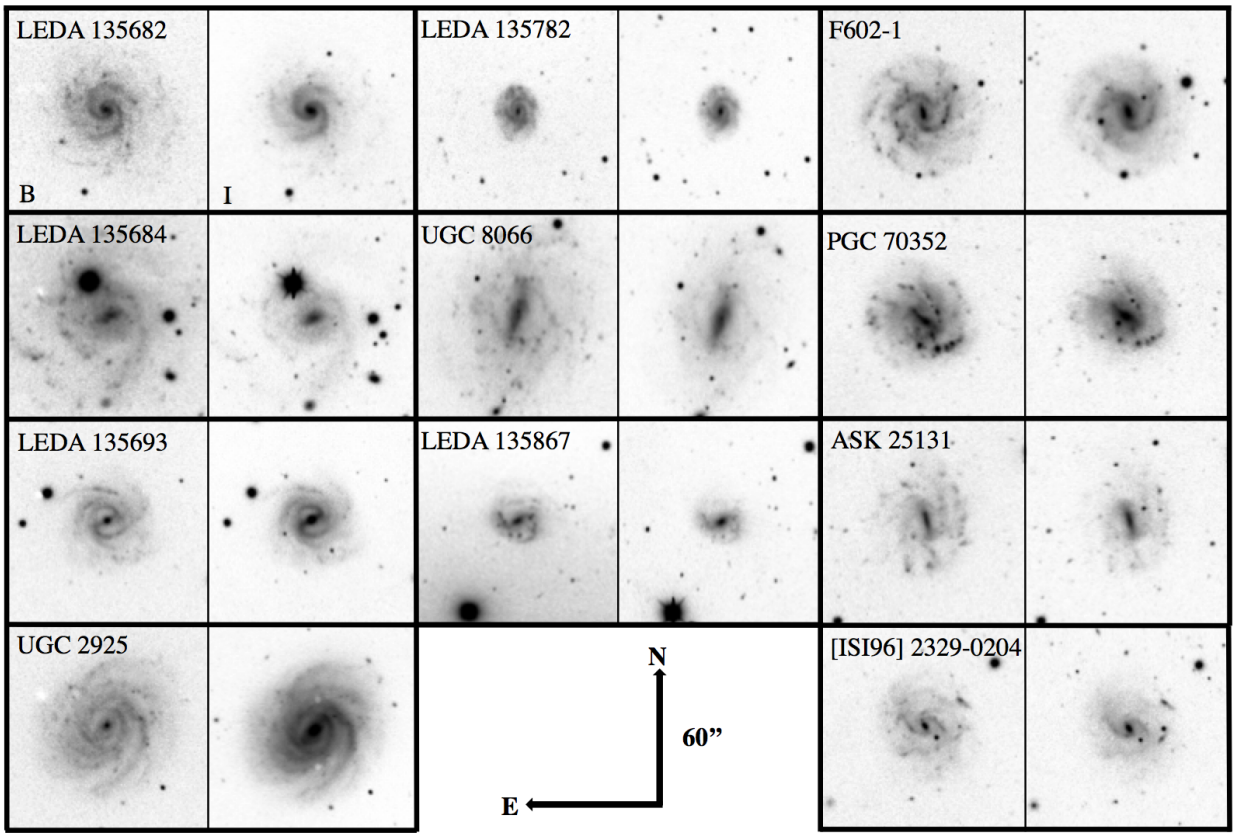

Figure 3.1: B- and I-band ARCTIC images of our sample. Galaxies are separated by thick black lines, with the B-band image on the left and the I-band image on the right for each galaxy. Each image is 400×400 pixels, or $1.52' \times 1.52'$, with each B-band image scaled identically. All I-band images are scaled identically with the exception of UGC 2925. All images are shown with `asinh` scaling to display structure more easily. North and East are indicated by the arrows in the bottom center, each arrow being $60''$ long. Images for UGC 628, F563-V2, F568-1, and F568-3 are in Chapter 2.

3.3.1 Methods

We follow the methods outlined in Chapter 2 for determining the bar length, strength, and corotation radius but we also employ a new bar length measure with the aim of improving the elliptical isophotal bar length measure for our sample. For a more detailed description of each of these methods, see Sec. 2.3 in Chapter 2. All of our measurements use the deprojected I-band galaxy images, since bars are stellar features and are more prominent and well-defined in redder photometric bands. For the sake of example, we will use LEDA 135782 as a walkthrough for each meaasurement. The remaining galaxies are shown in the additonal figures at the end of this chapter.

3.3.1.1 Bar Lengths

Since the bar strength and corotation radius are dependent on the bar radius, it is important that the bar radius be accurately determined. Therefore, as in Chapter 2, we use multiple methods for measuring the bar length: (1) elliptical isophotes (e.g., Wozniak et al. 1995; Aguerri et al. 1998, 2000a,b, 2009); (2) Fourier analysis of azimuthal light profiles (e.g. Ohta et al. 1990; Aguerri et al. 1998, 2000a); (3) azimuthal behaviour of the bar (Ohta et al. 1990). We briefly describe each method below. We select the best measurement of the bar length by visually comparing the various measures on the deprojected galaxy images (see Chapter 2). For a few targets, the bars are no longer than $2''$ ($\sim$8.77 pixels), so some methods are unable to find a bar length.

Elliptical Isophotes When fitting the light distribution of a galaxy with elliptical isophotes, a bar can be found by analyzing the behaviour of both the eccentricity and position angles of the ispohotes. For example, a traditional approach is to use the radius of maximum ellipticity as the bar length (e.g. Wozniak et al. 1995).

However, the bar length can be underestimated when using the radius of maximum ellipticity (Michel-Dansac & Wozniak 2006). In addition, because the bar strength and

relative bar pattern speed depend on the bar length, choosing the most accurate measure of the bar length is crucial. Due to this, we have employed an additional bar length measure using the elliptical isophotes that was not used in Chapter 2. This method defines the bar length to be the location where the position angle of the isophotes diverges a certain amount away from the position angle of the bar (Wozniak et al. 1995; Aguerri et al. 2009). We therefore have two measures using the elliptical isophotes: (1) R_e, the radius of maximum ellipticity, and (2) $R_{\rm PA}$, the radius where the P.A. of the isophotes differs by more than 5 degrees from the value at R_e.

The deprojected radial plots of eccentricity and P.A. for LEDA 135782 are shown in Fig. 3.2. In each panel, the vertical dashed line indicates the bar length from the respective method. Using the radius of maximum eccentricity, we find a bar length of $3.11'' \pm 0.30''$, and the bar length from the discontinuous P.A. is $3.77'' \pm 0.36''$. The errors for both these methods come from the radial spacing between the points. We find that discontinuous P.A. radius method fails for one of our galaxies, F563-V2.

The bar lengths for each galaxy are listed in Columns 1 and 2 in Table 3.2. Plots similar to Fig. 3.2 for the remaining galaxies are in shown in Fig. 3.19.

Fourier Analysis The Fourier analysis is done by decomposing our deprojected images into azimuthal light profiles $I_r(\theta)$, and then decomposing these via a Fourier transform:

$$\mathcal{F}(r) = \int_{-\pi}^{\pi} I_r(\theta) \exp(-2i\theta) d\theta. \tag{3.1}$$

The Fourier coefficients are

$$A_m(r) = \frac{1}{\pi} \int_0^{\pi} I_r(\theta) \cos(m\theta) d\theta \tag{3.2}$$

$$B_m(r) = \frac{1}{\pi} \int_0^{\pi} I_r(\theta) \sin(m\theta) d\theta \tag{3.3}$$

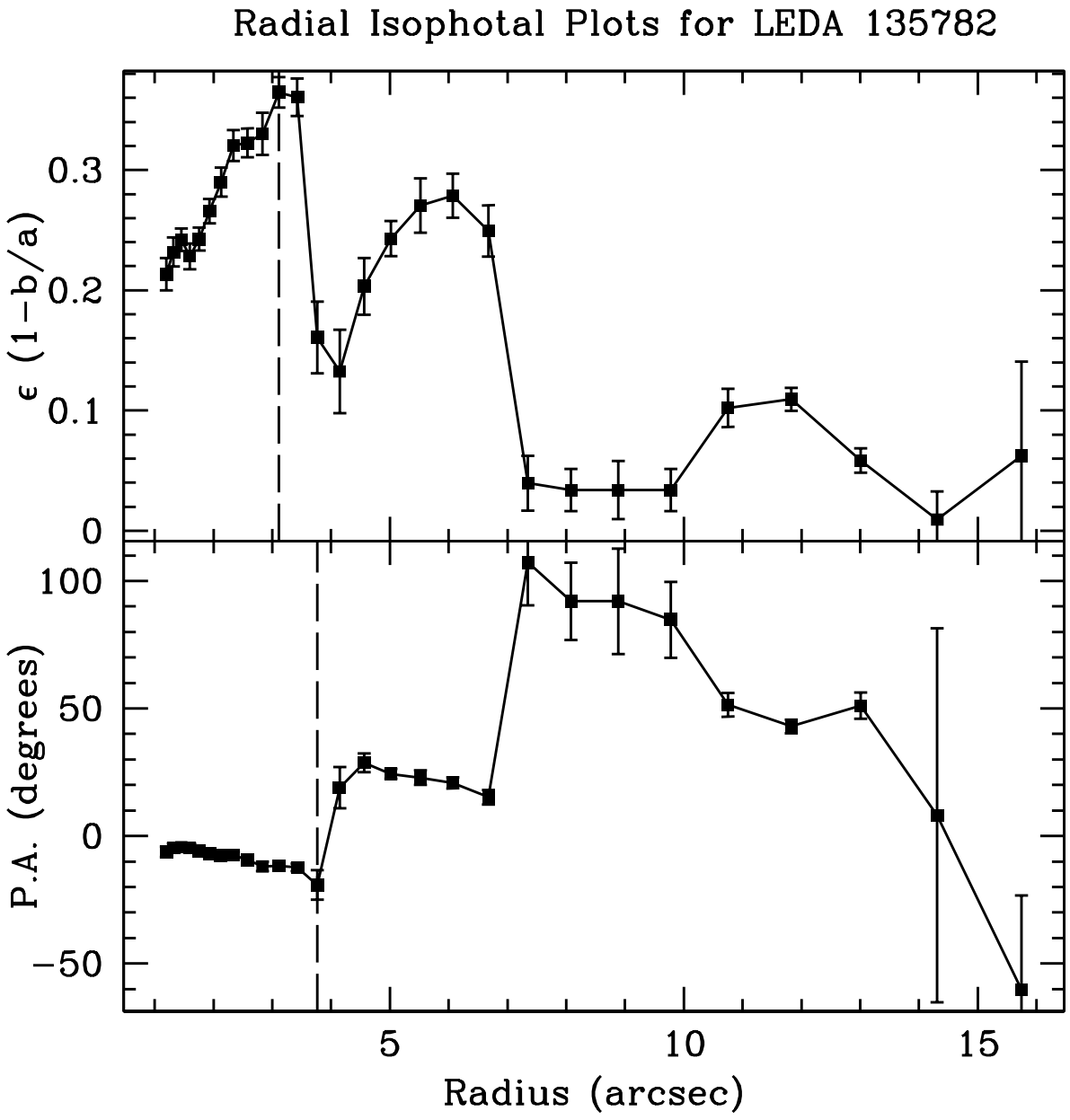

Figure 3.2: Radial plots of eccentricity (top panel) and P.A. (bottom panel) for LEDA 135782. The vertical dashed lines indicate the bar lengths based on maximum eccentricity (top panel) and position angle discontinuity (bottom panel).

and the amplitudes are

$$I_0(r) = \frac{A_0(r)}{2} \tag{3.4}$$

$$I_m(r) = \sqrt{A_m^2(r) + B_m^2(r)} \tag{3.5}$$

In order to determine the bar length, we use the bar/interbar (I_b/I_{ib}) Fourier intensities method from Aguerri et al. (2000a), where the bar region is defined as

$$\frac{I_b}{I_{ib}} > \frac{1}{2}\left[\left(\frac{I_b}{I_{ib}}\right)_{max} - \left(\frac{I_b}{I_{ib}}\right)_{min}\right] + \left(\frac{I_b}{I_{ib}}\right)_{min}. \tag{3.6}$$

The last radius at which the above is satisfied is taken to be the bar radius. The bar and interbar intensities are defined as

$$I_b = I_0 + I_2 + I_4 + I_6 \tag{3.7}$$

$$I_{ib} = I_0 - I_2 + I_4 - I_6 \tag{3.8}$$

While Aguerri et al. (2000a) state Equation 3.6 describes the bar region better than $(I_b/I_{ib}) > 2$, both our results from Chapter 2 and the results from Aguerri et al. (2009) show that this method can tend to overestimate the true bar length. Regardless, we use this method to determine how effective (or not) it is when applied to LSBs.

The bar/interbar Fourier intensity plot for LEDA 135782 is shown in Fig. 3.3, where the dashed horizontal line denotes Equation 3.6. We only consider data near the bar region as including radii in the disk can bias the method due to spiral arms, hence why the profile ends near $4''$. Using this method, we find a Fourier bar length of $3.5'' \pm 0.46''$. The error for this method comes from the radial spacing of the azimuthal light profiles.

LEDA 135782 has interesting Fourier amplitudes, shown in Fig. 3.4. Here we see strong $m = 2$ (deep blue) modes in the bar and disk region, which is not surprising for a barred spiral. However, we also see strong $m = 1$ (deep red) and $m = 3$ (yellow) modes in the disk.

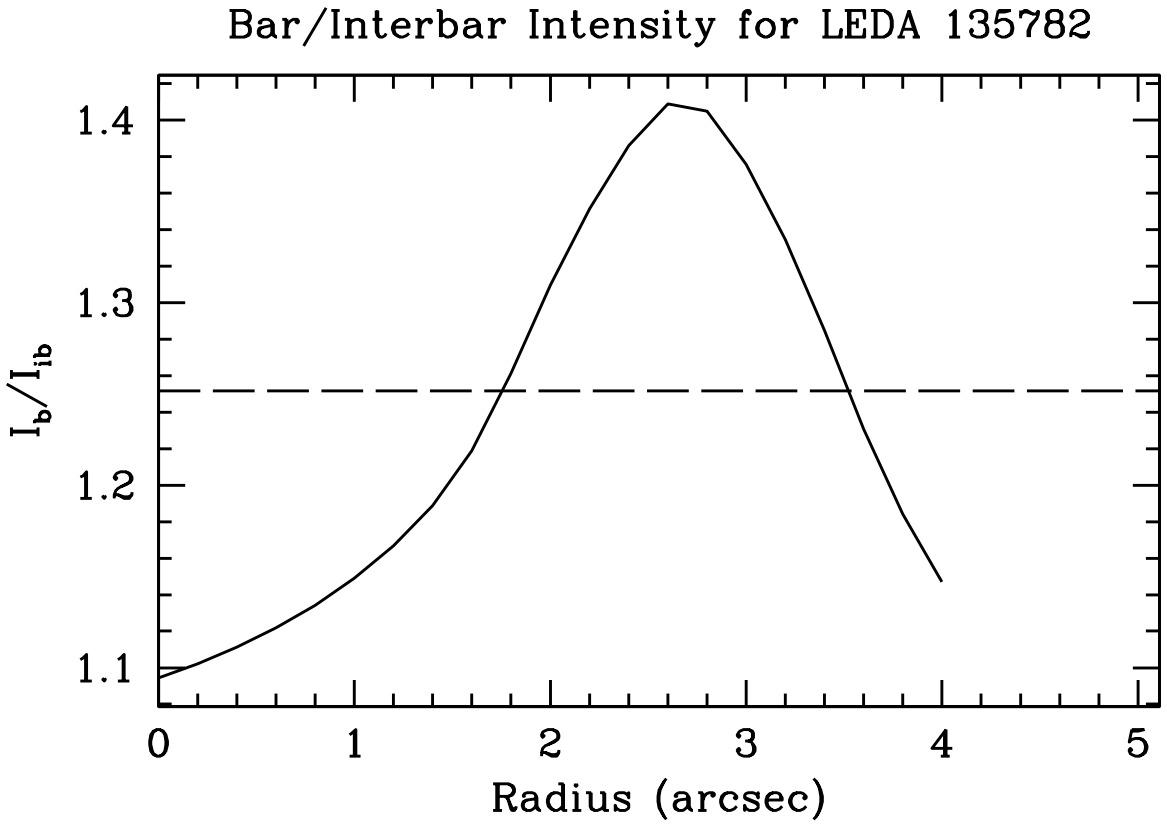

Figure 3.3: Bar/Interbar Fourier intensities for LEDA 135782. The dashed horizontal line denotes Equation 3.6, or the bar region. As the bar region is defined as where the ratio is *greater* than Equation 3.6, only the second crossing denotes the bar length.

When looking at Fig. 3.1, LEDA 135782 appears to have three spiral arms, consistent with the strong odd modes.

We find that the strength of the spiral arm pattern greatly affects the accuracy of this method. For instance, for those galaxies with a strong dual-arm pattern (see UGC 628 and F568-1 in Chapter 2 and LEDA 135682 in Fig. 3.1), the bar length is consistently overpredicted. The method finds the bar length more easily when the spiral arms are weaker.

In addition, we find the Fourier method fails to find a bar length for three of our galaxies, most likely due to the spiral arms: LEDA 135867, PGC 70352, and [ISI96] 2329-0204 (middle center, middle right, and bottom right in Fig. 3.1). When examining the Fourier amplitudes for these three galaxies, we find even modes that are stronger in the disk than in the bar, preventing the method from accurately determining a bar region.

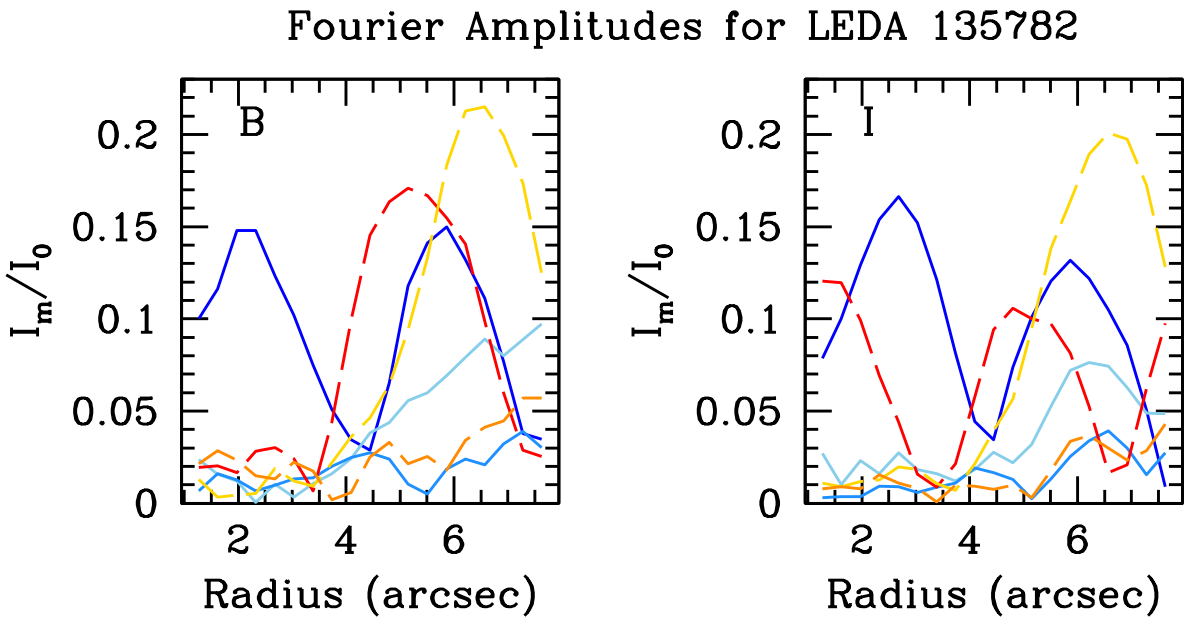

Figure 3.4: Fourier amplitudes for LEDA 135782: B band shown in the left panel and I band in the right panel. Bluer colors show even modes with deep blue being the $m = 2$ mode, and redder colors show odd modes with deep red being the $m = 1$ mode. Here we can see strong $m = 2$ modes in the bar region and disk region. Interestingly, we see strong $m = 1$ and $m = 3$ (yellow) modes in the disk region.

The bar lengths for each galaxy using the Fourier Analysis method are listed in Column 3 of Table 3.2. Figures similar to Fig. 3.3 and Fig. 3.4 for the remaining galaxies are shown in Fig. 3.20 and Fig. 3.21.

Azimuthal Light Profile Finally, we use azimuthal light profiles to characterize the azimuthal behaviour of the bar. Following the procedure outlined in Chapter 2, we determine the azimuthal centroid of the bar and track either where the humps in the azimuthal light profiles no longer trace a constant azimuthal centroid, or where the azimuthal profiles begin to trace the spiral arms at the end of the bar. To do this, we make the following assumptions: (1) the bar is constant in azimuthal angle, and (2) the (two) spiral arms, if present, are separated by 180° azimuthally. While these two assumptions may not always be true (e.g.

the bar may have internal structure that causes it to be warped), they allow us to analyze the behaviour of the bar in order to determine the length.

Due to the different morphologies of our sample and sizes of our galaxies on the sky, we varied the azimuthal spacing and starting radius when constructing the azimuthal light profiles, as opposed to leaving all galaxies with the same radial spacing of $0.46''$ and starting radii of $2''$ as was the case in Chapter 2. This allowed bars that were quite short, $<2''$, to be measured.

The B-band and I-band azimuthal light profiles for LEDA 135782 are shown in Fig. 3.5. Here, the profiles are plotted every $\sim 0.7''$ for clarity, and the color scheme indicates the radial position with redder colors at smaller radii. We can see the clear presence of a bar in both bands, as indicated by the black arrows at $\sim 90^\circ$ and $\sim 270^\circ$ in the inner radii, as well as a three arm pattern present in the outer radii (green profiles) in both bands.

We show the azimuthal information for the bar in LEDA 135782 in Fig. 3.6, deriving the azimuthal positions and errors of the humps by fitting gaussians to the profiles. Here we show the azimuthal positions of the bar 'humps' (top left), the azimuthal difference between the two humps (top right), the azimuthal difference from the bar centroid (bottom left), and the ADU intensity of the bar humps (bottom right). The dashed vertical line in the bottom left denotes the bar length, or where the azimuthal difference from the bar centroid has diverged. LEDA 135782 is a prime case of a very small bar (on the sky), which can pose a challenge when using this method. However, it is clear from looking at the bottom left panel that the first three points are relatively constant, best seen in the open yellow points, and show a dramatic change after the dashed line. We find a bar length of $2.66'' \pm 0.68''$. The errors are determined based on the behaviour of the azimuthal light profiles, as discussed in Chapter 2. We assign the larger errors due to the small bar in this galaxy.

For LEDA 135682 and [ISI96] 2329-0204, the bar is quite small on the sky ($\sim 2''$) and hard to measure with this method. In order to get as accurate a measurement as possible, we decreased the starting radius of our azimuthal light profiles to $1''$ for each galaxy, and

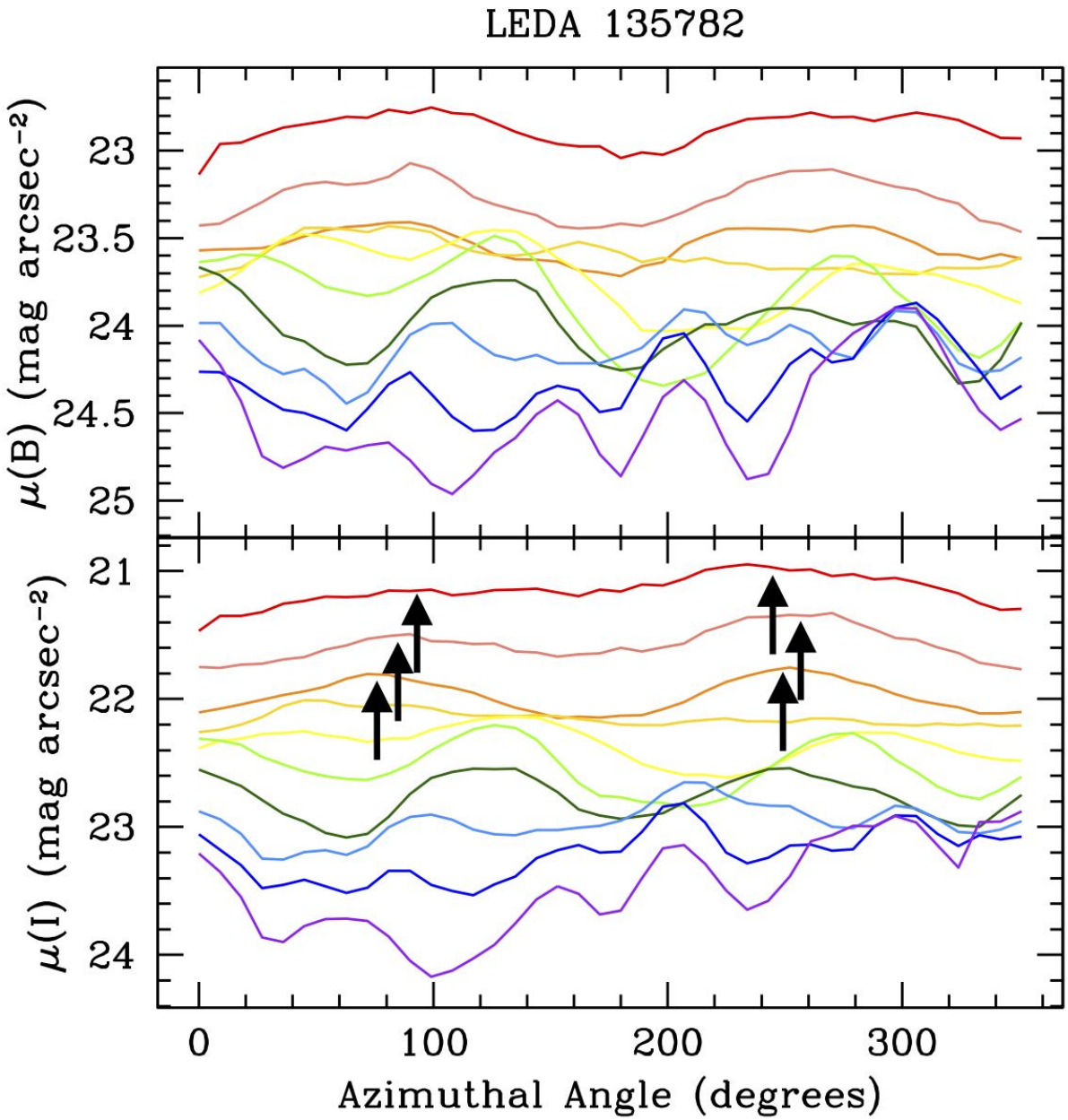

Figure 3.5: B-band (top) and I-band (bottom) azimuthal light profiles (in mag arcsec^{-2}) for LEDA 135782. Profiles are plotted every $\sim$0.7$''$ for clarity. Color scheme indicates radial position, with redder colors at smaller radii. The black arrows are placed to assist the reader in identifying the humps in the inner radii.

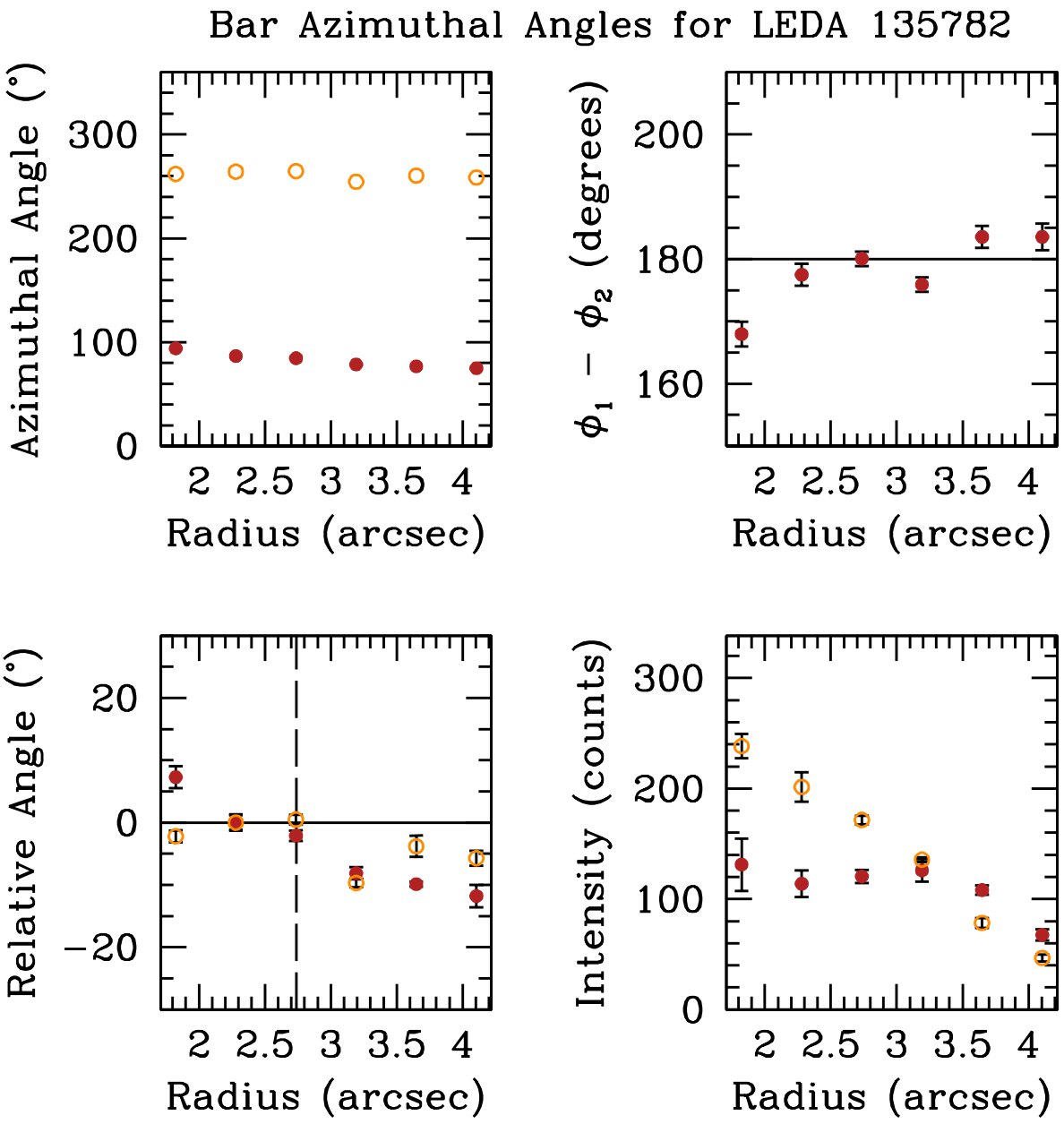

Figure 3.6: Bar azimuthal angle information for LEDA 135782. *Top Left*: azimuthal position of the two bar humps; *Top Right*: difference between azimuthal angles for two humps; *Bottom Left*: azimuthal difference from the bar centroid; *Bottom Right*: ADU intensity of the bar humps. The dashed vertical line in the bottom left panel denotes the azimuthal bar length, or where the azimuthal position of the humps has diverged from the bar azimuthal centroid.

lowered the radial spacing for LEDA 135682 to 1.5 pixels (0.34″) and to 1 pixel (0.228″) for [ISI96] 2329-0204. To ensure we maintained at least one pixel in each azimuthal division, we increased the size of the azimuthal bins to 9° for both galaxies. This is a loss of resolution on these azimuthal light profiles, but the azimuthal locations of the bar remained unchanged.

The bar lengths for each galaxy measured using azimuthal light profiles are listed in Column 4 of Table 3.2. Figures similar to Fig. 3.5 and Fig. 3.6 for the remaining galaxies are shown in Fig. 3.22 and Fig. 3.23 respectively.

3.3.1.2 Bar Strengths

Instead of using the same bar strength measure as in Chapter 2 (i.e. from Aguerri et al. 2000a), we modify the method to include the higher order even components, as these can be significant (Ohta et al. 1990):

$$S_b = \frac{1}{r_{bar}} \sum_{m=2,4,6} \int_0^{r_{bar}} \frac{I_m}{I_0} dr, \tag{3.9}$$

where $m = 2, 4, 6$ are the even modes, and r_{bar} is the bar radius from the azimuthal method. We note that our measure is only a lower limit, as we cannot probe down to $r = 0$, since this would result in azimuthal bins with no pixels when constructing the azimuthal light profiles.

3.3.1.3 Corotation Radii

We use the method put forth in Puerari & Dottori (1997) to measure the corotation radius ($R_{\rm CR}$) of the bar, the radius where disk orbits are equal to the pattern speed of the bar. This method determines $R_{\rm CR}$ via the intersection of phase profiles of the Fourier transforms of the B- and I-band images. The phase is given by

$$\Theta(r) = \arctan\left(\frac{\mathrm{Re}(\mathcal{F}(r))}{\mathrm{Im}(\mathcal{F}(r))}\right). \tag{3.10}$$

The idea behind this method is based on using the two different photometric bands, B and I, as proxies for two different stellar populations, young and old. We take the *first* phase intersection after the bar length to be the corotation radius. Corotation should not occur within the bar region (Contopoulos 1980; Bureau et al. 1999), and multiple intersections after the bar may be representative of the pattern speed of the disk (Puerari & Dottori 1997).

Again, we use LEDA 135782 as an example for this process. The phase profiles for LEDA 135782 are shown in Fig. 3.7. Here we see there are multiple phase intersections near the bar region: 2.2″, 2.8″, and 3.1″. Using the azimuthal bar length from Table 3.2, this means the bar corotation radius is at 2.8″, the first intersection after the bar radius. In addition, we find a phase intersection farther out, at 6.8″. This is likely a disk corotation radius.

Plots similar to Fig. 3.7 for the remaining galaxies are shown in Fig. 3.24.

3.3.2 Results

Here, we discuss the three bar properties (length, strength, corotation radius) for the entire sample. We do not discuss each galaxy individually, but we do focus on interesting or problematic galaxies when applicable (for more detailed discussion on these methods and individual results on our first sample, see Chapter 2). The bar lengths from each of the four techniques for each galaxy are listed in Table 3.2, and our final derived bar properties are listed in Table 3.3.

3.3.2.1 Bar Lengths

The bar lengths measured using each technique for each galaxy are listed in Table 3.2. We also include the bar length measurements from Chapter 2, as well as apply the $R_{\rm PA}$ measure to the four galaxies from Chapter 2. We determine the final bar length for all galaxies by visually plotting the various bar length measures over the deprojected I-band images (see Fig. 3.8, Fig. 3.25, and Chapter 2). We report these values as $R_{\rm bar}$ in Table 3.3. In general, we find an average bar length of 2.5 kpc for our sample.

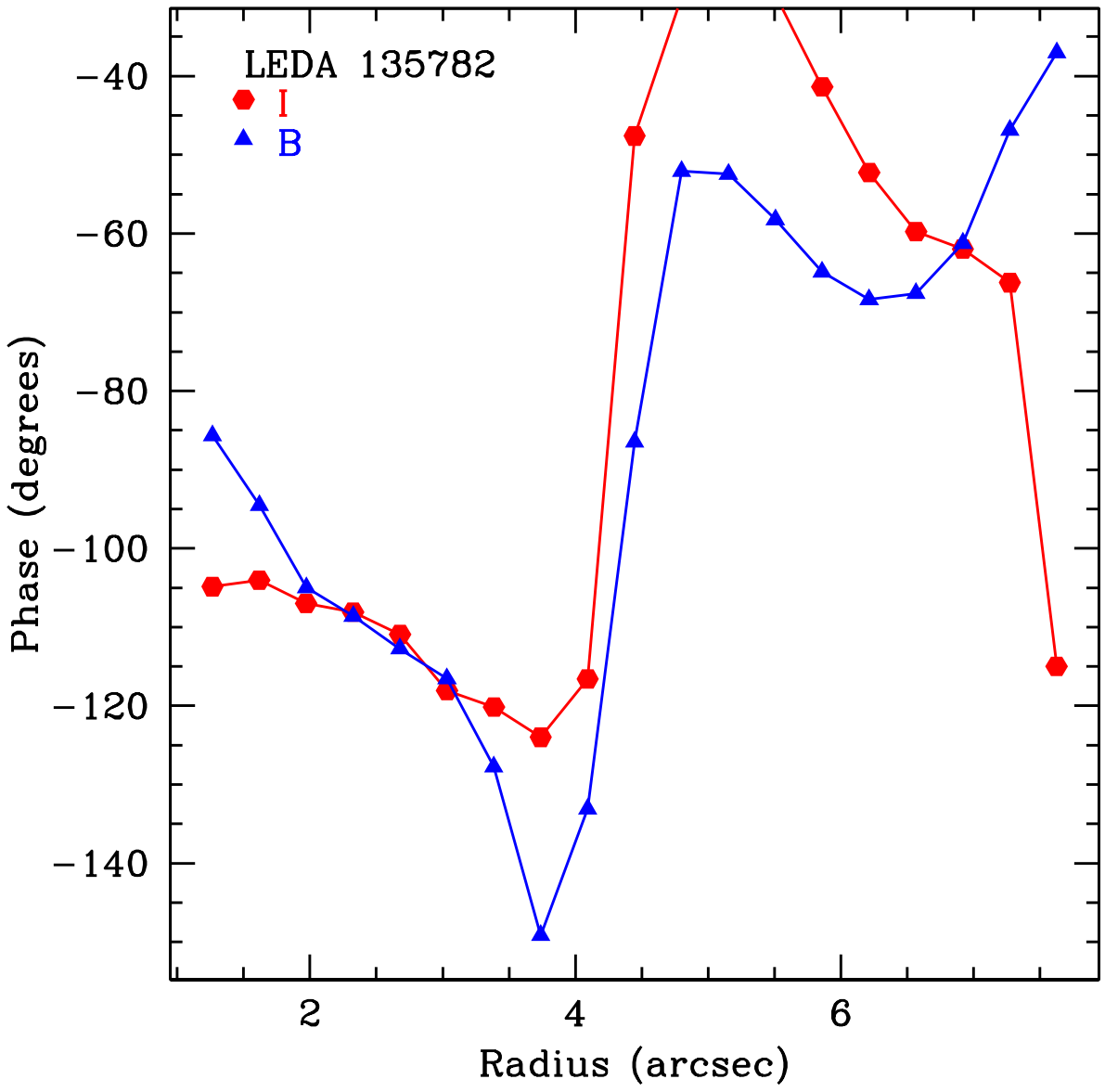

Figure 3.7: B-band (blue triangles) and I-band (red squares) phase profiles for LEDA 135782. Intersections of the phase profiles denote corotation radii, with the first intersection *after* the bar length being the bar corotation radius.

Table 3.2: Comparison of our various I-band bar length measures. All bar radii are in arcsec: radius of maximum ellipticity (R_e), radius of position angle discontinuity ($R_{\rm PA}$), Fourier method ($R_{\mathcal{F}}$), and the azimuthal method (R_{az}). '...' denotes where a given method failed for a given galaxy. Values for UGC 628, F563-V2, F568-1, and F568-3 are taken from Chapter 2.

Galaxy	R_e	$R_{\rm PA}$	$R_{\mathcal{F}}$	R_{az}
UGC 628	11.63 ± 0.68	14.36 ± 0.68	16.96 ± 0.46	11.21 ± 0.92
LEDA 135682	2.05 ± 0.2	2.73 ± 0.26	2.90 ± 0.23	2.05 ± 0.46
LEDA 135684	2.87 ± 0.27	9.01 ± 0.86	6.30 ± 0.46	7.07 ± 0.92
LEDA 135693	7.91 ± 0.76	8.70 ± 0.83	6.10 ± 0.46	5.70 ± 0.46
UGC 2925	11.60 ± 1.11	12.76 ± 1.22	9.10 ± 0.46	8.44 ± 0.92
F563-V2	5.02 ± 0.91	...	7.96 ± 0.46	6.65 ± 0.46
F568-1	8.44 ± 0.91	10.26 ± 0.91	7.76 ± 0.46	4.37 ± 0.46
F568-3	7.75 ± 0.68	16.64 ± 0.68	13.96 ± 0.46	8.93 ± 0.92
LEDA 135782	3.11 ± 0.3	3.77 ± 0.36	3.50 ± 0.46	2.66 ± 0.68
UGC 8066	6.07 ± 0.58	15.75 ± 1.50	16.50 ± 0.34	7.07 ± 0.68
LEDA 135867	6.77 ± 0.65	8.19 ± 0.78	...	4.39 ± 0.34
F602-1	1.19 ± 0.27	2.80 ± 0.27	4.20 ± 0.34	4.11 ± 0.34
PGC 70352	5.28 ± 0.50	7.03 ± 0.67	...	5.02 ± 0.68
ASK 25131	3.28 ± 0.30	9.36 ± 0.89	8.70 ± 0.34	7.76 ± 0.92
[ISI96] 2329-0204	1.64 ± 0.16	2.64 ± 0.25	...	2.05 ± 0.46

We plot the four different bar length measures over the deprojected I-band image of LEDA 135782 in Fig. 3.8. Here we see that the azimuthal bar length (blue) is the best measure of the bar in this galaxy, as the other three extend into the spiral arms. We find that this holds for the other galaxies in our sample (see Fig. 3.25), suggesting that the azimuthal method is the most accurate of the four used here, consistent with our findings in Chapter 2.

With this in mind, in Fig. 3.9 we show the various measures in relation to the azimuthal method. Here, $\Delta R_{\rm bar}$ denotes the difference between either R_e (red triangles), $R_{\rm PA}$ (open black squares), or $R_{\mathcal{F}}$ (blue circles) and R_{az}. We discuss each measure in relation to R_{az} below.

We find that the two bar length measures based on the behaviour of the elliptical isophotes do not produce consistent results. R_e equally over and under predicts the bar length compared to R_{az}. This is because the measure can be biased towards longer values due to a very elliptical bar or the presence of spiral arms, as well as biased towards shorter bars due to any highly elliptical feature in the inner regions.

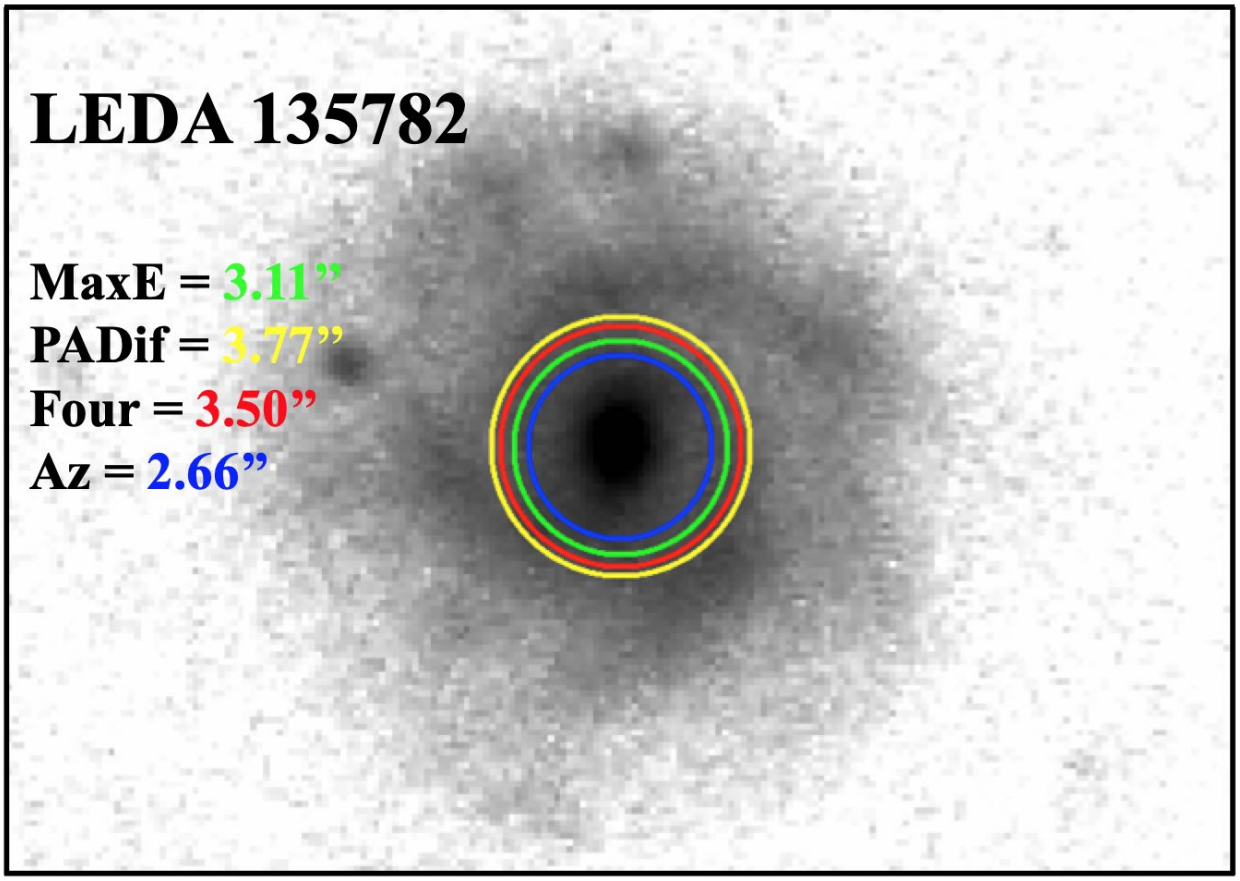

Figure 3.8: The four bar length measures plotted over the deprojected I-band image of LEDA 135782: R_e (green), $R_{\rm PA}$ (yellow), $R_{\mathcal{F}}$ (red), and R_{az} (blue). Here we can also see the three spiral arm pattern.

We find that $R_{\rm PA}$ almost consistently overpredicts the bar length, often quite extremely (i.e. $> 2''$). This is not too surprising, given that this measure is dependent on R_e. Since $R_{\rm PA}$ can only be larger than R_e, this method can only obtain an accurate measurement if R_e underpredicts the bar length.

In general, the Fourier method overpredicts the bar length compared to R_{az}. However, we find better results for this full sample when compared with our results from Chapter 2. In fact, $R_{\mathcal{F}}$ appears to be a better predictor of bar length than R_e or $R_{\rm PA}$ when looking at Fig. 3.9 (at least when $R_{az} < 9''$).

The azimuthal method does not rely on prior knowledge about the size of the bar, or the bar region. The three previous methods, however, can be biased towards shorter or longer

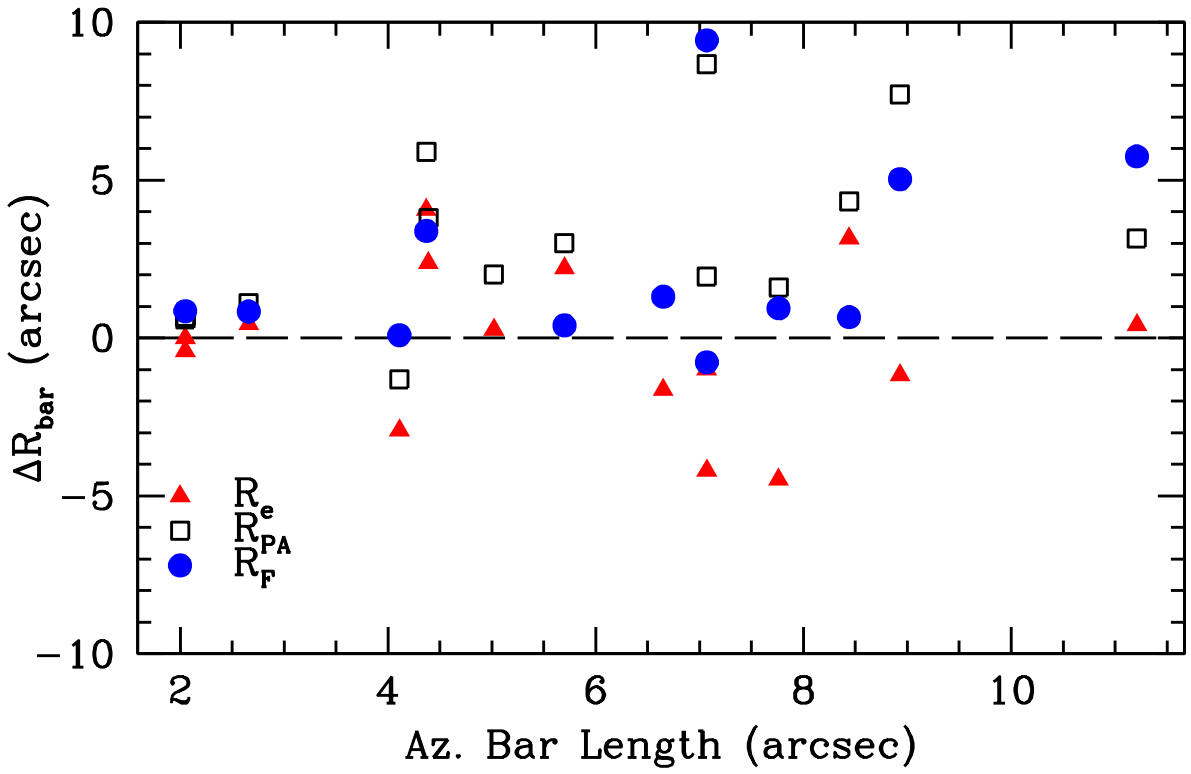

Figure 3.9: Comparison of our bar length measures relative to the azimuthal method (i.e. $\Delta R_{\rm bar} = R_{method} - R_{az}$): R_e shown as red triangles, $R_{\rm PA}$ shown as open black squares, and $R_{\mathcal{F}}$ shown as blue circles. By taking R_{az} as the true bar length, we find the other three measures generally overpredict the bar length, sometimes significantly.

values depending on how they are used. For example, if there is inner structure within the bar, the radius of maximum ellipticity (R_e) can be pushed inwards towards shorter values (see LEDA 135684, F602-1 and ASK 25131 in Table 3.2). This can in turn bias $R_{\rm PA}$, as this is determined via a change in P.A. relative to the value at R_e. To mitigate this effect, one can begin fitting isophotes at a larger initial radius, but this can lead to missing structure and requires knowledge about the bar length, possibly introducing bias. Our various bar length measures will be explored in more detail in Sec. 3.4.

In order to obtain final bar lengths, we have visually examined the bar lengths over the deprojected I-band images for all galaxies (see Fig. 3.8, Fig. 3.25, and Chapter 2). We have selected the best bar length from this examination and list them as the bar length in Table 3.3. In all cases, the best bar length measure comes from our azimuthal method.

3.3.2.2 Bar Strengths

Using Equation 3.9 and R_{az} as R_{bar}, we find bar strengths that range from 0.07 (LEDA 135682) to 0.49 (ASK 25131), with an average value of 0.25. As with Chapter 2, we examined the Fourier amplitudes of each galaxy and decreased the starting location of the azimuthal light profiles in order to gauge the confidence of our bar strength measure. We found that this did not significantly change the values, suggesting that our bar strengths, while lower limits, are accurate. We find that accounting for the higher order even modes gives a better picture of the bar strength, as some galaxies have significant contribution from these modes. For example, we find a bar strength of 0.25 for F568-3 here, and a bar strength of 0.19 in Chapter 2 where we only accounted for the $m = 2$ mode.

3.3.2.3 Corotation Radii

We find that the majority of the bar corotation radii in our sample occur very close to the end of the bars in our sample. This is consistent with results from HSBs (see e.g. Pérez et al. 2012; Aguerri et al. 2015; Sierra et al. 2015), and from the LSBs in Chapter 2. We address a problem galaxy, [ISI96] 2329-0204, below.

Special Note on [ISI96] 2329-0204 Measuring a corotation radius for [ISI96] 2329-0204 proves to be quite difficult. For this galaxy, we have $BVRI$ images, and thus create phase profiles for all four bands (see Fig 3.24). When examining the phase intersections, we find that the B-band behaves quite differently from the other three bands. So much so that it does not intersect the I-band phase profile until $\sim 11''$. This would leave us with a relative bar pattern speed that is $\sim$10, not a realistic number as this is more likely indicating the location of a disk corotation. This deviation from the other three bands is most pronounced at radii greater than $\sim 3''$, near the end of the bar.

Because this bar is quite small on the sky, we decreased the radial spacing of the azimuthal light profiles to one pixel, or $0.228''$. This did not produce better results, and no phase intersection between the B and I bands are observed at radii less than $11''$.

To add to this conundrum, the B band phase profile intersects the R band phase profile at $2.8''$ and $3''$, both at the end of the bar. Whether or not this is the radius of corotation is not entirely clear, as the method from Puerari & Dottori (1997) needs photometric bands separated by a large enough wavelength range. However, there has been previous work that uses 'bluer' bands than I- to determine the corotation radius (see Sierra et al. 2015). With this in mind, we will take the phase intersection between the B- and R-bands at $2.8''$ to be the corotation radius of the bar, as using the phase intersections between B and I is most likely not due to the bar.

3.3.3 Discussion of Bar Properties

Our final bar properties for the whole sample are listed in Table 3.3. Our sample has an average bar length of 2.5 kpc. This is shorter than what is typical for HSBs. When looking at surveys of HSBs, bars in these galaxies tend to be in the range 3 kpc $\leq R_{bar} \leq$ 5 kpc (see e.g. Erwin 2005; Marinova & Jogee 2007; Aguerri et al. 1998, 2009).

With the corotation radii of our sample, we can calculate the relative bar pattern speeds for our sample, $\mathcal{R} = R_{\rm CR}/R_{\rm bar}$, also listed in Table 3.3. Bars are considered 'fast' rotators if $\mathcal{R} < 1.4$ and 'slow' rotators if $\mathcal{R} > 1.4$ (Athanassoula 1992; Elmegreen et al. 1996; Debattista & Sellwood 2000). While historically the almost unanimous result for HSBs are fast bars (e.g. Pérez et al. 2012; Aguerri et al. 2015; Sierra et al. 2015), recent work has found an increasing number of 'slow' bars (Font et al. 2017; Guo et al. 2019). The results for dark matter dominated galaxies, LSBs specifically, are much more unclear due to the lack of pattern speed measurements.

Centrally dense, nonrotating, dark matter halos are expected to dynamically slow down bars over time (Weinberg 1985; Debattista & Sellwood 2000). Indeed, very slow bars in dark

Table 3.3: Final bar properties of the whole sample. Bar lengths are in arcsec ($R_{\rm bar}$) and kpc ($R'_{\rm bar}$), and corotation radii are in arcsec ($R_{\rm CR}$) and kpc ($R'_{\rm C}$), relative bar pattern speeds ($\mathcal{R}$), and lower limits on bar strength (S_b) are unitless. Lengths in kpc assume the distances in Table 3.1.

Galaxy	$R_{\rm bar}$ (arcsec)	$R'_{\rm bar}$ (kpc)	$R_{\rm CR}$ (arcsec)	$R'_{\rm CR}$ (kpc)	$\mathcal{R}$	$S_{\rm b}$
UGC 628	11.21 ± 0.92	4.67 ± 0.38	13.96 ± 0.46	5.81 ± 0.19	1.25 ± 0.11	0.30
LEDA 135682	2.05 ± 0.46	1.04 ± 0.23	2.70 ± 0.34	1.36 ± 0.17	1.32 ± 0.34	0.07
LEDA 135684	7.07 ± 0.92	1.57 ± 0.20	7.90 ± 0.46	1.75 ± 0.10	1.12 ± 0.16	0.30
LEDA 135693	5.70 ± 0.46	4.25 ± 0.69	7.30 ± 0.46	5.45 ± 0.34	1.28 ± 0.22	0.36
UGC 2925	8.44 ± 0.92	2.34 ± 0.26	12.50 ± 0.46	3.47 ± 0.13	1.48 ± 0.17	0.18
F563-V2	6.65 ± 0.46	1.95 ± 0.13	15.86 ± 0.46	4.64 ± 0.13	2.38 ± 0.18	0.28
F568-1	4.37 ± 0.46	1.94 ± 0.20	5.86 ± 0.46	2.61 ± 0.20	1.34 ± 0.18	0.13
F568-3	8.93 ± 0.46	3.61 ± 0.37	10.06 ± 0.46	4.07 ± 0.19	1.13 ± 0.13	0.25
LEDA 135782	2.66 ± 0.68	2.69 ± 0.69	2.80 ± 0.34	2.83 ± 0.34	1.05 ± 0.30	0.11
UGC 8066	7.07 ± 0.68	1.39 ± 0.13	7.50 ± 0.34	1.47 ± 0.07	1.06 ± 0.11	0.38
LEDA 135867	4.39 ± 0.34	2.53 ± 0.20	5.40 ± 0.34	3.11 ± 0.20	1.23 ± 0.12	0.37
F602-1	4.11 ± 0.34	2.09 ± 0.17	5.30 ± 0.34	2.70 ± 0.17	1.29 ± 0.14	0.21
PGC 70352	5.02 ± 0.68	1.79 ± 0.24	6.60 ± 0.46	2.35 ± 0.16	1.32 ± 0.20	0.13
ASK 25131	7.76 ± 0.92	4.02 ± 0.47	10.60 ± 0.46	5.49 ± 0.24	1.37 ± 0.17	0.49
[ISI96] 2329-0204	2.05 ± 0.46	...	2.80 ± 0.28	...	1.37 ± 0.34	0.18

matter dominated galaxies have been reported in the literature (Bureau et al. 1999; Chemin & Hernandez 2009; Banerjee et al. 2013). In order to examine possible trends between $\mathcal{R}$ and galaxy properties, Guo et al. (2019) used a sample of 53 barred galaxies and found a significant number of very slow bars. Interestingly, they found no correlation between a very slow bar and dark matter content. Our previous results in Chapter 2 indicated that three out of the four galaxies we analyzed were hosts to *fast* bars. Here we find that 13 out of the 15 galaxies in this work are hosts to fast bars.

Notably, only one galaxy in our sample has a *very* slow bar (i.e. $\mathcal{R} > 2$), F563-V2, and one galaxy, UGC 2925, has a slow bar that is comparable to previous results on HSBs (Aguerri et al. 1998; Sierra et al. 2015; Font et al. 2017; Guo et al. 2019). The remainder of the bars in our sample are *fast*. While this may seem to indicate that the bars in our sample have not been slowed down, dark matter halos are *not* static and can have significant angular momentum, arising from tidal exchanges during the formation of the galaxy (see Peebles 1969). This in turn means that the angular momentum exchange between the disk and the halo can be mitigated, sometimes significantly (Long et al. 2014). Thus, halos cannot serve as

a pure angular momentum sink, and the angular momentum of the halo, often characterized by the halo spin parameter λ, can dictate important aspects of a bar.

For example, Fujii et al. (2019) found that for high λ halos, bars actually *speed up*, while also becoming shorter and weaker. This is especially of note, as LSB disks are expected to form in high λ halos (e.g. Dalcanton et al. 1997; Jimenez et al. 1998; Kim & Lee 2013). Thus, without knowing λ, we cannot truly make a definitive statement on the implications of our relative bar pattern speeds.

We show $\mathcal{R}$ versus bar strength in Fig. 3.10, including the HSBs from Aguerri et al. (1998), as this work uses the same measure as used here for corotation radius and bar strength. This is an updated plot of Fig. 2.36 from Chapter 2. Here we also show the fit to both LSBs and HSBs, excluding the outlier of F563-V2 (the point far above the rest) and find $\mathcal{R} = 1.23 + 0.14S_b$ with a scatter of 0.13. This is close to identical to the relation from Chapter 2, with a near identical scatter, and is consistent with the lack of relation found by Guo et al. (2019). Our relation is plotted in Fig. 3.10 as the solid line, with the shaded region indicating the scatter.

When looking at Fig. 3.10, we find that LSBs and HSBs form a continuum, with the LSBs clustered on the weaker strength end (average ~ 0.25) transitioning into the stronger HSBs (0.37 for the HSBs shown here). This also then translates to surface brightness, with bars being fast rotators across all surface brightnesses.

As both the strength and relative bar pattern speed are dependent on the bar length, it is crucial that this property be measured as accurately as possible. For this reason, we have employed the four different measurement techniques here and have found that our R_{az} method performs the best for all the galaxies in our sample. However, in order to be as confident in this method as possible, we have tested the four methods used here on simulated galaxy images consisting of a disk and bar. This is therefore an idealized case for each method, as no spiral arms or disk features can affect the measurement. We spend the entirety of the next section discussing this process. Because the azimuthal bar length performs so well on

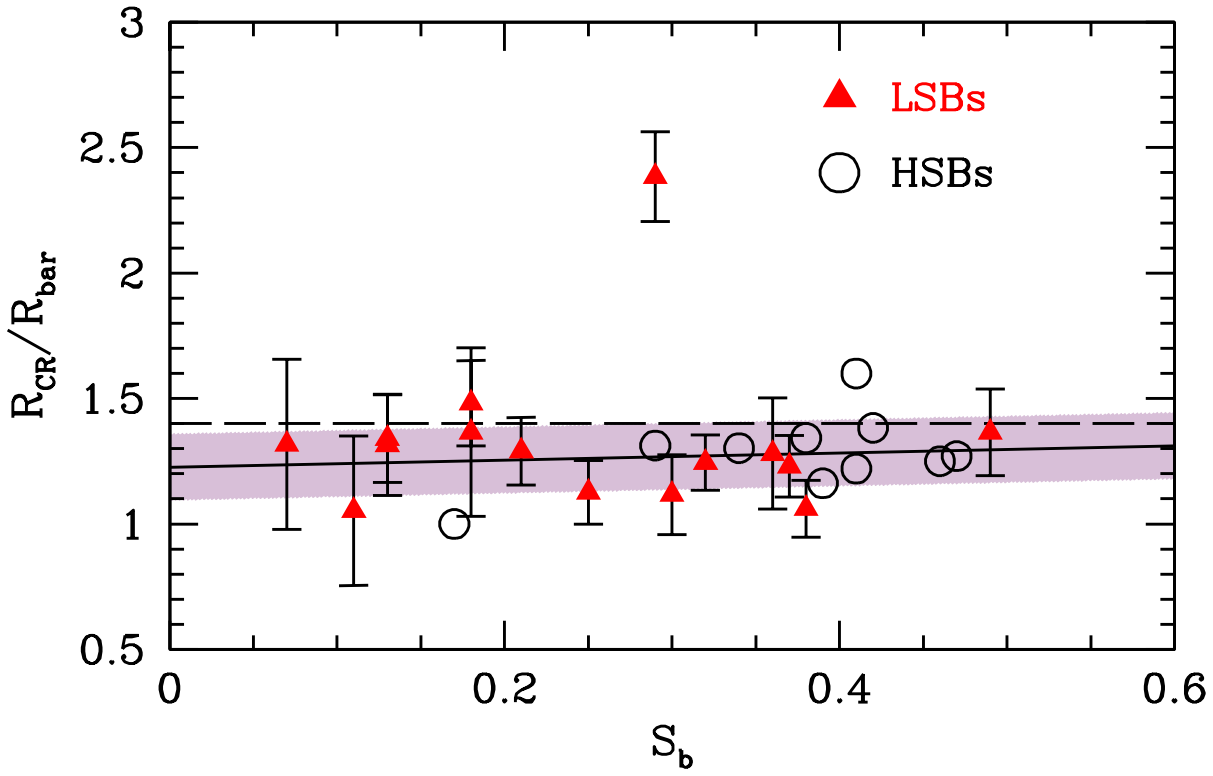

Figure 3.10: Relative bar pattern speed ($\mathcal{R} = R_{\rm CR}/R_{\rm bar}$) as a function of bar strength (S_b) for our sample (red triangles) and HSBs from Aguerri et al. (1998) (open circles). The solid line indicates the fit to the HSBs and LSBs, excluding the outlier discussed in the text: $\mathcal{R} = 1.23 + 0.14S_b$. The shaded region shows the scatter in the relation: $\sigma = 0.13$. The horizontal dashed line is the separator between fast and slow bars (i.e. $\mathcal{R} = 1.4$).

our data, we expect this method to perform just as well on the simulated images. However, the lack of spiral arms or disk features could affect the accuracy of the other three methods as well.

3.4 Analysis of Mock Galaxy Images

In order to determine how well we can determine the bar properties of our galaxies, we constructed fake galaxy images with randomised structural and photometric parameters. We used observational parameters similar to those of our observed sample and those of the ARCTIC imager in order to compare with our observations. We broadly follow the procedure in Aguerri et al. (2009).

3.4.1 Creating the Images

For each galaxy, we assume two components: an exponential disk and a Ferrers bar (see Laurikainen et al. 2005). We do not consider a bulge component since LSBs do not typically have a bulge (Pahwa & Saha 2018), and because our sample lacks significant bulges. In addition, we do not include spiral arms in our images in order to provide an ideal scenario for each bar length fitting method. The intensity profile of an exponential disk is given by

$$I(r) = I_0 e^{-r/h}, \tag{3.11}$$

where I_0 is the central disk intensity and h is the disk scale length. The intensity profile of a Ferrers bar is given by

$$I(r) = I_0 \left(1 - \left(\frac{r}{r_{bar}}\right)^2\right)^{n_{bar}+0.5}, \tag{3.12}$$

where I_0 is the central bar intensity, r_{bar} is the length of the bar, and n_{bar} is the bar shape parameter. The intensity is defined to be zero for $r > r_{bar}$. The radial coordinate is given by

$$r = \left(|x|^c + \left|\frac{y}{1-\epsilon_{bar}}\right|^c\right)^{1/c}, \tag{3.13}$$

where ϵ_{bar} is the ellipticity of the bar, and c is a parameter that controls the shape of the bar isophotes (Athanassoula et al. 1990). Pure elliptical isophotes have $c = 2$, boxy isophotes have $c > 2$, and disky isophotes have $c < 2$.

In order to construct observationally accurate galaxies for our purposes, we selected galaxy properties that match the general LSB population, with bar values similar to our results from Chapter 2 and from Sec. 3.3.2. We begin by randomly assigning a disk central surface brightness

$$22.5 < \mu_{0,B} < 24 \tag{3.14}$$

and bar central surface brightness

$$22.0 < \mu_{0,B} < 23.0 \tag{3.15}$$

with the condition that the central bar surface brightness may not exceed the disk central surface brightness by more than 1 magnitude. This condition was chosen in order to closely match the photometric properties of our sample (see Sec. 3.5). We then convert these to intensity values via

$$I = tp^2 10^{(Z-\mu)/2.5}, \tag{3.16}$$

where t is the exposure time, p is the plate scale of the detector, and Z is the photometric zeropoint. We used values that matched our observations to obtain images similar to our observed galaxies: $t = 600$ sec., $p = 0.228$ arcsec pix^{-1}, and $Z_B = 25$. In order to produce images similar to our observations, we select distances

$$70 \text{ Mpc} < D < 200 \text{ Mpc}. \tag{3.17}$$

For the other parameters, such as bar ellipticity and disk inclination, we broadly follow the methods laid out in Aguerri et al. (2009). For the bar length, we select from a range representative of our results in Sec. 3.3.2. We also force the bar length to be shorter than the disk scale length in order to prevent constructing very unrealistic galaxies (i.e. a bar length of $15''$ and a disk scale length of $3''$ is not considered realistic).

After the galaxy images were created, we added noise to each pixel in order to closely match our observations. The gain and read-out noise of ARCTIC are 1.98 e$^-$ ADU^{-1} and 3.8 e^{-1} respectively. Sky noise was added in assuming a 600 sec. exposure in B. Finally, to account for seeing, we convolved the images with a 2D Moffat PSF

$$PSF(r) = \frac{\beta - 1}{\pi\alpha^2}\left(1 + \frac{r^2}{\alpha}\right)^{-\beta}, \tag{3.18}$$

where $\alpha = \mathrm{FWHM}/(2\sqrt{2^{1/\beta}-1})$ is the seeing parameter, and β is typically taken to be $\sim$3.5 (see Trujillo et al. 2001). To test a wide range of observations, we randomly select our seeing to be between $0.8''$ and $2''$, consistent with the average seeing values of our observations (Table 3.1).

Examples of the images we created are shown in Fig. 3.11. These images were randomly selected, and are representative of the types of galaxy images we have created. In total we have created 200 images. Histograms of bar lengths, ellipticity, and seeing are shown in Fig. 3.12. Here we can see that we are sampling a large range of bar lengths, but that we have a large oversampling of shorter bar lengths. This is because the bar lengths in our sample are quite short (Sec. 3.3.2) and we are hoping to gauge how well the various methods work for our sample. We see that we are sampling a large range of bar ellipticities, $\sim 0.2 \leq \epsilon_{bar} \leq \sim 0.8$. The two peaks in the seeing histogram arise from the distributions around 'good' and 'bad' seeing, which we have defined here to be $\sim 1''$ and $\sim 1.8''$ respectively.

3.4.2 Measurements of Mock Images

To maintain consistency, we follow the same reduction process as our real observations. We determine the sky value by using the box method of Schombert & McGaugh (2014) and use `ELLIPSE` and `GEOTRAN` to deproject our images. We then use our four methods described in Sec. 3.3.1 to determine the bar length.

As opposed to our real galaxies (see Sec. 3.3.2), we do not have concerns over spiral arms influencing our isophotal bar length measures, as we have explicitly not included them. Therefore, we have an ideal scenario for each measurement technique.

Due to the large number of images tested (200), we automated the azimuthal light profile measurement by standardizing each set of profiles. We did this by finding the azimuthal centroid of the bar, usually located at the maximum value of the profile. We then adjusted the entire set of profiles so that the bar centroid is aligned with either 90° or 270°, depending on which is closest to the centroid. It is then assumed that the two humps in the azimuthal

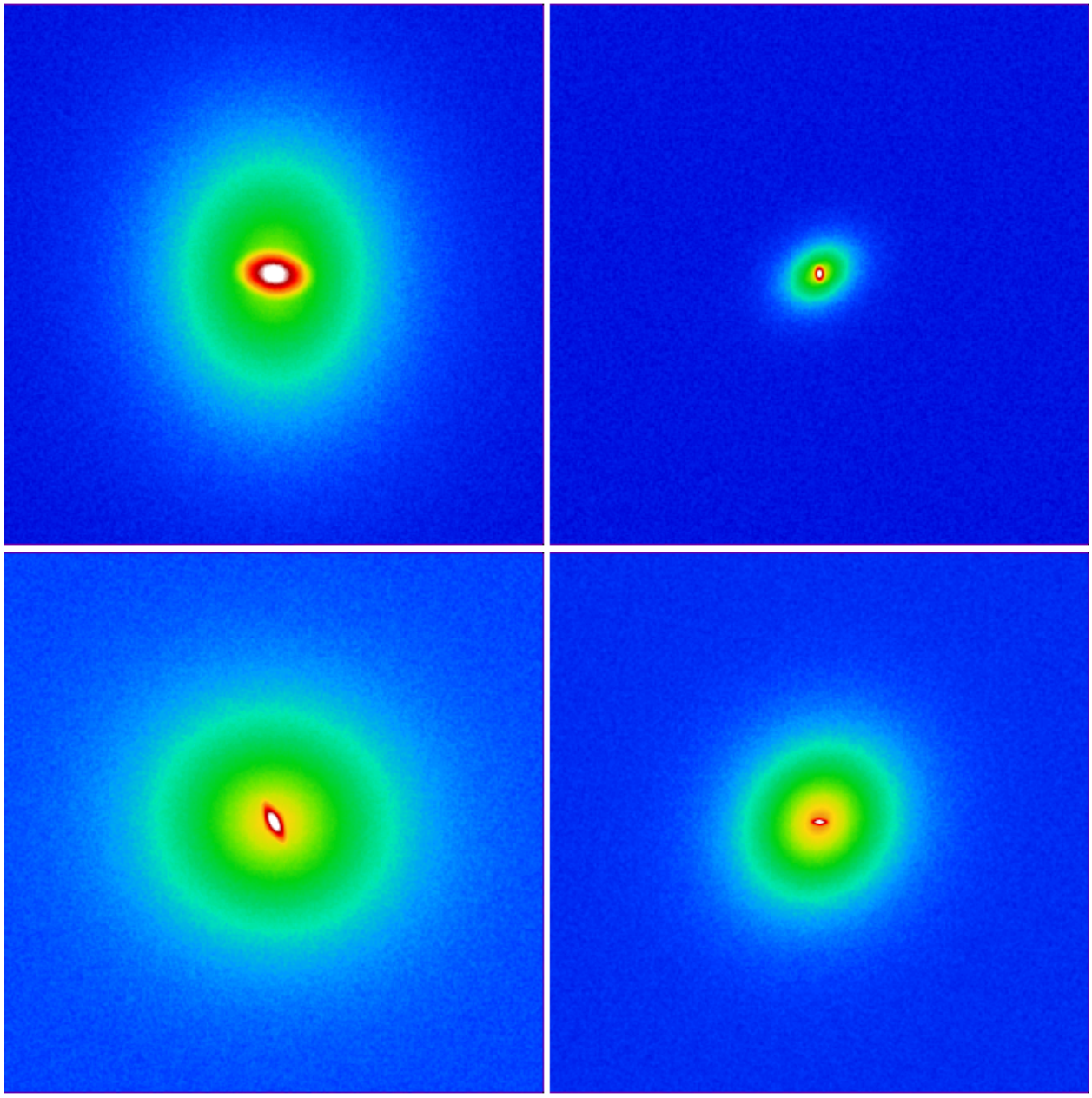

Figure 3.11: Examples of the mock images showcasing various sized bars and disks. Each image is 200×200 pixels (45.6″×45.6″) and is scaled the same way.

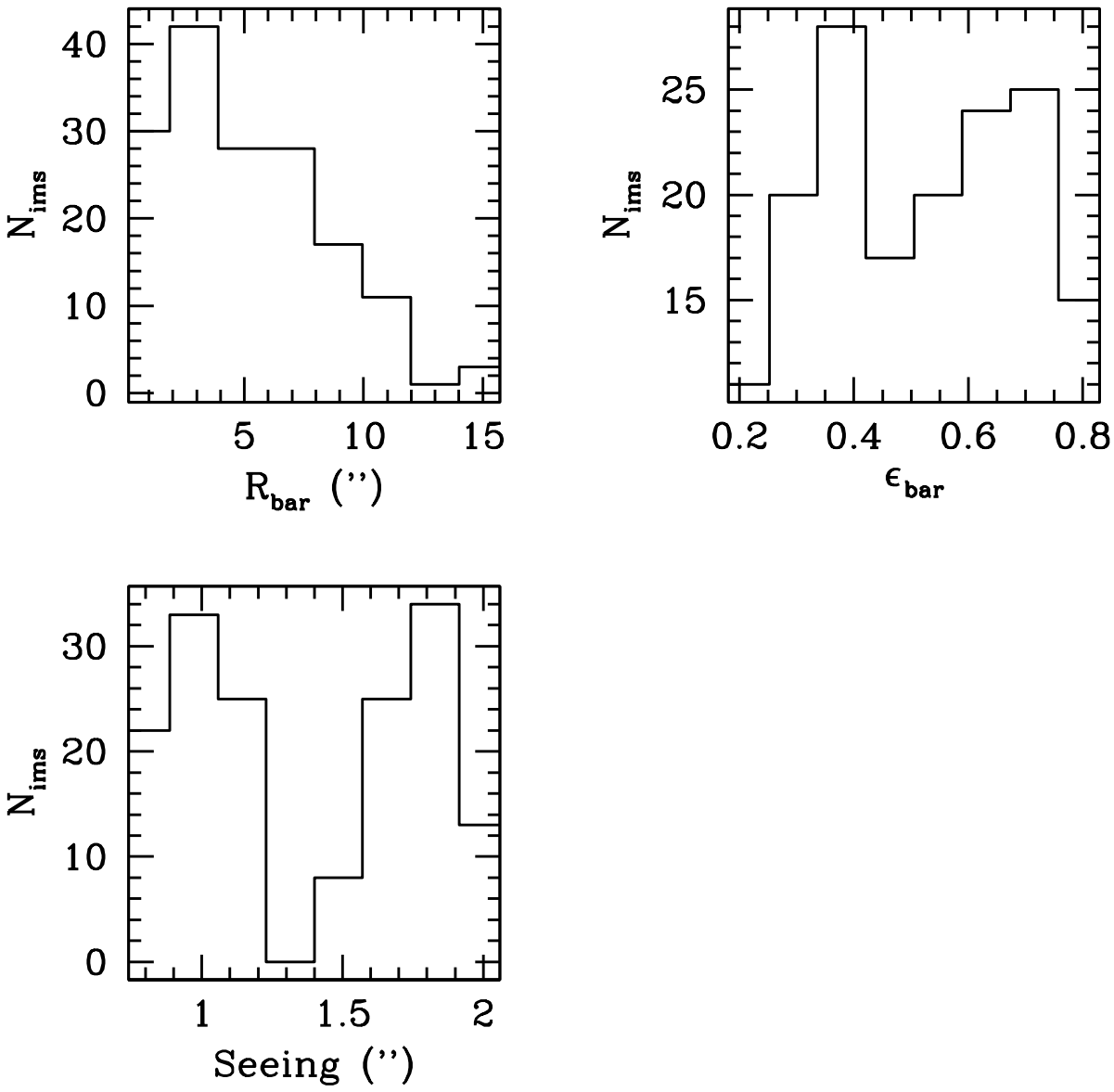

Figure 3.12: Histograms of bar length (top left), ellipticity (top right), and seeing (bottom left) for our mock images.

light profiles will remain at 90° and 270°. As there are no spiral arms in our images, we instead use the relative intensity of the bar hump to the disk to determine where the bar ends.

3.4.3 Results of Measurements

We show the comparison between the true and measured bar length for our mock images in Fig. 3.13: R_ϵ (top left), $R_{\rm P.A.}$ (top right), R_{az} (bottom left), and $R_{\mathcal{F}}$ (bottom right). Blue points denote those images with less than $1''$ seeing, and red points denote images with greater than $1''$ seeing. In each of these subfigures the solid line denotes unity, and the dashed lines are fits to the blue points (i.e. those with good seeing). It is clear from Fig. 3.13 that the seeing in each image greatly increases the scatter of the measurement.

We find that the radius of maximum ellipticity (top left panel) does a poor job of measuring the bar length, often measuring a length 50% shorter than the true length. This is an expected result, especially for Ferrers bars (Michel-Dansac & Wozniak 2006; Aguerri et al. 2009). The fit for this measure is $R_e = 0.44R_{bar} + 0.49$. Even though $R_{\rm P.A.}$ (top right panel) depends on R_e, we find that it does an excellent job of finding the bar length, only really failing at larger radii (i.e. $r > 5''$). The fit for this measure is $R_{\rm P.A.} = 0.82R_{bar} + 0.59$. Our bar length measure using the azimuthal light profiles (bottom left), R_{az}, performs the best out of the four methods tested, albeit only slightly better than $R_{\rm P.A}$. The fit for this measure is $R_{az} = 0.85R_{bar} + 0.80$. Lastly, we find that $R_{\mathcal{F}}$ under predicts the bar length, contrary to our results using real data (see UGC 628 and F568-1 in Chapter 2 and LEDA 135682 in Fig. 3.1, for example) and previous works (Aguerri et al. 2009), suggesting that spiral arms can heavily bias this method to longer bar lengths. The fit for this measure is $R_{\mathcal{F}} = 0.63R_{bar} + 0.46$.

Based on this modeling, we find that the bar length measure based on the behaviour of the azimuthal light profiles to be the best measure out of the four used here. While $R_{\rm P.A.}$ almost performs as well, the dependence on R_ϵ for this measure is concerning, and can result in wrong measurements. That $R_{\rm P.A}$ performs so much better here than with our real data is

surprising, although this could simply be that R_ϵ underpredicts the bar length so significantly here. In addition, the change in P.A. used here is simply following what has been used before (i.e. from Aguerri et al. 2009). Contrary to this, there is strong motivation for the azimuthal method, as it traces the location of the bar and any spiral arms in the galaxy, only being limited by the resolution and seeing. We do, however, note the large amount of scatter at smaller bar lengths for R_{az}. In addition, we see that this technique fails to find an accurate bar length for three bars, seen as the wildly inaccurate points in the bottom left panel of Fig. 3.13. When examining these images, we found that these failures were caused by a combination of factors. First, all three images contain bars and disks that have central surface brightnesses within $\sim$0.4 mag arcsec^{-2} of each other, making it somewhat hard to distinguish the two components in the azimuthal light profiles. Second, the position angles of the bars and disks are all within $\sim5^\circ$ of each other, which causes the bar to become slightly lost in the inclined disk. Finally, two of the failures have poor seeing, which further amplifies the issues caused by the first two points.

This suggests that our bar properties reported in Sec. 3.3.2 are accurate. More importantly, this means that the bars in our LSBs are indeed *fast* (but see Sec. 3.7).

3.5 Photometry

In this section, we detail our methods for measuring the photometry, and present our results. The surface brightness profiles, magnitudes, and colors for the 11 targets not in Chapter 2 are new measurements, as to the best of our knowledge no such measurements have been previously published.

3.5.1 Methods

Here we detail how we construct surface brightness profiles, as well as obtaining total magnitudes and colors.

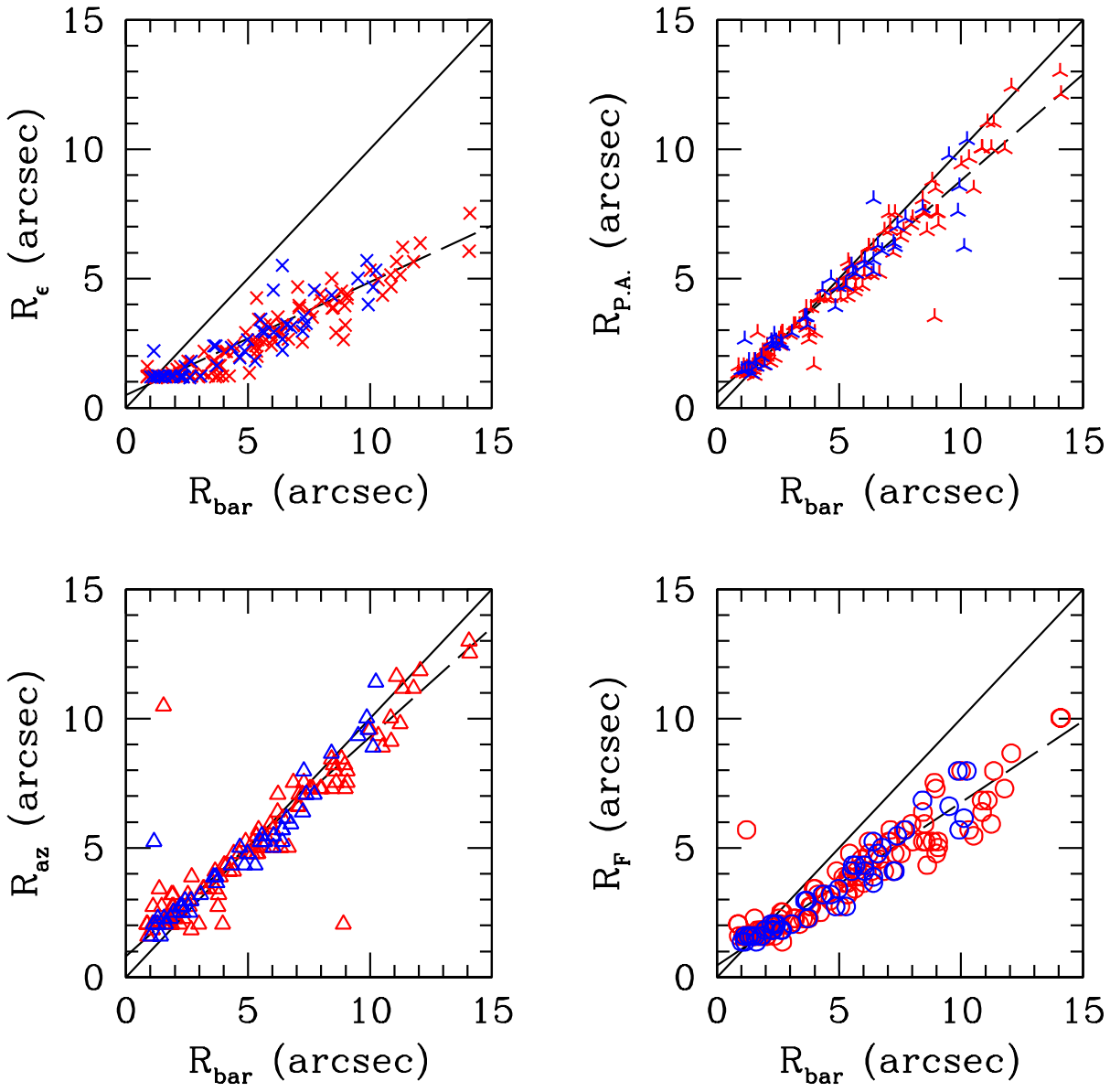

Figure 3.13: Our four bar length measures when applied to fake galaxy images: R_e (top left), $R_{\rm PA}$ (top right), R_{az} (bottom left), and $R_{\mathcal{F}}$ (bottom right). Images with seeing less than $1''$ are shown as blue points, and images with seeing greater than $1''$ are shown as red points. The dashed lines in each panel show the linear fits to the blue points.

3.5.1.1 Surface Brightness Profiles

We first obtain intensity profiles ($I(r)$) of our galaxies using the `IRAF` routine `ELLIPSE`. This method of constructing surface brightness profiles for LSBs has been used succesfully in the literature (e.g. Wittmann et al. 2017). We then convert these to surface brightness values via:

$$\mu(r) = -2.5 \log \left(\frac{I(r)}{t\ p^2} \right) + Z_p, \tag{3.19}$$

where t is the exposure time in seconds, p is the plate scale of the instrument, and Z_p is the photometric zeropoint of the observation (Sec. 3.2.2). We then fit for the central surface brightness (μ_0) and disk scale length (h), starting beyond the bar region, $r > R_{\rm bar}$ (see Sec. 3.3.2).

In order to correct for the likely low internal dust extinction in our galaxies (e.g. Bothun et al. 1997; Matthews & Wood 2001; Wyder et al. 2009; Hinz et al. 2007; Honey et al. 2016), we assume the disks are optically thin slabs. The correction for this assumption is simply:

$$\mu_0 = \mu_0^f - 2.5 \log (a/b) \tag{3.20}$$

where μ_0 is the observed central surface brightness, μ_0^f is the face-on central surface brightness, and a and b are the semi-major and -minor axes respectively (Table 3.1). This correction increases with the inclination, making magnitudes brighter for highly inclined disks.

3.5.1.2 Magnitudes

Due to the faint nature of LSBs, using a typical m_{25} magnitude is not an adequate measure of the total luminosity. Instead, we follow de Blok et al. (1995) and use the total magnitude, m_T, of the disk, found via

$$m_T = \mu_0 - 2.5 \log (2\pi h^2) - 2.5 \log (\cos i) \tag{3.21}$$

where i is the inclination of the disk (Table 3.1). Integrating out to infinity involves extrapolating the disk scale length, which can introduce error. To counter this, de Blok et al. (1995) also use another magnitude measure, m_{apt}, which takes the entire data of the galaxy disk into account. As their data probe down to ∼28 mag arcsec^{-2} in B, almost all the light of the galaxy is being probed. Our observations are not quite as deep, down to ∼26 mag arcsec^{-2} in B for most targets, so we do not use m_{apt} here.

3.5.1.3 Colors

Color profiles were obtained by subtracting the B- and I-band surface brightness profiles from each other.

We obtain three different total colors for each galaxy:

1. a **bar color** consisting of the average color within the bar region ($r < R_{bar}$)
2. a **disk color** consisting of the average color outside the bar region ($r > R_{bar}$)
3. an **area-weighted color** within the 25.5 B-mag arcsec^{-2} isophote (e.g. McGaugh & Bothun 1994; de Blok et al. 1995) ($r < R_{25.5}$)

We measure these three colors in the same manner. First, we create a $(B - I)$ color map for each galaxy by rebinning each image by a factor of 2 to reduce the noise, and subtracting the new I-band image from the B-band image after converting the units of the image from intensity to surface brightness, obtaining a color in each pixel (see de Blok et al. 1995; Schombert et al. 2011). We finally obtain colors by taking the mean value in each of the defined regions, rejecting divergent pixels and those with large errors.

3.5.2 Results

We list central surface brightnesses, magnitudes, disk scale lengths and other information for our whole sample in Table 3.4. All surface brightnesses and magnitudes reported are corrected for Galactic extinction using A_λ values from Schlafly & Finkbeiner (2011), also

listed in Table 3.4. Data for F563-V2, F568-1, and F568-3 are taken from McGaugh & Bothun (1994) and de Blok et al. (1995). Although LSBs are thought to have low dust content, we correct for any internal dust by assuming the disks are optically thin slabs (see Sec. 3.5.1.1).

With the exception of UGC 628, F563-V2, F568-1, and F568-3, the surface brightness profiles, magnitudes, and colors are all new. In addition, this is one of the few samples of exclusively barred LSB photometry.

3.5.2.1 Surface Brightness Profiles

Our B- and I-band surface brightness profiles and $(B-I)$ color profiles are shown in Fig. 3.14. We do not have photometrically calibrated ARCTIC data for F563-V2, F568-1, or F568-3. The majority of our galaxies exhibit very nearly Freeman Type I profiles (Freeman 1970), or pure exponential disks. For some galaxies, the bar is not noticeable in these surface brightness profiles, LEDA 135782 or PGC 70352 for example. For others, it very clearly dominates the inner light profile, as in the case of LEDA 135693 or [ISI96] 2329-0204.

The mean B-band and I-band central surface brightnesses are 22.39 and 20.28 mag arcsec^{-2} respectively, consistent with the findings in Zhong et al. (2008), who looked at roughly 12000 LSBs from the SDSS catalog. We find a mean B-band disk scale length of 3.68 kpc and a mean I-band disk scale length of 2.03 kpc. We find no correlation between scale length and central surface brightness, consistent with previous works (McGaugh & Bothun 1994; de Blok et al. 1995; Zhong et al. 2008; Pahwa & Saha 2018), as shown in the top panel of Fig. 3.15. Here, black points are our data, blue squares are from de Blok et al. (1995), and red triangles are from McGaugh & Bothun (1994), both of which use comparable methods for both barred and unbarred LSBs. We can see that roughly one dex in scale length spans roughly 4 mag in central surface brightness.

Table 3.4: B- and I-band central surface brightness (μ_0), disk scale lengths in arcsec (h) and kpc ($h^{'}$), and total apparent magnitudes (m_T) and absolute magnitudes (M_T) for our LSBs. Data for F568-1, and F568-3 are taken from de Blok et al. (1995). Data for F563-V2 are taken from McGaugh & Bothun (1994) (no I-band photometry available). Central surface brightness and magnitudes are corrected using the A_λ values in Column 8 (Schlafly & Finkbeiner 2011). As a reminder, there is no distance available for [ISI96] 2329-0204. Other distance-dependent values use the distances listed in Table 3.1.

Galaxy	Band	μ_0 (mag arcsec^{-2})	h (arcsec)	$h^{'}$ (kpc)	m_T (mag)	M_T (mag)	A_λ (mag)
UGC 628	B	22.36	13.87	5.78	15.35	-19.32	0.158
	I	20.15	8.33	3.47	14.25	-20.42	0.065
LEDA 135682	B	22.31	10.09	5.10	15.49	-19.60	0.380
	I	20.97	7.27	3.67	14.86	-20.23	0.158
LEDA 135684	B	22.37	10.61	2.13	15.61	-17.69	0.344
	I	21.58	9.58	1.40	15.05	-18.25	0.143
LEDA 135693	B	21.42	6.30	4.70	15.51	-20.43	1.086
	I	20.17	5.72	4.27	14.47	-21.47	0.451
UGC 2925	B	20.71	10.18	2.83	13.86	-19.93	1.781
	I	18.75	8.99	2.50	12.19	-21.60	0.739
F563-V2	B	21.95	7	2.05	15.87	-18.18	...
	I	...	...	...	...	...	...
F568-1	B	23.65	12.86	5.72	16.23	-18.58	...
	I	22.32	12.17	5.41	15.02	-19.79	...
F568-3	B	22.79	10.76	4.35	15.91	-18.70	...
	I	21.04	8.37	3.38	14.70	-19.91	...
LEDA 135782	B	22.22	4.58	4.63	17.16	-19.43	0.094
	I	20.41	3.35	3.38	16.01	-20.58	0.039
UGC 8066	B	23.34	14.04	2.76	16.10	-16.94	0.063
	I	21.83	11.34	2.23	15.07	-17.97	0.026
LEDA 135867	B	22.38	4.92	2.84	17.19	-18.19	0.179
	I	21.07	4.15	2.39	16.24	-19.14	0.074
F602-1	B	22.47	11.87	4.92	15.24	-19.87	0.169
	I	20.92	9.66	4.65	14.14	-20.97	0.070
PGC 70352	B	21.58	7.64	2.72	15.33	-19.00	0.261
	I	20.18	6.64	2.37	14.24	-20.09	0.108
ASK 25131	B	23.09	9.14	4.74	16.55	-18.59	0.135
	I	21.16	6.49	3.36	15.36	-19.78	0.056
[ISI96] 2329-0204	B	23.14	9.38	...	16.48	...	0.162
	I	21.62	9.04	...	15.02	...	0.067

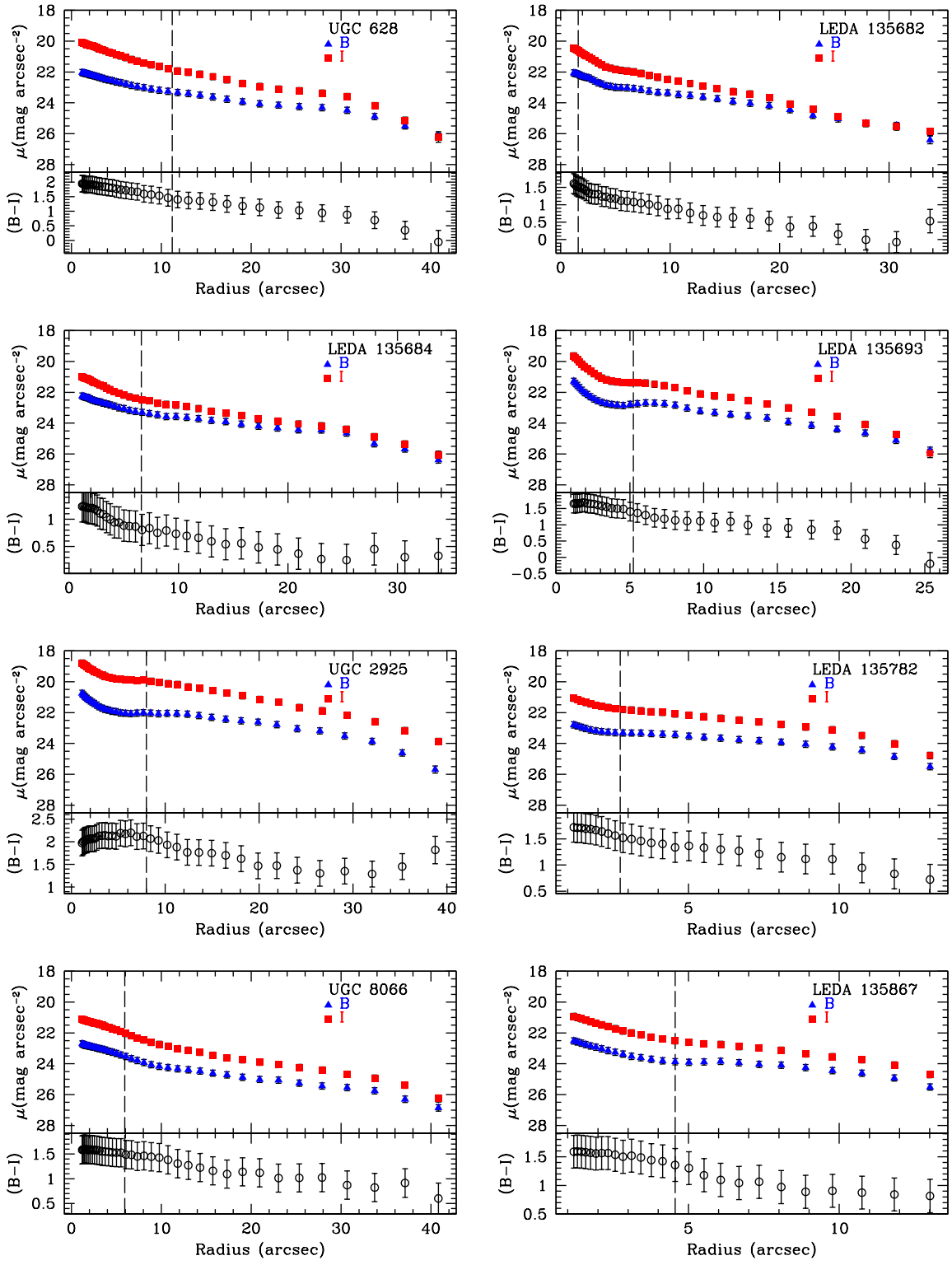

Figure 3.14: B-band (blue triangles) and I-band (red squares) surface brightness profiles (top panels), and $(B-I)$ radial color profiles (bottom panels). The vertical dashed lines indicate the bar length from Table 3.3.

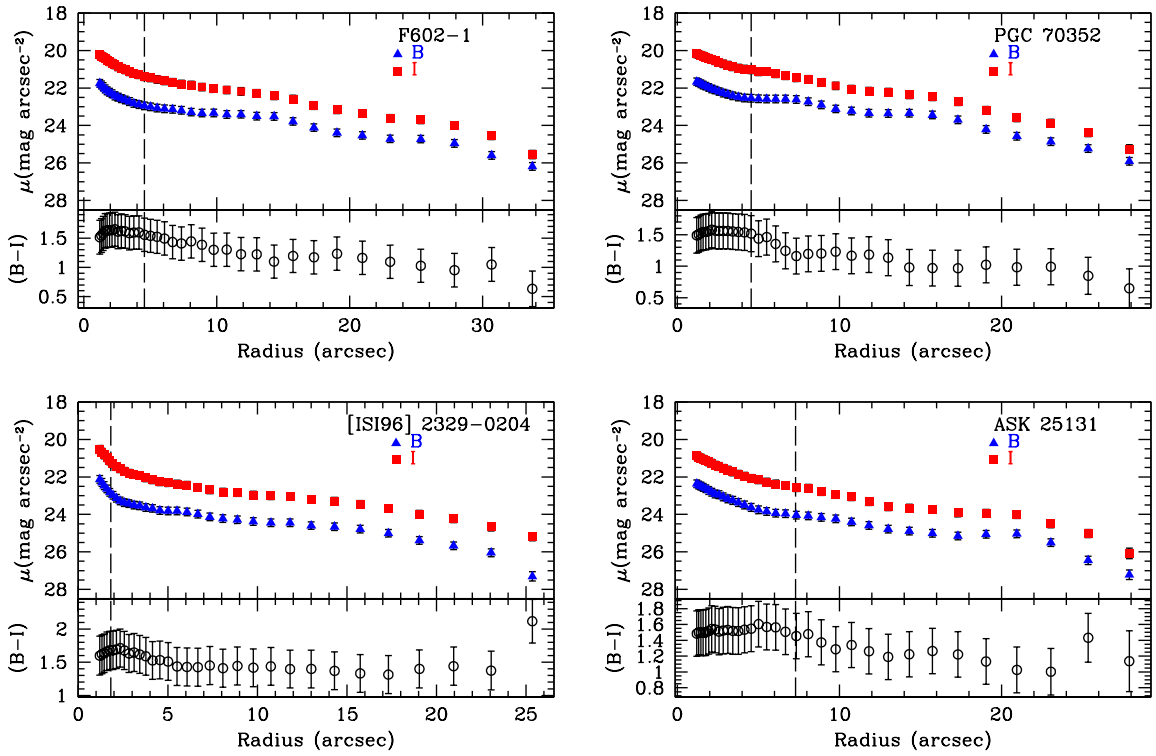

Figure 3.14: *continued*

3.5.2.2 Magnitudes

The mean absolute B-band and I-band magnitudes are -18.89 and -20.01 respectively. We find a relation between absolute magnitude and disk scale length, shown as the longer dashed line in the bottom panel of Fig. 3.15. The relation is given by $\log h = -0.09 M_B - 1.44$, with a scatter of $\sigma = 0.13$ (shown as the shaded gray region in Fig. 3.15). This is slightly shallower than the relation for the general LSB population in Zhong et al. (2008). We also fit for the unbarred LSBs in Fig. 3.15 from McGaugh & Bothun (1994) and de Blok et al. (1995) and found the relation $\log h = -0.17 M_B - 2.45$, shown as the shorter dashed line, indicating a significantly different slope between the two LSB populations.

In the Fig. 3.16 we show a comparison of the B-band central surface brightness ($\mu_0(B)$) and absolute magnitude (M_B^T) for our barred sample (black circles) with the unbarred LSBs in McGaugh & Bothun (1994) (red triangles) and de Blok et al. (1995) (blue squares). We

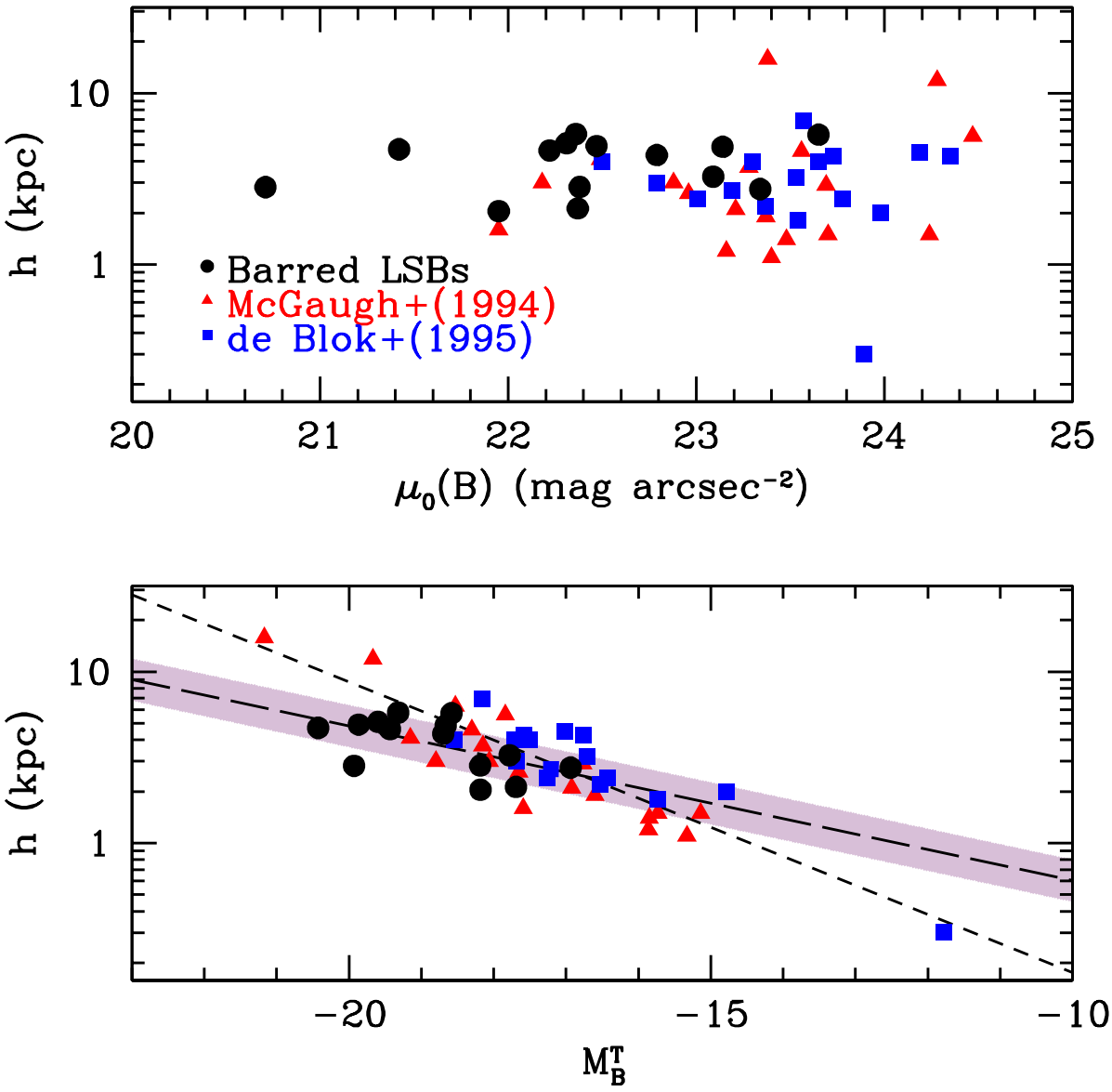

Figure 3.15: Comparison of our disk scale length (kpc) and B-band central surface brightness ($\mu_0(B)$) and absolute B-band magnitude (M_B^T): our data (black circles), McGaugh & Bothun (1994) (red triangles), and de Blok et al. (1995) (blue squares). The galaxies plotted here from McGaugh & Bothun (1994) and de Blok et al. (1995) are unbarred. The long dash line in the bottom panel shows the fit $\log h = -0.09 M_B - 1.44$. The gray shaded region denotes a scatter of $\sigma = 0.13$ about the fit. The short dashed line shows the fit to the unbarred LSBs from the red and blue points.

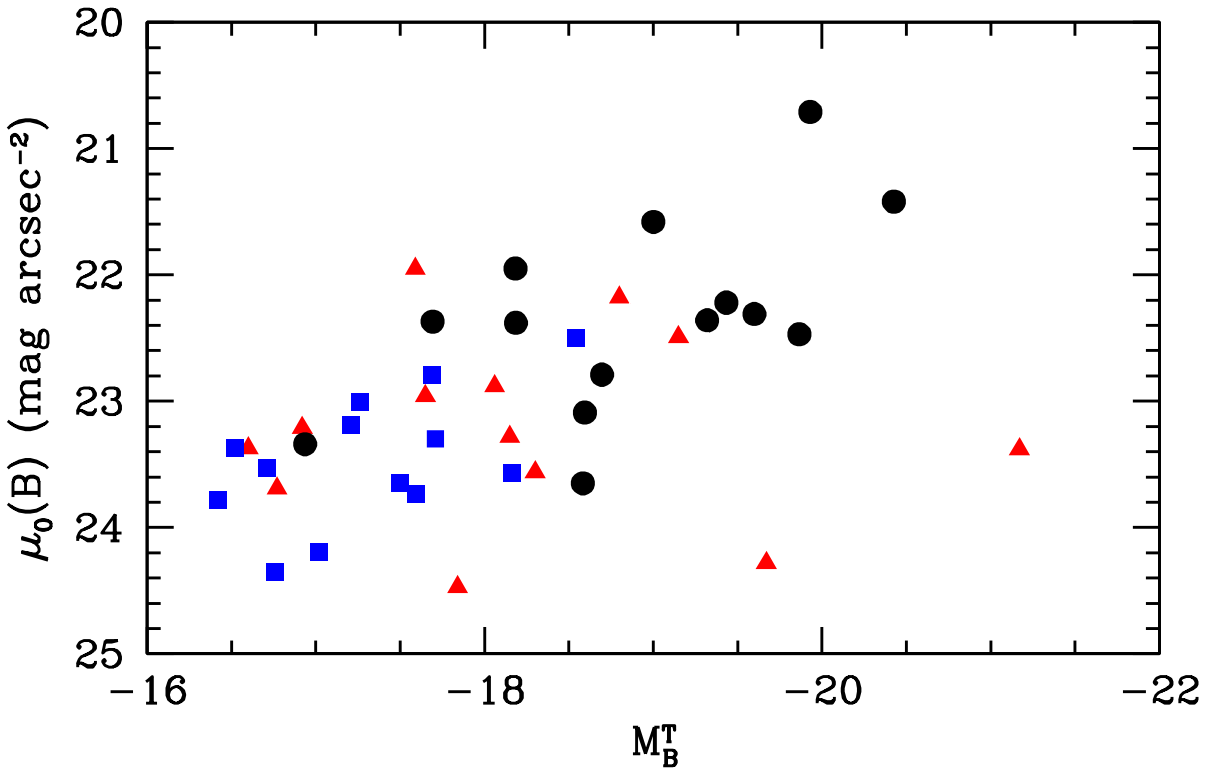

Figure 3.16: Comparison of B-band central surface brightnesses ($\mu_0(B)$) and absolute magnitudes (M_B^T): same color scheme as in Fig. 3.15.

find that our barred LSBs are noticeably brighter than their unbarred counterparts, extending off of the trend of the unbarred LSBs.

3.5.2.3 Colors

Here we discuss our radial color profiles, three different total color measures, and our color maps.

Radial Profiles We show the radial $(B-I)$ profiles in the bottom panels of Fig. 3.14. We can see that our galaxies are rather blue, with $(B-I)$ values of roughly 1 in the disk region outside the bar. In addition, we find that most color profiles are more red and constant within the bar region, consistent with a primarily stellar feature. All show a clear trend towards bluer values with increasing radius, as expected for LSBs (de Blok et al. 1995).

Table 3.5: Bar, disk, and area $(B-I)$ colors. Data for F563-V2 are taken from McGaugh & Bothun (1994), and data for F568-1 and F568-3 are taken from de Blok et al. (1995) and McGaugh & de Blok (1997). Average colors are listed at the bottom of the table.

Galaxy	bar	disk	area
UGC 628	1.49	0.98	1.08
LEDA 135682	1.61	0.54	0.55
LEDA 135684	0.93	0.45	0.49
LEDA 135693	1.52	0.86	0.90
UGC 2925	1.94	1.53	1.55
F563-V2	1.64	...	1.57
F568-1	1.57	...	1.32
F568-3	1.58	...	1.29
LEDA 135782	1.61	1.05	1.09
UGC 8066	1.52	1.04	1.06
LEDA 135867	1.46	0.87	0.96
F602-1	1.57	1.13	1.14
PGC 70352	1.57	1.03	1.05
ASK 25131	1.53	1.20	1.24
[ISI96] 2329-0204	1.64	1.41	1.42
averages	1.54±0.20	1.01±0.30	1.11±0.30

Total Colors Our three total color measures (see Sec 3.5.1.3) are shown in Table 3.5. Color data for F563-V2 are taken from McGaugh & Bothun (1994) and data for F568-1 and F568-3 are taken from de Blok et al. (1995) and McGaugh & de Blok (1997) respectively. Average colors are also listed at the bottom of the table.

We find our bar colors (average value of 1.54±0.20) are comparable to the nuclear colors found in McGaugh & Bothun (1994) (average value of 1.52) and de Blok et al. (1995) (average value of 1.47). In these works, the nuclear region was defined to be the color within a 5″ aperture for all galaxies. Here, our bar color is the color within the bar region for each galaxy, which is dependent on each individual galaxy.

Our disk colors are noticeably bluer than the bar colors, with an average value of 1.01±0.30. We find that our area color is often very close to the value of the disk color, with an average value of 1.11±0.30. Since the bars in our sample are quite small, it is not surprising that the area colors are heavily weighted towards the larger area of the bluer disk.

Color Maps We show the $(B-I)$ maps of the galaxies in our sample with calibrated photometry used to determine the total colors in Sec. 3.5.2.3 in Fig. 3.17. Here, we use a color bar ranging $0 < (B-I) < 2$ (with the exception of UGC 2925). Spiral arms are present in these maps as the slightly bluer (whiter) band in some of our maps (LEDA 135693 and F602-1, for example). In addition, a few galaxies show HII regions as white blobs in spiral arms (PGC 70352 and [ISI96]2329-0204, for example). The bars in our galaxies are clear as the redder (darker) regions in the centers of the maps.

All of our galaxies show a stark contrast between the bar and disk regions, with an almost immediate shift from redder colors to much bluer, consistent with our radial color plots and total colors. For those galaxies with more tenuous disk structure (LEDA 135867 or ASK 25131, for example), the color maps are not as clear or defined, quickly getting lost in the noise.

Interestingly, some galaxies show bluer regions within the bar: notably F602-1, ASK 25131, and PGC 70352. This is not a result of the images being misaligned when combining, but instead a real feature. When examining the B- and I-band images individually (Fig. 3.1), it is noticeable that the bar in the B-band is noticeably different than in the I-band for these galaxies. Most noticeable is F602-1, which has a very narrow bar in B compared with I.

3.6 Gas Fraction

We have shown that bars in LSBs are characteristically shorter and weaker than those in HSBs (Sec. 3.3.3). It is thought that high gas content in galaxies prohibits bar formation, as well as forms shorter and weaker bars (e.g. Mayer & Wadsley 2004; Cervantes Sodi & Sánchez García 2017). Therefore, we wish to examine the gas fractions of the galaxies in our sample in order to see if this explains the short and weak nature of the bars found.

To obtain gas fractions of our sample, we require estimates of both the gas and stellar mass. We use the `HyperLeda` online database[4] (Makarov et al. 2014) to obtain 21cm HI

[4]http://leda.univ-lyon1.fr/

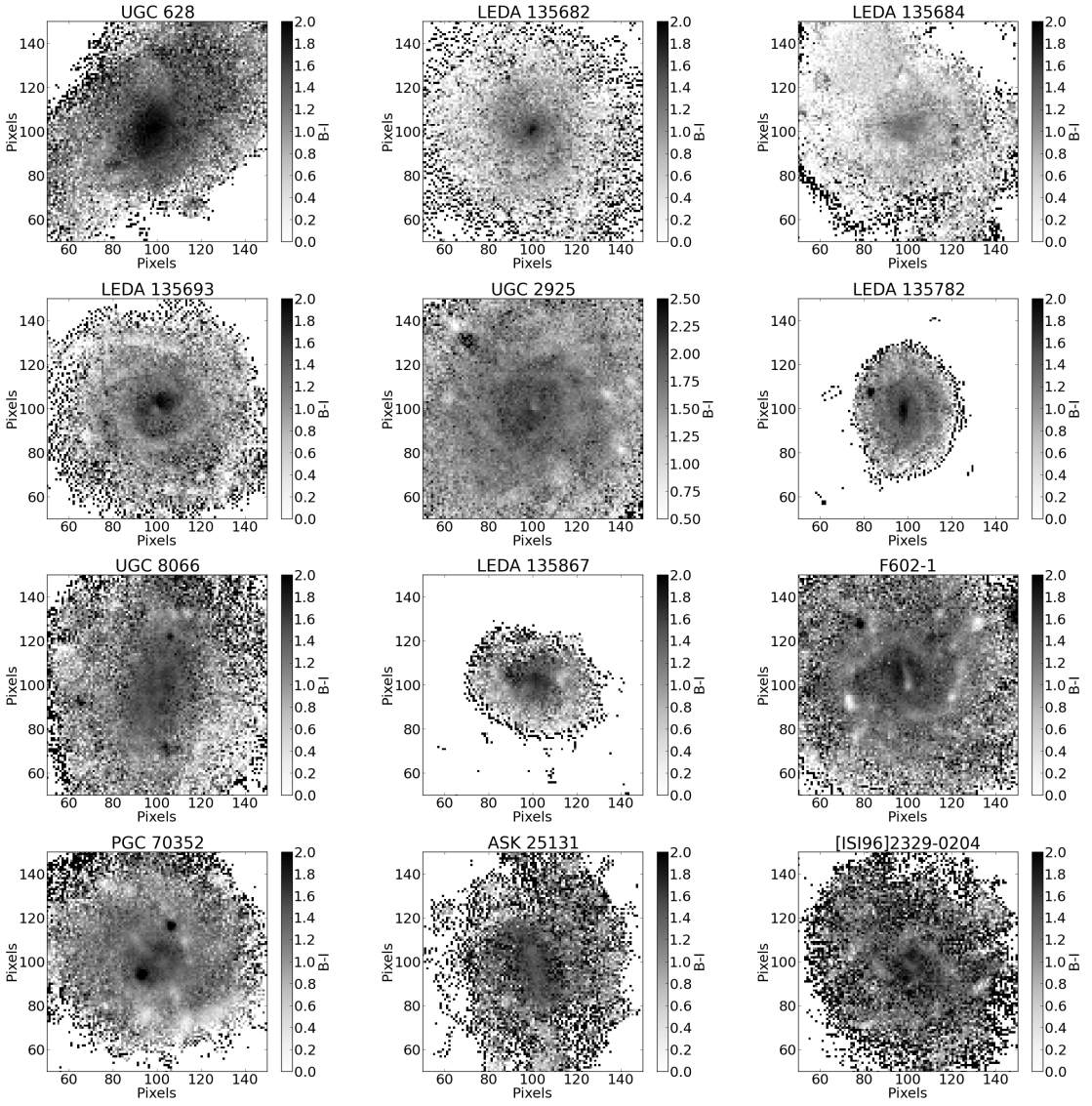

Figure 3.17: $(B-I)$ maps of our barred LSBs, created from 2x2 rebinned B- and I-band images. North is up, and east is to the left in all maps, and each map is $0.84' \times 0.84'$. The two black dots in the map for PGC 70352 (bottom left) are two very bright stars in the I-band image that were not masked out to prevent distorting the bar. All maps use the same colorbar, with the exception of UGC 2925.

fluxes ($F_{\rm HI}$). Out of our whole sample, ten galaxies have published HI magnitudes, or m_{21}, which we convert into fluxes. We then convert these fluxes to HI masses via the relation from Haynes & Giovanelli (1984):

$$M_{\rm HI} = 2.36 \times 10^5 D^2 F_{\rm HI}\ (M_\odot), \tag{3.22}$$

where D is the distance in Mpc (Table 3.1). Although LSBs are thought to generally contain very little molecular gas (Mihos et al. 1999), we obtain the gas mass by $M_{gas} = 1.4 M_{\rm HI}$.

With our I-band magnitudes and $(B-I)$ colors it is possible to obtain a stellar mass via a mass-to-light ratio, which requires using stellar population models. We first use our I-band absolute magnitudes (Table 3.4) to determine the I-band luminosity for each galaxy. We then use the $(B-I)$ area color (Table 3.5) to obtain an I-band stellar mass-to-light ratio using the appropriate equation from Into & Portinari (2013):

$$\log \Upsilon_*^I = -0.997 + 0.641(B-I) \tag{3.23}$$

Because we do not have an I-band absolute magnitude for F563-V2, we take the apparent magnitude from `HyperLeda`, and use the distance reported in Table 3.1. Finally, we obtain gas fractions via

$$f_{gas} = \frac{M_{gas}}{M_{gas} + M_*} \tag{3.24}$$

In Table 3.6 we report the HI fluxes ($F_{\rm HI}$), HI masses ($\log M_{\rm HI}$), I-band luminosity ($\log L_I$), stellar mass-to-light ratios (Υ_*^I), stellar masses ($\log M_*$) for our sample, and gas fractions (f_{gas}).

The mean HI mass for our galaxies is $\log (M_{\rm HI}/M_\odot) = 9.64 \pm 0.25$, consistent with the total LSB spiral population in Honey et al. (2018). The mean stellar mass for our galaxies is $\log (M_*) = 9.29 \pm 0.60$. We find that the majority of our galaxies are gas rich ($f_{gas} > 0.5$), with only one galaxy being gas poor, UGC 2925. Specifically, the majority of our sample

Table 3.6: Gas fractions for those galaxies in our sample with available HI magnitudes. HI flux ($F_{\rm HI}$), HI mass ($\log M_{\rm HI}$), I-band luminosity ($\log L_I$), I-band mass-to-light ratio (Υ_*^I), stellar mass ($\log M_*$), and gas fraction ($f_{gas} = M_{gas}/(M_{gas} + M_*)$).

Galaxy	$F_{\rm HI}$ (Jy km/s)	$\log M_{\rm HI}$ ($M_\odot$)	$\log L_I$ ($L_\odot$)	Υ_*^I	$\log M_*$ ($M_\odot$)	f_{gas}
UGC 628	4.37	9.88	9.81	0.50	9.51	0.77
LEDA 135684	7.52	9.57	8.94	0.21	8.26	0.97
UGC 2925	4.66	9.56	10.28	1.01	10.28	0.21
F563-V2	3.57	9.49	8.75	1.02	8.76	0.88
F568-1	1.91	9.58	9.56	0.71	9.41	0.67
F568-3	2.31	9.58	9.60	0.68	9.43	0.66
LEDA 135782	1.45	10.17	9.87	0.50	9.57	0.85
UGC 8066	4.06	9.20	8.83	0.54	8.56	0.86
F602-1	1.94	9.70	10.03	0.54	9.76	0.55
PGC 70352	3.38	9.63	9.68	0.47	9.36	0.72

have $f_{gas} > 0.65$. This is consistent with barred LSBs (Pahwa & Saha 2018) and LSBs in general (de Blok et al. 1996).

In Fig. 3.18 we show $\log(M_{\rm HI}/M_*)$ as a function of $\log(M_*)$. The solid line is the fit $\log(M_{\rm HI}/M_*) = -0.81\log(M_*) + 7.88$, slightly steeper than the relation for general LSB spirals in Honey et al. (2018), $\log M_{\rm HI}/M_* = -0.71\log M_* + 7$ (the dashed line in Fig. 3.18). The scatter about our relation, $\sigma = 0.22$, is shown as the shaded region in Fig. 3.18.

3.7 Discussion and Conclusions

We have measured the photometric bar properties (length, strength, and corotation radius) of fifteen barred LSB disk galaxies assembled from Schombert et al. (1992) and Impey et al. (1996) using optical B- and I-band photometry. We have found that bars in LSBs are shorter and weaker than those in HSBs, consistent with numerical simulations. Our mean bar length and strength are 2.5 kpc and 0.19 respectively. In order to determine the best measure of the bar length, we have created and analyzed fake galaxy images consisting of an exponential disk and a bar. We have found that our azimuthal bar length technique performs best out of the four tested here, and that the $R_{\rm P.A.}$ measure, while dependent on the inaccurate R_ϵ measure, also does an excellent job at measuring the bar length.

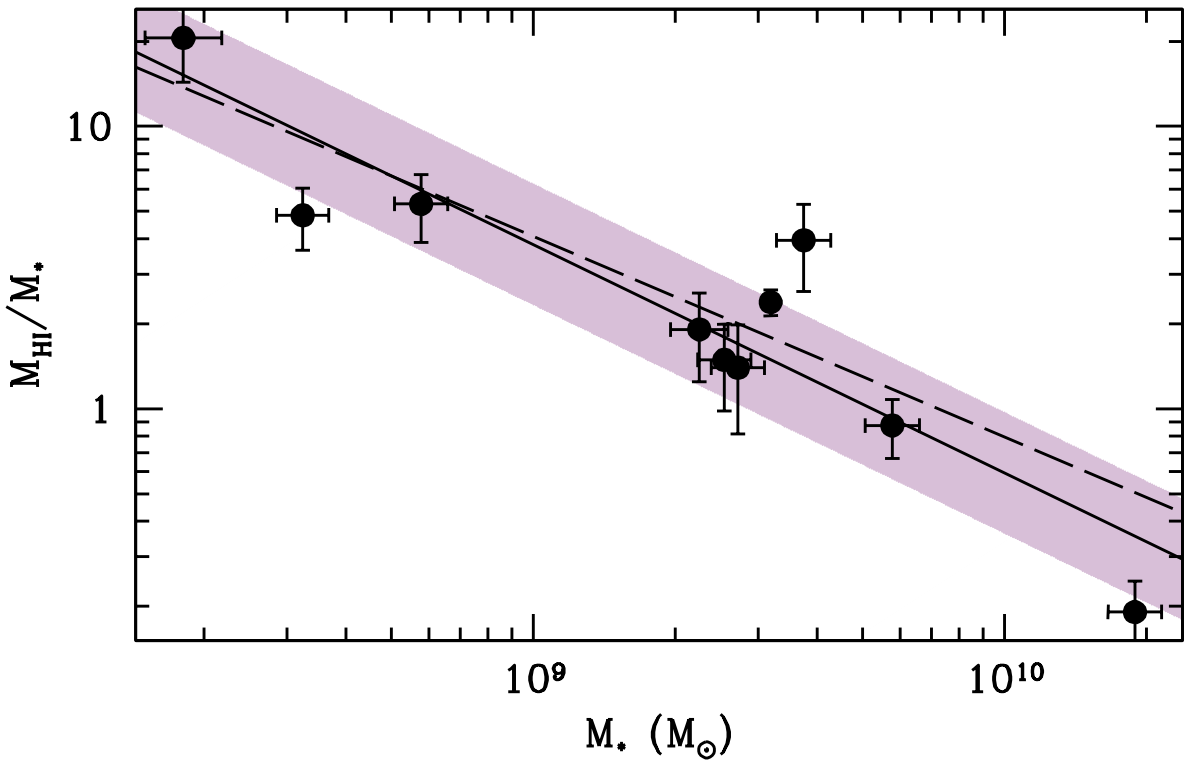

Figure 3.18: $\log(M_{\rm HI}/M_*)$ vs $\log(M_*)$. The solid line denotes the fit $\log(M_{\rm HI}/M_*) = -0.81\log(M_*) + 7.88$, and the shaded region denotes the scatter of 0.22. The dashed line shows the fit to general LSB spirals from Honey et al. (2018), $\log M_{\rm HI}/M_* = -0.71\log M_* + 7$.

Interestingly, we find that the corotation radius of the bar falls very close to the end of the bar for our sample, implying that bars in LSBs are fast rotators. In addition, the only *very* slow bar is located in the only galaxy without any clear spiral structure, F563-V2. Recent mergers are thought to decrease the bar pattern speed (Gerin et al. 1990), but LSBs are known to be more isolated than HSBs (Bothun et al. 1993; Mo et al. 1994; Rosenbaum & Bomans 2004; Du et al. 2015; Honey et al. 2018). In addition, there are no known companions to F563-V2.

As discussed in Chapter 2, the dark matter halos should dynamically slow down any bar that may be present (Weinberg 1985; Debattista & Sellwood 2000), although this only applies to nonrotating halos (see Sec. 3.3.3 why this is likely not the case for LSBs). While there have been reports of slow bars found in dark matter dominated objects (see Bureau et

al. 1999; Chemin & Hernandez 2009; Banerjee et al. 2013), our results imply that bars in LSBs are generally fast. The reason for this remains unclear, and requires further detailed spectroscopic analysis in order to obtain bar pattern speeds. However, the faint nature and rough disks of LSBs makes application of the only direct bar pattern speed measurement (Tremaine & Weinberg 1984) prohibatively difficult.

In addition, it is possible that $\mathcal{R}$ can give misleading information regarding the actual rotational speed of the bar. Font et al. (2017) found that by examining the bar pattern speeds (Ω_b) of a large sample of galaxies, some bars that were considered fast (i.e. $\mathcal{R} < 1.4$) were actually some of the slowest rotators. In order to determine this, they examined the 'normalised' bar pattern speed which they defined as $\Gamma = \Omega_b/\Omega_d$ with Ω_d being the disk pattern speed. By setting a deliminator of $\Gamma = 2$ as a means of separating fast and slow rotators, they found that bars with $\mathcal{R} < 1.4$ could have $\Gamma < 2$, meaning the bar rotates at a comparable rate to the disk. Because of this, the authors conclude that bars have indeed been slowed down due to the dark matter halos, despite the prevalance of bars with $\mathcal{R} < 1.4$, and suggest Γ as a better means of separating fast and slow rotators.

The galaxies in our sample have only been shallowly observed before. We have therefore presented B- and I-band surface brightness profiles, magnitudes, and colors of our sample. We have found that barred LSBs are brighter than unbarred LSBs, and fall on a shallower $\log h$ vs M_B relation. The disk scale lengths of our sample are identical to those of unbarred LSBs. Our sample is also quite blue, having a mean $(B-I)$ area color of 1.11, while the bar region is significantly redder, with a mean color of 1.54. Due to the small bars in our galaxies, it is not surprising that our area colors are heavily weighted towards the bluer disk.

Finally, we have used available 21cm HI fluxes to determine the HI masses and population synthesis models to get stellar masses of our sample and found our galaxies to be quite gas rich. Our sample falls on the same $\log(M_{\rm HI}/M_*)$ vs $\log(M_*)$ relation as the general LSB spiral population. It is thought that gas rich, low luminosity galaxies with high halo spin λ

form short and weak bars (Cervantes-Sodi et al. 2013; Cervantes Sodi 2017), consistent with our findings here.

We list our major conclusions based on our observed sample here.

1. Bars in LSBs are shorter and weaker than those in HSBs, with an average length and strength of 2.5 kpc and 0.19 respectively.

2. Bars in LSBs are fast rotators ($\mathcal{R} < 1.4$), with the corotation radius occuring close to the end of the bar. Barred LSBs also show multiple B- and I-band phase intersections, possibly indicating disk corotation radii.

3. Barred LSBs are slightly brighter than unbarred LSBs, with average central surface brightnesses of $\mu_0(B) = 22.39$ mag arcsec^{-2} and $\mu_0(I) = 20.28$ mag arcsec^{-2}, and average absolute magnitudes of $M_B = -18.89$ and $M_I = -20.01$.

4. Barred LSBs fall on a slightly shallower $\log h$ vs. M_B relation than unbarred LSBs.

5. Barred LSBs have HI masses that are nearly identical to the general spiral LSB population, and are just as gas rich as unbarred LSBs ($f_{gas} > 0.5$).

6. In order to fully probe the nature of the dark matter halos of barred LSBs, extensive spectroscopy is required in order to obtain bar pattern speeds and halo spin parameters (λ).

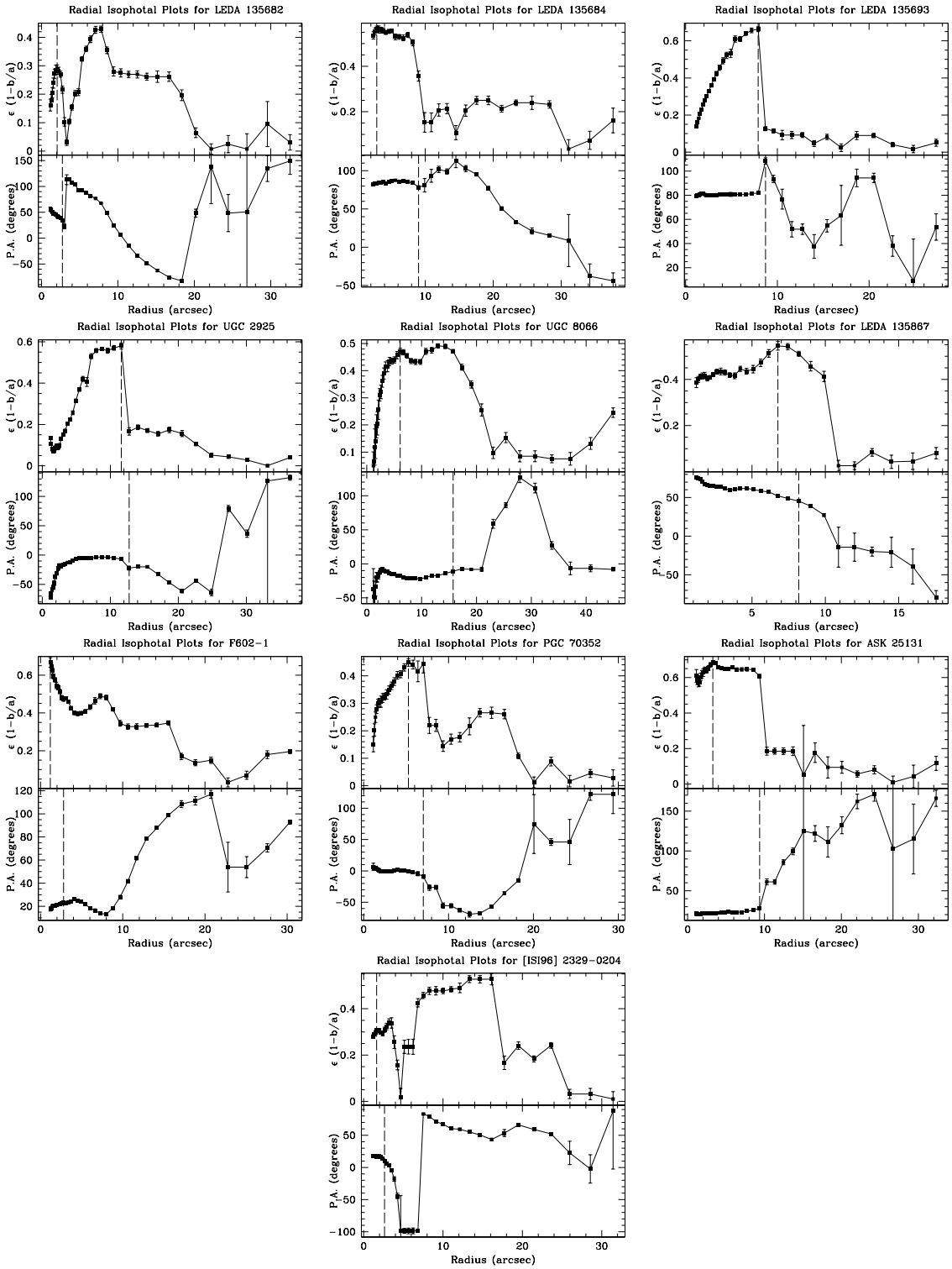

Figure 3.19: Radial plots of ellipticity (top panels) and position angle (bottom panels) for the remainder of our sample. The vertical lines in each panel denote the bar length measures R_e and $R_{\rm PA}$.

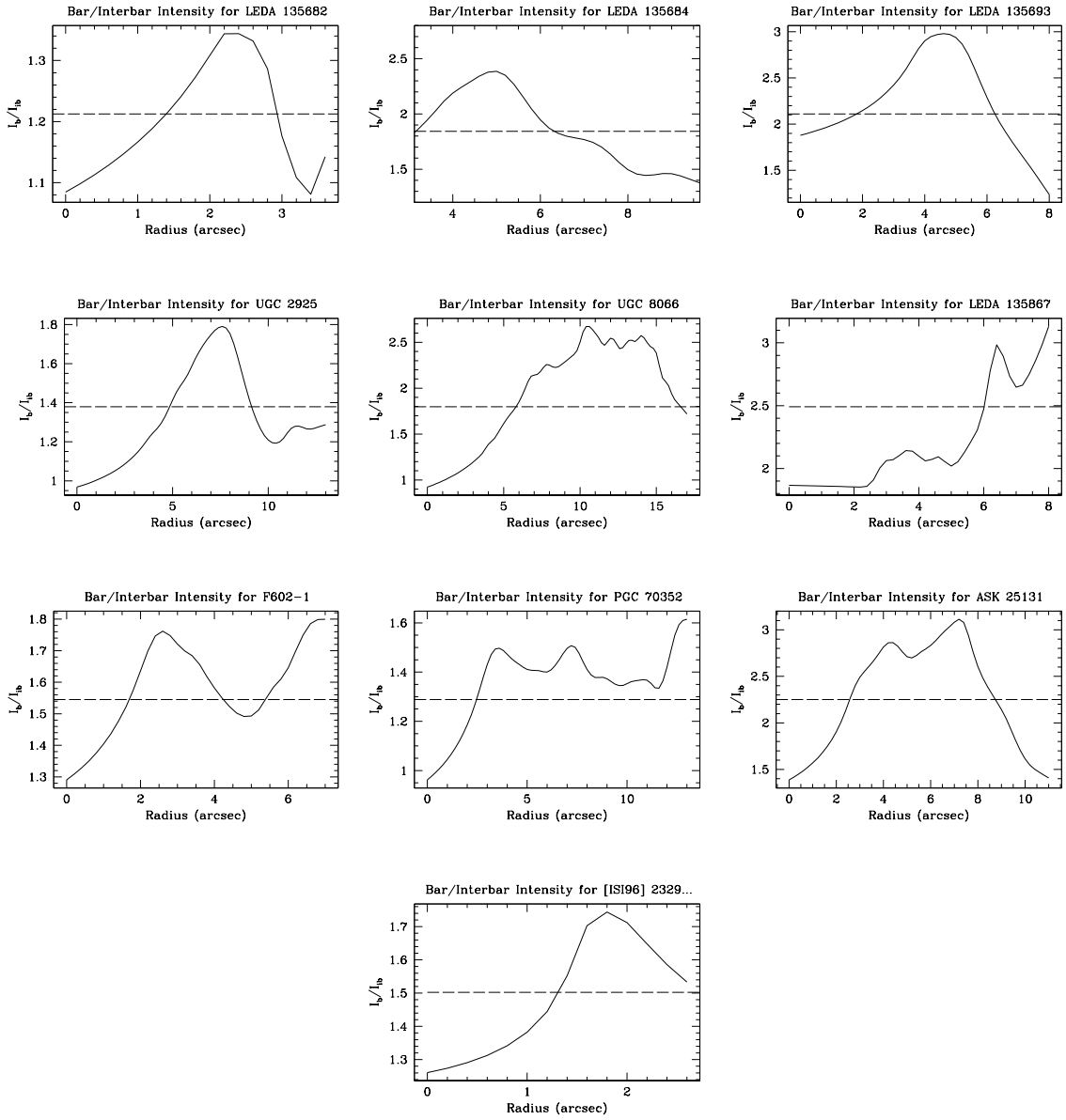

Figure 3.20: Radial plots of the Fourier bar (I_b) and interbar (I_{ib}) intensity ratio.

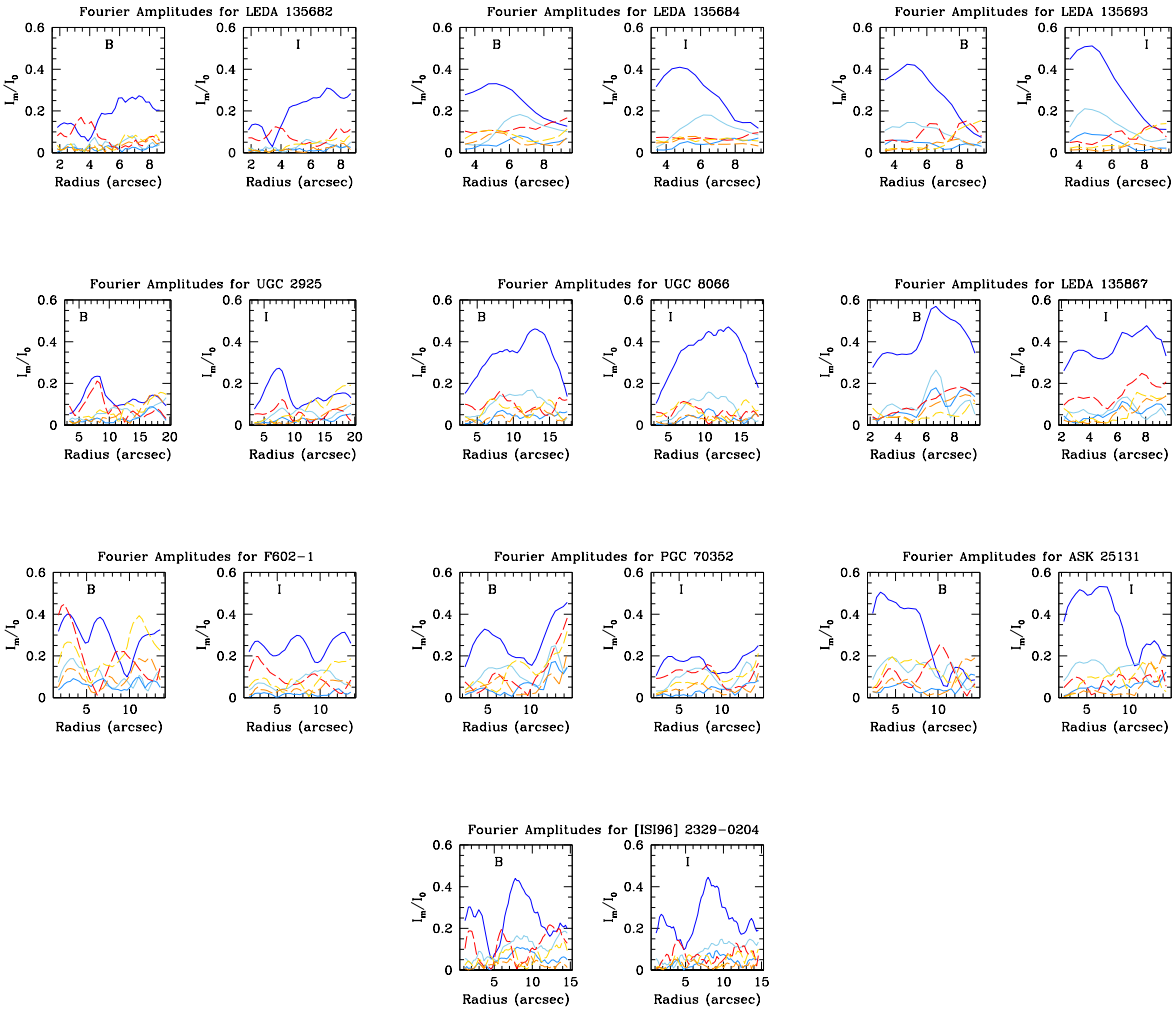

Figure 3.21: Fourier amplitudes for the remainder of our sample.

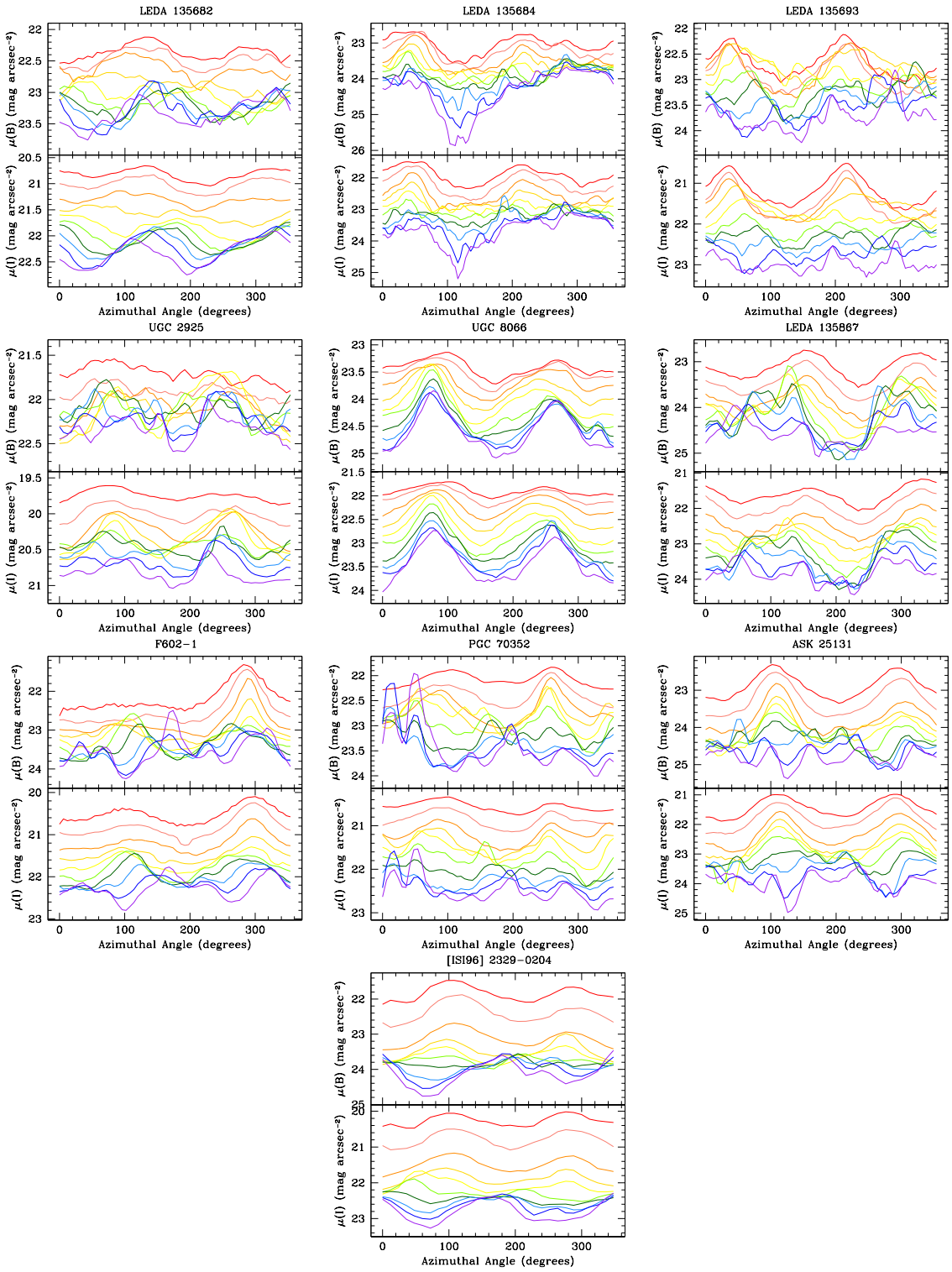

Figure 3.22: Azimuthal light profiles (in mag arcsec^{-2}) for the remainder of our sample; the B-band profiles are in the top panel and the I-band profiles are in the bottom panel for each subfigure.

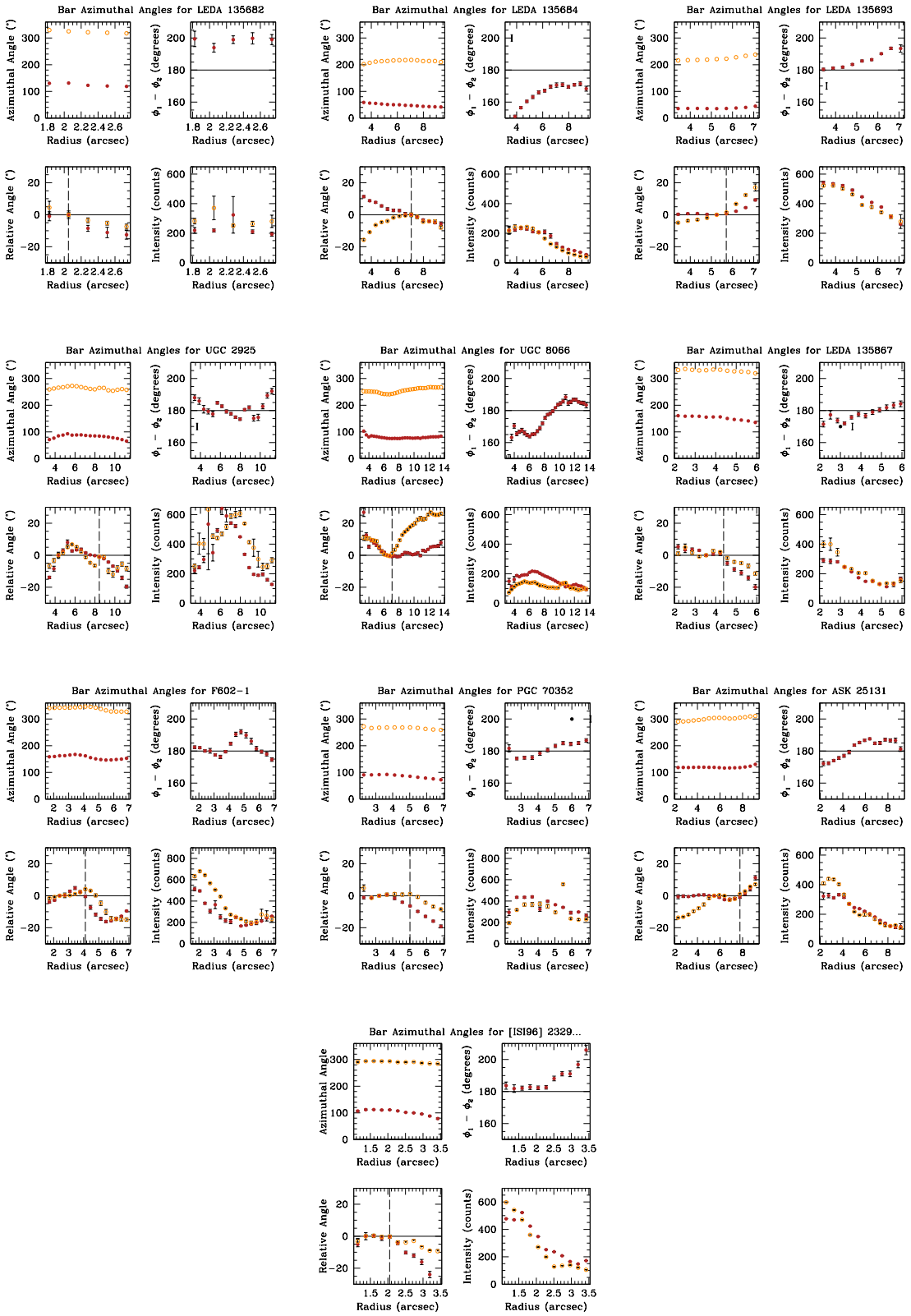

Figure 3.23: Azimuthal positions of the bars in our galaxies. Dashed vertical lines in the bottom left panels indicate the azimuthal bar length (R_{az}).

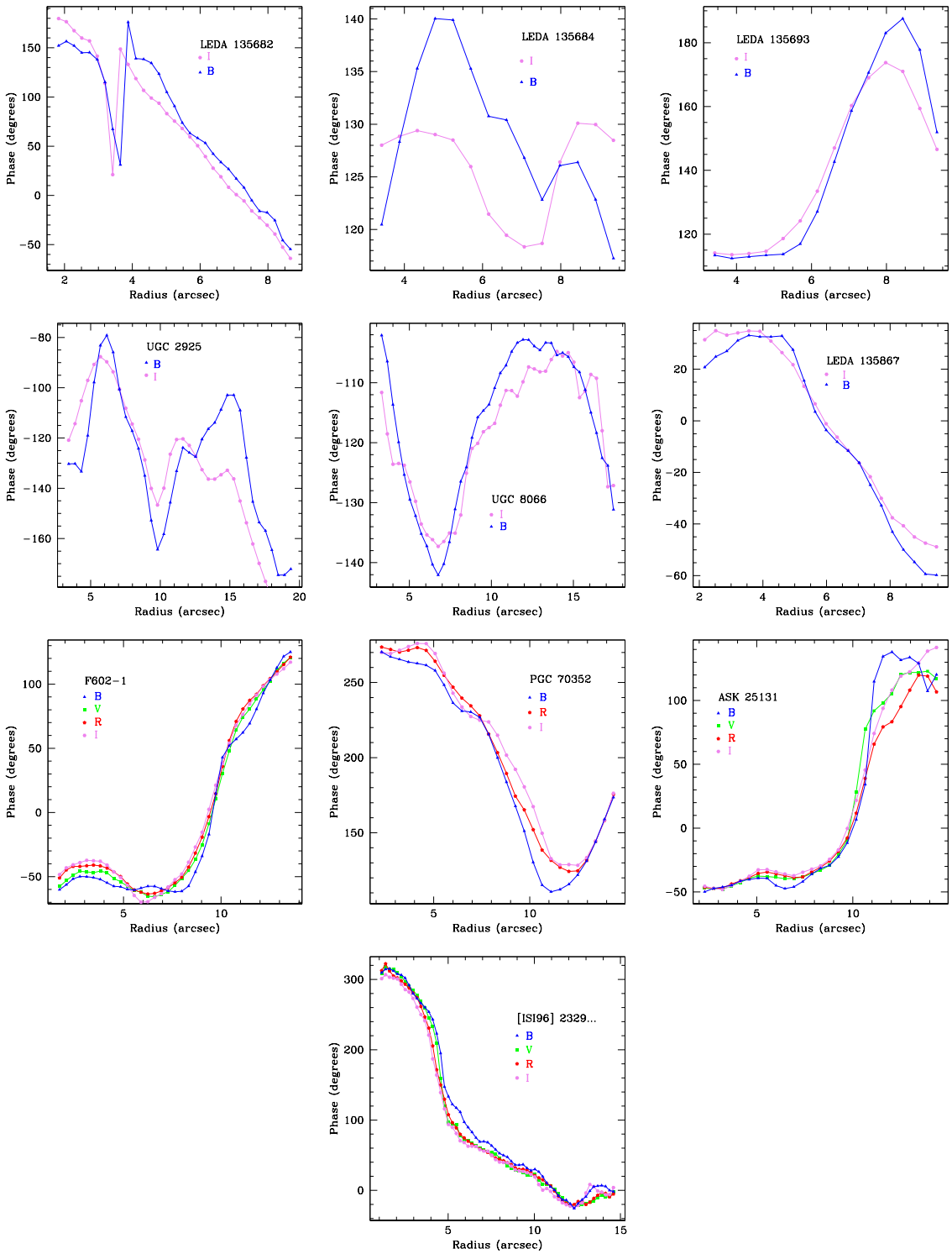

Figure 3.24: B- (blue) and I-band (violet) phase profiles for the remainder of our sample. Note that four galaxies have additional bands: V (green) and R (red).

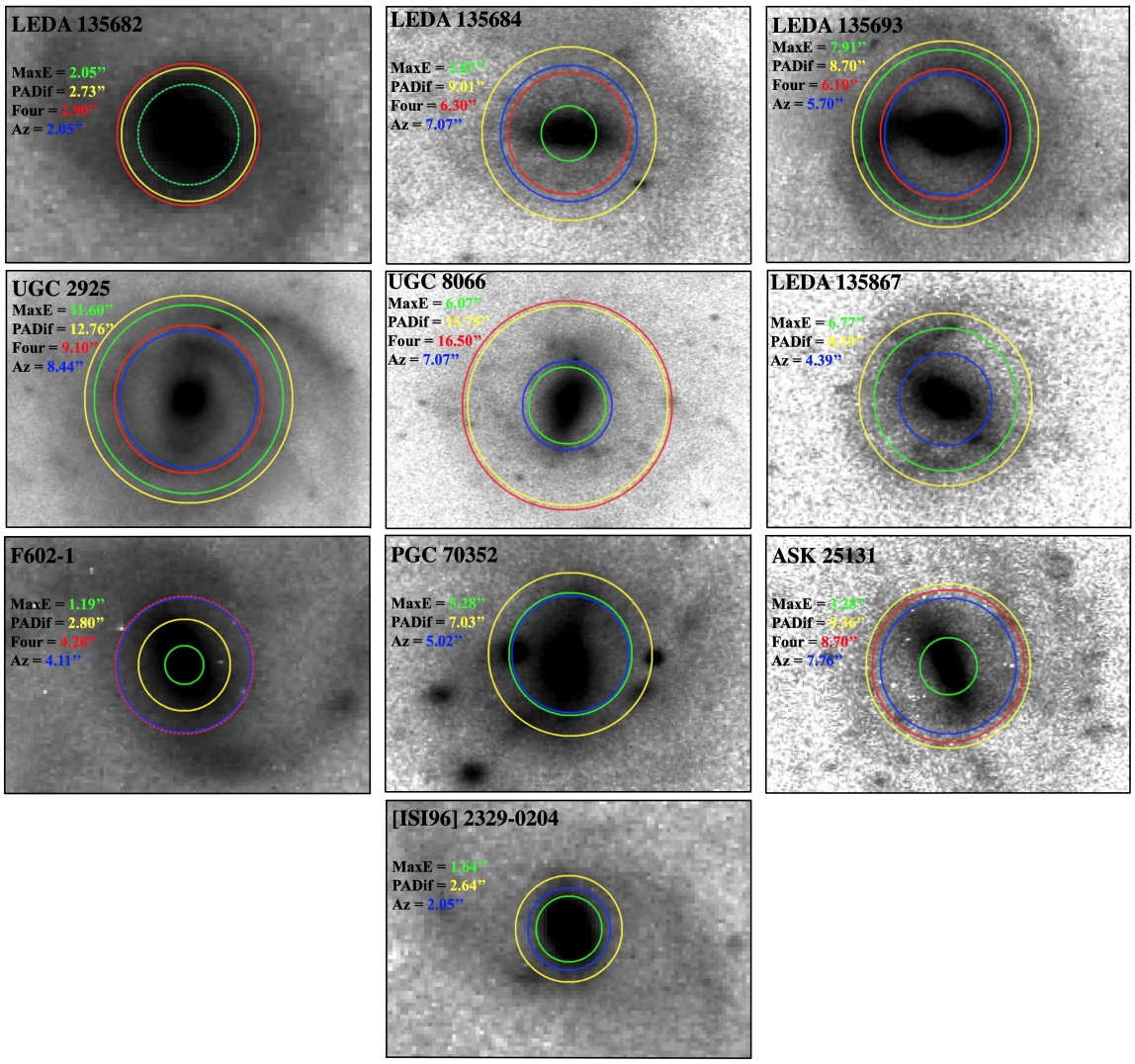

Figure 3.25: Comparison of the four bar length measures plotted over the deprojected I-band images for the remainder of our sample: R_ϵ (green), $R_{\mathrm{P.A.}}$ (yellow), $R_{\mathcal{F}}$ (red), and R_{az} (blue).

Chapter 4

The Bar Continuum Between Low Surface Brightness and High Surface Brightness Galaxies

4.1 Introduction

In the context of galaxies forming in dark matter halos, low surface brightness galaxies (LSBs) are thought to be the result of a high angular momentum halo (e.g. Dalcanton et al. 1997; Jimenez et al. 1998), characterized by the spin parameter λ. Galaxies living in high λ halos are mostly stable against disk instabilities, including bars, due to the dark matter halo being dynamically dominant at nearly all radii (e.g. Ostriker & Peebles 1973; Efstathiou et al. 1982; Long et al. 2014; Cervantes Sodi et al. 2015). Likewise, numerical simulations predict LSBs to be stable against bar formation (Mihos et al. 1997; Mayer & Wadsley 2004), as well as observational work suggesting high gas content in galaxies suppresses bar formation (Masters et al. 2012).

However, if a bar *does* form in a galaxy in a high spin halo, it is thought that it will be shorter and weaker when compared with bars that form in galaxies residing in low spin halos (Cervantes-Sodi et al. 2013; Cervantes Sodi & Sánchez García 2017). In addition, there is a strong dependence on the bar fraction with color, where redder galaxies are hosts to longer bars, and bluer galaxies are hosts to shorter bars (Lee et al. 2012). Given that LSBs are blue and likely formed in high spin halos, LSBs should be hosts to weaker and shorter bars when compared with high surface brightness galaxies (HSBs).

In Chapter 3 we showed that bars in LSBs were indeed generally shorter and weaker than those in previous studies of HSBs, but had comparable relative bar pattern speeds. We also found that barred LSBs were just as gas-rich as the general LSB population. Since LSBs contain as much HI gas as HSBs (Burkholder et al. 2001), but have lower total baryonic masses (i.e. $M_* + M_{gas}$), it becomes clear that HSBs are stellar dominated systems and LSBs are gas dominated. It stands to reason then that there should exist a continuum for the bar properties that extends across surface brightness. This chapter is aimed at exploring this continuum in more detail, specifically at increasing the number of HSBs being compared, as well as applying the same measurement techniques used on our LSBs to the HSBs.

In Chapters 2 and 3, we used the HSB sample of Aguerri et al. (1998) as a means of comparing bars between LSBs and HSBs. However, in order to provide a more meaningful comparison, we desire a larger and more morphologically complete sample of HSBs. In addition, as Aguerri et al. (1998) uses different bar length measures, it will be more insightful to apply our own measurement techniques, specifically our azimuthal bar length measure, to a group of HSBs. Rather than obtaining additional observations of HSBs, we will take advantage of the large number of high quality images available in the literature.

This chapter is organized as follows. In Section 4.2 we discuss our sample selection and data acquisition. Our methods for measuring the bar properties and obtaining stellar and gas mass estimates are detailed in Sec. 4.3, and the results are shown in Sec. 4.4. Finally, we discuss our results and conclusions in Sec. 4.5.

4.2 Sample and Data

In this section we detail our sample selection (Sec. 4.2.1) and data acquisition and processing (Sec. 4.2.2).

4.2.1 Sample Selection and Justification

To capitalize on the numerous HSB surveys available in the literature, we have selected galaxies from various surveys that are present in the Sloan Digital Sky Survey (SDSS; York et al. 2000; Blanton et al. 2017) catalog. Although SDSS has worse resolution than that of our LSB observations taken with the ARCTIC imager on the Apache Point Observatory (APO) 3.5m telescope ($0.396''$ pixel^{-1} vs. $0.228''$ pixel^{-1}) and worse resolution than available images from one of the surveys described below, maintaining a single resolution across our HSB sample will make analysis much easier and, more importantly, more consistent.

In addition to the difference in plate scale just mentioned, the filter system used by SDSS, *ugriz*, is different from that used in Chapter 3, Johnson-Cousins $UBVRI$ (Johnson et al. 1966; Cousins 1984). A comparison of the transmissions for the two filter sets is shown in Fig. 4.1. From this figure, we can see that the two filter systems cover roughly the same wavelength regime, but that the SDSS filters provide more consistent transmission past 4000Å. Due to this, one can make and compare measurements in the two different systems, as long as a band is selected from each system that occupies the same wavelength space. In addition, there exists transformations between the two systems if that is desired.

We have identified two large surveys from which to draw a sample of HSBs. First, we have selected the 11 barred galaxies from the Carnegie-Irvine Galaxy Survey (CGS) (Ho et al. 2011) that appear in SDSS and fall within only one frame. CGS is a sample of 605 of the brightest galaxies in the southern hemisphere. As SDSS is a northern hemisphere survey, only 6% of CGS is present in SDSS. However, as the survey is statistically complete over $-16 \leq M_{B_T} \leq -23$, we feel confident in selecting from this survey to obtain a representative selection of HSBs. Our selected galaxies span $-18.87 \leq M_{B_T} \leq -21.78$ and do not appear to be biased towards longer or shorter bars compared with the barred galaxies in CGS.

Second, we have selected 15 barred galaxies present in the Calar Alto Legacy Integral Field Area (CALIFA) Survey (Sánchez et al. 2012), already identified in Aguerri et al. (2015). CALIFA is a large, comprehensive integral field unit (IFU) survey with the goal of providing

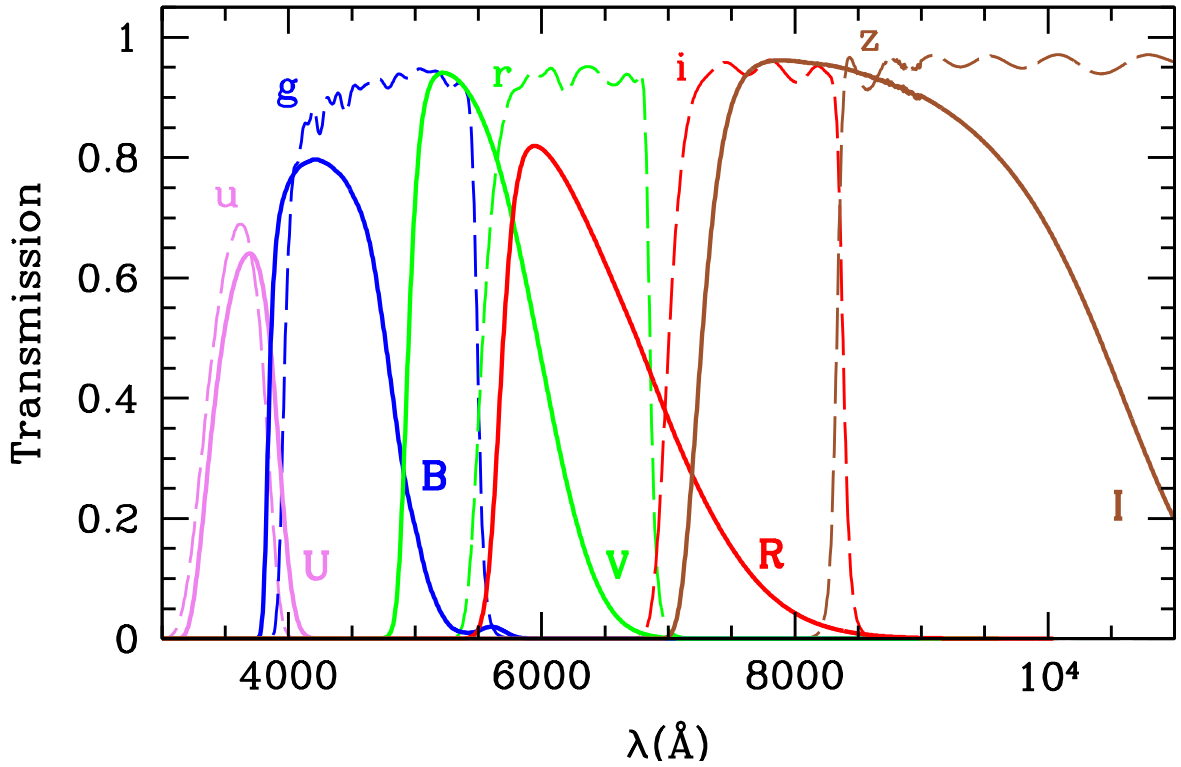

Figure 4.1: Transmission curves for Johnson-Cousin filters (solid lines) and SDSS filters (dashed lines). From shorter to longer wavelengths, the Johnson-Cousin filters are $UBVRI$ and the SDSS filters are $ugriz$.

spectroscopic measurements of a statistically complete sample of the local universe. Aguerri et al. (2015) identified the barred galaxies in CALIFA and measured the relative bar pattern speeds, finding that bars were fast rotators across the Hubble sequence.

To confirm that our galaxies are indeed HSBs, we have obtained $ugri$ total magnitudes and disk scale lengths. Although the SDSS lists photometric information for a large portion of their sample, it is not always reliable to simply extract these parameters as certain fits often fail. This is because the SDSS pipeline fits general de Vaucouleurs and exponential light profiles to each photometric object. Final magnitudes in the SDSS pipeline are weighted combinations of these two light profiles. While this approach generally works, it does not always succeed in accurately fitting the galaxy light for specific targets, including under-

representing the magnitude and disk scale lengths. We therefore opt to measure our own *ugri* magnitudes and disk scale lengths in order to estimate both $\mu_0(B)$ and stellar masses.

We first obtain *ugri* images for each galaxy from the SDSS Sky Server and convert the image units from nanomaggies to counts. With these images we then construct surface brightness profiles by using the `IRAF` routine `ELLIPSE` using the SDSS photometric magnitude zero points: 24.63, 25.11, 24.80, 24.36 in *ugri* respectively.

From these surface brightness profiles, we fit two exponential profiles: one for the disk and one for the inner bar region. With these two profiles we obtain a disk and bar magnitude by integrating out to infinity for each profile as was done in Chapter 3. We use two profiles here, as the inner light profile of HSBs often contributes quite significantly to the overall magnitude of the galaxy, as opposed to LSBs often being almost entirely represented by their disk component. We obtain a total magnitude by adding the disk and bar magnitudes together appropriately:

$$m_{tot} = -2.5 \log \left(10^{-m_{disk}/2.5} + 10^{-m_{bar}/2.5}\right) \tag{4.1}$$

Although the light profiles of bars are not well represented by an exponential profile, we find that our simple approach approximates the profiles reasonably well and that we find our total magnitudes agree with those from SDSS for galaxies with good quality data. In addition, we are able to obtain magnitudes for our entire sample, whereas a significant number of the HSBs are missing from the final SDSS photometric database. With these total magnitudes, we obtain central surface brightnesses in each band by following the approach laid out in Zhong et al. (2008):

$$\mu_0 = m + 2.5 \log \left(2\pi a^2\right) + 2.5 \log \left(q\right), \tag{4.2}$$

where a is the disk scale length and q is the axis ratio (b/a). We do not account for cosmological dimming as our galaxies are close enough for this correction to be minuscule (corrections

are < 0.08 magnitudes). Finally, we estimate the B-band central surface brightness via the relation from Cervantes-Sodi et al. (2013):

$$\mu_0(B) = \mu_0(g) + 0.47\,(\mu_0(g) - \mu_0(r)) + 0.17, \tag{4.3}$$

where $\mu_0(g)$ and $\mu_0(r)$ are the g and r band central surface brightnesses respectively. We find that all of the selected galaxies, with the exception of PGC 3853, are consistent with being HSBs (i.e. $\mu_0(B) < 22.5$ mag arcsec^{-2}).

We list our full sample of 26 barred HSB galaxies in Table 4.1, comprising a subsample from two large, statistically complete surveys. As an added benefit, both of these surveys have bar lengths already measured, which will provide us with an additional and independent check for our bar length measurements. Finally, Aguerri et al. (2015) determined the relative bar pattern speeds ($\mathcal{R}$) for their sample, which will provide a check for our own measurements.

The photometric disk position angle (P.A.) and inclination (i) and morphologies in Table 4.1 are taken directly from the CGS database and Aguerri et al. (2015). Distances are taken from The NASA/IPAC Extragalactic Database[1] (NED), and typically have errors of a few Mpc. With the exception of a few targets (NGC 1645, NGC 5339, NGC 5378, NGC 5947, NGC 6497), all distances are redshift independent via the Tully-Fisher relation. We also list our estimated B-band central surface brightnesses and r-band disk scale length here.

In Fig. 4.2 we show a comparison of basic sample properties between the LSBs from Chapter 3 (dashed blue line) and the HSB sample (solid red line). We find that our two samples are mostly comparable in terms of observational parameters, with most deviations due to the difference in sample size. Our LSBs are at the higher distance end when compared to the HSBs, with two LSBs at extreme distances. The LSBs and HSBs extend over roughly the same disk inclination range, with more HSBs having higher inclinations.

[1]The NASA/IPAC Extragalactic Database (NED) is operated by the Jet Propulsion Laboratory, California Institute of Technology, under contract with the National Aeronautics and Space Administration.

We find that our HSB and LSB samples have distinct central surface brightness distributions, with the HSBs peaking around $\mu_0(B) \sim 21$ mag arcec^{-2} and the LSBs peaking around $\mu_0(B) \sim 22.5$ mag arcec^{-2}. We find that the two HSB and LSB populations are distinct, finding a 99.4% probability the null-hypothesis (that the two populations are the same) is rejected via a Kolmogorov-Smirnov Test.

Finally, we find our LSBs to be composed of mostly later Hubble types (T), a very useful numerical representation of galaxy morphology (de Vaucouleurs 1959), and the HSB sample to extend over a wider range of T, although they are mostly comprised of early type spirals. Here, early galaxy types are lower T (including negative values for ellipticals) and later galaxy types are higher T (with irregulars having $T = 11$).

Table 4.1: Comparison sample of high surface brightness galaxies. Sample is made up of barred galaxies taken from the Carnegie-Irvine Galaxy Survey (CGS) (Ho et al. 2011, denoted by 1 in col. 10) and the Calar Alto Legacy Integral Field Area (CALIFA) Survey (Sánchez et al. 2012, denoted by 2 in col 10.) present in the SDSS database (York et al. 2000; Blanton et al. 2017). We list the R.A. (col. 2) and Dec. (col. 3) coordinates, photometric disk position angles (col. 4) and inclinations (col. 5), distances (col. 6), morphologies (col. 7), i-band disk scale lengths (col. 8), and estimated B-band central surface brightnesses (col. 9). Distances that are not redshift independent are denoted by *. Disk scale lengths and estimated B-band central surface brightnesses are calculated using the available SDSS *ugri* images.

Galaxy	R.A. (J2000)	Dec. (J2000)	P.A. (°)	i (°)	D (Mpc)	Morph.	h (kpc)	$\mu_0(B)$ (mag arcsec^{-2})	Survey
NGC 36	00:11:22.30	06:23:22.73	23.4	57.2	83.65	SBb	7.83±0.28	21.77±0.19	2
NGC 151	00:34:02.79	-09:42:19.21	68.0	55.7	50.36	SB(r)bc	5.94±0.16	21.45±0.13	1
NGC 337	00:59:50.09	-07:34:40.70	-60.0	50.8	19.56	SB(s)d	1.74±0.03	19.46±0.11	1
NGC 701	01:51:03.84	-09:42:09.40	45.0	63.1	23.00	SB(rs)c	2.08±0.01	21.38±0.07	1
NGC 1022	02:38:32.71	-06:40:38.70	24.5	24.7	18.16	SB(s)a	1.93±0.05	21.23±0.17	1
NGC 1645	04:44:06.39	-05:27:56.17	84.7	64.5	71.68*	SB0a	6.33±0.15	21.91±0.16	2
NGC 3300	10:36:38.44	14:10:15.97	-8.0	57.2	50.45	SB0a	4.30±0.22	21.14±0.23	2
NGC 4691	12:48:13.63	-03:19:57.77	-3.0	30.9	21.36	SB(S)0/a	3.39±0.30	21.11±0.15	1
NGC 4699	12:49:02.23	-08:39:53.49	32.3	34.9	25.56	SAB(rs)b	2.63±0.14	19.53±0.29	1
NGC 5068	13:18:54.81	-21:02:20.80	-28.0	32.9	14.43	SAB(rs)cd	4.63±0.15	22.38±0.21	1
NGC 5205	13:30:03.58	62:30:41.66	-9.9	50.0	27.52	SBbc	2.23±0.10	21.81±0.25	2
NGC 5334	13:52:54.46	-01:06:52.68	12.3	43.9	24.60	SB(rs)c	5.00±0.08	22.39±0.12	1
NGC 5339	13:54:00.27	-07:55:50.40	37.6	42.3	44.54*	SB(rs)a	3.79±0.12	20.71±0.19	1
NGC 5378	13:56:51.02	37:47:50.08	86.5	37.8	47.69*	SBb	3.46±0.13	21.67±0.24	2
NGC 5406	14:00:20.12	38:54:55.50	-68.2	44.9	79.44	SBb	6.86±0.25	21.22±0.19	2
NGC 5885	15:15:04.16	-10:05:09.63	57.4	38.9	32.23	SAB(r)c	5.19±0.10	22.27±0.12	1
NGC 5947	15:30:36.60	42:43:01.73	72.5	44.6	88.14*	SBbc	4.38±0.13	21.32±0.31	2
NGC 6497	17:51:17.97	59:28:15.18	-68.0	60.9	89.84*	SBab	5.12±0.13	20.88±0.23	2
NGC 6941	20:36:23.47	-04:37:07.48	-52.5	42.3	87.64	SBb	5.32±0.32	21.81±0.18	2
NGC 6945	20:39:00.62	-04:58:21.30	-53.9	51.3	51.81	SB0	4.70±0.29	21.88±0.27	2
NGC 7321	22:36:28.02	21:37:18.50	13.4	48.3	100.15	SBbc	6.44±0.17	20.91±0.17	2
NGC 7563	23:15:55.93	13:11:46.04	-30.2	55.8	56.12	SBa	3.21±0.14	20.57±0.28	2
NGC 7591	23:18:16.28	06:35:08.90	-36.0	57.6	67.63	SBbc	5.58±0.22	22.03±0.18	2
PGC 3853	01:05:04.88	-06:12:44.60	-65.8	42.4	11.46	SAB(rs)d	2.77±0.09	23.21±0.13	1
UGC 3253	05:19:41.90	84:03:09.33	-88.0	56.8	60.27	SBb	3.65±0.13	21.47±0.33	2
UGC 12185	22:47:35.06	31:22:24.70	-19.0	56.8	93.11	SBb	4.47±0.20	21.70±0.24	2

4.2.2 Data

For our analysis in this chapter, we obtain g- and i-band images directly from the SDSS image server. We have selected these filters as they allow us to cover roughly the same wavelength range to that used in Chapter 3 via the B- and I-bands (see Fig. 4.1). In addition, we do not opt for the more red z-band as most galaxies are almost entirely missed due to the short exposure time, 59 seconds. However, it is worth noting that these filters are not directly comparable: the effective wavelengths for g and B are 4770Å and 4353Å respectively, and 7625Å and 8797Å for i and I.

Before analyzing these images, we use information in the header files to reorient the images to be true on-sky orientation, as well as convert the units of the images from nanomaggies to counts. No sky subtraction is necessary, as SDSS provides fully reduced images. We show the on-sky i-band images for our sample in Fig. 4.3

In order to compare the results from these HSBs with our LSBs in Chapter 3, we also obtain available HI magnitudes from the `HYPERLEDA` database[2], leaving us with a subsample of 21 barred HSBs.

4.3 Methods

In this section, we detail the methods used to obtain the photometric bar properties (Sec. 4.3.1) and estimates of stellar and gas masses (Sec. 4.3.2) for our HSB comparison sample.

As with the analysis in the previous chapters, we deproject each image so that the galaxy appears face-on. To do this, we use the photometric disk P.A. and i given from each survey, shown in Table 4.1. These values have been determined through elliptical isophotes, and we confirm that deprojecting the images with these values results in the outer isophotes being nearly circular.

[2]http://leda.univ-lyon1.fr/

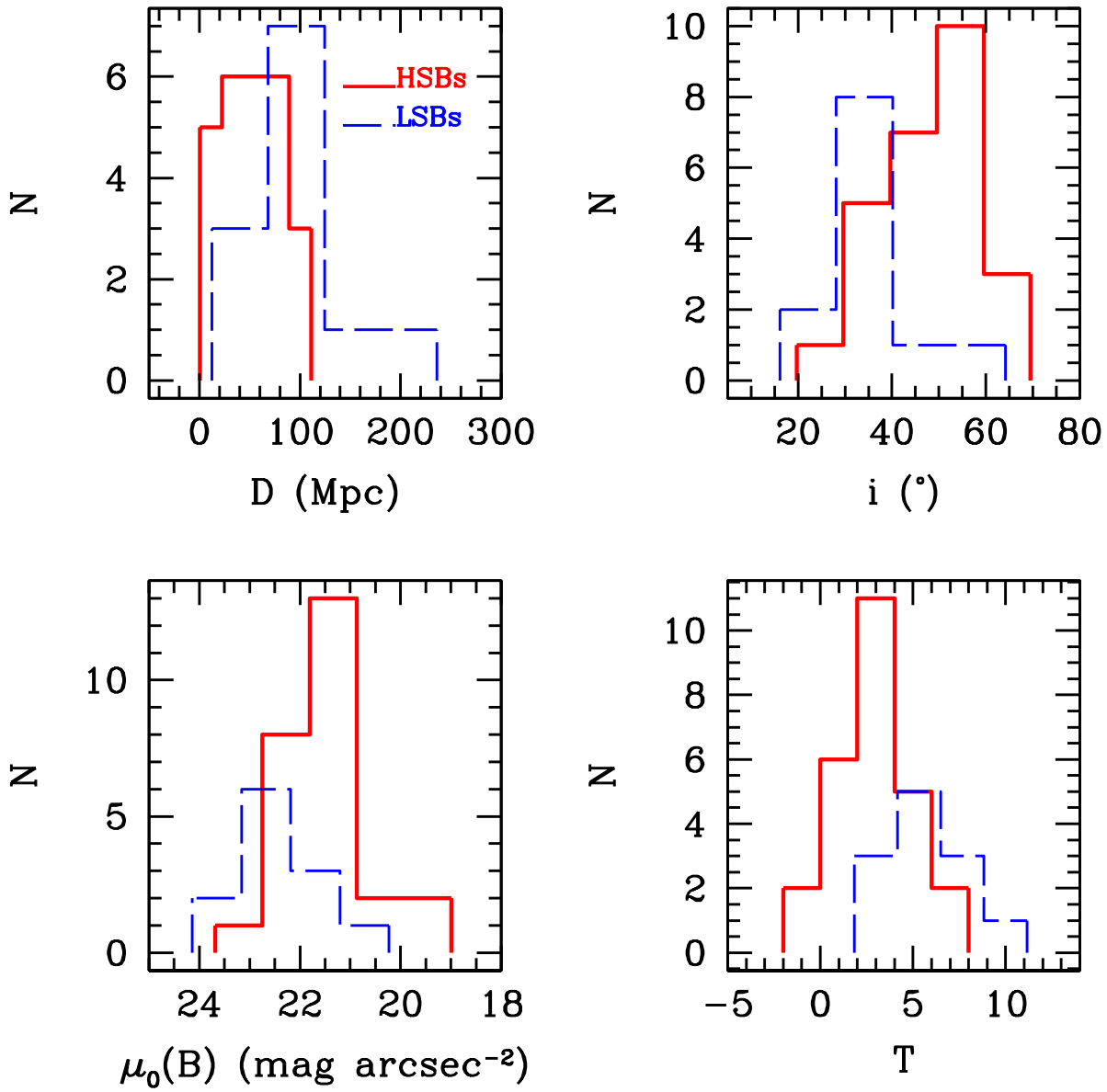

Figure 4.2: Comparison of basic properties for our LSB (dashed blue line) and HSB (solid red line) samples. *Top Left*: distance (Mpc); *Top Right*: inclination (°); *Bottom Left*: central surface brightness in B-band ($\mu_0(B)$); *Bottom Right*: morphological type T.

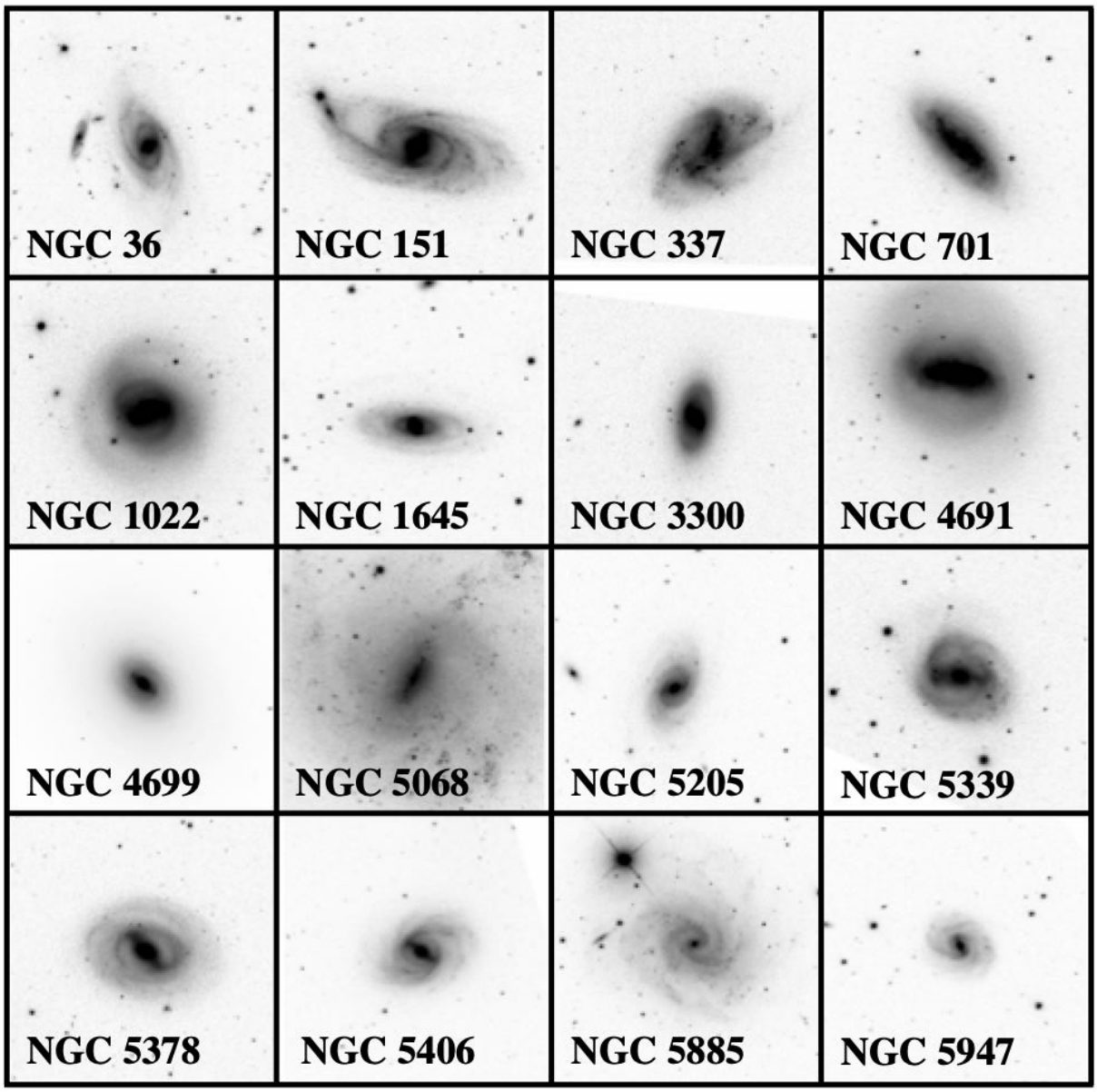

Figure 4.3: On-sky i-band images of our HSB comparison sample. Directions are indicated by the arrows, and each image is 600×600 pixels, or $2.38' \times 2.38'$. Images are all scaled with `asinh` scaling, but each image has different scaling limits to best show the disk and bar structure within each galaxy. White areas in images are the result of rotating the images to align north upwards and east to the left, not real features of the images.

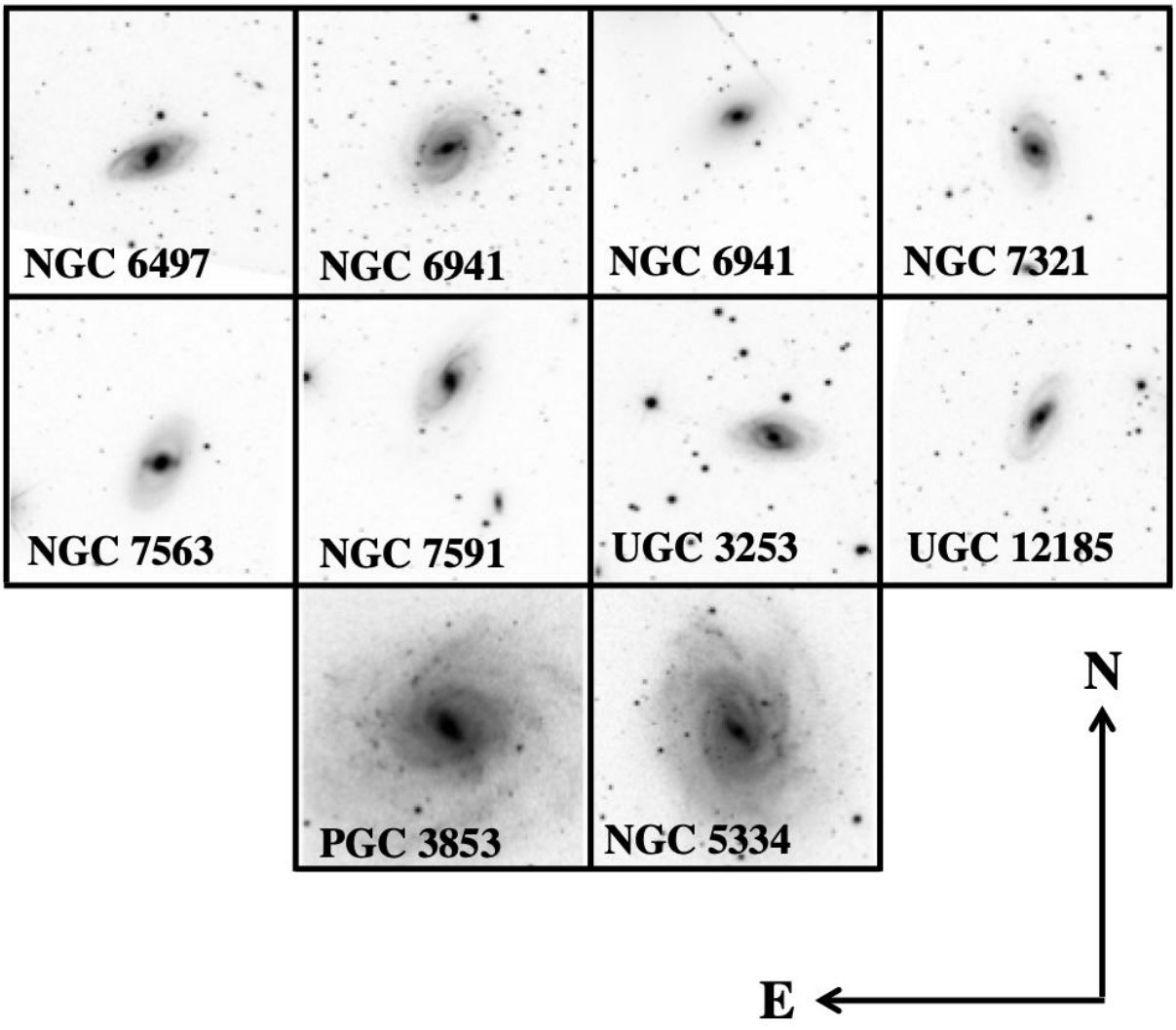

Figure 4.3: *continued*

4.3.1 Bar Properties

In the following sections, we detail the methods used to obtain the photometric bar properties: bar length (Sec. 4.3.1.1), bar strength (Sec. 4.3.1.2), and corotation radii (Sec. 4.3.1.3).

4.3.1.1 Bar Lengths

In this section, we detail the methods for our four different bar length measures: use of azimuthal light profiles, Fourier analysis, and two different methods based on analysis of elliptical isophotes. It is important to determine the bar length as accurately as possible, as a wrong bar length will propagate through both the bar strength and corotation radius (Michel-Dansac & Wozniak 2006). We do not average the four different measurements to obtain a final bar length, but instead use the method that provides the most accurate measurement in each individual case. In some galaxies, a given method could be biased towards shorter or longer values, and thus would bias any averaging taking place (see Sec. 3.3.2.1 in Chapter 3).

Azimuthal Light Profiles For our first bar length measure, we opt to use the method we put forth in Chapters 2 and 3: analysis of azimuthal light profiles. As a reminder, azimuthal light profiles are a useful means of analyzing galaxy structure. Instead of obtaining a light profile radially in a galaxy, we can obtain light as a function of azimuthal angle for various radii.

We construct the azimuthal light profiles for each galaxy in the same way, only adjusting the starting and ending radius. Each set of profiles has a radial spacing of one pixel, or $0.396''$, and has 60 azimuthal divisions at each radius (i.e. each division is 6°). In Fig. 4.4 we show an example set of g (top panel) and i-band (bottom panel) azimuthal light profiles for NGC 36. Profiles are plotted in the range $3'' < R < 35''$ every $3''$ for clarity. The rainbow color scheme in each panel corresponds to radius, with red (top profile) indicating closer in and violet (bottom profile) indicating farther out. Plots similar to Fig. 4.4 for the remainder of the HSB sample are shown in Fig. 4.24. Here we can see that there are a wide range of

profiles found in each galaxy, ranging from the very smooth and well-behaved (e.g. NGC151, NGC 1645, NGC 3300, NGC 7653) to the very messy (e.g. NGC 337, NGC 701, NGC 7691).

We then fit Gaussians to the humps in the i-band azimuthal light profiles due to the bar in order to obtain centroids. Finally, we track the movement of these centroids as a function of radius to determine where the humps follow the behavior described in Ohta et al. (1990). As the two humps may not diverge from the bar length at the same radius due to the bar not being perfectly symmetrical, we take the bar length to be the average of where each of the humps diverge, with the error being the difference between the humps and the bar length. As our radial spacing between azimuthal light profiles is one pixel, this places a lower limit on our error for this method of $0.396''$.

In Fig. 4.5 we show an example plot of the bar azimuthal centroid information as a function of radius for NGC 36. Here, the bar centroids are shown in the top left panel, the difference between the two centroids in the top right panel, the difference between each hump and the bar centroid in the bottom left panel, and peak surface brightness $\mu(i)$ (mag arcsec^{-2}) for each hump in the bottom right panel. We can see from the bottom left panel that the two humps remain close to the azimuthal centroid of the bar before diverging sharply towards higher angles. This is because the humps are no longer tracing the location of the bar, but instead the location of the spiral arms. The vertical dashed line indicates the bar length: $R_{\rm az} = 18.01'' \pm 0.60''$. Plots similar to Fig. 4.5 for the remainder of the sample are shown in Fig. 4.25.

Fourier Analysis Our next bar length measure is based on a Fourier analysis of the azimuthal light profiles described above. We can decompose the profiles via a Fourier transform:

$$\mathcal{F}(R) = \int_{-\pi}^{\pi} I_R(\theta) \exp(-2i\theta) d\theta \tag{4.4}$$

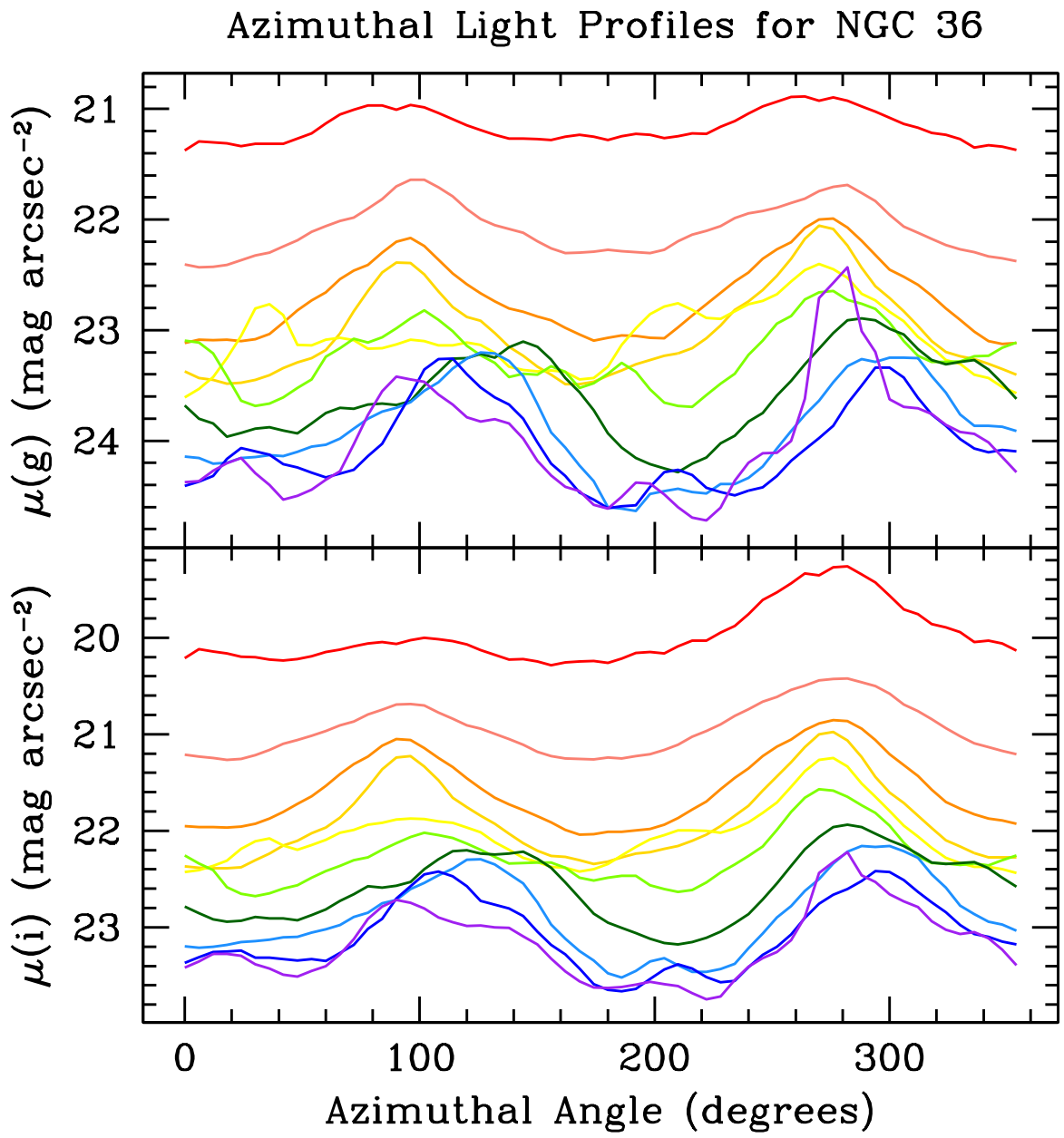

Figure 4.4: Azimuthal light profiles for NGC 36. *Top panel*: g-band; *Bottom Panel*: i-band. Profiles are plotted in the range $3'' < R < 35''$ every $3''$ for clarity. The rainbow color scheme in each panel corresponds to radius, with red (top profile) indicating closer in and violet (bottom profile) indicating farther out.

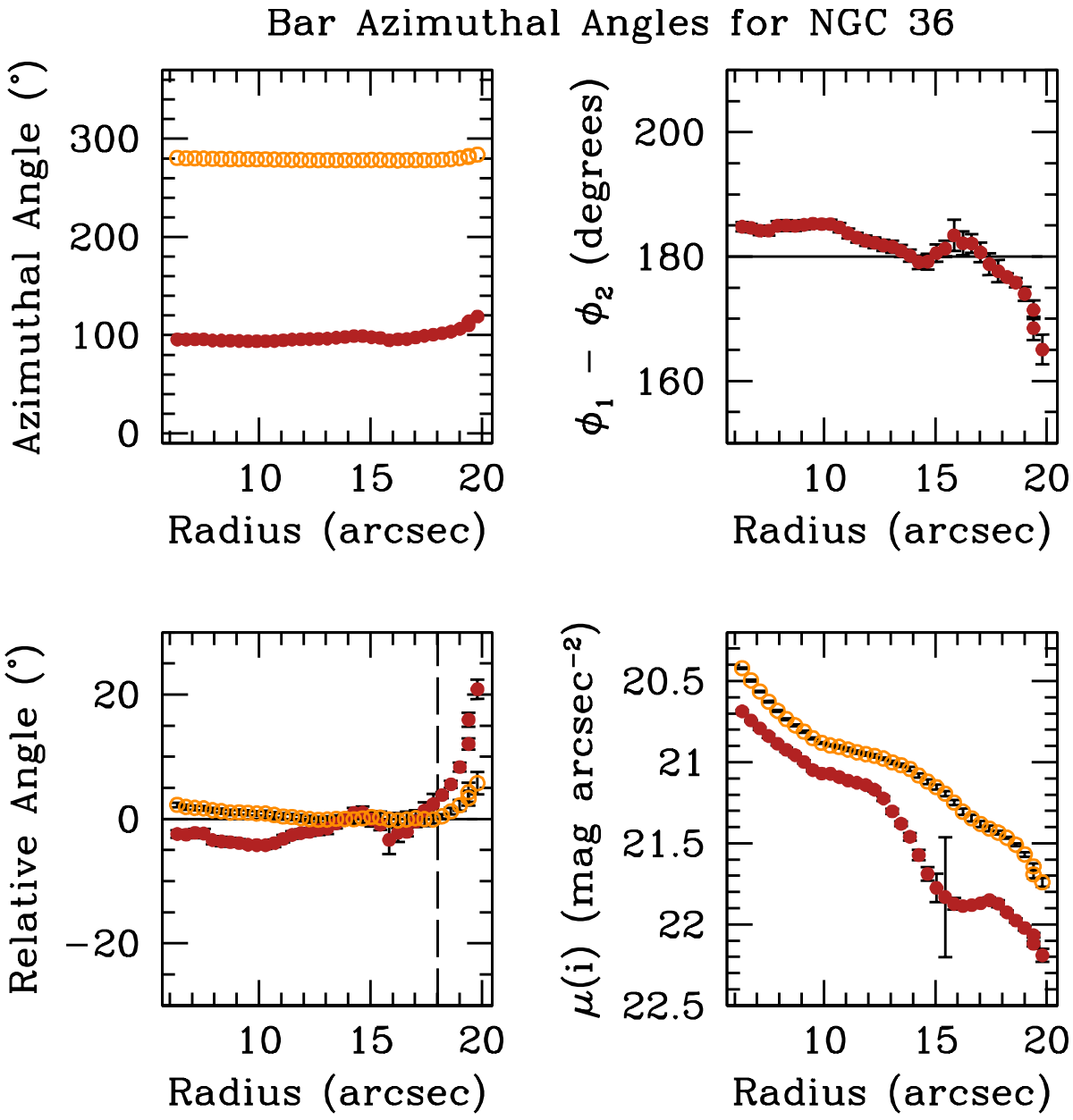

Figure 4.5: Bar azimuthal centroids for NGC 36. *Top Left*: azimuthal centroids for the two humps present in the azimuthal light profiles; *Top Right*: azimuthal difference between the two humps ($\phi_1 - \phi_2$), the solid line shows 180°; *Bottom Left*: difference between each hump and the bar centroid, solid line shows 0°and the vertical dashed line indicates the bar length $R_{\rm az} = 18.01'' \pm 0.60''$; *Bottom Right*: peak surface brightness $\mu(i)$ (mag arcsec^{-2}) for each hump.

where $I_R(\theta)$ are the azimuthal light profiles, and θ is the azimuthal angle. The Fourier coefficients are given by

$$A_m = \frac{1}{\pi}\int_0^{2\pi} I_R(\theta)\cos(m\theta)d\theta \tag{4.5}$$

$$B_m = \frac{1}{\pi}\int_0^{2\pi} I_R(\theta)\sin(m\theta)d\theta, \tag{4.6}$$

and the amplitudes are

$$I_0(r) = \frac{A_0(r)}{2} \tag{4.7}$$

$$I_m(r) = \sqrt{A_m^2(r) + B_m^2(r)}. \tag{4.8}$$

Aguerri et al. (2009) define the bar region via the relation

$$\frac{I_b}{I_{ib}} > \frac{1}{2}\left[\left(\frac{I_b}{I_{ib}}\right)_{max} - \left(\frac{I_b}{I_{ib}}\right)_{min}\right] + \left(\frac{I_b}{I_{ib}}\right)_{min} \tag{4.9}$$

where I_b and I_{ib} are the bar and interbar Fourier intensities respectively, defined as

$$I_b = I_0 + I_2 + I_4 + I_6 \tag{4.10}$$

$$I_{ib} = I_0 - I_2 + I_4 - I_6. \tag{4.11}$$

The last radius where Eq. 4.9 is satisfied is taken to be the bar length, $R_{\mathcal{F}}$.

We show an example plot of the bar/interbar Fourier intensities for NGC 36 in Fig. 4.6, and the rest in Fig. 4.26. Here, the horizontal dashed line denotes equation 4.9. We find $R_{\mathcal{F}} = 14.90'' \pm 0.40''$.

Elliptical Isophotes Finally, we employ two methods based on elliptical isophotes: the radius of maximum ellipticity (R_ϵ), and the radius of discontinuity in position angle ($R_{\rm P.A.}$). The first measure, R_ϵ, is simply the radius at which the radial profile of eccentricity reaches a local maximum (Wozniak et al. 1995; Michel-Dansac & Wozniak 2006).

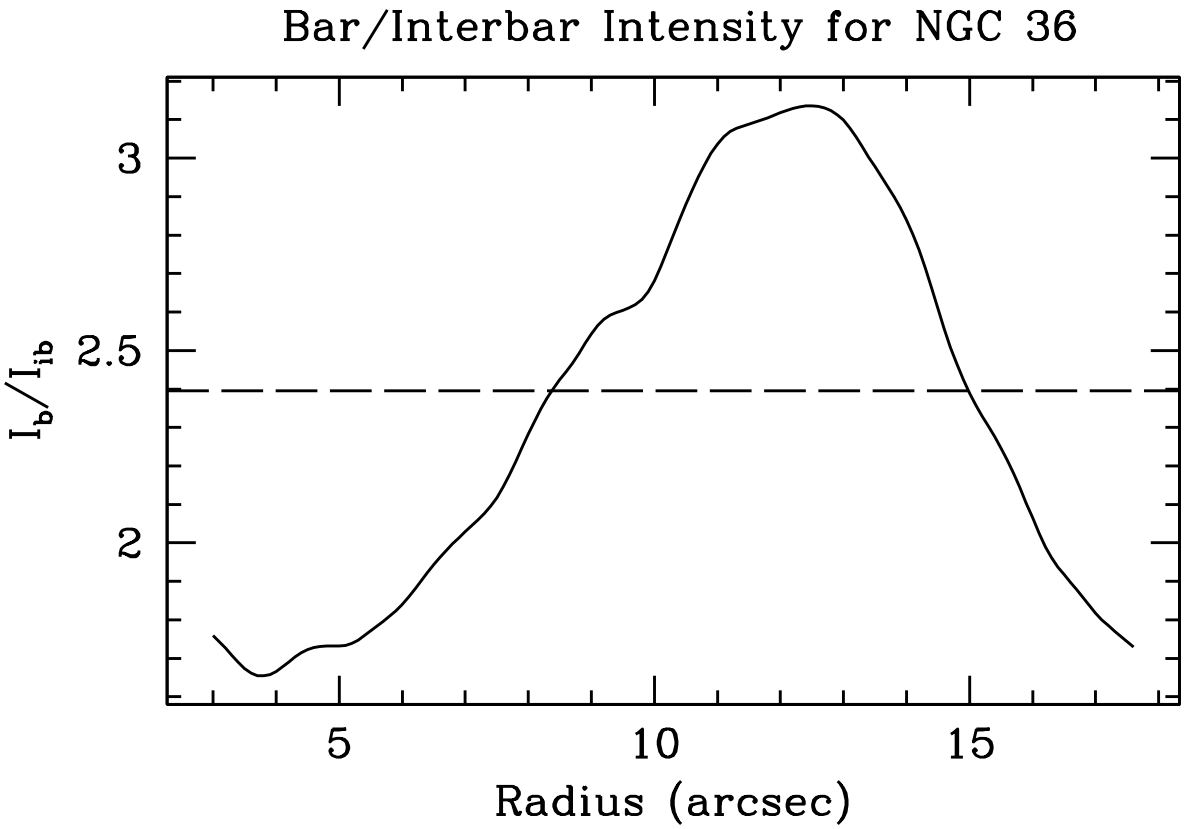

Figure 4.6: Bar/Interbar Fourier intensities for NGC 36. The dashed line indicates Eq. 4.9, and the last intersection is taken to be the bar length, $R_{\mathcal{F}} = 14.90'' \pm 0.40''$.

The second measure, $R_{\rm P.A.}$, is based on the behavior of the position angle of the elliptical isophotes. The P.A. remains constant within the bar region, and then changes to the value of the disk P.A. (Wozniak et al. 1995). Traditionally, a change in the P.A. greater than 5° compared to the value at R_ϵ is taken to be the bar radius (see Aguerri et al. 2009).

We show radial plots of eccentricity and position angle for NGC 36 in Fig. 4.7. The vertical line in the top panel denotes $R_\epsilon = 18.47'' \pm 1.76''$, and in the bottom panel denotes $R_{\rm P.A.} = 24.59'' \pm 2.35''$. Plots similar to Fig. 4.7 for the rest of our sample are shown in Fig. 4.27.

4.3.1.2 Bar Strengths

We determine bar strengths via:

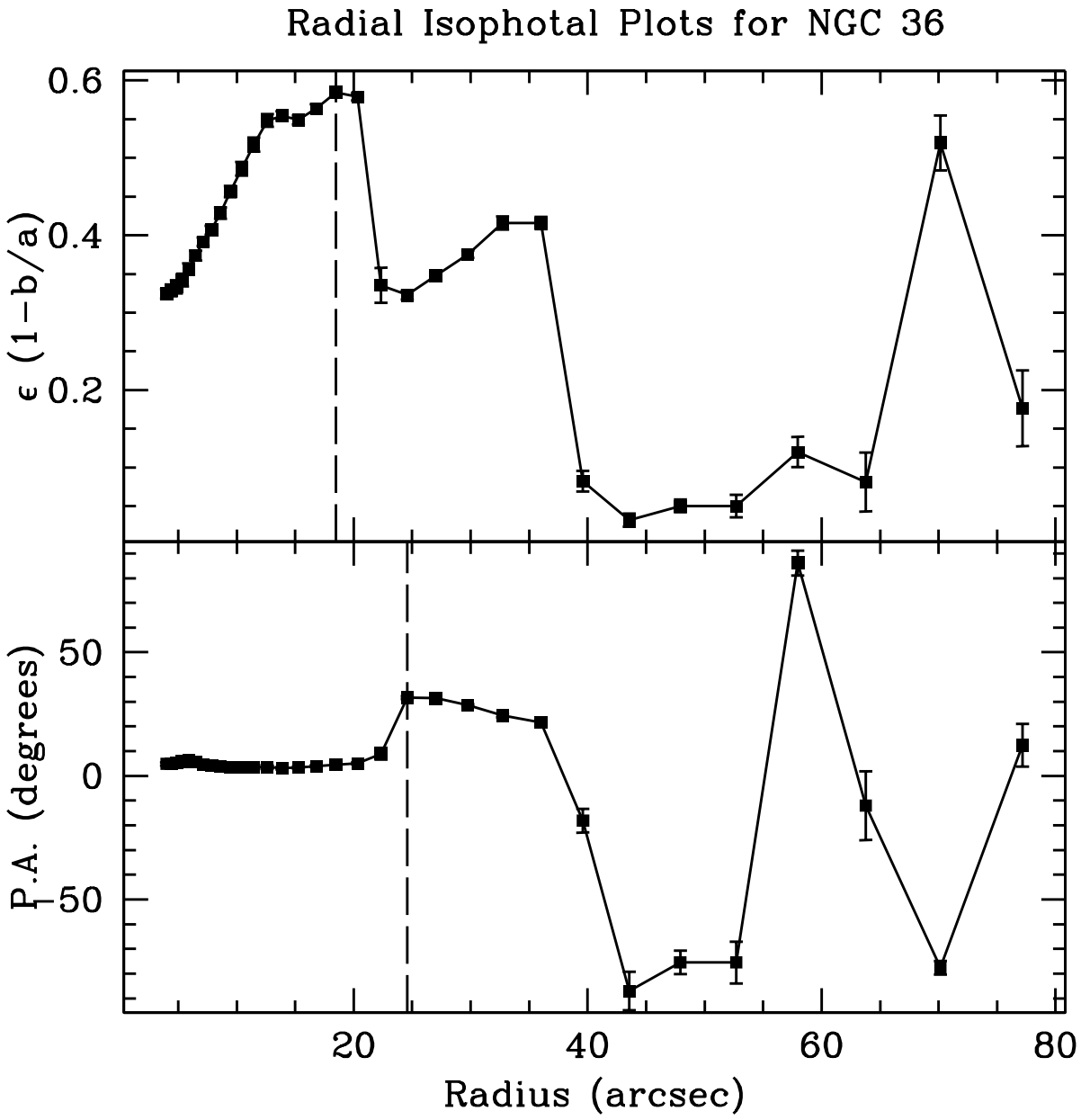

Figure 4.7: Radial plots of eccentricity (top panel) and position angle (bottom panel) of elliptical isophotes for NGC 36. The dashed lines indicate bar lengths derived via the radius of maximum ellipticity ($R_\epsilon = 18.47'' \pm 1.76$) and radius of discontinuity in P.A. ($R_{\rm P.A.} = 24.59'' \pm 2.35$).

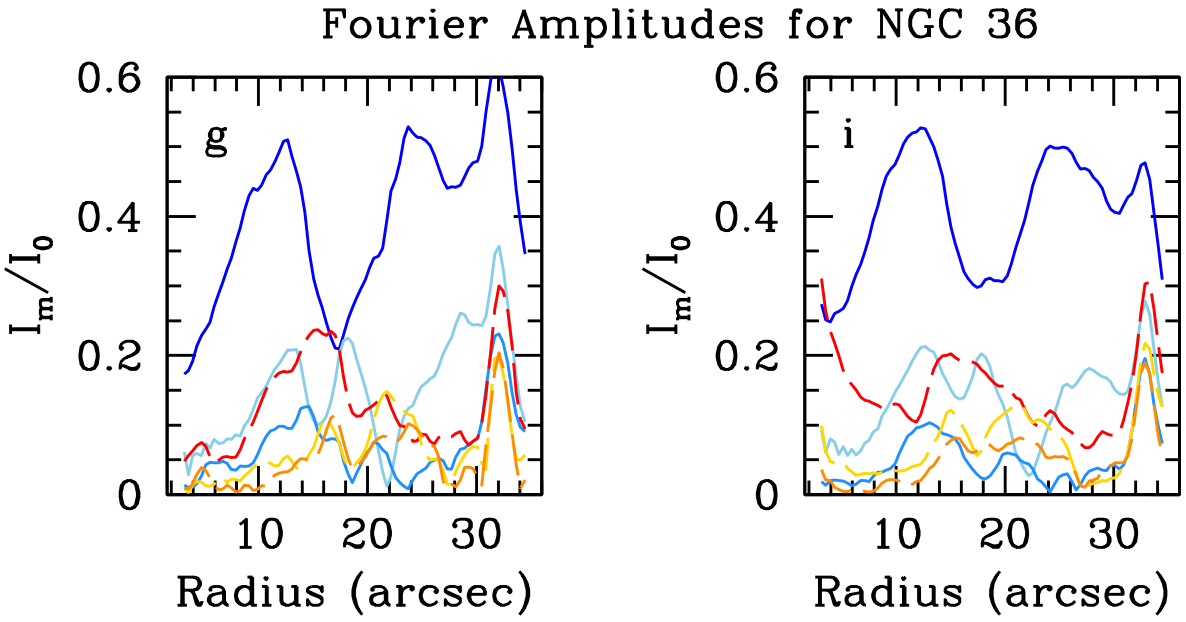

Figure 4.8: Fourier amplitudes for NGC 36. g band is shown in the left panel and i band in the right panel. Bluer colors shown even modes with deep blue being $m = 2$, and redder colors show odd modes with deep red being $m = 1$.

$$S_{\rm b} = \frac{1}{R_{\rm bar}} \sum_{m=2,4,6} \int_0^{R_{\rm bar}} \frac{I_m}{I_0} dr, \tag{4.12}$$

where $R_{\rm bar}$ is the bar radius and I_m are the even Fourier amplitudes. Since our azimuthal light profiles cannot begin at $R = 0$, our bar strengths are only lower limits.

We show an example plot of the Fourier amplitudes for NGC 36 in Fig. 4.8. Here we can see strong $m = 2$ modes in the inner $15''$ due to the bar, as well as strong even modes in the disk due to the spiral arms. Plots similar to Fig. 4.8 for the remainder of our sample are shown in Fig. 4.28.

4.3.1.3 Corotation Radii

To obtain the corotation radii, $R_{\rm CR}$, we use the method from Puerari & Dottori (1997). This method relies on calculating phase profiles of two images separated by a large wavelength

range, originally the B- and I-bands. As we are using SDSS images, we cannot obtain phase profiles in the B- and I-bands. Instead, we use the g- and i- bands as proxies for the two different stellar populations, as has been done before (see Sierra et al. 2015). In addition, we have used phase profiles from B-band and 3.6μm images, a much larger difference in wavelength space, to success in Chapter 2. We therefore feel confident in using these two bands, g and i, to determine the bar corotation radius.

The method itself determines the corotation radius by locating the intersection of phase profiles of two different images. We calculate the phase via:

$$\Theta(r) = \arctan\left(\frac{\mathrm{Re}(\mathcal{F}(r))}{\mathrm{Im}(\mathcal{F}(r))}\right), \tag{4.13}$$

where $\mathrm{Re}(\mathcal{F}(r))$ and $\mathrm{Im}(\mathcal{F}(r))$ denote the real and imaginary components of the Fourier transform respectively. We take the *first* phase crossing after the bar radius to be the bar corotation radius, as it is thought that corotation occurring within the bar would cause the bar to become unstable (Contopoulos 1980; Bureau et al. 1999). It is worth noting that this method is not limited to finding bar corotation radii. Instead, an intersection of phase profiles simply denotes *a* corotation radius.

Once R_{CR} has been calculated, it is useful to further calculate the dimensionless parameter $\mathcal{R}$, or the relative bar pattern speed:

$$\mathcal{R} = \frac{R_{\mathrm{CR}}}{R_{\mathrm{bar}}} \tag{4.14}$$

where R_{bar} is the final bar length measure. As a reminder, fast rotators are defined as having $\mathcal{R} < 1.4$, and slow rotators as having $\mathcal{R} > 1.4$.

We show the g and i-band phase profiles for NGC 36 in Fig. 4.9, and find $R_{\mathrm{CR}} = 19.80'' \pm 0.40''$. Plots similar to this one for the remainder of the HSB sample are shown in Fig. 4.29.

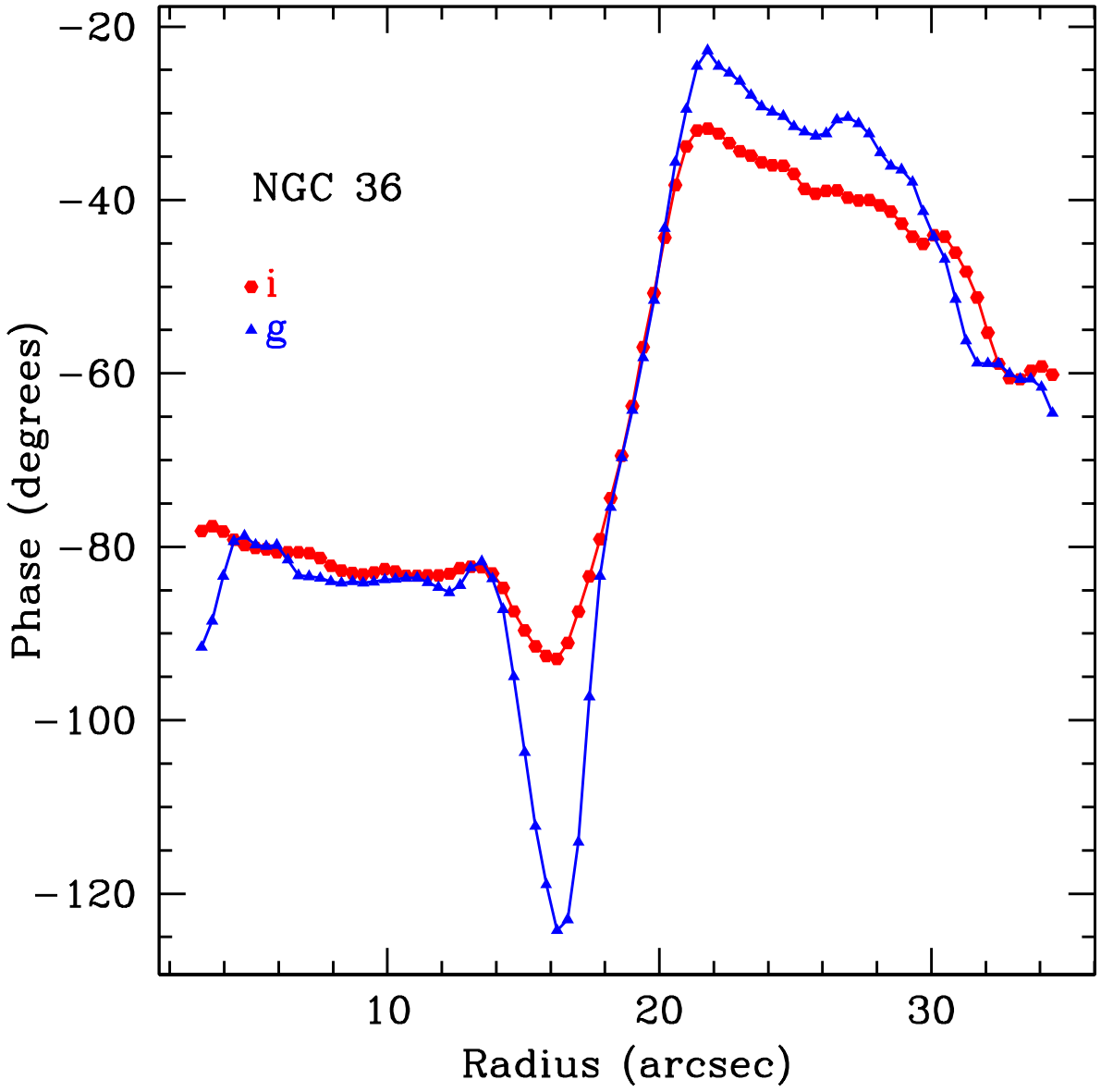

Figure 4.9: Phase profiles for NGC 36. Blue triangles denote the g-band and red circles denote the i-band. Intersections of the profiles denote corotation radii, the first of which after the bar length is the bar corotation radius.

4.3.2 Gas and Stellar Masses

We calculate HI masses using the relation from Haynes & Giovanelli (1984)

$$M_{\rm HI} = 2.36 \times 10^5 D^2 F_{\rm HI}(M_\odot), \tag{4.15}$$

where D is the distance in Mpc listed in Table 4.1, and $F_{\rm HI}$ is the HI flux using the HI magnitudes from `HYPERLEDA`. We then calculate the total gas mass as $M_{gas} = 1.4 M_{\rm HI}$ to account for Helium and metals (McGaugh et al. 2000).

In Chapter 3, we estimated stellar masses using the I-band mass-to-light ratios from Into & Portinari (2013) via $(B-I)$ colors. The use of this model was motivated due to having only B- and I-band photometry available for our LSBs in Chapter 3. However, it is known that this model generally underpredicts stellar mass due to contamination from inclusion of thermally pulsing asymptotic giant branch (TP-AGB) stars (McGaugh & Schombert 2014). This underprediction is worse in the near infrared (NIR) due to the TP-AGB stars being brightest in redder bands and not affecting the rest of the optical wavelength range. To bypass this, Schombert et al. (2019) give new stellar mass-to-light ratios for the V-band:

$$\log \Upsilon_*^V = -1.224(B-V)^2 + 3.120(B-V) - 1.271 \tag{4.16}$$

We can obtain V-band magnitudes and $(B-V)$ colors via SDSS photometry using the galaxy transformation equations from Cook et al. (2014), similar to the process in Erwin (2018):

$$(B-i) = 1.27(g-i) + 0.16 \tag{4.17}$$

$$(V-u) = -0.82(u-r) - 0.02 \tag{4.18}$$

$$(B-V) = 0.89(g-r) + 0.16 \tag{4.19}$$

Finally, based on the consistency of using the V-band (McGaugh & Schombert 2014; Schombert et al. 2019), we opt to use Equation 4.16 to obtain stellar mass estimates for our HSBs. For more discussion on this, see Appendix B. We then obtain gas fractions via:

$$f_{gas} = \frac{M_{gas}}{M_{gas} + M_*}. \tag{4.20}$$

Errors on HI mass and stellar mass are propagated through assuming the errors in distance, and errors on HI from `HYPERLEDA`. We are limited to those galaxies that both have available HI data *and* SDSS photometry, limiting our mass estimates to 21 galaxies. In addition, we also opt to obtain new stellar mass estimates for our LSBs using the same methods described above. We find that while 14 of our 15 LSBs have available SDSS images to obtain *ugri* magnitudes, only 9 have HI fluxes in `HYPERLEDA`.

4.4 Results

Here we compare the results between the HSB and LSB bar properties (Sec. 4.4.1) and explore any possible trends with stellar and gas mass (Sec. 4.4.2).

4.4.1 Bar Properties

We discuss the results for each parameter in the subsections below: bar lengths in Sec. 4.4.1.1, bar strengths in Sec. 4.4.1.2, and corotation radii in Sec. 4.4.1.3. We finally compare the final HSB bar properties with those from the LSBs in Chapter 3 in Sec. 4.4.1.4.

4.4.1.1 Bar Lengths

In Table 4.2 we show the four different bar length measures for each galaxy: analysis of azimuthal light profiles ($R_{\rm az}$), Fourier analysis ($R_{\mathcal{F}}$), the radius of maximum ellipticity (R_{ϵ}), and the radius of discontinuity in position angle ($R_{\rm P.A.}$). Based on our analysis of mock galaxy images in Chapter 3, we found that our azimuthal measure gave the most accurate

Table 4.2: Bar lengths based on our four methods: analysis of azimuthal light profiles ($R_{\rm az}$), Fourier analysis ($R_{\mathcal{F}}$), the radius of maximum ellipticity (R_{ϵ}), and the radius of discontinuity in position angle ($R_{\rm P.A.}$). All bar lengths are in arcsec.

Galaxy	$R_{\rm az}$ (arcsec)	$R_{\mathcal{F}}$ (arcsec)	R_{ϵ} (arcsec)	$R_{\rm P.A.}$ (arcsec)
NGC 36	18.01±0.60	14.90±0.40	18.47±1.76	24.59±2.35
NGC 151	31.08±0.40	28.20±0.40	32.73±3.12	39.60±3.78
NGC 337	29.70±0.80	25.50±0.40	15.27±1.46	24.59±2.35
NGC 701	10.50±0.40	10.30±0.40	10.43±1.00	16.79±1.60
NGC 1022	21.38±2.38	21.60±0.40	18.47±1.76	22.35±2.13
NGC 1645	21.78±0.80	16.50±0.40	16.79±1.60	24.59±2.35
NGC 3300	20.39±0.40	16.80±0.40	15.27±1.46	20.32±1.94
NGC 4691	37.03±0.60	18.40±0.40	16.66±1.59	35.70±3.41
NGC 4699	14.65±1.19	14.40±0.40	12.51±1.19	16.66±1.59
NGC 5068	23.36±1.19	24.40±0.40	10.34±0.99	39.27±3.75
NGC 5205	15.25±0.99	29.60±0.40	15.14±1.45	20.15±1.92
NGC 5334	17.80±0.40	17.00±0.40	22.17±2.20	24.39±2.33
NGC 5339	26.54±0.40	33.50±0.40	29.51±2.82	35.70±3.41
NGC 5378	22.96±0.40	24.20±0.40	26.82±2.56	32.46±3.10
NGC 5406	20.00±0.99	23.60±0.40	22.17±2.12	26.82±2.56
NGC 5885	9.11±1.98	11.70±0.40	16.66±1.59	18.32±1.75
NGC 5947	9.70±0.40	14.00±0.40	12.51±1.19	15.14±1.45
NGC 6497	21.19±0.99	15.50±0.40	18.32±1.75	22.17±2.12
NGC 6941	13.07±0.79	14.50±0.40	13.76±1.31	16.66±1.59
NGC 6945	10.69±0.40	17.90±0.40	12.51±1.19	15.14±1.45
NGC 7321	16.04±0.99	12.10±0.40	11.47±1.09	15.27±1.46
NGC 7563	27.52±0.40	22.60±0.40	27.05±1.58	32.73±3.12
NGC 7591	14.85±0.40	20.20±0.40	10.43±1.00	20.32±1.94
PGC 3853	22.37±2.97	24.10±0.40	15.27±1.46	36.00±3.44
UGC 3253	19.20±1.39	30.90±0.40	20.32±1.94	22.35±2.13
UGC 12185	12.67±0.79	21.30±0.40	13.88±1.32	27.05±2.58

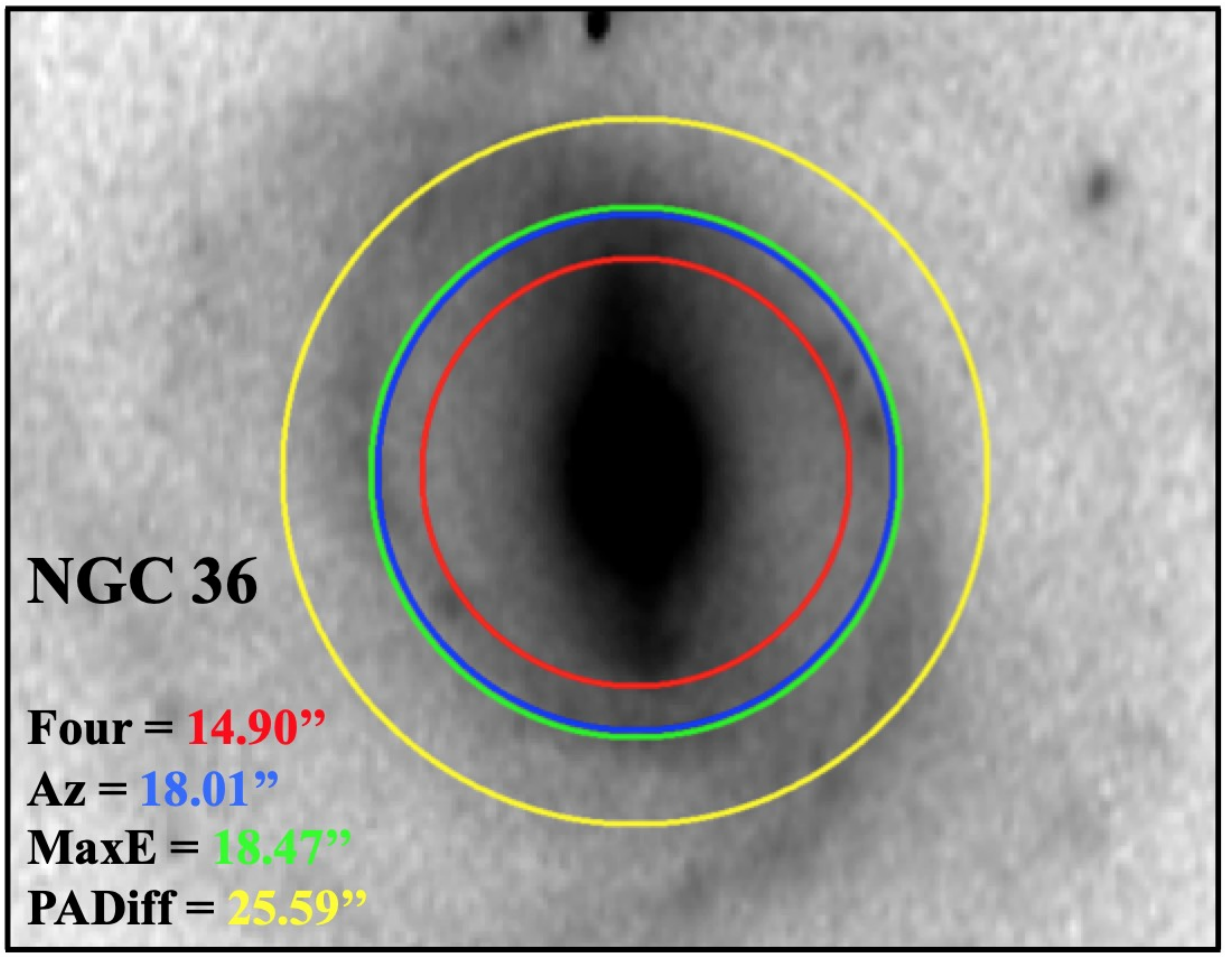

Figure 4.10: Visual comparison of the four bar length measures for NGC 36. Bar measures are listed in increasing value. Red: Fourier bar length; blue: azimuthal bar length; green: radius of maximum ellipticity; yellow: radius of discontinuity in position angle.

bar length across various galaxy properties and seeing. We therefore select this bar length measurement as the final bar length for all of our galaxies. However, in order to check that this method works for bars in HSBs as well, we visually plot each over the deprojected i-band image. In Fig. 4.10 we show an example plot of this for NGC 36, from which, it is clear that $R_{\mathrm{P.A.}}$ (yellow) overpredicts the bar length. While it may seem that $R_{\mathcal{F}}$ is the best measure, there is actually a ring at the end of the bar length that both R_{ϵ} and R_{az} locate making these bar lengths more accurate. Plots similar to Fig. 4.10 for the remainder of our sample are shown in Fig. 4.30.

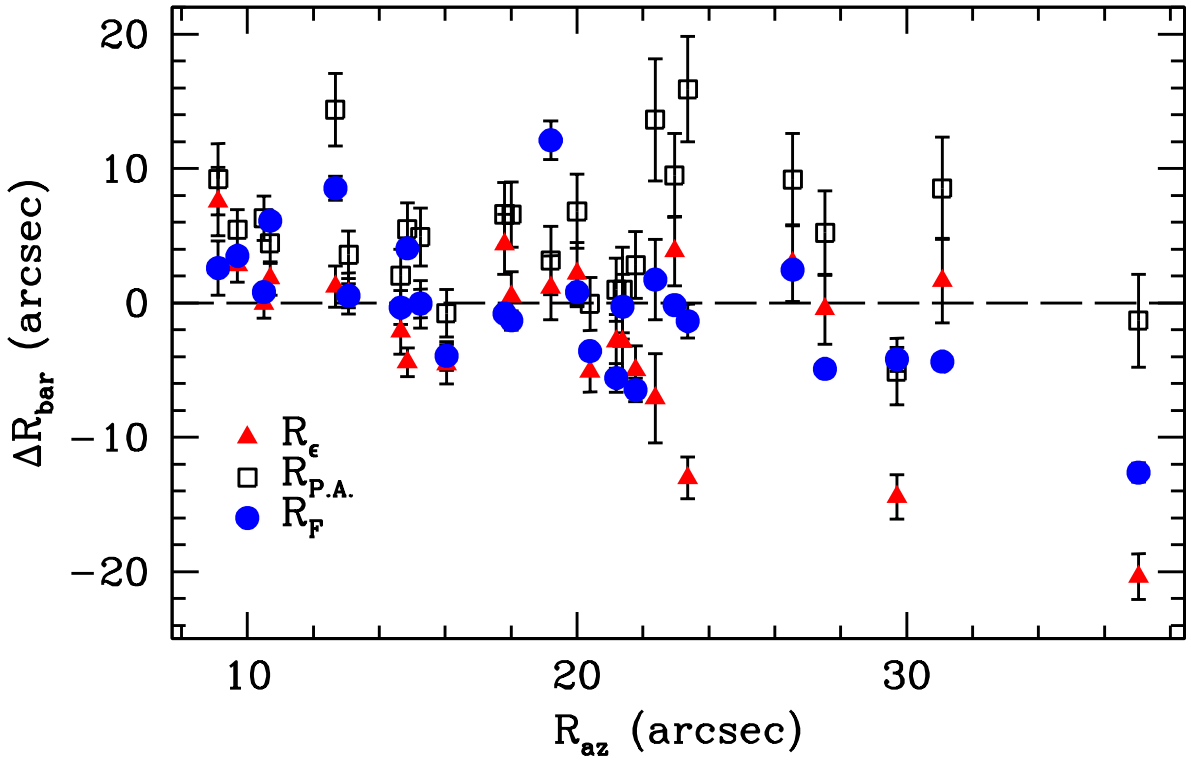

Figure 4.11: Comparison of bar length measures relative to the azimuthal method (i.e. $\Delta R_{\rm bar} = R_{method} - R_{\rm az}$) for our HSB sample. The radius of maximum ellipticity, R_ϵ, is shown as red triangles; the radius of discontinuity in position angle, $R_{\rm P.A.}$, is shown as open squares; the Fourier bar radius, $R_\mathcal{F}$, is shown as blue circles.

We show a visual comparison of the bar length measures in Fig. 4.11. Here, ΔR_{bar} shows the difference between a given method and $R_{\rm az}$. There appears to be a slight downward trend between R_ϵ and $R_{\rm az}$, with ΔR_{bar} generally positive at $R < 20''$, and generally more negative $R > 20''$. Without the point at $R \sim 35''$ $R_\mathcal{F}$ does not show any trend. In general, we find that $R_\mathcal{F}$ and R_ϵ broadly agree with the $R_{\rm az}$, although there is quite significant scatter. In practically all cases we find that $R_{\rm P.A.}$ overpredicts the bar length when compared with the other three measures. Based on this, as well as visual inspection of the bar lengths overplotted on the galaxy images (Fig. 4.10 and 4.30), we take $R_{\rm az}$ to be our bar length for each galaxy. This is consistent with our findings in both Chapter 2 and Chapter 3.

In the top panel of Fig. 4.12 we show a comparison between our measured bar lengths ($R_{\rm az}$) to those from CGS (bar lengths are given in Li et al. 2011), shown as triangles, and

CALIFA (bar lengths taken from Aguerri et al. 2015) galaxies, shown as circles. Here $\Delta R_{\rm bar} = R_{\rm bar} - R_{\rm bar,lit}$, where $R_{\rm bar}$ is our measured bar length in Table 4.4. We find that our bar lengths agree fairly well with those reported in the literature, at least when considering the errors, with no clear trend present in the residuals $\Delta R_{\rm bar}$. In addition, there is no trend present when looking at $\Delta R_{\rm bar}$ for each survey. There is a typical spread of $\sim 5''$ between our measured bar lengths and those reported in the literature.

Both Li et al. (2011) and Aguerri et al. (2015) use common bar length measurements: behavior of elliptical isophotes and Fourier analysis. For an in-depth comparison between these measurement techniques and our azimuthal bar length measure, see Sec. 3.4 in Chapter 3. Here, we find the azimuthal method to perform quite well on the HSBs (see Fig. 4.5 and Fig. 4.25), due to the fact that these galaxies extend significantly farther on the sky when compared with the majority of the LSBs from Chapter 3, leading to comparatively small errors.

4.4.1.2 Bar Strengths

We find bar strengths that range from 0.18 (NGC 5885) to 1.2 (NGC 4691), and a mean bar strength of $\sim 0.5 \pm 0.2$ for our HSBs. Due to the relatively large extent that the bars in these galaxies have across the sky, we found that decreasing the starting radius of the azimuthal light profiles did not affect the resulting bar strength.

4.4.1.3 Corotation Radii

We show a comparison between our measured relative bar pattern speeds and those in Aguerri et al. (2015) in the bottom panel of Fig. 4.12. Here $\Delta\mathcal{R} = \mathcal{R} - \mathcal{R}_{\rm lit}$, where $\mathcal{R}$ is our measured relative bar pattern speed in Table. 4.4. As Aguerri et al. (2015) reports four different measurements of $\mathcal{R}$ using the Tremaine-Weinberg method (Tremaine & Weinberg 1984), we take the average value to compare with our value, with the error being propagated through this averaging.

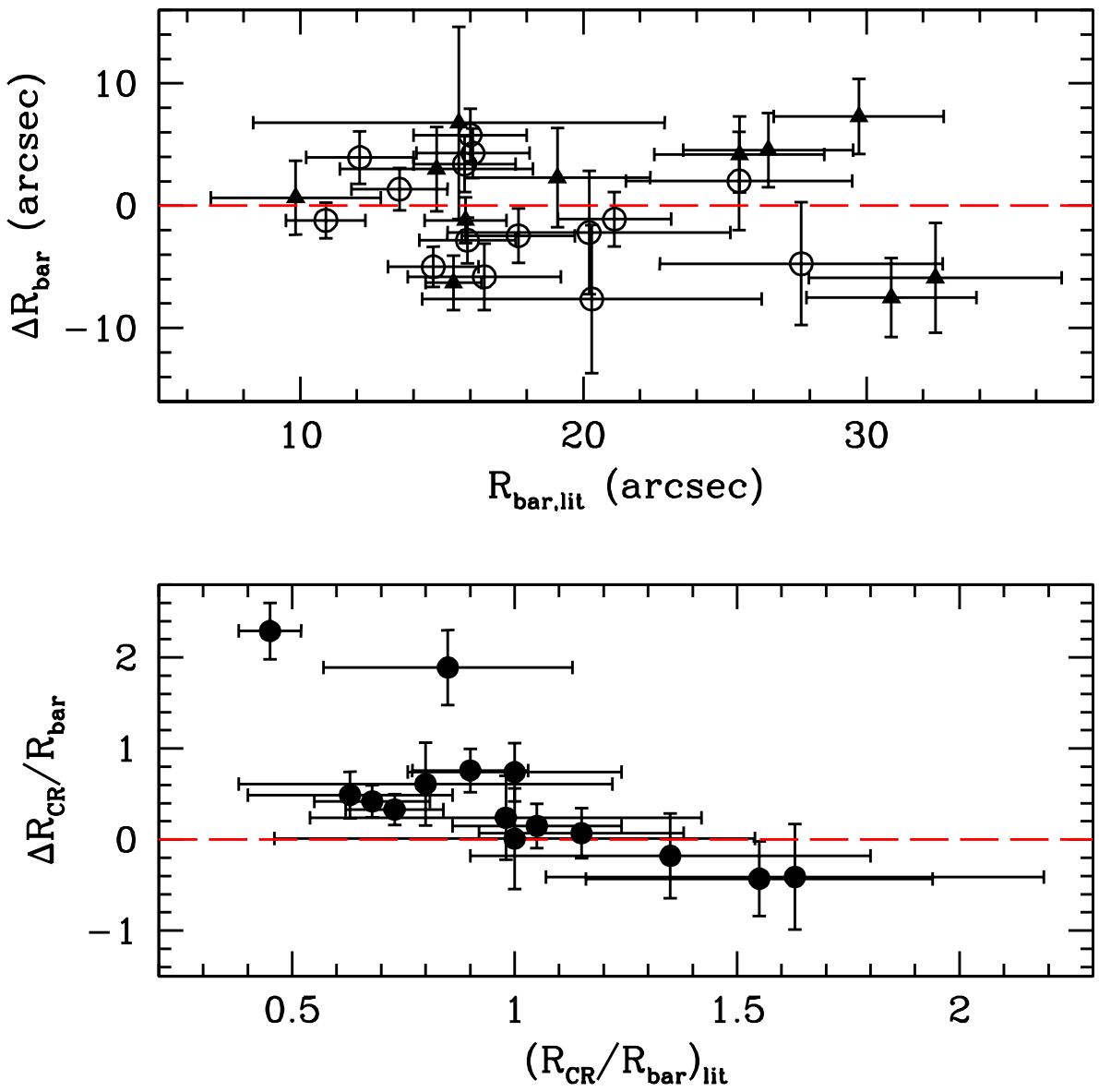

Figure 4.12: Comparison of our bar lengths (top) and relative bar pattern speeds (bottom) with available literature values for our HSB sample. In the top panel, galaxies from CALIFA are shown as closed triangles and galaxies from Aguerri et al. (2015) are shown as open circles. Filled circles in the bottom panel are galaxies from Aguerri et al. (2015).

We find that there is significant deviation between our relative pattern speeds with those from Aguerri et al. (2015), with the majority of our values being much larger. A major reason for this is that Aguerri et al. (2015) allows relative bar pattern speeds to be less than 1, or in other words allow corotation to occur within the bar. Bars with $\mathcal{R}<1$ are referred to as 'ultrafast' bars, and have also been reported in various studies (e.g. Corsini et al. 2007; Buta & Zhang 2009).

Because Aguerri et al. (2015) determined $R_{\rm CR}$ via the Tremaine-Weinberg (TW) method (Tremaine & Weinberg 1984), this could be the reason they were able to locate corotation within the bar. Since the TW method determines $R_{\rm CR}$ by finding the radius at which the rotation curve is equal to the bar pattern speed, there is no restriction on corotation occurring outside the bar region.

In order to see whether there are ultrafast bars in our sample, we have re-examined the phase profiles and report two corotation radii in Table 4.3: the *last* phase intersection *before* the end of the bar, $R_{\rm CR_1}$, and the *first* phase intersection *after* the end of the bar, $R_{\rm CR_2}$ (what is reported earlier in Table 4.4). We also report the two different relative bar pattern speeds associated with these two corotation radii, $\mathcal{R}_1$ and $\mathcal{R}_2$ respectively. $\mathcal{R}_2$ is the value reported in Table 4.4.

We find inner corotation radii for all of our HSBs, with the exceptions of NGC 337 and NGC 701. That all galaxies in our sample are hosts to ultrafast bars seems unlikely, due to theoretical expectations (Athanassoula 1980; Contopoulos 1980). Indeed, Guo et al. (2019) find that when determining the relative bar pattern speed through the Tremaine-Weinberg (TW) method the determination of disk position angle (P.A.) greatly affects the result. When using a P.A. derived from photometry, they find 15 out of 53 galaxies to host ultrafast bars. This decreases to 2 ultrafast bars when only using the kinematic P.A. to derive the pattern speed. This dependence on P.A. is well known, resulting from the fact that the TW method requires flux weighted spectroscopy *exactly* along slits parallel to the major axis, otherwise the observed velocities are not representative of the full flux (Debattista 2003). In fact, errors

of $\sim$5° in P.A. can lead to errors in the bar pattern speed of $\sim$100% (Debattista & Williams 2004).

Due to the uncertainty with ultrafast bars, we feel more confident in reporting the relative bar pattern speeds associated with the first phase crossing after the bar length, $\mathcal{R}_2$ in Table 4.3 and $\mathcal{R}$ in Table 4.4. Based on this, we find the majority of our HSB sample to be hosts to fast bars (i.e. $\mathcal{R}$<1.4). However, we do note a relatively large number of slow bars, roughly 25% of our sample. While bars have been generally found to be fast in the literature (Pérez et al. 2012; Aguerri et al. 2015), there has been an increasing number of slow bars found (see Font et al. 2017; Guo et al. 2019). Although it bears noting the extremely large uncertainties in Guo et al. (2019) make this issue less clear than it appears.

4.4.1.4 Comparison with LSBs

Our final bar properties for our HSB subsample are shown in Table 4.4: bar lengths (taken as $R_{\rm az}$) in arcsec (col. 2) and kpc (col. 3), corotation radius in arcsec (col. 4) and kpc (col. 5), relative bar pattern speed (col. 6), and lower limits on bar strength (col. 7).

As a reminder to the reader, we have a sample of 26 barred HSBs and a sample of 15 barred LSBs. We find a mean bar length of $\sim 4.8 \pm 2.5$ kpc for our HSB sample, consistent with large scale surveys of barred galaxies (e.g. Erwin 2005; Marinova & Jogee 2007). This is strongly contrasted with a mean bar length of $\sim 2.3 \pm 1.2$ kpc for our LSBs. Likewise, we find a larger mean lower limit on bar strength for our HSB sample than for our LSBs, $\sim 0.5 \pm 0.2$ vs. $\sim 0.3 \pm 0.1$ respectively. As the size of galaxy disks is related to the morphology of a galaxy, it is worthwhile to examine the bar length normalized to the disk scale length. The disk scale lengths (h) for the HSBs are measured from derived surface brightness profiles, and from Chapter 3 for the LSBs.

In Fig. 4.13 we show histograms of bar length normalized to the disk scale length (left panel) and bar strength (right panel) for the LSBs from Chapter 3 (in blue) and the HSBs in this chapter (in red). The normalized bar length allows us to better compare the bar sizes

Table 4.3: Corotation radii for our HSB sample within the bar (R_{CR_1}) and outside the bar (R_{CR_2}) in arcsec. Relative bar pattern speeds associated with these corotation radii are also listed, assuming the bar lengths in Table 4.4. We do not find an inner corotation radii for NGC 337 or NGC 701. Columns 4 and 5 are repeated from Table 4.4 for easy comparison.

Galaxy	R_{CR_1} (arcsec)	$\mathcal{R}_1$	R_{CR_2} (arcsec)	$\mathcal{R}_2$
NGC 36	13.60±0.40	0.76±0.08	19.80±0.40	1.10±0.12
NGC 151	17.80±0.40	0.57±0.06	31.80±0.40	1.02±0.10
NGC 337	...	...	42.20±0.40	1.42±0.15
NGC 701	...	...	15.00±0.40	1.43±0.16
NGC 1022	9.20±0.40	0.43±0.07	28.60±0.40	1.33±0.20
NGC 1645	12.60±0.40	0.58±0.06	22.00±0.40	1.01±0.11
NGC 3300	18.60±0.40	0.91±0.09	22.80±0.40	1.12±0.12
NGC 4691	33.60±0.40	0.91±0.09	39.60±0.40	1.07±0.11
NGC 4699	12.80±0.40	0.87±0.12	20.40±0.40	1.39±0.18
NGC 5068	14.80±0.40	0.63±0.08	40.80±0.40	1.75±0.20
NGC 5205	9.20±0.40	0.60±0.08	16.20±0.40	1.06±0.13
NGC 5334	17.20±0.40	0.97±0.10	20.20±0.40	1.13±0.12
NGC 5339	23.40±0.40	0.88±0.09	30.60±0.40	1.15±0.12
NGC 5378	18.60±0.40	0.81±0.08	25.80±0.40	1.12±0.11
NGC 5406	10.40±0.40	0.52±0.06	24.40±0.40	1.22±0.14
NGC 5885	5.60±0.40	0.61±0.07	17.40±0.40	1.91±0.46
NGC 5947	6.60±0.40	0.68±0.07	26.60±0.40	2.74±0.30
NGC 6497	20.60±0.40	0.97±0.11	27.80±0.40	1.31±0.15
NGC 6941	11.20±0.40	0.86±0.10	18.40±0.40	1.41±0.17
NGC 6945	7.60±0.40	0.71±0.08	12.80±0.40	1.20±0.13
NGC 7321	9.40±0.40	0.75±0.09	12.00±0.40	1.22±0.14
NGC 7563	26.60±0.40	0.97±0.10	28.20±0.40	1.03±0.10
NGC 7591	6.20±0.40	0.42±0.05	17.40±0.40	1.17±0.12
PGC 3853	11.80±0.40	0.53±0.09	33.80±0.40	1.51±0.26
UGC 3253	7.40±0.40	0.39±0.05	31.80±0.40	1.66±0.20
UGC 12185	8.80±0.40	0.69±0.09	22.00±0.40	1.74±0.21

Table 4.4: Bar properties for our HSB comparison sample. Bar lengths (taken as $R_{\rm az}$) are in arcsec ($R_{\rm bar}$) and kpc ($R'_{\rm bar}$), corotation radii are in arcsec ($R_{\rm CR}$) and kpc ($R'_{\rm CR}$), relative bar pattern speeds ($\mathcal{R}$) and lower limits on bar strengths ($S_{\rm b}$) are unitless. Lengths in kpc assume the distances in Table 4.1.

Galaxy	$R_{\rm bar}$ (arcsec)	$R'_{\rm bar}$ (kpc)	$R_{\rm CR}$ (arcsec)	$R'_{\rm CR}$ (kpc)	$\mathcal{R}$	$S_{\rm b}$
NGC 36	18.01±0.60	7.30±0.57	19.80±0.40	8.03±0.59	1.10±0.12	0.50
NGC 151	31.08±0.40	7.59±0.54	31.80±0.40	7.76±0.55	1.02±0.10	0.62
NGC 337	29.70±0.79	2.82±0.22	42.20±0.40	4.00±0.29	1.42±0.15	0.51
NGC 701	10.50±0.40	1.17±0.09	15.00±0.40	1.67±0.13	1.43±0.16	0.42
NGC 1022	21.38±2.38	1.88±0.25	28.60±0.40	2.52±0.18	1.34±0.20	0.36
NGC 1645	21.78±0.79	7.57±0.60	22.00±0.40	7.65±0.55	1.01±0.11	0.71
NGC 3300	20.39±0.40	4.70±0.37	22.80±0.40	5.58±0.41	1.12±0.12	0.51
NGC 4691	37.03±0.60	3.84±0.28	39.60±0.40	4.10±0.30	1.07±0.11	1.20
NGC 4699	14.65±1.19	1.82±0.20	18.80±0.40	2.53±0.19	1.39±0.18	0.26
NGC 5068	23.36±1.19	1.63±0.15	40.80±0.40	2.85±0.21	1.75±0.20	0.28
NGC 5205	15.25±0.99	2.04±0.19	16.20±0.40	2.16±0.16	1.06±0.13	0.38
NGC 5334	17.80±0.40	2.13±0.16	20.20±0.40	2.41±0.18	1.13±0.12	0.24
NGC 5339	26.54±0.40	5.73±0.41	30.60±0.40	6.61±0.47	1.15±0.12	0.46
NGC 5378	22.96±0.40	5.31±0.39	25.80±0.40	5.97±0.43	1.12±0.11	0.49
NGC 5406	20.00±0.99	7.70±0.66	24.40±0.40	9.40±0.68	1.22±0.14	0.56
NGC 5885	9.11±1.98	1.42±0.33	17.40±0.40	2.72±0.20	1.91±0.46	0.18
NGC 5947	9.70±0.40	4.15±0.34	26.60±0.40	11.37±0.82	2.74±0.30	0.51
NGC 6497	21.19±0.99	9.23±0.78	27.80±0.40	12.11±0.87	1.31±0.15	0.48
NGC 6941	13.07±0.79	5.55±0.51	18.40±0.40	7.82±0.57	1.41±0.17	0.34
NGC 6945	10.69±0.40	2.69±0.21	12.80±0.40	3.22±0.25	1.20±0.13	0.29
NGC 7321	16.04±0.99	7.79±0.73	19.60±0.40	9.52±0.69	1.22±0.15	0.27
NGC 7563	27.52±0.40	7.49±0.54	28.20±0.40	7.67±0.55	1.03±0.10	0.76
NGC 7591	14.85±0.40	4.87±0.37	17.40±0.40	5.71±0.42	1.17±0.12	0.60
PGC 3853	22.37±2.97	1.24±0.54	33.80±0.40	1.88±0.14	1.51±0.26	0.36
UGC 3253	19.20±1.39	5.61±0.19	31.80±0.40	9.29±0.66	1.66±0.20	0.32
UGC 12185	12.67±0.79	5.72±0.56	22.00±0.40	9.93±0.72	1.74±0.21	0.51

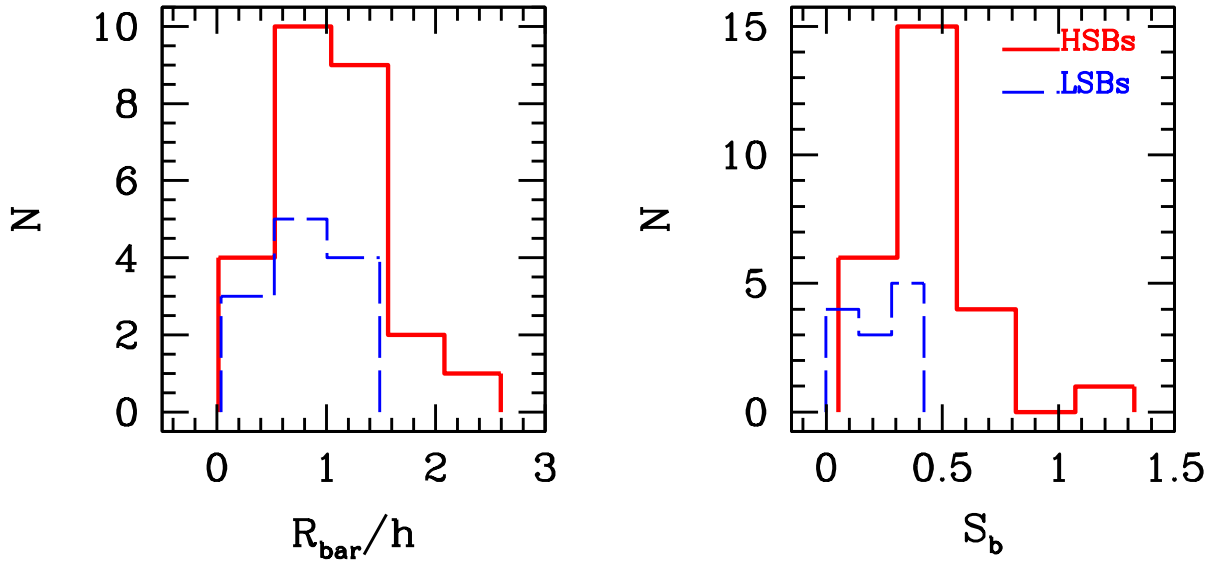

Figure 4.13: Comparison of bar properties between LSBs (dashed blue line) and HSBs (solid red line). *Left*: Normalized bar length ($R_{\rm bar}/h$); *Right*: Bar strength.

between HSBs and LSBs as we can now see the bar length compared to the size of the galaxy disk (see Erwin 2005). When using this metric, we can see that bars in HSBs and LSBs are similar in length compared to the size of the galaxy disk, with HSB bars having a mean normalized length of 1.06 and LSB bars having a mean normalized length of 0.81. In fact, there is a 14% probability that the null-hypothesis (that both populations are the same) is not rejected when performing a Kolmogorov-Smirnov (KS) test. However, the bar strengths for the two galaxy populations are quite distinct, with a KS test rejecting the null-hypothesis at 99.6%.

In Fig. 4.14 we show the relative bar pattern speed ($\mathcal{R}$) vs. bar strength ($S_{\rm b}$) for the LSBs from Chapter 3 (blue triangles) and the HSBs in this chapter (red circles). As in Chapter 3, we do not find any relation between bar strength and relative bar pattern speed. The HSB with the very strong bar is NGC 4691.

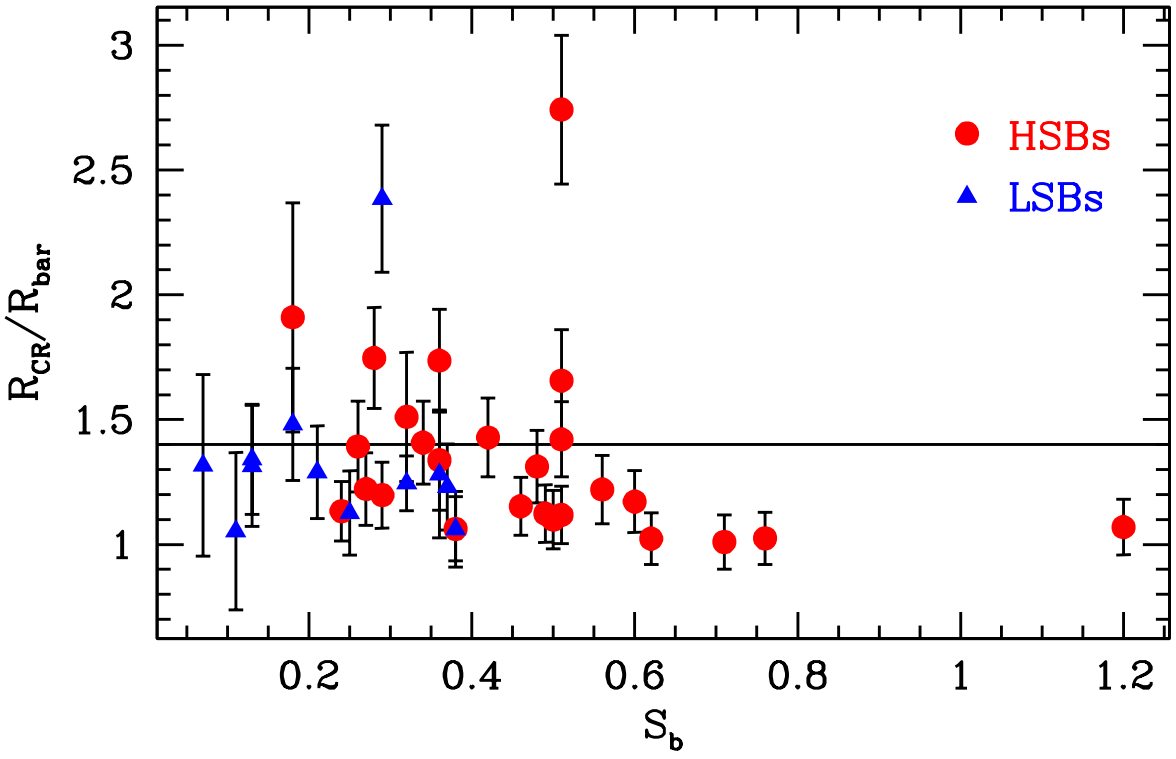

Figure 4.14: Relative bar pattern speed ($\mathcal{R}= R_{\rm CR}/R_{\rm bar}$) vs. bar strength ($S_{\rm b}$). Blue triangles show the LSBs from Chapter 3, and red circles show the HSBs from this chapter. The horizontal line at $\mathcal{R}= 1.4$ is the separator of fast and slow bars.

In Fig. 4.15 we show bar length in kpc and normalized bar length as functions of bar strength for both HSBs and LSBs. Consistent with previous works (e.g. Díaz-García et al. 2016; Guo et al. 2019), we find a clear trend between the two: bar strength increases with increasing bar length. For bar length in kpc we find $R_{\rm bar}$ (kpc) $= 5.32S_b + 1.71$ with a scatter of 1.98 and Spearman coefficient of 0.54. For normalized bar length, we find $(R_{\rm bar}/h) = 1.12S_b + 0.53$ with a scatter of 0.38 and Spearman coefficient of 0.64.

In Fig. 4.16 we show normalized bar length, bar strength, and relative bar pattern speed as functions of Hubble type (T). We find that there is a clear dependence on all three parameters with T. In the top two panels, bar length and strength clearly decrease as one moves to later T. Erwin (2005) found a similar result, with early type galaxies having bars that extend up to 10 kpc, and later type galaxies having bars that only extend up to 3.5 kpc.

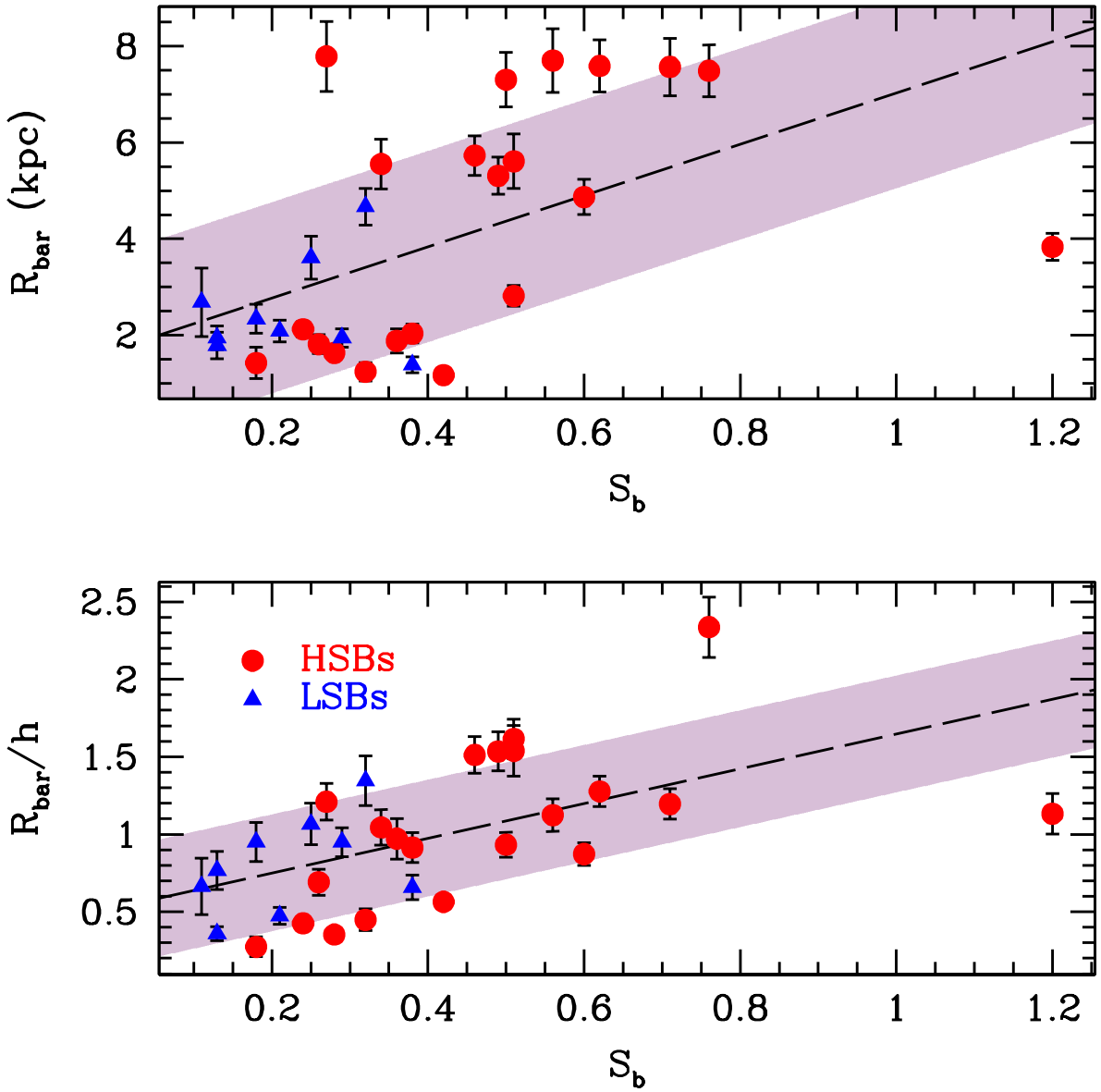

Figure 4.15: Bar length as a function of bar strength. *Top*: bar length in kpc; *Bottom*: normalized bar length. Red circles are HSBs and blue triangles are LSBs. The dashed lines and shaded regions indicate the fits described in the text.

We also find that the bar length compared to the disk decreases as one moves to later T. We find the inverse relation in the bottom panel, with relative bar pattern speed weakly increasing as one moves to later T, similar to the findings in Rautiainen et al. (2005) and Font et al. (2019). The two *very* slow bars (i.e. $\mathcal{R} > 2$) are the HSB NGC 5947 and LSB F563-V2. Such slow bars have been reported in the literature (see the HSBs in Font et al. 2017; Guo et al. 2019). We note that this is an expected result for F563-V2, as it is an LSB, but that it is unexpected to find such a slow bar in an HSB.

4.4.2 Gas and Stellar Masses

Our final HI masses, stellar masses, and gas fractions for our HSB subsample are shown in Table 4.5: HI flux (col. 2), HI mass (col. 3), V-band luminosity (col. 4), $B-V$ (col. 5), V-band stellar mass-to-light ratio Υ_*^V (col. 6), stellar mass (col. 7), and gas fraction (col. 8). We find a mean HI and stellar mass of $\sim 6.2 \times 10^9 M_\odot$ and $\sim 2.5 \times 10^{10} M_\odot$ respectively. We find our HSBs to be stellar dominated (i.e. most have $f_{gas} < 0.5$).

4.4.2.1 Comparison with LSBs

In Fig. 4.17 we show $\log(M_{\rm gas}/M_*)$ vs. $\log M_*$ for our LSBs (blue triangles) and HSB comparison sample (red circles). From this, we can see that both barred LSBs and HSBs fall along the same relation, with the two populations occupying different regions and forming a continuum between them. The two LSBs with large errors are F602-1 and PGC 70352, who have large uncertainties on their r-band magnitudes. The solid line is the fit $\log(M_{\rm gas}/M_*) = -0.80 \log(M_*) + 7.73$, with the shaded region showing the scatter of 0.43. We find a Spearman coefficient of -0.72. This is similar to the relation between $\log(M_{\rm HI}/M_*)$ and $\log(M_*)$ found in Chapter 3 (see Sec. 3.6), albeit with a larger scatter (0.43 vs. 0.22).

In Fig. 4.18 we show histograms of stellar, gas, and total baryonic mass (i.e. $M_* + M_{gas}$) for the LSBs and HSBs. These two galaxy populations clearly occupy different mass regimes.

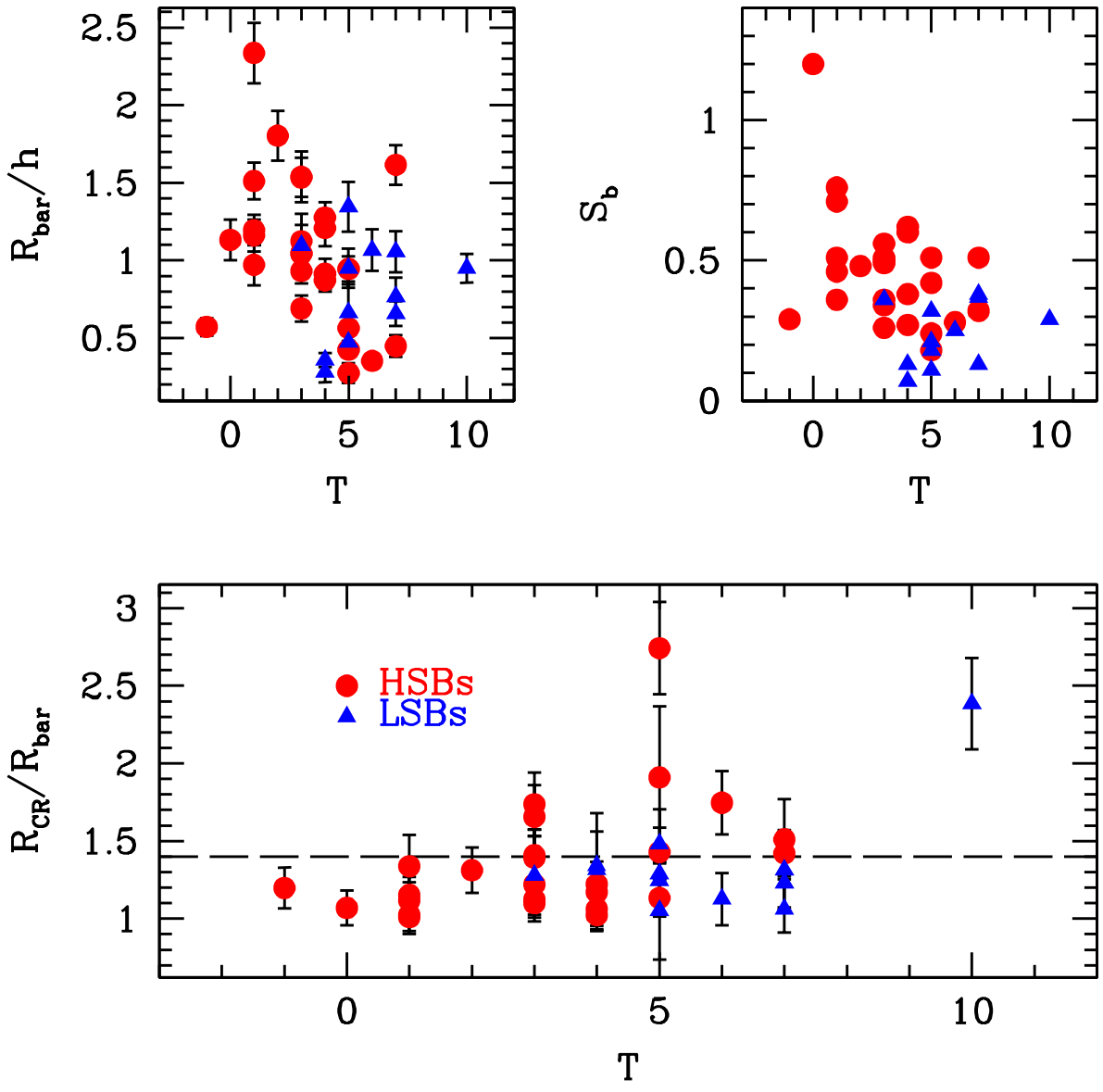

Figure 4.16: Bar properties as a function of Hubble type (T) for both the HSB sample (red circles) and LSB sample (blue triangles). *Top Left*: normalized bar length; *Top Right*: lower limit on bar strength; *Bottom*: relative bar pattern speed. The dashed line in the bottom left panel separates slow and fast bars. The two *very* slow bars (i.e. $\mathcal{R} > 2$) are the HSB NGC 5947 and LSB F563-V2.

Table 4.5: Gas and stellar masses for our HSB subsample. HI flux (col. 2, $F_{\rm HI}$), HI mass (col. 3, $\log M_{\rm HI}$), V-band luminosity (col. 4, $\log L_V$), $B-V$ color (col. 5), V-band mass-to-light ratio (col. 6, Υ_*^V), stellar mass (col. 7, $\log M_*$), and gas fraction (col. 8, $f_{gas} = M_{gas}/(M_{gas}+M_*)$). V-band luminosities are calculated using the distances in Table 4.1.

Galaxy	$F_{\rm HI}$ (Jy km/s)	$\log M_{\rm HI}$ ($M_\odot$)	$\log L_V$ ($L_\odot$)	$(B-V)$	Υ_*^V	$\log M_*$ ($M_\odot$)	f_{gas}
NGC 36	8.09	10.13	10.47	0.63	1.64	10.69	0.28
NGC 151	19.05	10.06	10.45	0.75	2.40	10.83	0.19
NGC 337	38.73	9.54	9.85	0.43	0.70	9.69	0.50
NGC 701	18.54	9.36	9.49	0.85	3.13	9.99	0.25
NGC 1022	3.87	8.48	9.59	0.78	2.60	10.00	0.04
NGC 1645	9.20	10.05	10.22	0.75	2.40	10.60	0.28
NGC 4691	4.29	8.66	9.97	0.70	2.04	10.28	0.03
NGC 4699	26.79	9.62	10.55	0.68	1.92	10.83	0.08
NGC 5068	103.75	9.71	10.13	0.52	1.04	10.15	0.34
NGC 5205	10.38	9.27	9.46	0.60	1.44	9.61	0.39
NGC 5334	3.60	8.71	9.92	0.38	0.53	9.65	0.14
NGC 5339	5.86	9.44	10.17	0.54	1.16	10.24	0.18
NGC 5378	3.56	9.28	10.04	0.72	2.22	10.39	0.10
NGC 5406	4.88	9.86	10.53	0.77	2.53	10.94	0.11
NGC 5885	31.33	9.89	10.07	0.46	0.82	9.98	0.53
NGC 6941	7.31	10.12	10.38	0.76	2.47	10.77	0.24
NGC 7321	5.60	10.12	10.62	0.50	0.96	10.60	0.32
NGC 7563	1.74	9.11	10.16	0.77	2.53	10.56	0.05
NGC 7591	20.32	10.34	10.21	0.80	2.79	10.66	0.40
PGC 3853	46.99	9.16	9.12	0.57	1.30	9.24	0.54
UGC 3253	5.65	9.69	9.99	0.71	2.16	10.33	0.24

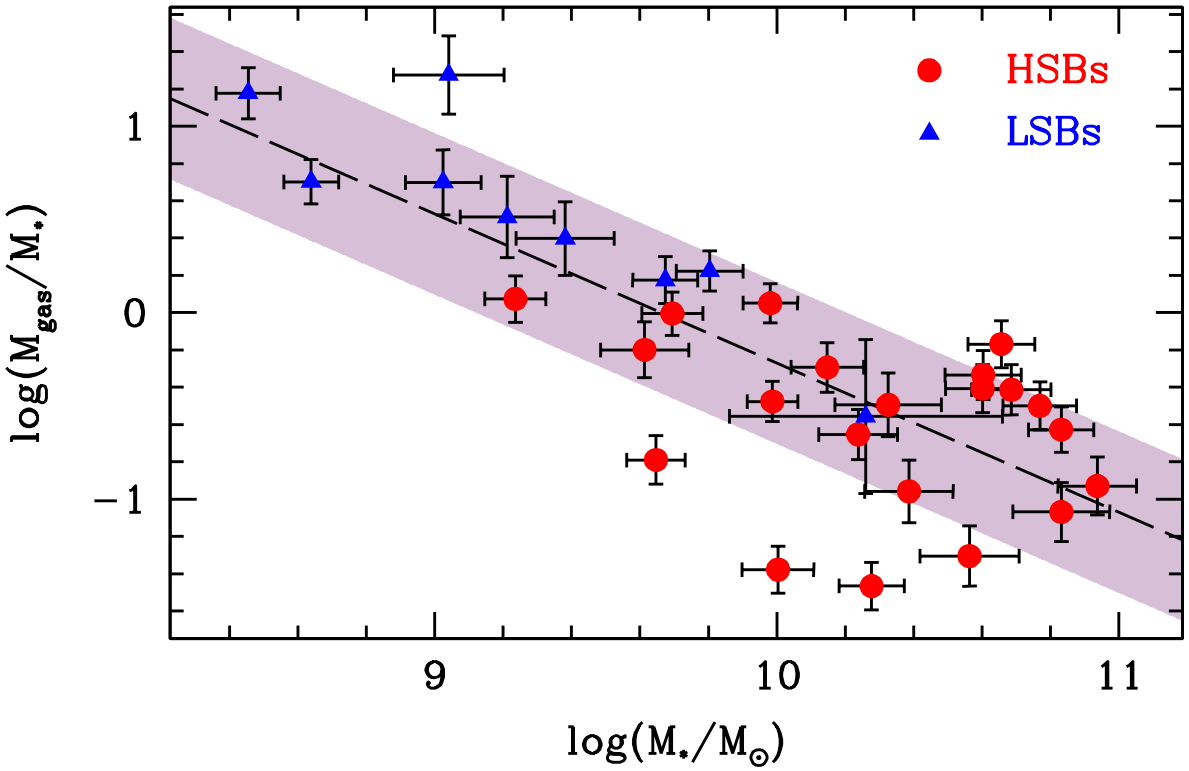

Figure 4.17: $\log(M_{\rm gas}/M_*)$ vs $\log(M_*)$ for our LSBs (blue) and HSB (red) sub sample. The solid line is the fit $\log(M_{\rm gas}/M_*) = -0.80\log(M_*) + 7.73$, with the shaded region showing the scatter of 0.43.

In the top left panel, we can see that barred LSBs extend across 3 decades in stellar mass, down to $\sim \times 10^8$ $M_\odot$, while barred HSBs occupy the higher 2 decades of mass, up to nearly 10^{11} $M_\odot$. In the top right panel, we see that barred LSBs and HSBs occupy the same gas mass range, with both distributions peaking around $\sim 0.5 \times 10^9$ $M_\odot$. When examining the total baryonic masses (bottom left panel in Fig. 4.18), we can see that the LSB total baryonic mass remains roughly unaffected by the stellar mass, while the HSB total baryonic mass is mostly determined by the stellar mass.

In Figures 4.19, 4.20, and 4.21 we explore if there is a dependence of the bar properties on stellar (M_*), gas ($M_{\rm gas}$), and total baryonic mass ($M_{\rm tot}$) respectively. In each of these figures, the top left panel shows normalized bar length (i.e. $R_{\rm bar}/h$), the top right panel shows bar strength, and the bottom panel shows relative bar pattern speed. The dashed lines in the top

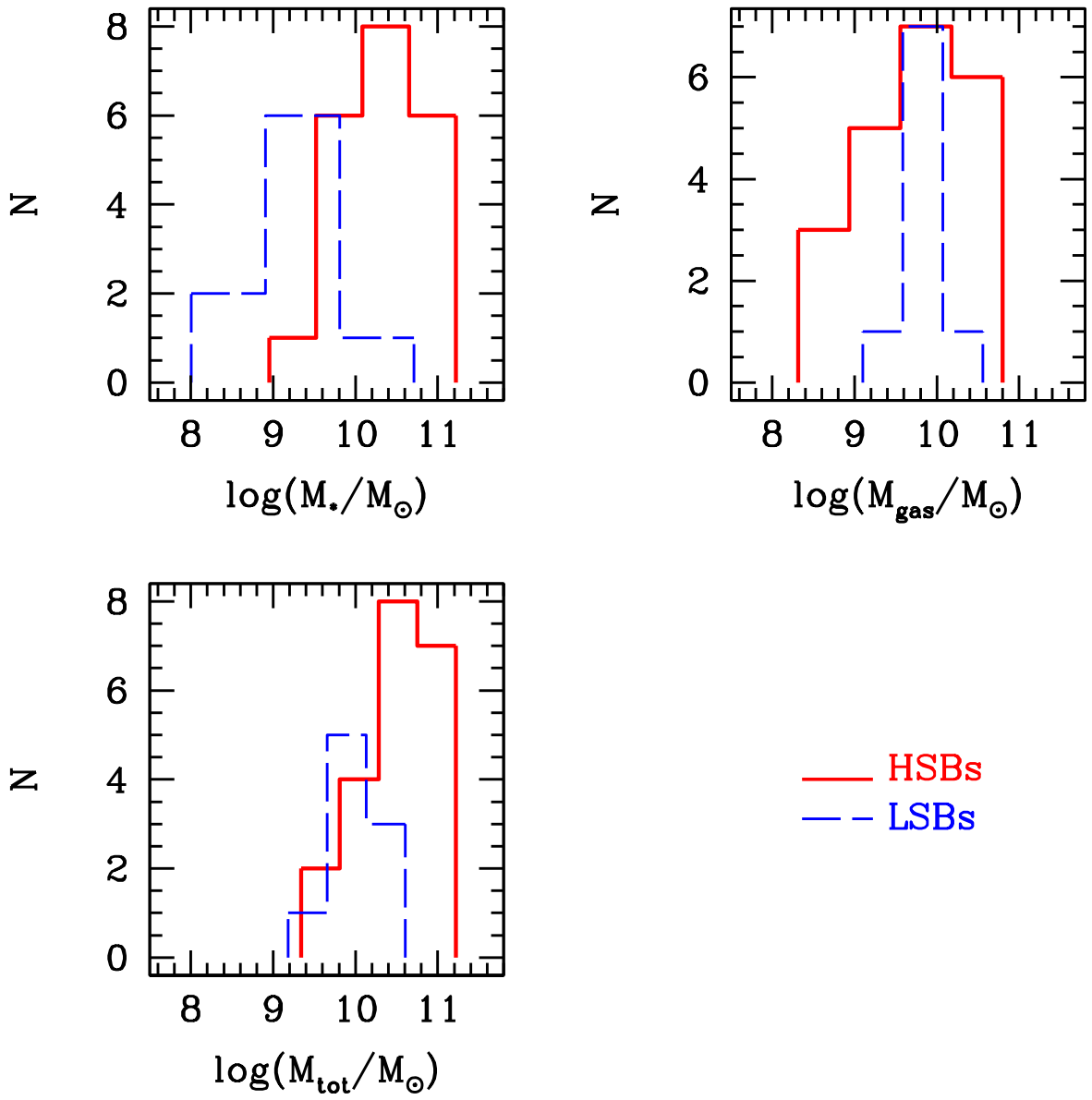

Figure 4.18: Histograms of masses for LSBs (blue dashed line) and HSBs (red solid line). *Top Left*: stellar mass; *Top Right*: gas mass; *Bottom Left*: total baryonic mass (i.e. $M_* + M_{gas}$).

panels of each of these figures indicate a fit to the data, with the shaded regions indicating the scatter. The HSB at $(R_{\rm bar}/h) \sim 2.3$ in all three figures is NGC 7563 and is excluded from the fits. The HSB at $S_b \sim 1.2$ is NGC 4691 and is excluded from the fits as well. The *very* slow bar is the LSB F563-V2.

For normalized bar length, we find the following best fits, scatters (σ), and Spearman coefficients (ρ):

$$\begin{aligned}
(R_{\rm bar}/h) &= 0.27 \log (M_*/M_\odot) - 1.68,\ \sigma = 0.42,\ \rho = 0.43 \\
(R_{\rm bar}/h) &= -0.02 \log (M_{\rm gas}/M_\odot) + 1.21,\ \sigma = 0.45,\ \rho = -0.02 \\
(R_{\rm bar}/h) &= 0.37 \log (M_{\rm tot}/M_\odot) - 2.83,\ \sigma = 0.42,\ \rho = 0.39
\end{aligned} \tag{4.21}$$

For bar strength, we find:

$$\begin{aligned}
S_b &= 0.16 \log (M_*/M_\odot) - 1.16,\ \sigma = 0.20,\ \rho = 0.55 \\
S_b &= -0.10 \log (M_{\rm gas}/M_\odot) + 1.36,\ \sigma = 0.22,\ \rho = -0.10 \\
S_b &= 0.18 \log (M_{\rm tot}/M_\odot) - 1.45,\ \sigma = 0.21,\ \rho = 0.41
\end{aligned} \tag{4.22}$$

We find both bar length and bar strength to show a clear relation with stellar and total mass, consistent with Díaz-García et al. (2016) and Font et al. (2017). This is not too surprising considering bars are stellar features. Supporting this, we find that both bar length and strength are relatively independent of gas mass, having roughly flat slopes.

We do not find a relation for relative bar pattern speed with mass (bottom panels), consistent with Font et al. (2017). Instead, we find that there appear to be fast and slow rotators (the horizontal dashed line show the deliminator of $\mathcal{R} = 1.4$) at all masses, with the majority of all masses being fast.

In all three plots of mass vs. bar length (top left panels of Figs. 4.19, 4.20, 4.21), we find a clear transition from LSBs (blue triangles) to HSBs (red circles). While there is overlap between the two populations, with some HSBs having quite short bar lengths, LSBs clearly

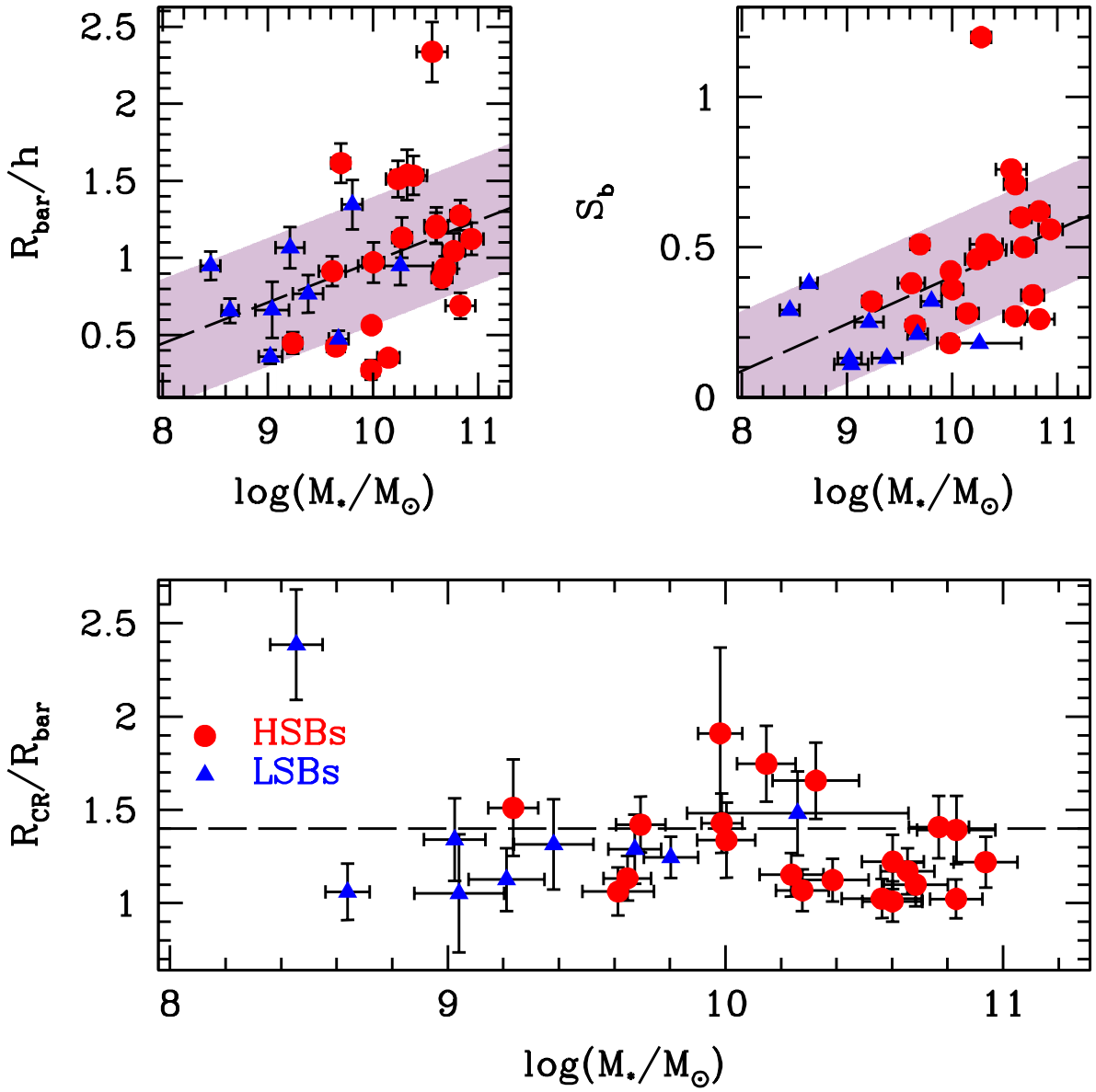

Figure 4.19: Stellar mass vs. bar properties for the full sample. HSBs are red circles, and LSBs are blue triangles. *Top Left*: bar length in kpc; *Top Right*: bar strength; *Bottom*: relative bar pattern speed. The dashed lines in the top panels indicate the fits $(R_{\rm bar}/h) = 0.27\log(M_*/M_\odot) - 1.68$ and $S_b = 0.16\log(M_*/M_\odot) - 1.16$ respectively. The shaded regions indicate the scatter about each fit: 0.42 and 0.20 respectively. The HSB at $(R_{\rm bar}/h) \sim 2.3$ is NGC 7563 and is excluded from the fit. The HSB at $S_b \sim 1.2$ is NGC 4691 and is excluded from the fit. The horizontal dashed line in the bottom left panel separates fast and slow bars ($\mathcal{R} = 1.4$). The *very* slow bar is the LSB F563-V2.

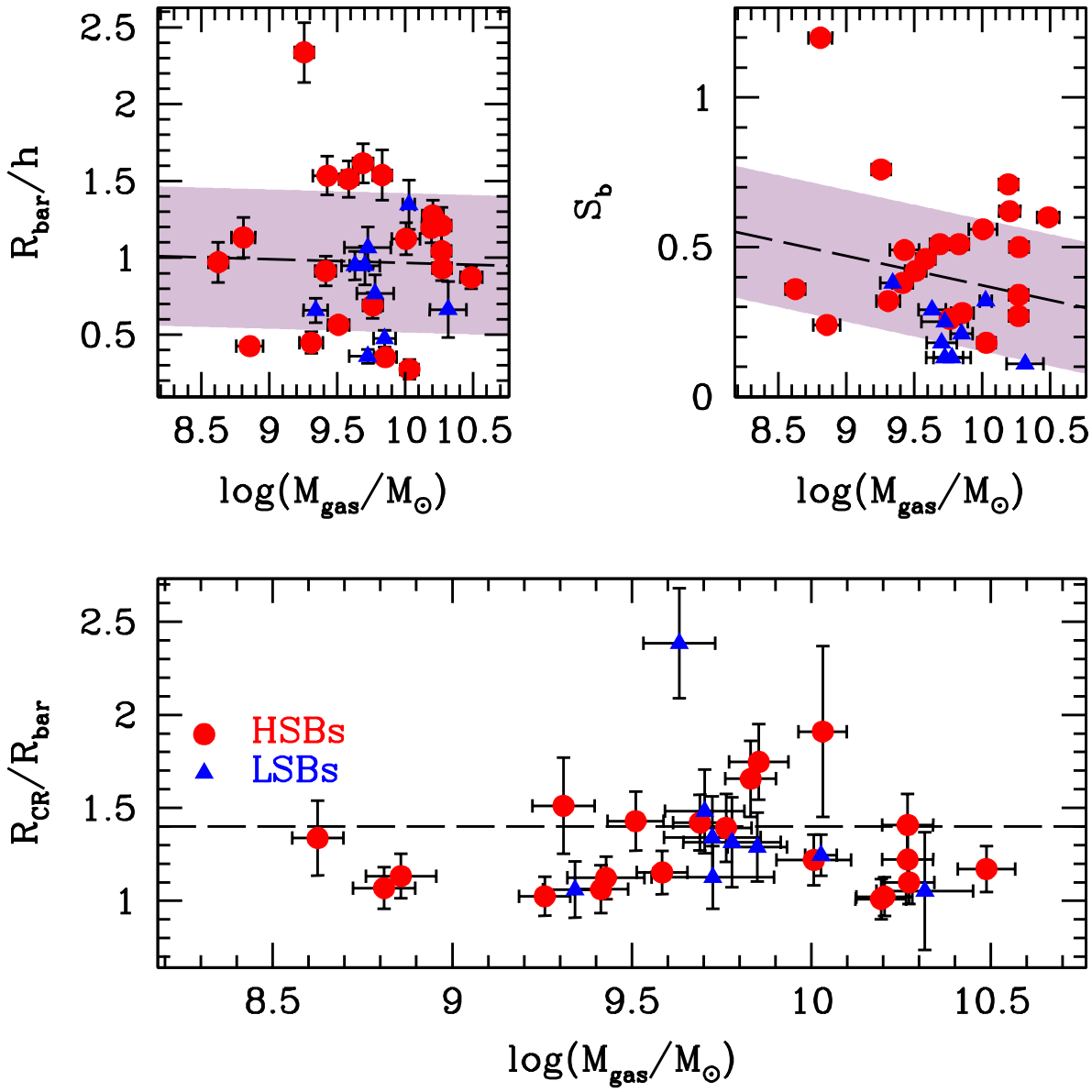

Figure 4.20: Same as Fig. 4.19, but with gas mass. The indicated fits are $(R_{\rm bar}/h) = -0.02\log(M_{\rm gas}/M_\odot) + 1.21$ and $S_b = -0.10\log(M_{\rm gas}/M_\odot) + 1.36$, with scatters of 0.45 and 0.22 respectively. The HSB at $(R_{\rm bar}/h) \sim 2.3$ is NGC 7563 and is excluded from the fit. The HSB at $S_b \sim 1.2$ is NGC 4691 and is excluded from the fit. The *very* slow bar is the LSB F563-V2.

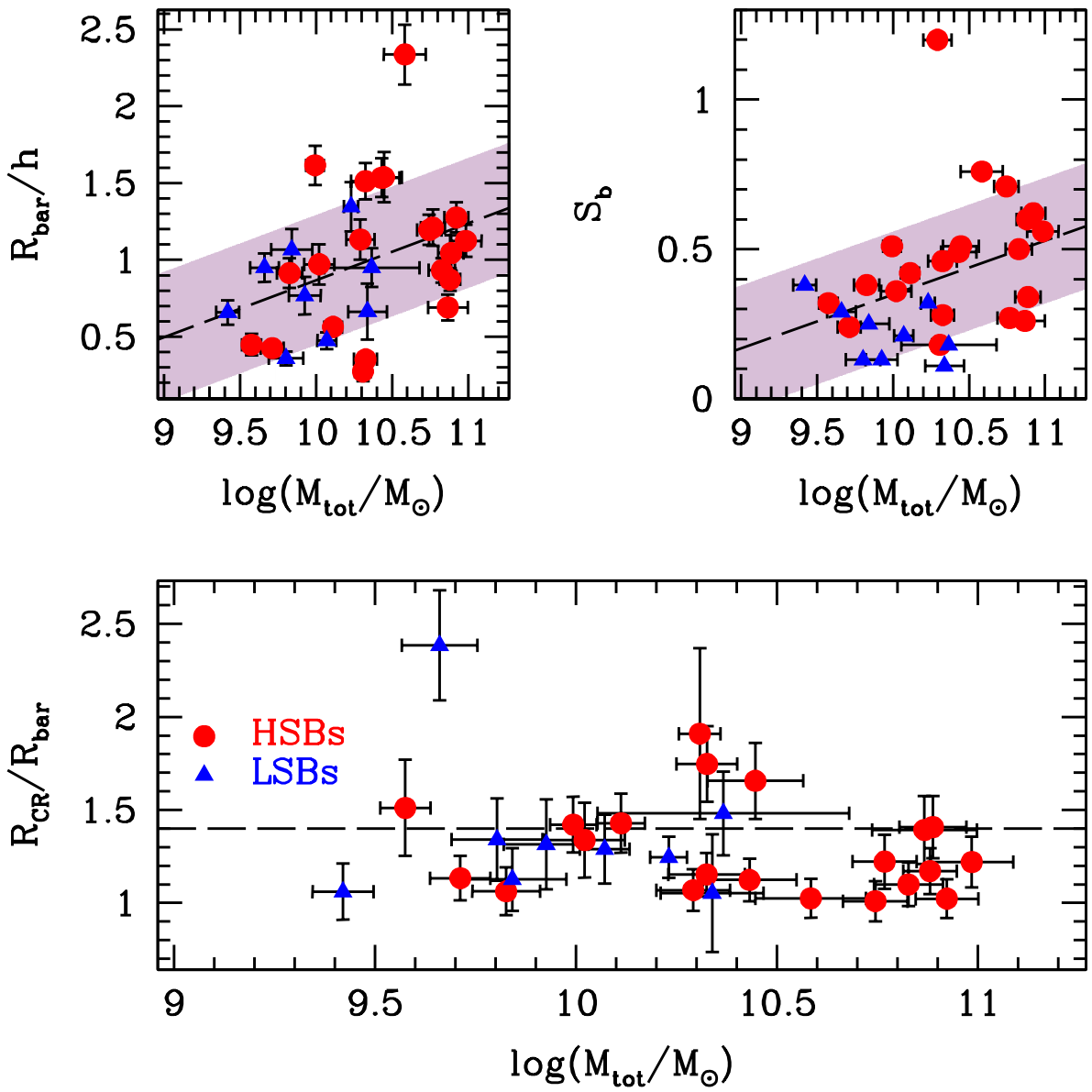

Figure 4.21: Same as Fig. 4.19, but with total baryonic mass (i.e. $M_{gas} + M_*$). The indicated fits are $(R_{\rm bar}/h) = 0.37 \log(M_{\rm tot}/M_\odot) - 2.83$ and $S_b = 0.18 \log(M_{\rm tot}/M_\odot) - 1.45$, with scatters of 0.42 and 0.21 respectively. The HSB at $(R_{\rm bar}/h) \sim 2.75$ is NGC 7563 and is excluded from the fit. The *very* slow bar is the LSB F563-V2.

occupy the lower mass, shorter bar regime. In other words, it is not that HSBs cannot be hosts to short and weak bars, but that it appears that LSBs cannot be hosts to long and strong bars.

We show normalized bar length and bar strength as a function of both $\mu_0(B)$ (left panels) and $\log(M_{\rm gas}/M_*)$ (right panels) in Fig. 4.22. We find clear relations for all four comparisons. For normalized bar length we find the following best fitting relations, scatters (σ), and Spearman coefficients (ρ):

$$\begin{aligned}(R_{\rm bar}/h) &= -0.27\mu_0 + 6.75,\ \sigma = 0.38,\ \rho = -0.62 \\ (R_{\rm bar}/h) &= -0.26\log(M_{\rm gas}/M_*) + 0.91,\ \sigma = 0.42,\ \rho = -0.40\end{aligned} \tag{4.23}$$

and for bar strength we find:

$$\begin{aligned}S_b &= -0.08\mu_0 + 2.09,\ \sigma = 0.21,\ \rho = -0.44 \\ S_b &= -0.19\log(M_{\rm gas}/M_*) + 0.35,\ \sigma = 0.18,\ \rho = -0.52\end{aligned} \tag{4.24}$$

Interestingly, we find very similar slopes between the two different comparisons, suggesting an underlying correlation between μ_0 and $\log(M_{\rm gas}/M_*)$. Supporting this, there is a clear separation between HSBs and LSBs at $\log(M_{\rm HI}/M_*) \sim 0$, suggesting the designation of $\mu_0(B) \sim 22.5$ mag arcsec^{-2} as the low surface brightness regime corresponds to the turn over from stellar to gas domination. We stress that the designation of our LSBs and HSBs was solely based on surface brightness before any analysis had been done.

Finally, we show $\mathcal{R}$ as a function of both $\mu_0(B)$ (top) and $\log(M_{HI}/M_*)$ (bottom) in Fig. 4.23. We find no relation between $\mathcal{R}$ and surface brightness (top panel), with bars in galaxies with $\mu_0(B) \approx 23$ mag arcsec^{-2} rotating just as fast as those in galaxies with $\mu_0(B) \approx 20$ mag arcsec^{-2}. Likewise, we find no relation with $\mathcal{R}$ and $\log(M_{HI}/M_*)$. Perhaps worth noting is an apparent 'jump' in $\mathcal{R}$ at the transition between LSBs and HSBs, although

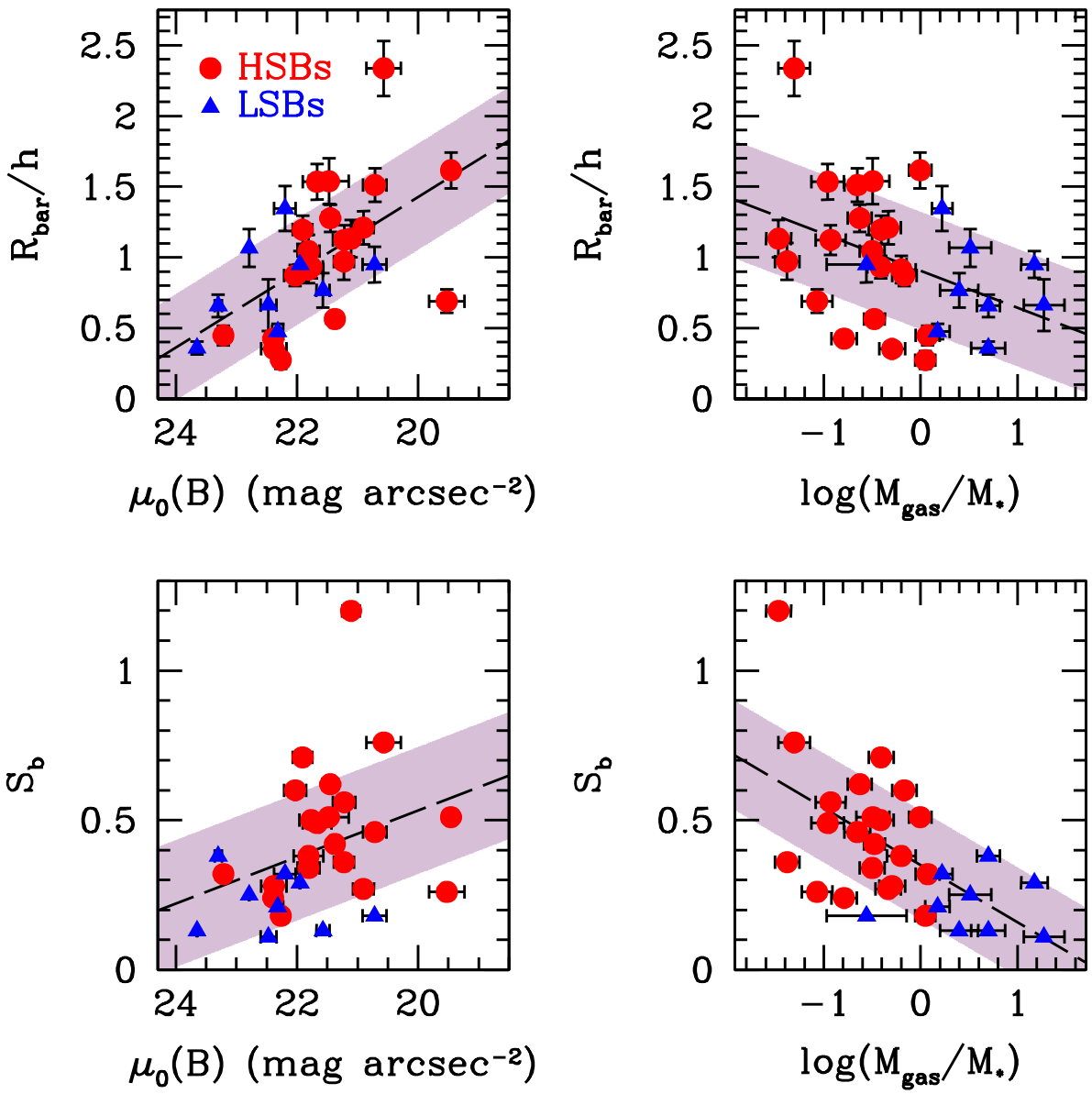

Figure 4.22: Normalized bar length and bar strength as functions of central surface brightness $\mu_0(B)$ and $\log(M_{\rm HI}/M_*)$. LSBs are shown as blue triangles, and HSBs are shown as red circles. The dashed lines and shaded regions in each panel indicate the fits and scatters described in the text. The HSB at $\mathcal{R} \sim 2.3$ is NGC 7563 and is not excluded from the fits.

this is most likely not indicating an underlying process and could be a result of the limited sample size.

4.5 Discussion and Conclusions

We have measured three bar properties for a sample of high surface brightness galaxies (HSBs) to compare with bars in low surface brightness galaxies (LSBs): bar length, strength, and corotation radius. We have explored these properties across various galaxy properties: Hubble type, surface brightness, and mass. We find clear trends across all three of these properties, with a smooth transition between the two galaxy populations. When examining trends with $(M_{\rm gas}/M_*)$, we find that HSBs generally have longer and stronger bars than those in LSBs with a clear suppression of bar length and strength in the latter occurring at $\log(M_{\rm gas}/M_*) \sim 0$. In addition, while bars in HSBs can be short (~ 2 kpc), our results seem to imply that bars in LSBs cannot exceed ~ 5 kpc, with a mean bar length of only $\sim 2.3 \pm 1.2$kpc. Finally, when looking at the normalized bar length $(R_{\rm bar}/h)$, bars in LSBs have bars that are shorter than their scale lenghts, with a mean normalized length of $\sim 0.8 \pm 0.3$. On the other hand, bars in HSBs span a much larger range, with a mean normalized length of $\sim 1.1 \pm 0.5$. Finally, while the two populations have statistically similar normalized bar lengths, we find clear relations between bar length and galaxy properties with a continuum present between the two galaxy populations.

Finding results similar to ours, Cervantes Sodi & Sánchez García (2017) interpreted the trend of bar length with μ_0 as evidence of an underlying trend between μ_0 and halo spin (λ). In other words, the high spin of the dark matter halo that an LSB is embedded in plays a part in regulating the bar length. In addition, the high gas content of barred LSBs we find is consistent with the general picture of gas both prohibiting the formation of and inhibiting the further growth of bars due to the transfer of angular momentum between the gas and bar (Villa-Vargas et al. 2010; Masters et al. 2012; Cervantes Sodi 2017). When examining bar length and strength as functions of $(M_{\rm gas}/M_*)$, we find a clear separation between LSBs and

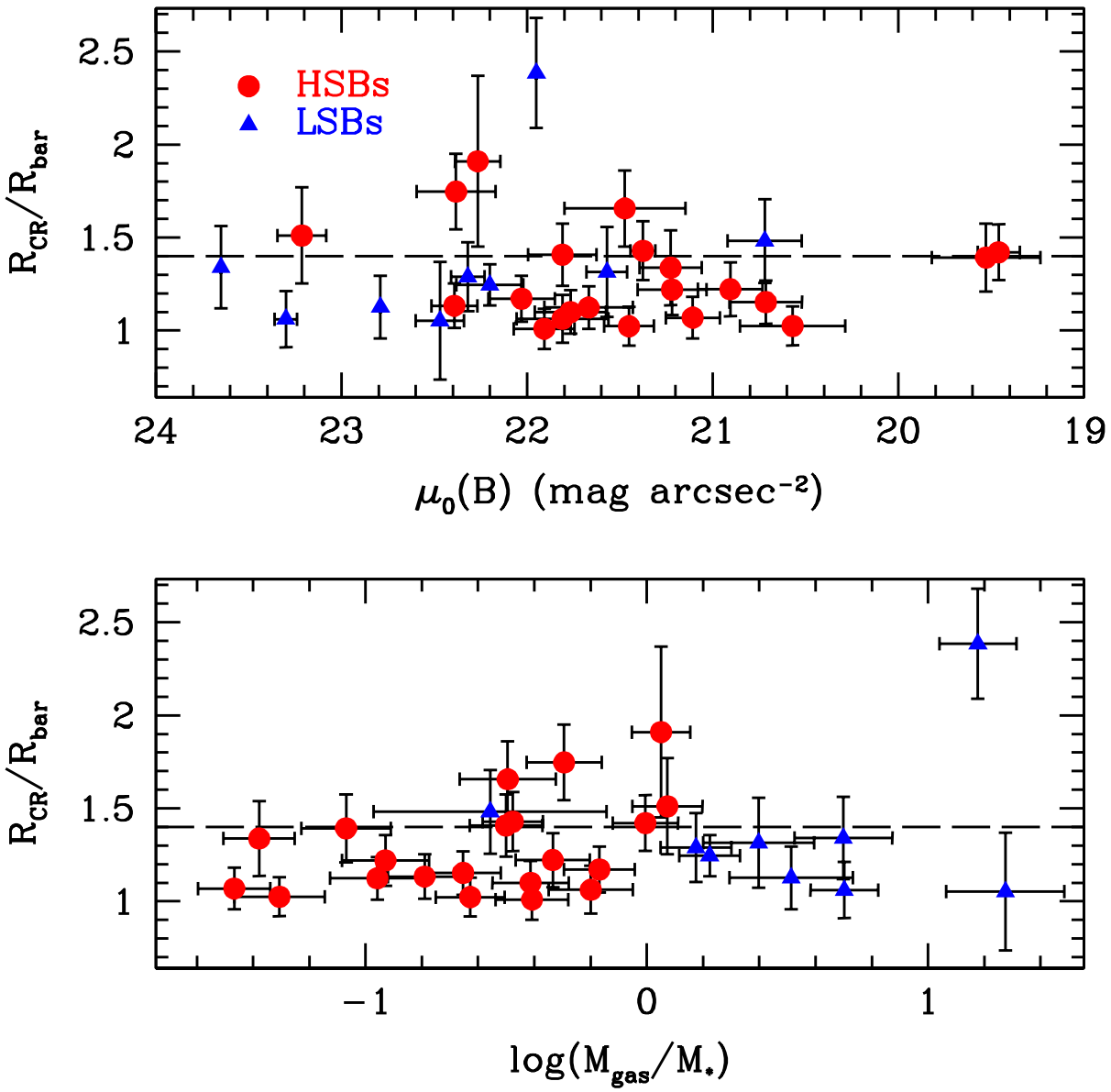

Figure 4.23: Relative bar pattern speed as functions of central surface brightness and $\log(M_{\rm gas}/M_*)$. LSBs are shown as blue triangles, and HSBs are shown as red circles. In both panels the horizontal line at $\mathcal{R} = 1.4$ separates slow and fast rotators.

HSBs about $\log(M_{\rm gas}/M_*) \sim 0$, supporting the idea that these two galaxy populations have a different underlying evolutionary history.

We find that the relative bar pattern speed ($\mathcal{R}$) does not correlate well with any of the galaxy properties, only suggesting a weak trend towards slower values with increasing T. Numerous works have found a similar result, namely Pérez et al. (2012) who found $\mathcal{R} < 1.4$ across redshifts $0 < z < 0.8$, and Aguerri et al. (2015) who found bars to be fast for late type galaxies (SB0 $< T <$ SBbc). Taking both works into account, it seems that bars form fast and remain fast regardless of Hubble type. With our LSBs, we are able to both confirm and extend this conclusion to later Hubble types, as well as show that $\mathcal{R}$ is also independent of surface brightness and gas content. This therefore suggests that there has not been significant bar slowdown due to angular momentum transfer between the bar and dark matter halo, contrary to expectations from numerical simulations. For LSBs, the fact that we find short, weak, and fast bars is strong evidence that these galaxies reside in high spin dark matter halos, consistent with both predictions (e.g. Dalcanton et al. 1997; Jimenez et al. 1998) and observations (e.g. Cervantes-Sodi et al. 2013; Cervantes Sodi & Sánchez García 2017).

Before concluding, it bears note to mention the recent findings of Font et al. (2017) regarding $\mathcal{R}$. Based on measuring $\mathcal{R}$ and Ω_{bar} (the bar pattern speed), it appears as though $\mathcal{R}$ is not as true of a measure of a bar's rotation as previously thought. In fact, aspects of a galaxy's evolutionary history can conspire to make $\mathcal{R} < 1.4$. For instance, there are galaxies in their sample that have bars classified as slow, despite having bar pattern speeds greater than those of bars that are classified as fast. They suggest instead measuring $\Gamma = \Omega_{bar}/\Omega_{disk}$, or the ratio of the bar and disk pattern speeds, to classify bars as fast or slow. By doing so, they conclude that most bars actually have been slowed down due to dark matter halos. While this has tantalizing implications for LSBs, such a measurement is beyond the scope of this chapter and must be left to a future study, as obtaining pattern speed measurements requires spectroscopy.

We list our major conclusions here:

1. **Bars in LSBs are characteristically shorter and weaker than those in HSBs.** This is due to the high gas fractions in LSBs, with values $\log(M_{\rm gas}/M_*) > 0$ clearly suppressing both bar length and strength.

2. **The relative bar pattern speed shows no correlation with galaxy properties.** We find fast rotators across all Hubble types and masses, again consistent with barred LSBs residing in high λ halos. However, based on recent findings regarding $\mathcal{R}$, measurements of Ω_{bar} and Ω_{disk} for barred LSBs are required to determine if bars in LSBs have experienced significant slowdown due to the dark matter halo.

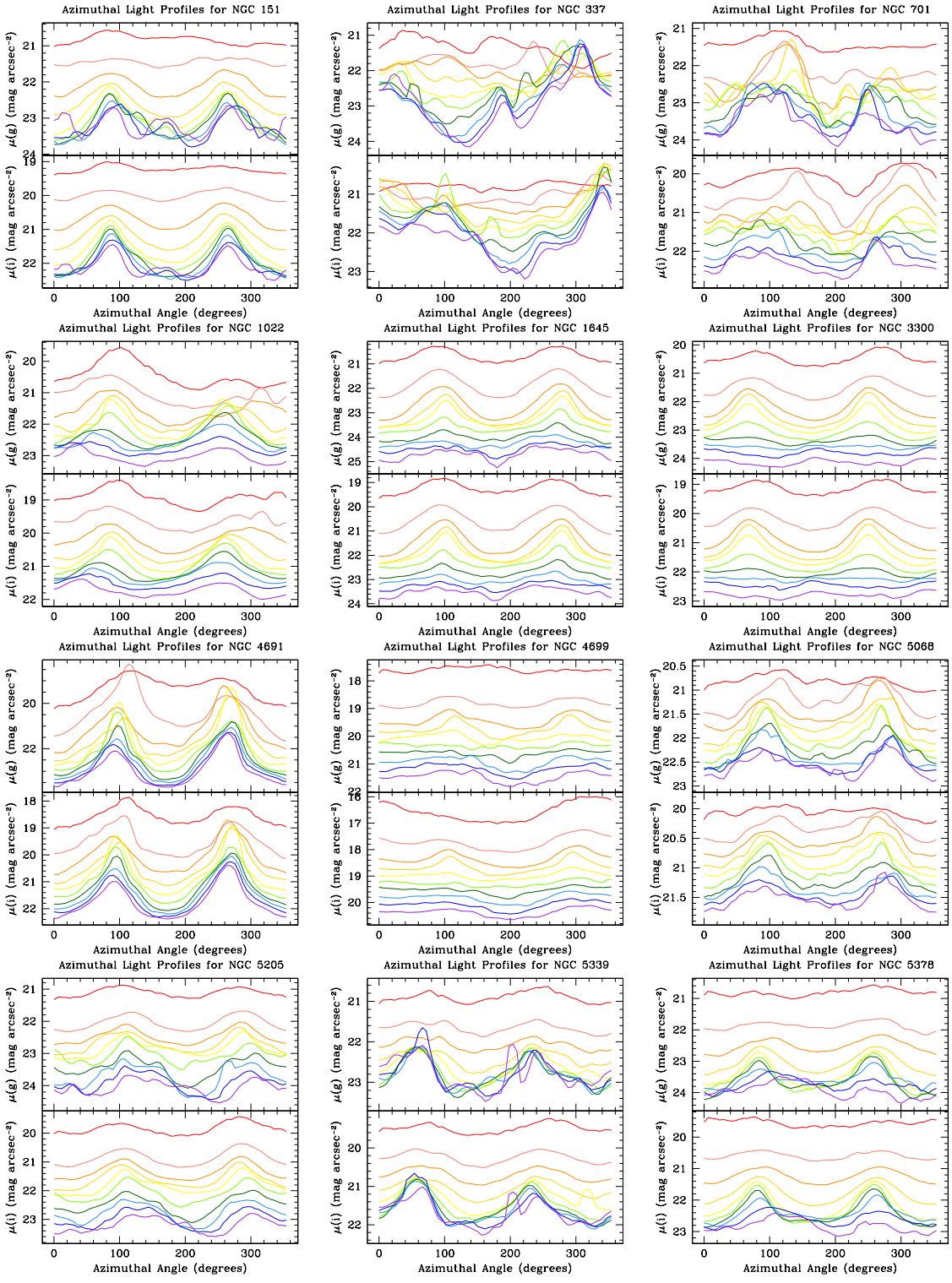

Figure 4.24: Same as Fig. 4.4 for the remainder of the HSB sample.

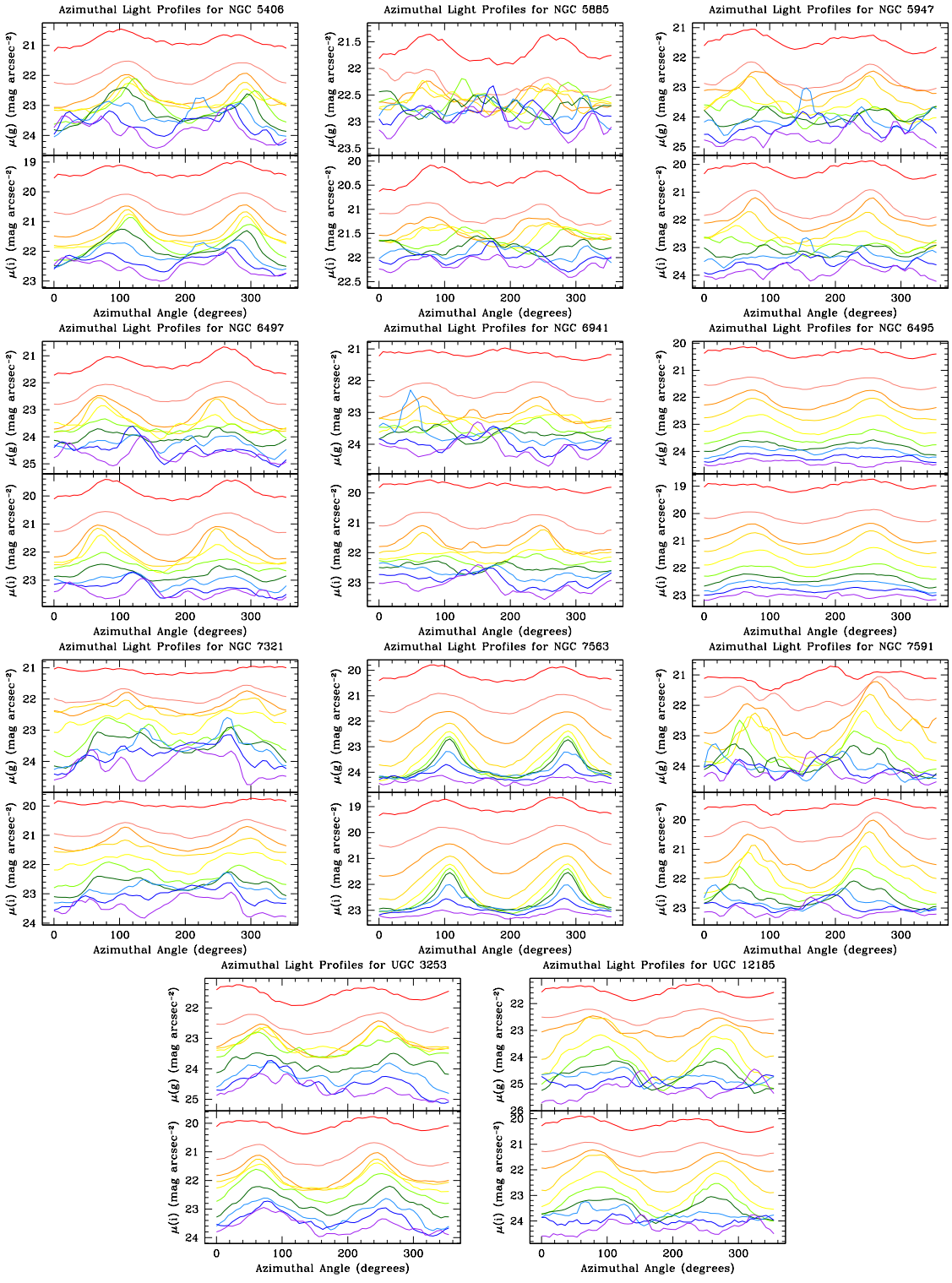

Figure 4.24: *continued*

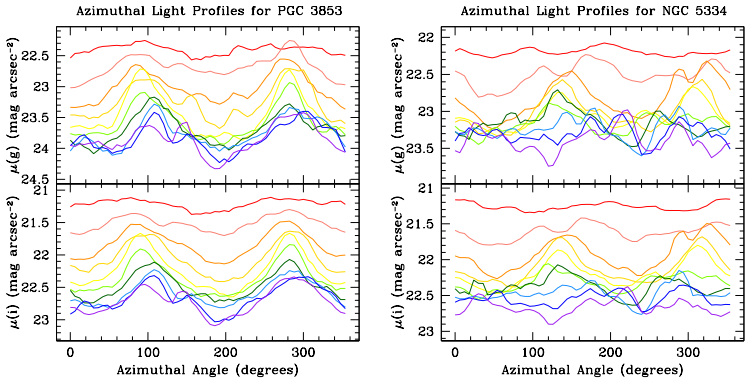

Figure 4.24: *continued*

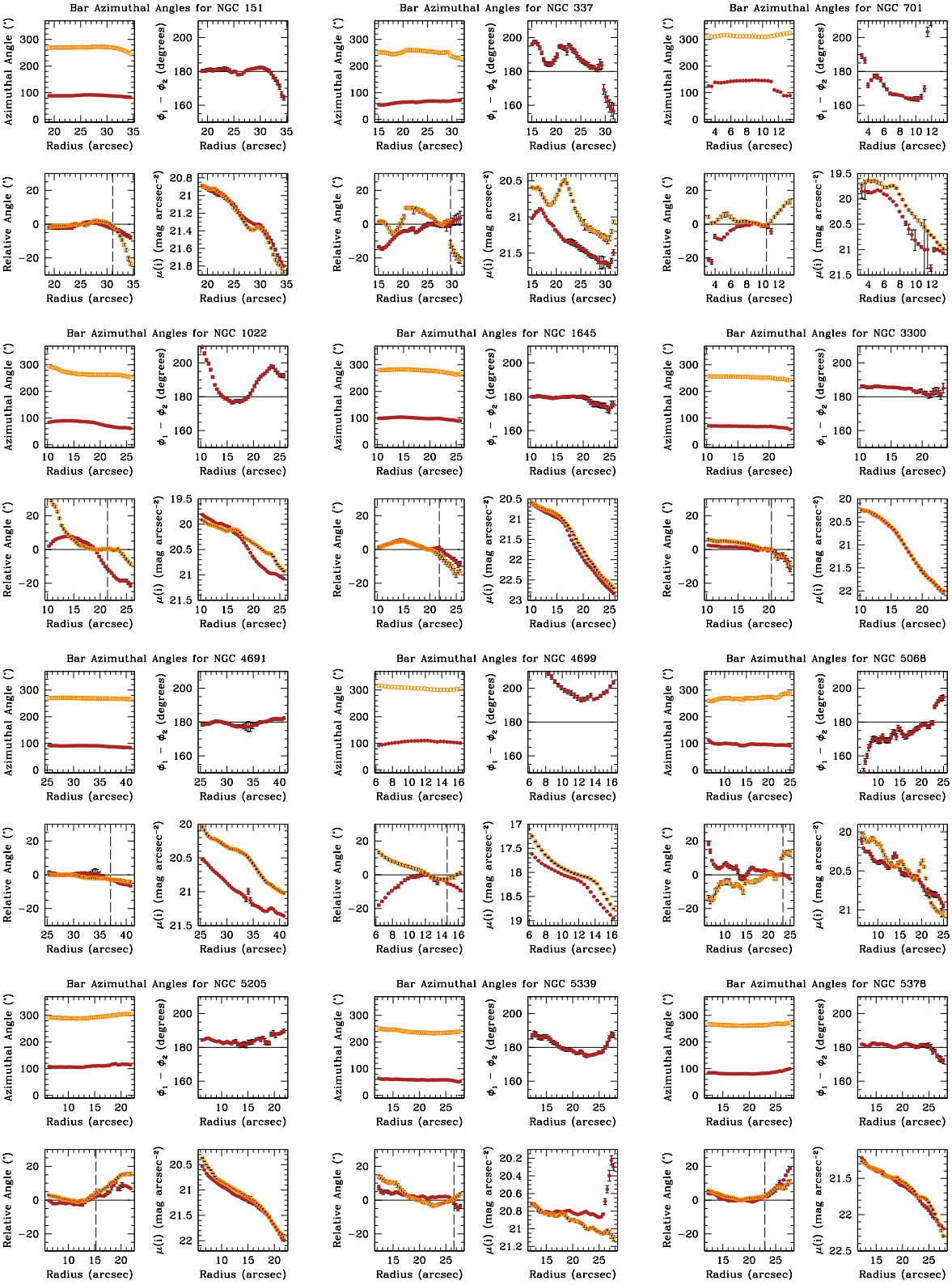

Figure 4.25: Same as Fig. 4.5 for the remainder of the HSB sample.

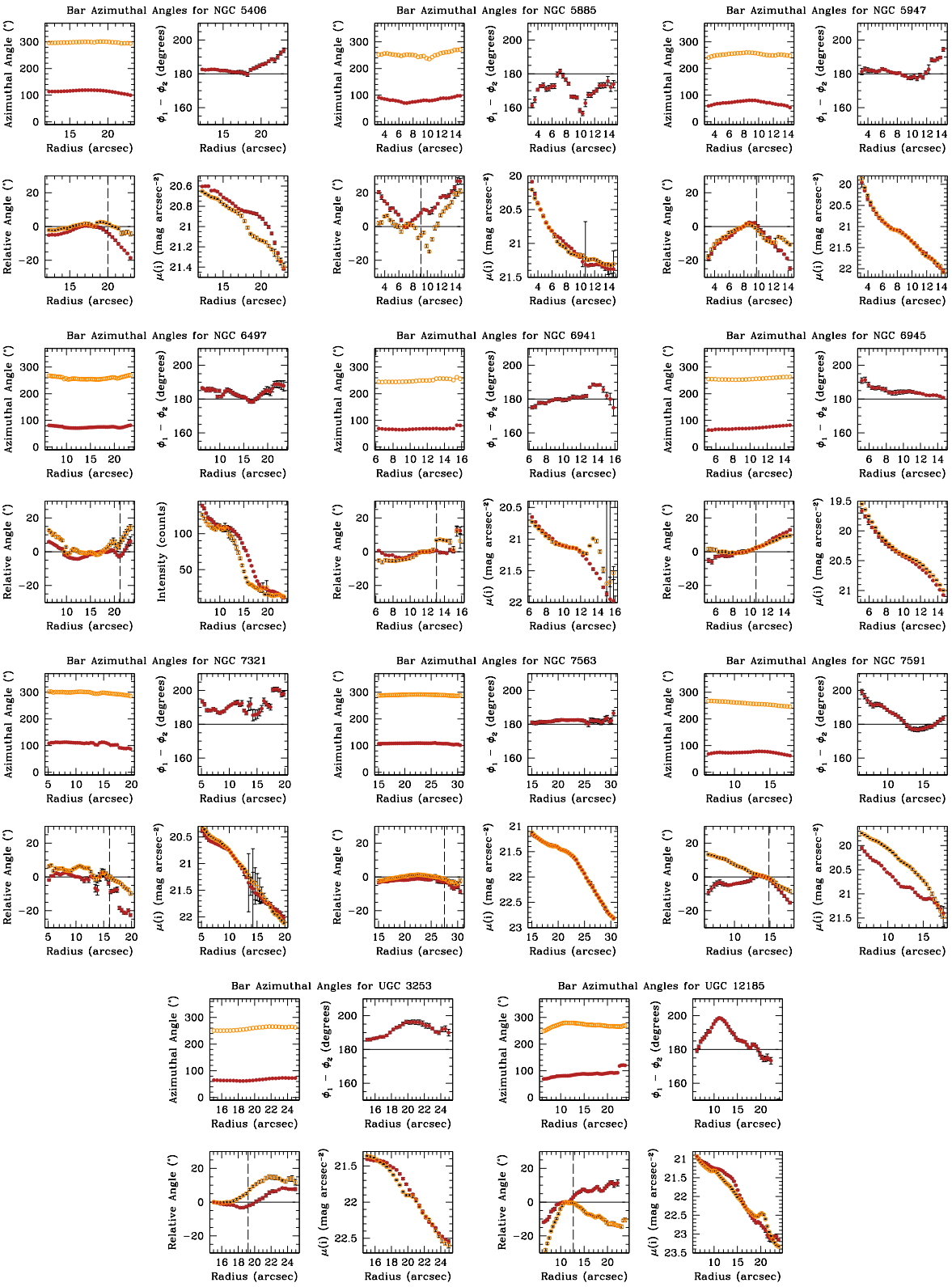

Figure 4.25: *continued*

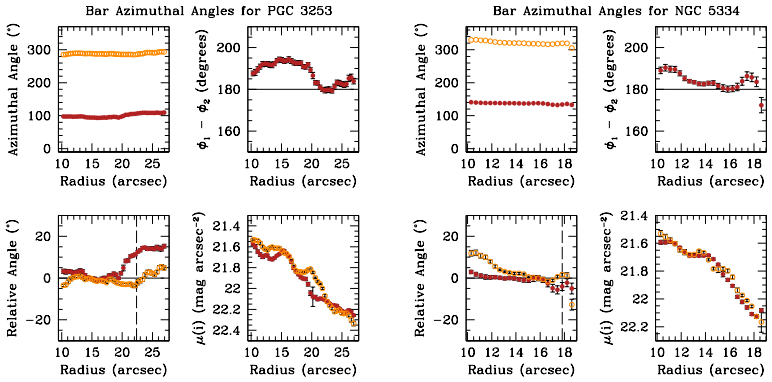

Figure 4.25: *continued*

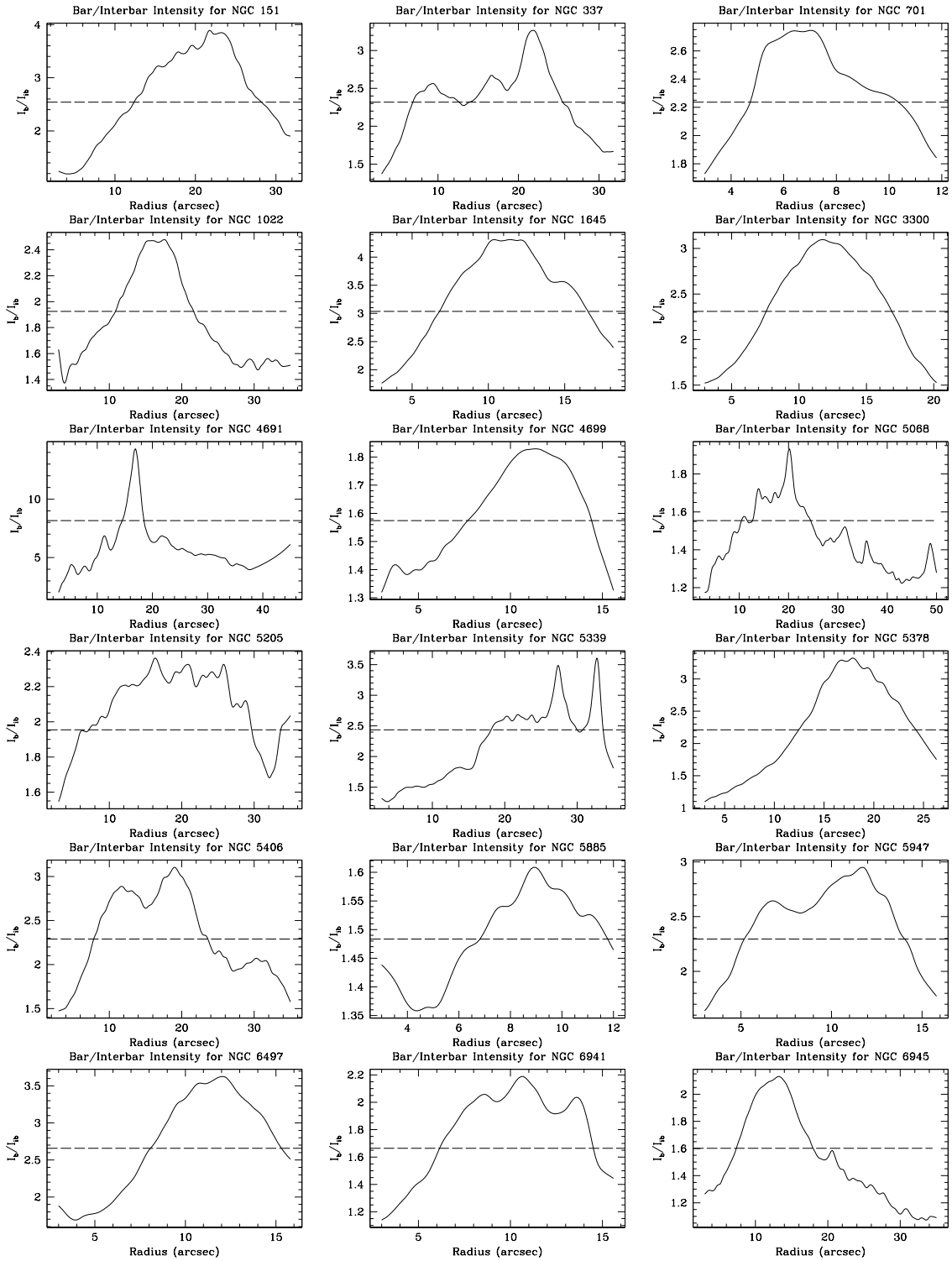

Figure 4.26: Same as Fig. 4.6 for the remainder of the HSB sample.

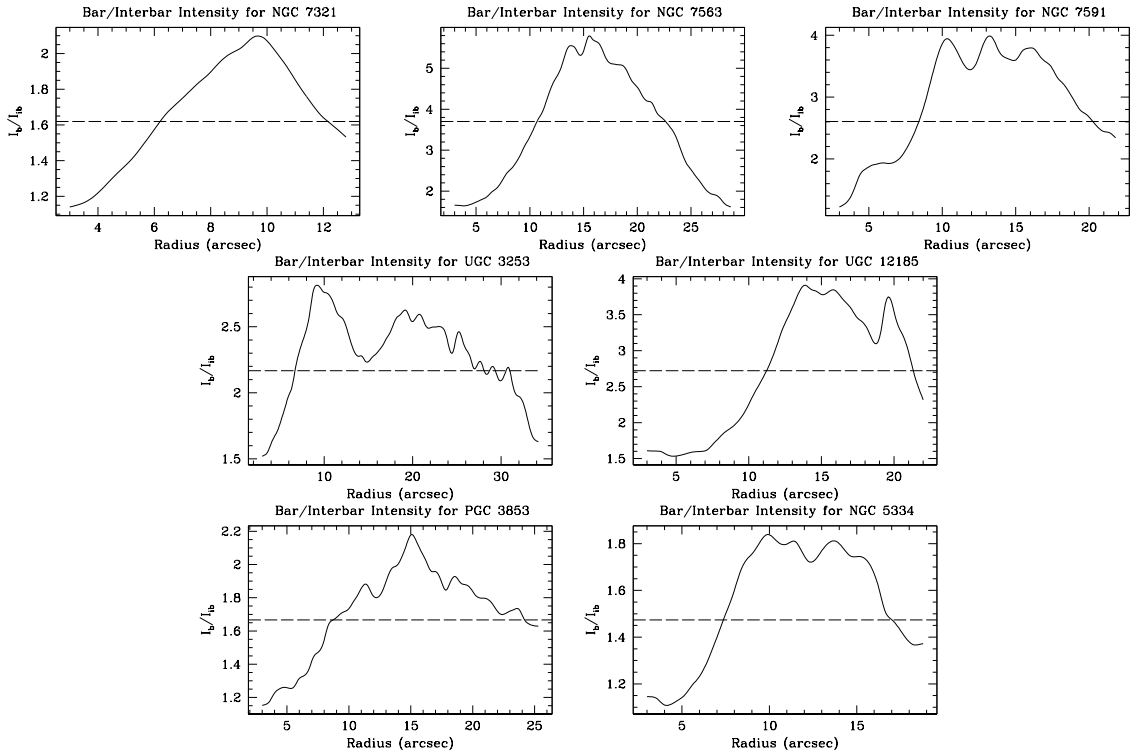

Figure 4.26: *continued*

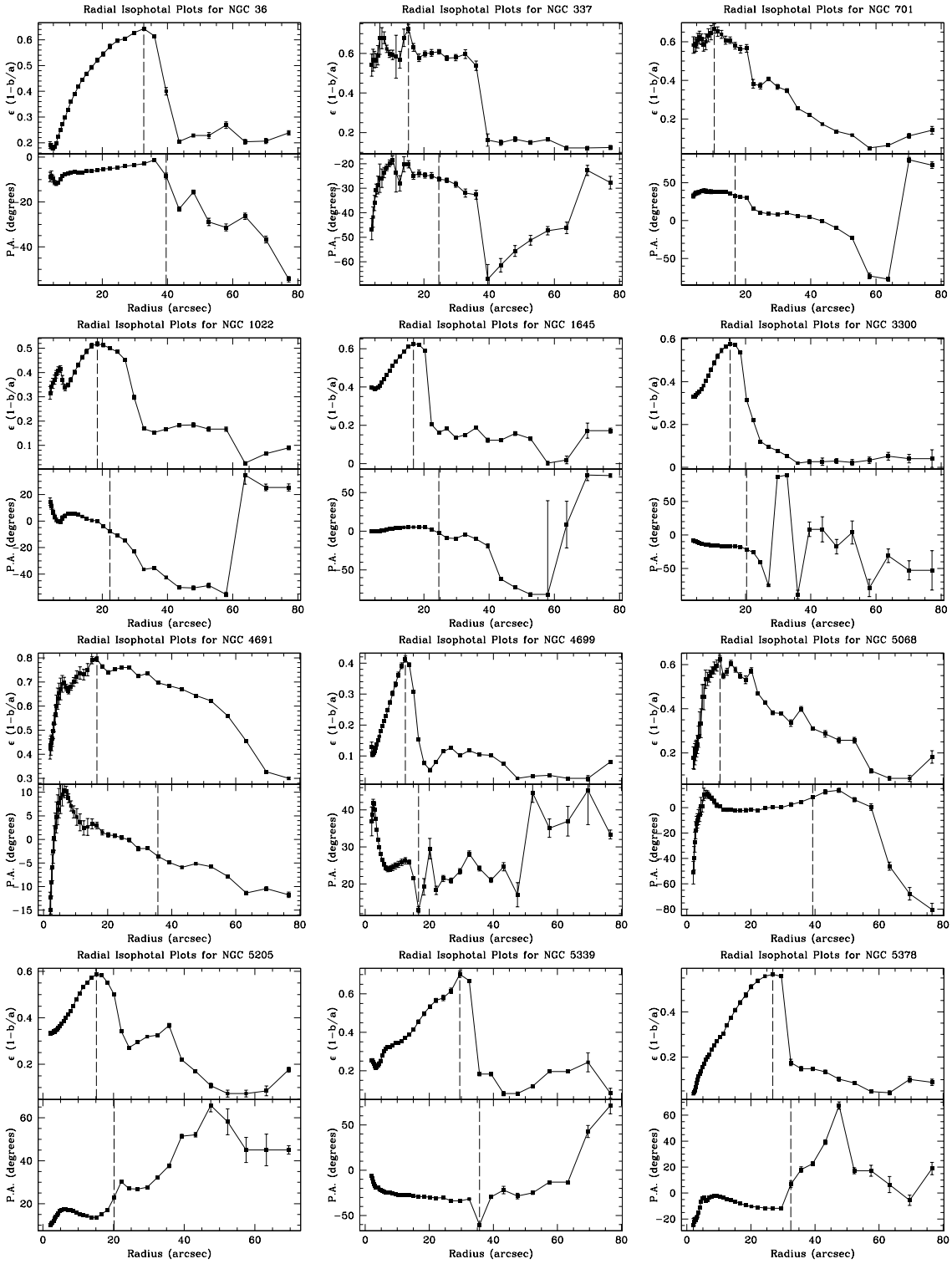

Figure 4.27: Same as Fig. 4.7 for the remainder of the HSB sample.

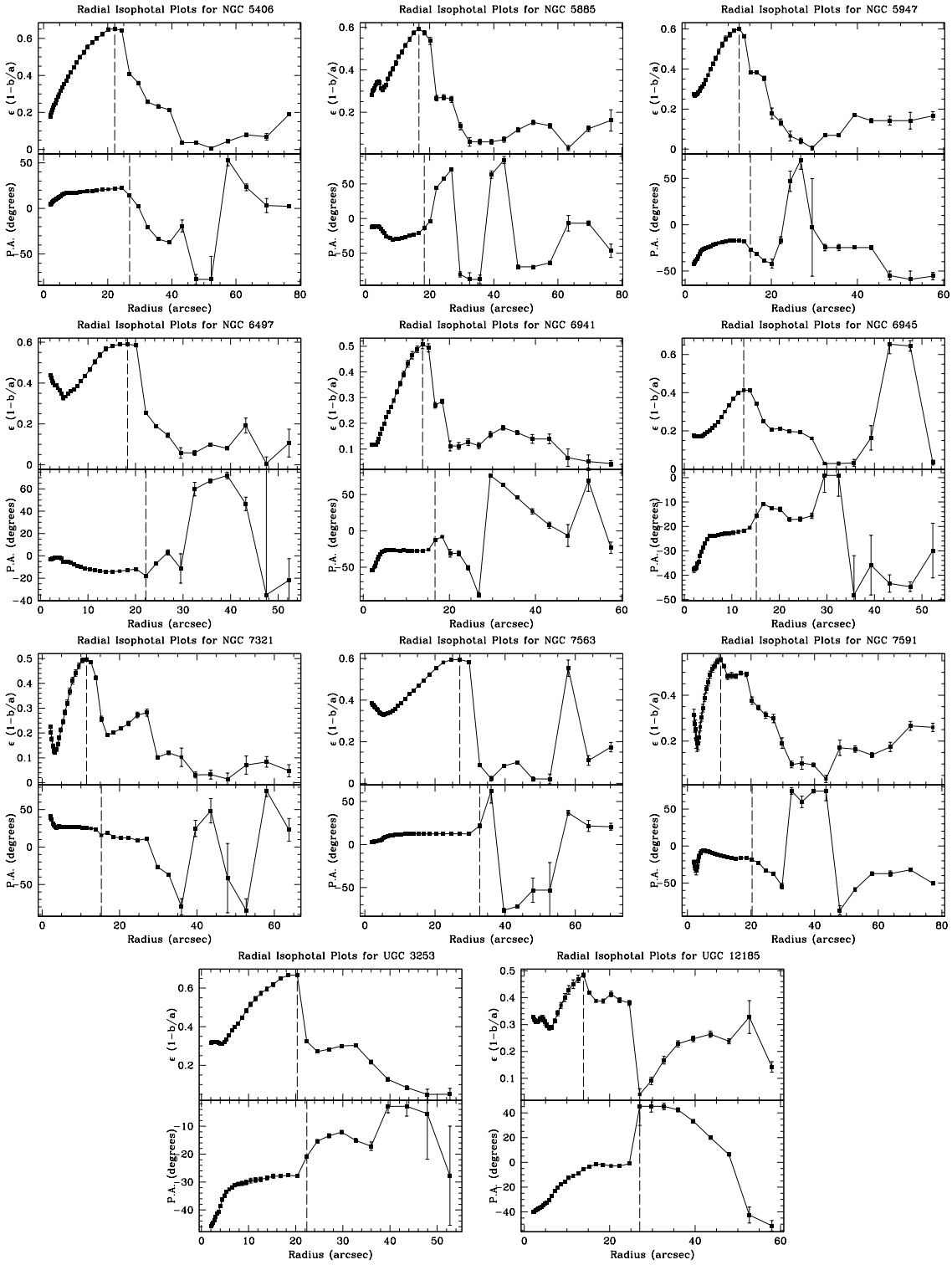

Figure 4.27: *continued*

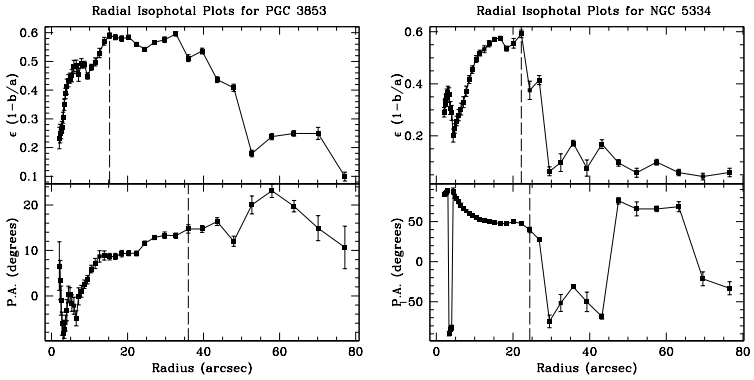

Figure 4.27: *continued*

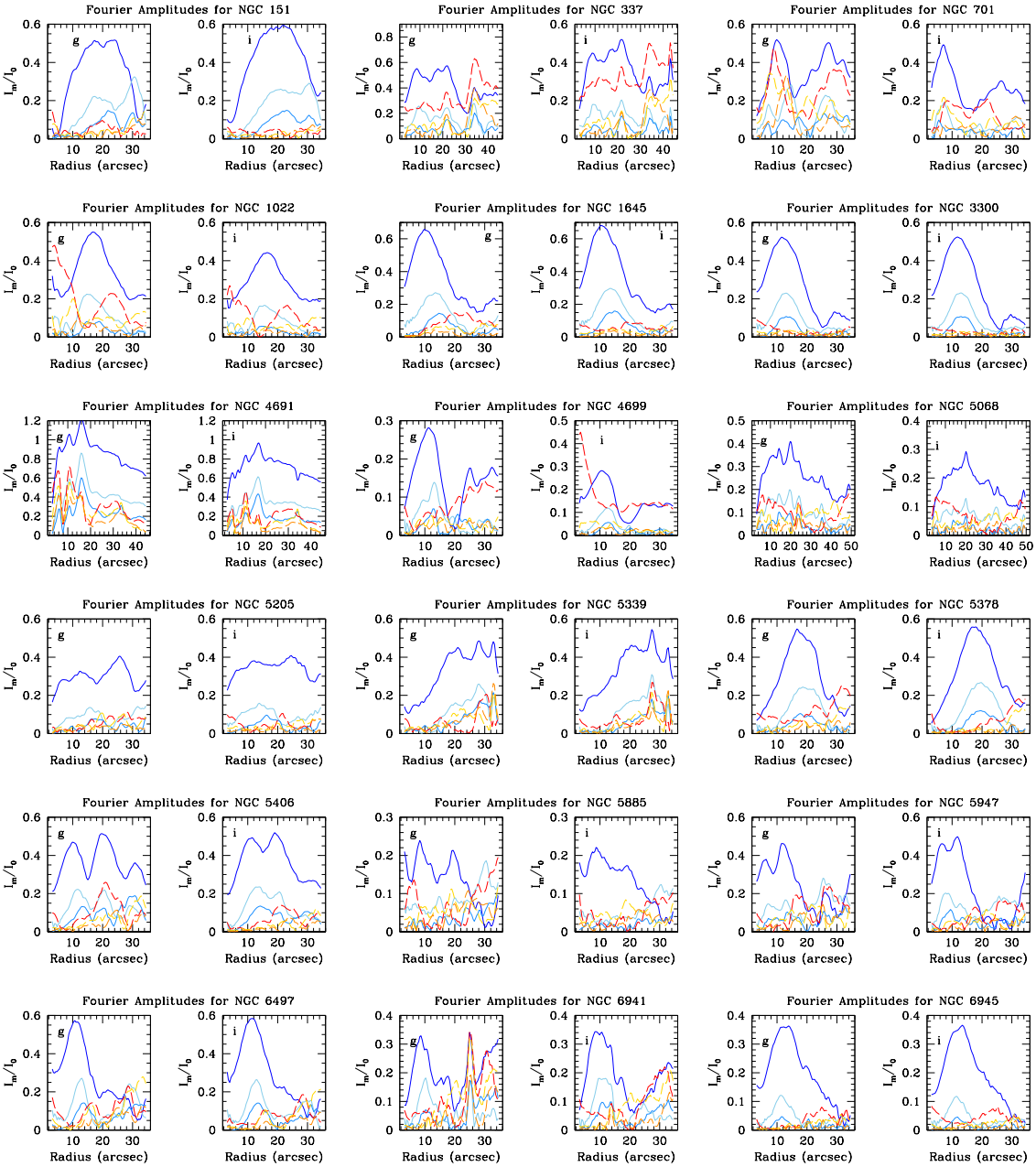

Figure 4.28: Same as Fig. 4.8 for the remainder of the HSB sample.

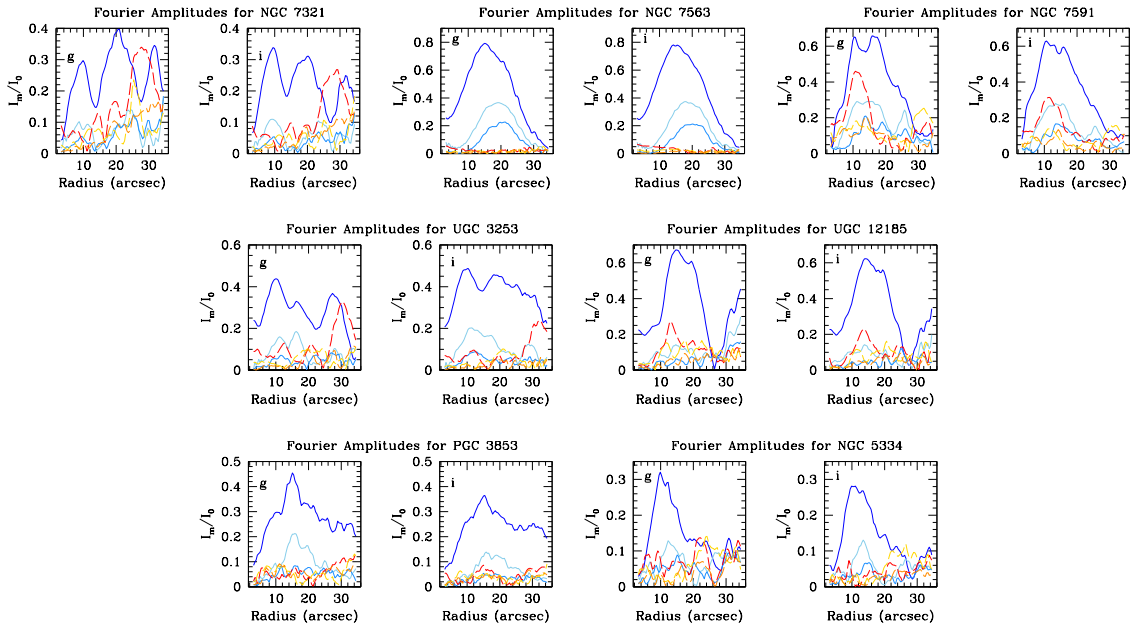

Figure 4.28: *continued*

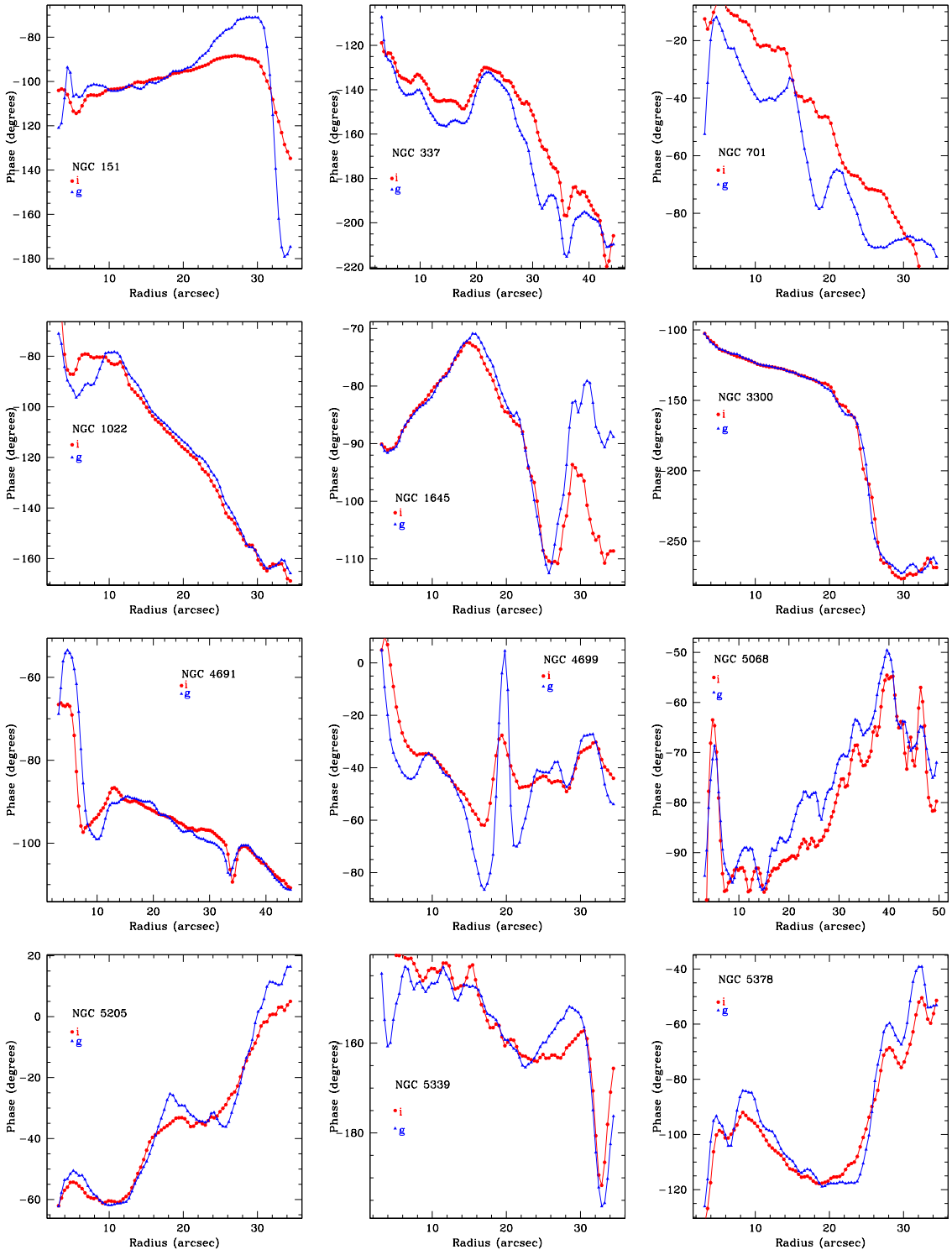

Figure 4.29: Same as Fig. 4.9 for the remainder of the HSB sample.

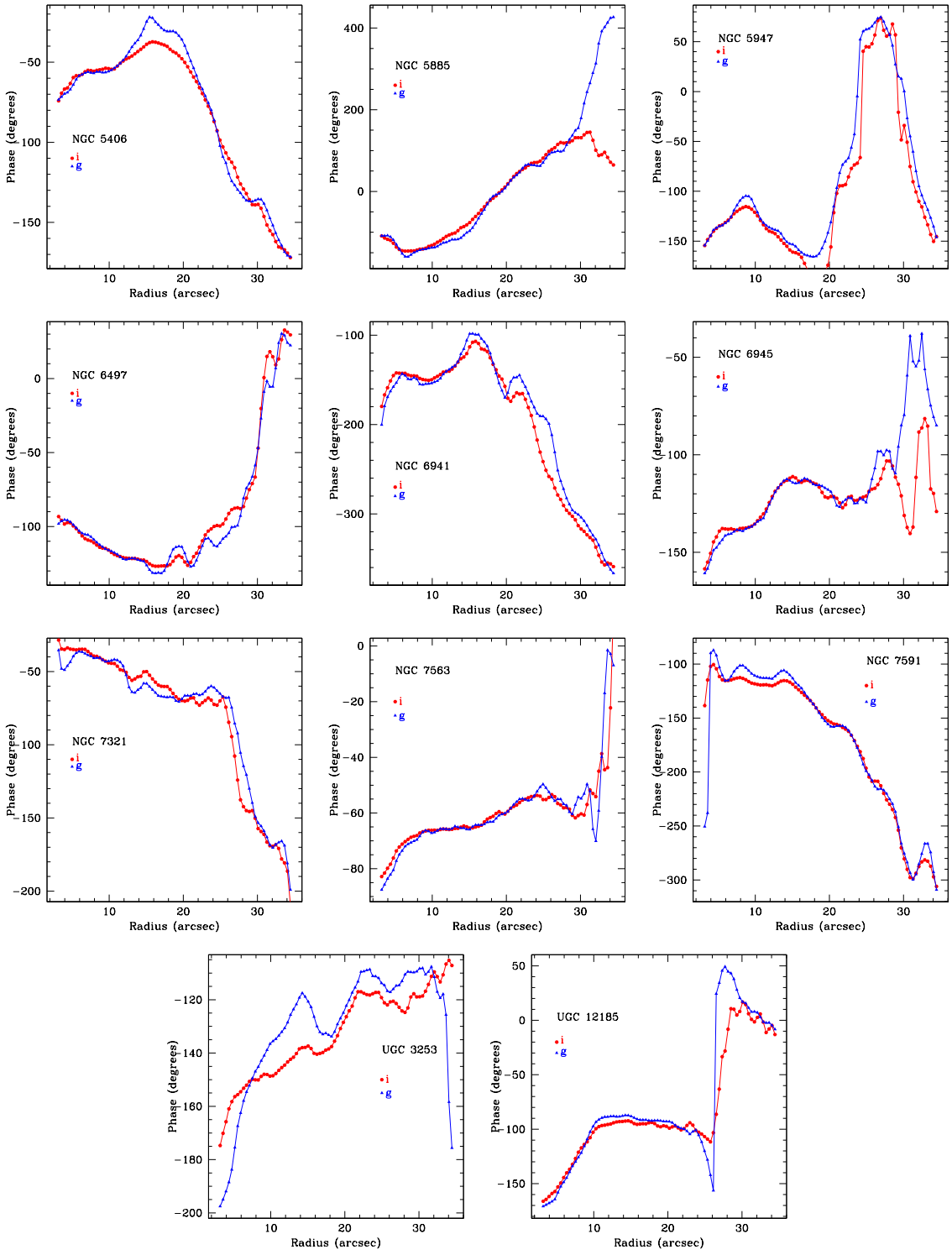

Figure 4.29: *continued*

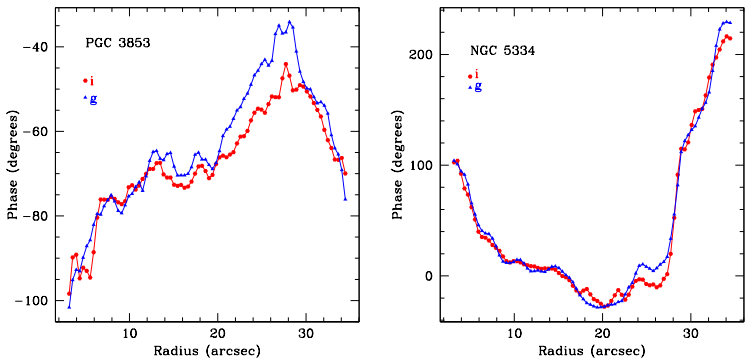

Figure 4.29: *continued*

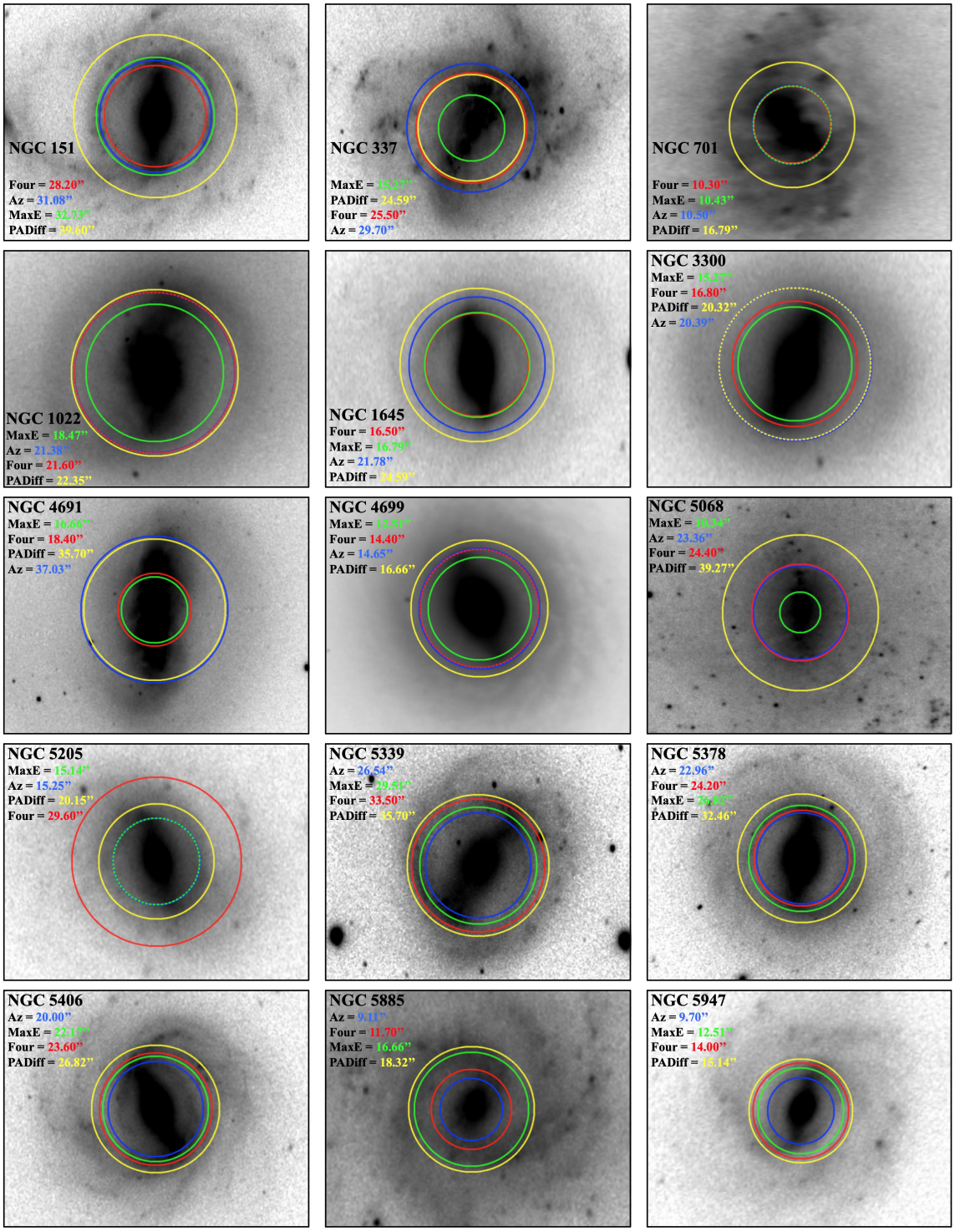

Figure 4.30: Same as Fig. 4.10 for the remainder of the HSB sample.

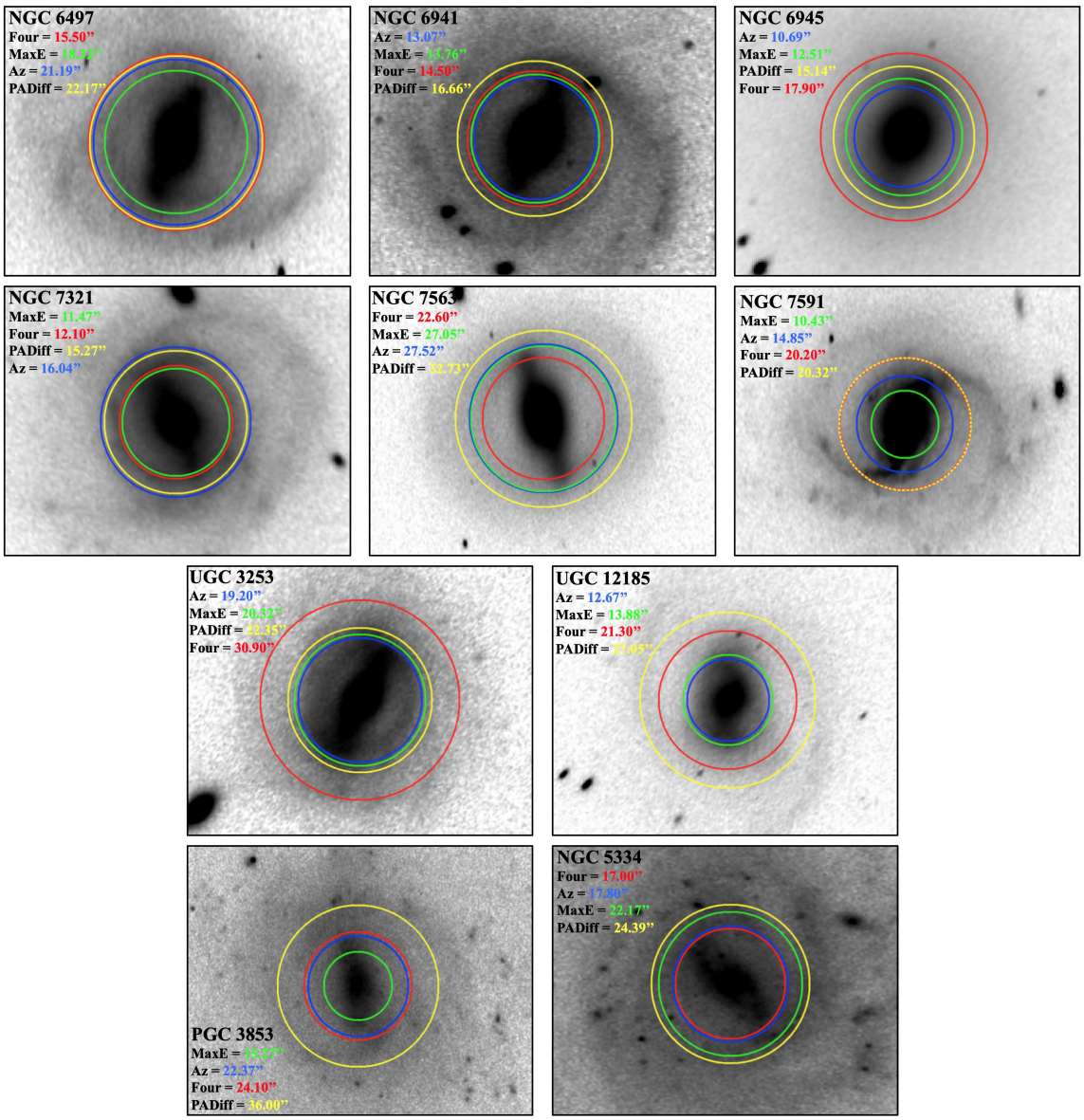

Figure 4.30: *continued*

Chapter 5

Discussion and Future Work

5.1 Introduction

Low surface brightness galaxies (LSBs) make up a significant fraction of the overall galaxy population (McGaugh et al. 1995b; Impey & Bothun 1997), making them vital to our understanding of galaxy formation and evolution. However, while certain aspects of LSBs are relatively well understood, bars in LSBs are not. This dissertation has attempted to shed additional light on barred LSBs, namely by characterizing the three bar properties: length, strength, and corotation radius.

In this chapter, we summarize both the current understanding of bars in LSBs as well as our findings from the previous chapters in Sec. 5.2. We go into the implications of our results in the broader galaxy formation picture in Sec. 5.3, touching on the relation between halo spin and bar properties. Finally, we discuss the next steps that need to be taken to answer the remaining questions about bars in LSBs in Sec. 5.4.

5.2 Bars in Low Surface Brightness Galaxies

Compared to bars in HSBs, there is a significant lack of data for bars in LSBs. At first, this was due to a combination of both a lack of data for LSBs in general, as well as numerical work that showed LSB disks were quite stable to both local and global instabilities (see Mihos et al. 1997; Mayer & Wadsley 2004). Indeed, Mihos et al. (1997) showed that the bar fraction for LSBs was only $\sim 4\%$, and visually going through the large LSB catalogs of Schombert et

al. (1992) and Impey et al. (1996) one can confirm the bar fraction is only a few percent when excluding Malin 1 type LSBs (massive bulge dominated galaxies, with large, extended LSB disks). However, recent work has identified an increasing number of barred LSBs, from $\sim 8\%$ in Honey et al. (2016) to $\sim 20\%$ in Cervantes Sodi & Sánchez García (2017) and $\sim 18\%$ in Pahwa & Saha (2018). While not as high as $\sim 60\%$ for HSBs (when examining near infrared imaging), the finding that roughly a fifth of LSBs are hosts to bars is a significant enough fraction that begs additional study.

5.2.1 Relevance of this Work

In Chapter 4, we confirmed recent work that showed bars in LSBs were both shorter and weaker than those in HSBs. ***More importantly, we presented currently the largest sample of relative bar pattern speed ($\mathcal{R} = R_{\rm CR}/R_{\rm bar}$) measurements for LSBs.*** In fact, prior to this work, there was only *one* LSB with a relative bar pattern speed measurement in the literature, UGC 628 (Chemin & Hernandez 2009; Chequers et al. 2016); measurements for dark matter dominated dwarf galaxies also exist (Bureau et al. 1999; Banerjee et al. 2013). These previous studies relied on using the Tremaine-Weinberg (TW) method (Tremaine & Weinberg 1984) and numerical simulations to measure the corotation radius of the bar ($R_{\rm CR}$) by measuring the bar pattern speed (Ω_{bar}), finding the bar to be quite slow ($\mathcal{R} \sim 2$).

We identified another method of measuring $R_{\rm CR}$ that bypasses the time expensive nature of the TW method in order to greatly expand the measurements of $\mathcal{R}$ for LSBs. Based on spiral density theory, Puerari & Dottori (1997) determined that it would be possible to measure $R_{\rm CR}$ via crossings in phase profiles of B- and I-band images. This method has been succesfully applied to a large number of HSBs (Aguerri et al. 1998, 2000a, 2015; Sierra et al. 2015). When applying this method to an initial sample of four barred LSBs (see Chapter 2), we found that 3 were hosts to fast bars, including UGC 628. We found that the determination of the bar radius was vital to measuring $\mathcal{R}$, as the B- and I-band phase profiles of UGC 628 showed two intersections: one near $\sim 14''$ and one near $\sim 30''$. If one were to use the bar

radius reported in Chemin & Hernandez (2009) and Chequers et al. (2016), the intersection far into the disk must be used, as corotation is thought not to occur within the bar. However, we found that these bar lengths were overestimating the length by roughly 3″, bringing the first phase intersection *outside* the bar region and therefore meant UGC 628 was host to a fast bar.

Based on the discrepancy of the bar length measurements between our azimuthal light profile method and three traditionally used methods in the literature, in Chapter 3 we tested the four methods against mock galaxy images and found our azimuthal method to give the most consistent bar length measures. In that chapter, we also identified 11 additional barred LSBs from Schombert et al. (1992) and Impey et al. (1996) and found that 9 were hosts to fast bars. Finally in Chapter 4, we compiled an HSB comparison sample to explore bar properties across surface brightness. We found in Chapter 4 that bars in HSBs were generally hosts to longer and stronger bars than those in LSBs, both in kpc as well as relative to the disk size. **In total, we measured the relative bar pattern speeds of 15 barred LSBs and found 13 to be hosts to fast bars.**

5.3 Implications

Based on the results from Chapter 4, it becomes clear that high gas content is likely a major factor in the size and strength of bars in LSBs. This is in line with both predictions (Mayer & Wadsley 2004) and recent findings (Masters et al. 2012; Cervantes Sodi 2017). However, Cervantes Sodi & Sánchez García (2017) found that HSBs are hosts to longer and stronger bars than LSBs at equal (M_{HI}/M_*), suggesting another underlying cause in addition to gas content. They found an anticorrelation between surface brightness and halo spin λ, leading to the conclusion that bars in LSBs are shorter and weaker than those in HSBs due to the high λ halos that LSBs reside in.

Further lending evidence to our barred LSBs living in high spin halos is the fact that we find $\sim 75\%$ of our sample to be hosts to fast bars. Centrally dense, static dark matter halos

are expected to invoke a significant amount of braking on a bar due to angular momentum transfer (Weinberg 1985; Debattista & Sellwood 2000). High spin halos, on the other hand, cannot serve as a pure angular momentum sink. There is even evidence that high spin halos can actually speed up bar rotation (Fujii et al. 2019). Based on this, it seems that all three bar properties (length, strength, corotation radius) of our LSBs suggest an underlying high spin halo.

On the other hand, Collier et al. (2018) show how halos with $\lambda > 0.03$ lead to shorter and slower bars, with $\mathcal{R} > 1.4$. Given that LSBs are thought to form in halos with spins greater than $\lambda \geq 0.03$ (Long et al. 2014) or $\lambda \geq 0.05$ (Boissier et al. 2003; Kim & Lee 2013), it is then surprising that we find the majority of our LSBs to be hosts to fast bars (i.e. $\mathcal{R} < 1.4$). A possible reason for this is the lack of inclusion of gas in Collier et al. (2018), which they claim to have a minor role in the damping process. However, we have shown that barred LSBs contain a significant amount of gas (most have $f_{gas} > 0.5$), which can provide a significant angular momentum sink for these galaxies.

And yet, there is a very good chance that $\mathcal{R}$ gives misleading information about the true rotation of a bar. Font et al. (2017) showed via numerical simulations how various evolutionary scenarios for a galaxy can cause a bar to appear fast over its entire life. For instance, the angular momentum transfer from both the gas and halo will cause a bar to grow in length and slow down (Font et al. 2019), causing $\mathcal{R}$ to remain roughly constant. This can lead to galaxies having bars that are classified as slow rotators despite having pattern speeds *faster* than bars classified as fast. Thus, they conclude that slowdown effects on bars caused by interactions with dark matter halos have been underestimated. To counter this, they propose measuring $\Gamma = \Omega_{bar}/\Omega_{disk}$ as a better means of classifying bars as fast or slow.

Bringing all this together, we seem to have conflicting information about the underlying halos of our barred LSBs. On one hand, we find clear evidence that bars in LSBs have experienced significant supression in their growth due to both their gas content, as well as possibly indicating that they reside in high spin halos. We also find that bars in LSBs

have relative bar pattern speeds comparable to those in HSBs, suggesting a high spin halo has either formed a fast bar or sped it up and kept it short over the lifetime of the galaxy, conspiring to keep $\mathcal{R}$ fast. On the other hand, there is recent work that suggests $\mathcal{R}$ is not a valid measure of bar rotation and that bars have indeed been slowed down due to the dark matter halo.

In order to fully understand the nature of the dark matter halos that barred LSBs are embedded in, it becomes clear that measurements of λ are required. The original definition of the spin parameter λ of a system is given in Peebles (1971) as

$$\lambda = \frac{L|E|^{1/2}}{GM^{5/2}} \tag{5.1}$$

where E is the total energy, M is the total mass, L is the total angular momentum, and G is the gravitational constant. Based on a series of assumptions, namely that the disk and halo have the same angular momentum, Hernandez & Cervantes-Sodi (2006) offer an approximation of λ based on observables:

$$\lambda = 21.8 \left(\frac{R_d}{V_d^{3/2}} \right), \tag{5.2}$$

where R_d is the disk scale length in kpc and V_d is the flat portion of the rotation curve in km s^{-1}. Cervantes-Sodi et al. (2008) found this approximation to accurately match predictions from numerical simulations. We can therefore get a rough estimate of λ for those LSBs in our sample with published rotation curves. From high quality rotation curves in the literature, we can estimate V_d from the outer portion of the rotation curves, and we can use the I-band scale lengths compiled from the literature in Chapter 3. From de Blok & Bosma (2002) we obtain $V_d = 130$ km s^{-1} for UGC 628, and from de Blok et al. (2001b), we obtain $V_d = 130,\ 100,\ 120$ km s^{-1} for F568-1, F568-3, and F563-V2 respectively.

Using the available data, we find the following λ estimates: for UGC 628, $\lambda = 0.051$; for F568-1, $\lambda = 0.080$; for F568-3, $\lambda = 0.074$; and for F563-V2, $\lambda = 0.033$. This is consistent

with LSBs being embedded in halos with $\lambda > 0.05$. F563-V2 stands out as having the lowest spin value, as well as being the only barred LSB with $\mathcal{R} \gg 1.4$. Finding such a clear result, we would like to obtain estimates of λ for those LSBs and HSBs with available stellar mass estimates from Chapter 4: 15 HSBs and 11 LSBs.

For consistency, we can use our I-band disk scale lengths in Chapter 3 for our LSBs, and the r-band scale lengths from SDSS DR15 for our HSBs. However, rather than following the procedure in Cervantes Sodi (2017) of adopting the r-band Tully-Fisher (TF) relation from Pizagno et al. (2007) to obtain V_d, we instead adopt the Baryonic Tully-Fisher (BTF) relation from Lelli et al. (2019) and use our total baryonic masses ($M_{bar} = 1.4M_{HI} + M_*$) from Chapter 3 and Chapter 4 to obtain V_d:

$$\log(V_d) = 0.256 * \log(M_{bar}) - 0.52. \tag{5.3}$$

We use the BTF here as it has long been know that the TF breaks down for gas rich, stellar poor systems (see O'Neil et al. 2000; McGaugh et al. 2000). We can therefore obtain V_d across all masses. However, for completeness, the r-band TF relation from Pizagno et al. (2007) is given as

$$\log V_{80} = -0.135(M_r + 21.107) + 2.21 \tag{5.4}$$

where V_{80} is the velocity at the radius that contains 80% of a galaxy's light (R_{80}), and M_r is the absolute r-band magnitude. For a pure exponential disk $R_{80} = 3.03R_d$.

In Table 5.1 we show V_d, R_d, λ, and $\mathcal{R}$ for the 11 LSBs in Chapter 3 and the 15 HSBs in Chapter 4 that have both photometry and mass estimates. Here, LSBs are in the top half of the table, and HSBs are in the bottom half. In Fig. 5.1, we show bar properties as functions of $\log(\lambda)$. In the top left panel, we plot the bar in kiloparsecs and find that bar length increases as you move to slower spinning halos. As λ is calculated with the disk scale length, we do not explore trends with the normalized bar length here. We find the following fit: $R_{\rm bar} = -2.63\log(\lambda) + 0.66$ with a scatter of 2.20, and a Spearman coefficient of -0.26.

Table 5.1: Estimates of the halo spin parameter λ for barred LSBs and HSBs based on the model from Hernandez & Cervantes-Sodi (2006). V_d values are caulculated using the Baryonic Tully-Fisher Relation from Lelli et al. (2019), with total baryonic mass ($M_{tot} = 1.4M_{\rm HI} + M_*$) taken from Chapter 4 using the Υ_*^V relation from Schombert et al. (2019). R_d values for the LSBs are taken from our surface brightness profiles in Chapter 3. R_d values for the HSBs are taken from Chapter 4. $\mathcal{R}$ values are taken from Chapter 3 and Chapter 4.

	Galaxy	V_d (km s^{-1})	R_d (kpc)	λ	$\mathcal{R}$
LSBs	UGC 628	138.02±8.72	3.47±0.30	0.11±0.01	1.25±0.11
	UGC 2925	149.72±64.65	2.47±0.07	0.11±0.07	1.48±0.22
	F563-V2	98.10±12.74	2.05	0.16±0.03	2.38±0.30
	F568-1	106.88±16.73	5.41	0.24±0.06	1.34±0.22
	F568-3	109.34±20.32	3.38	0.16±0.04	1.13±0.17
	LEDA 135782	147.26±25.99	4.05±0.29	0.05±0.01	1.05±0.32
	UGC 8066	84.97±8.87	2.11±0.07	0.30±0.05	1.06±0.15
	F602-1	125.48±10.79	4.40±0.17	0.13±0.02	1.29±0.19
	PGC 70352	114.99±16.70	2.33±0.10	0.12±0.03	1.31±0.24
HSBs	NGC 36	197.27±10.11	7.83±0.28	0.062±0.005	1.10±0.12
	NGC 151	208.91±9.76	5.94±0.16	0.043±0.003	1.02±0.10
	NGC 337	119.74±4.17	1.74±0.03	0.029±0.002	1.42±0.15
	NGC 701	128.58±4.53	2.08±0.01	0.031±0.002	1.43±0.16
	NGC 1022	121.78±7.32	1.94±0.05	0.031±0.003	1.34±0.20
	NGC 1645	187.80±9.04	6.33±0.15	0.054±0.004	1.01±0.11
	NGC 4691	143.18±7.88	3.39±0.30	0.043±0.004	1.07±0.11
	NGC 4699	202.03±15.78	2.63±0.14	0.020±0.002	1.39±0.18
	NGC 5068	146.14±6.60	4.63±0.15	0.057±0.004	1.75±0.20
	NGC 5205	108.35±5.46	2.23±0.10	0.043±0.003	1.06±0.13
	NGC 5334	101.20±4.54	4.99±0.08	0.107±0.007	1.13±0.12
	NGC 5339	146.04±8.30	3.79±0.12	0.047±0.004	1.15±0.12
	NGC 5378	155.68±10.88	3.46±0.13	0.039±0.004	1.12±0.11
	NGC 5406	216.82±13.41	6.86±0.25	0.047±0.004	1.22±0.14
	NGC 5885	144.57±4.47	5.19±0.10	0.065±0.003	1.91±0.46
	NGC 6941	204.59±10.22	5.32±0.32	0.040±0.003	1.41±0.17
	NGC 7321	190.40±9.06	6.44±0.17	0.053±0.004	1.22±0.14
	NGC 7563	170.56±14.08	3.21±0.14	0.031±0.004	1.02±0.10
	NGC 7591	203.71±8.10	5.58±0.22	0.042±0.002	1.17±0.12
	PGC 3853	93.23±3.48	2.77±0.09	0.067±0.004	1.51±0.26
	UGC 3253	157.06±11.21	3.65±0.13	0.040±0.004	1.66±0.20

We find a similar trend in the top right panel with bar strength, with strength increasing with decreasing halo spin: $S_b = -0.34 \log(\lambda) - 0.02$ with a scatter of 0.20, and a Spearman coefficient of -0.54. Finally, we find no trend between $\mathcal{R}$ and λ in the bottom panel: bars are

fast across various underlying halo spins. As a reminder, LSBs are expected to form in high spin halos, with $\lambda > 0.05$ ($\log(\lambda) = -1.30$), shown as the vertical short dashed line in each panel of Fig. 5.1.

Finding such strong correlations between $R_{\rm bar}$ and S_b with λ, we suspect that the correlations discussed in Chapter 4 are more likely reflecting the underlying halo spin. To explore this, we show both central surface brightness and $\log(M_{\rm gas}/M_*)$ as functions of λ in Fig. 5.2. We find strong relations in each panel, with λ dictating both the gas content and surface brightness of the galaxies. The dashed lines in each panel indicate the fits $\mu_0 = 2.37\log(\lambda) + 24.57$ and $\log(M_{\rm gas}/M_*) = 1.61\log(\lambda) + 1.69$, with the shaded regions indicating the scatters 0.68 and 0.52, and Spearman coefficients of 0.69 and 0.66 respectively. It is important to note that the top panel is not too surprising, given that surface brightness and disk scale length are related via the Tully-Fisher relation. However, this concern is not relevant to the bottom panel.

Based on these results, we agree with Cervantes Sodi & Sánchez García (2017) that the underlying driver of bar length and strength appears to be the halo spin. **In other words, the correlations we found between bar properties and Hubble type, masses, and surface brightness appear to be best explained via the high spin nature of the halos that LSBs are embedded in.**

5.4 Future Work: Searching MaNGA For Barred LSBs

While increasing the sample of measured barred LSB galaxies would obviously be beneficial to shedding additional light on the bar properties of LSBs, obtaining high quality, integral field unit (IFU) spectroscopic data for these galaxies should be the next priority in order to obtain bar and disk pattern speeds from kinematics. Currently, only UGC 628 has a bar pattern speed measurement. The advent of large-scale IFU surveys like the Calar Alto Legacry Integral Field Area Survery (CALIFA, Sánchez et al. 2012) and the Mapping Nearby Galaxies at APO Survey (MaNGA, Bundy et al. 2015) make it possible to obtain bar pattern speed

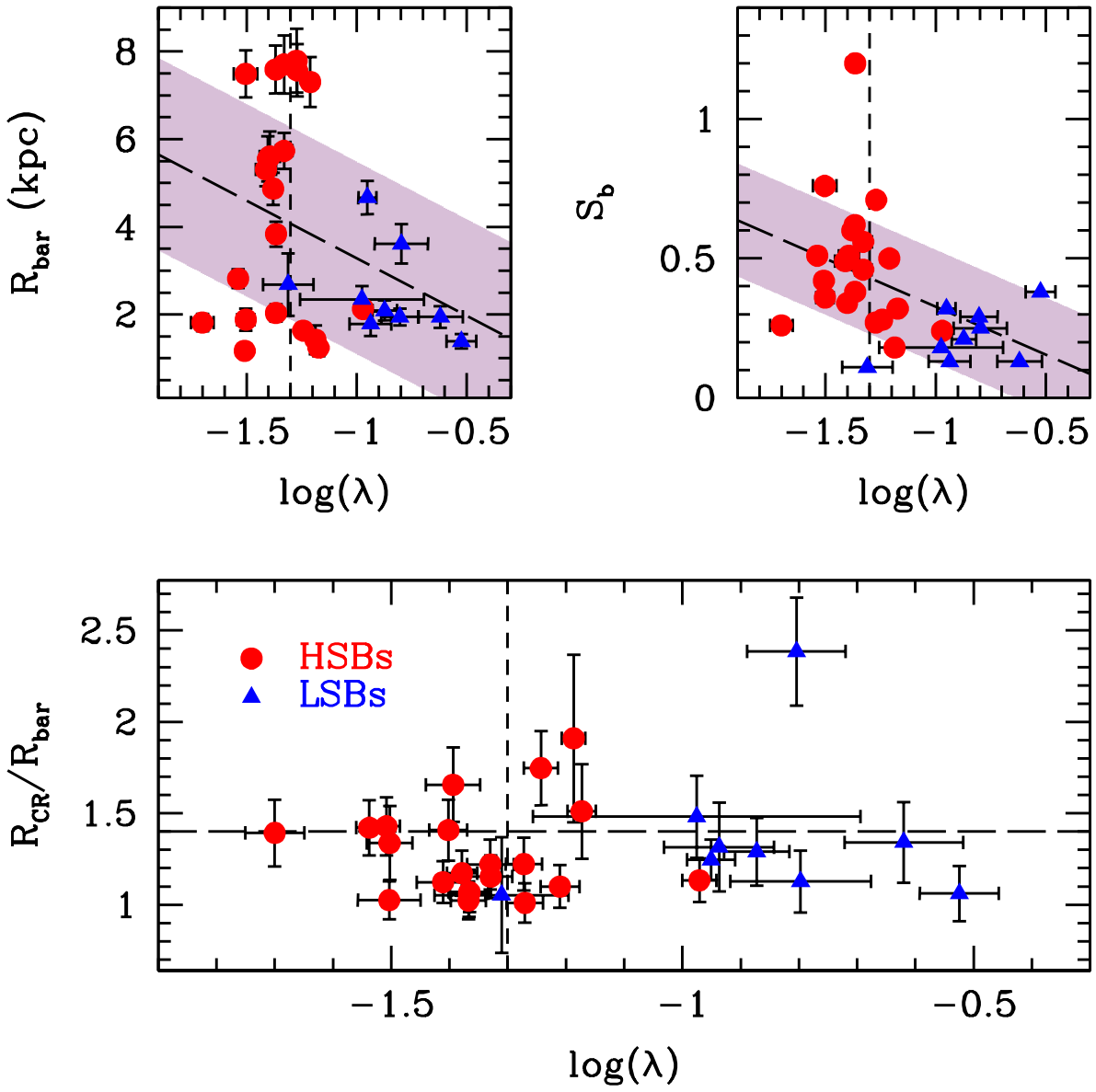

Figure 5.1: Bar properties as functions of $\log(\lambda)$. *Top Left*: bar length in kpc; *Top Right*: bar strength; *Bottom*: relative bar pattern speed. LSBs are shown as blue triangles, and HSBs are shown as red circles. The HSB at $S_b \sim 1.2$ is NGC 4691 and is excluded from the fit. The dashed horizontal line in the bottom panel separates fast and slow bars, $\mathcal{R} = 1.4$. As a reminder, LSBs are expected to form in high spin halos, with $\log(\lambda) > -1.30$, shown in all panels as the vertical short dashed line. The *very* slow LSB bar is F563-V2.

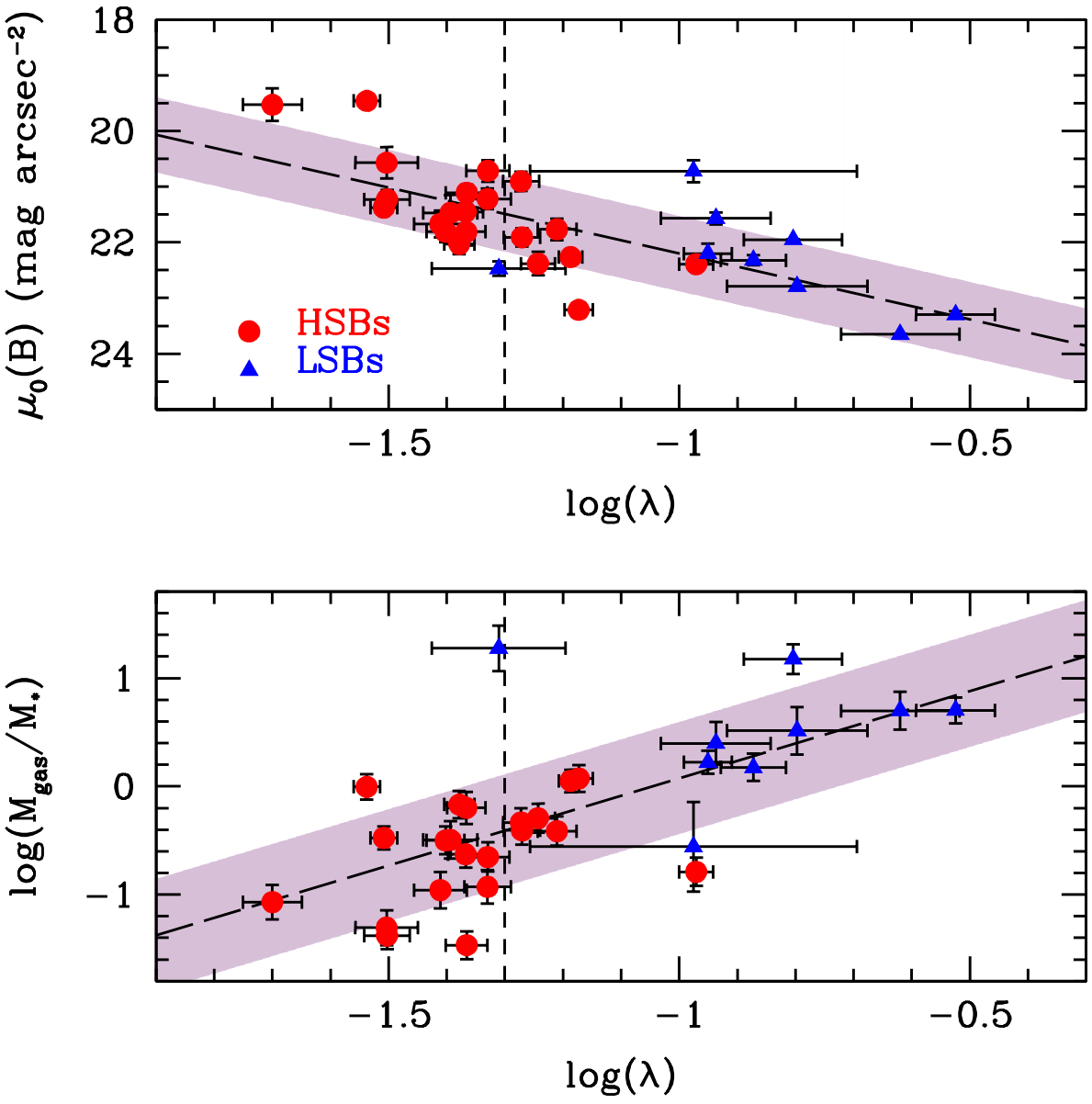

Figure 5.2: Central surface brightness, μ_0, and $\log(M_{\rm gas}/M_*)$ as functions of λ. The dashed lines in each panel indicate the fits $\mu_0 = 2.37\log(\lambda)+24.57$ and $\log(M_{\rm gas}/M_*) = 1.61\log(\lambda)+1.69$, with the shaded regions indicating the scatters 0.68 and 0.76. As a reminder, LSBs are expected to form in high spin halos, with $\log(\lambda) > -1.30$, shown as the vertical short dashed line in both panels.

measurements for a large number of galaxies. For example, Guo et al. (2019) successfully apply the TW method to 53 galaxies in the MaNGA catalog, *although none of these galaxies are LSBs.*

The MaNGA IFU system consists of 1423 fibers, 2 arcsec in diameter, mounted on the SDSS 2.5m telescope at Apache Point Observatory (APO). IFU bundles pointed at each galaxy range from 19 to 127 fibers, and have fields of view ranging from $12'$ to $32'$. In order to obtain high spatial resolution of the galaxy targets, a three-point dither pattern is used to bring the final pixel size to 0.5 arcsec for each map. The primary MaNGA sample is determined from a subsample of the SDSS Main Galaxy Legacy Area by selecting galaxies in a certain redshift range and, most importantly, having stellar masses $M_* > 10^9\ M_\odot$. When adding in the additional LSBs from Chapter 4, we have shown that barred LSBs span roughly three decades of stellar mass, from $\sim 10^8\ M_\odot$ to $\sim 10^{10}\ M_\odot$. In other words, this selection criteria eliminates a portion of our LSB sample, as well as possibly only selecting those LSBs with the highest stellar masses. However, it is still worthwhile to estimate the number of LSBs in MaNGA.

To obtain a rough number of LSBs possibly in MaNGA, we use available SDSS photometry for the MaNGA sample to estimate g- and r-band central surface brightnesses via

$$\mu_0 = m + 2.5\log(2\pi a^2) + 2.5\log(q) - 10\log(1+z). \tag{5.5}$$

B-band central surface brightnesses are then finally estimated via:

$$\mu_0(B) = \mu_0(g) + 0.47(\mu_0(g) - \mu_0(r)) + 0.17. \tag{5.6}$$

As obtaining pattern speeds can be difficult for galaxies with very high or very low inclinations (Corsini 2011), we follow Guo et al. (2019) and constrain the axis ratio to the range $0.25 < b/a < 0.8$ (or inclinations between 37° and 76°). It is also important to select galaxies with low errors on position angle (Debattista 2003), although we cannot make such a cut to this

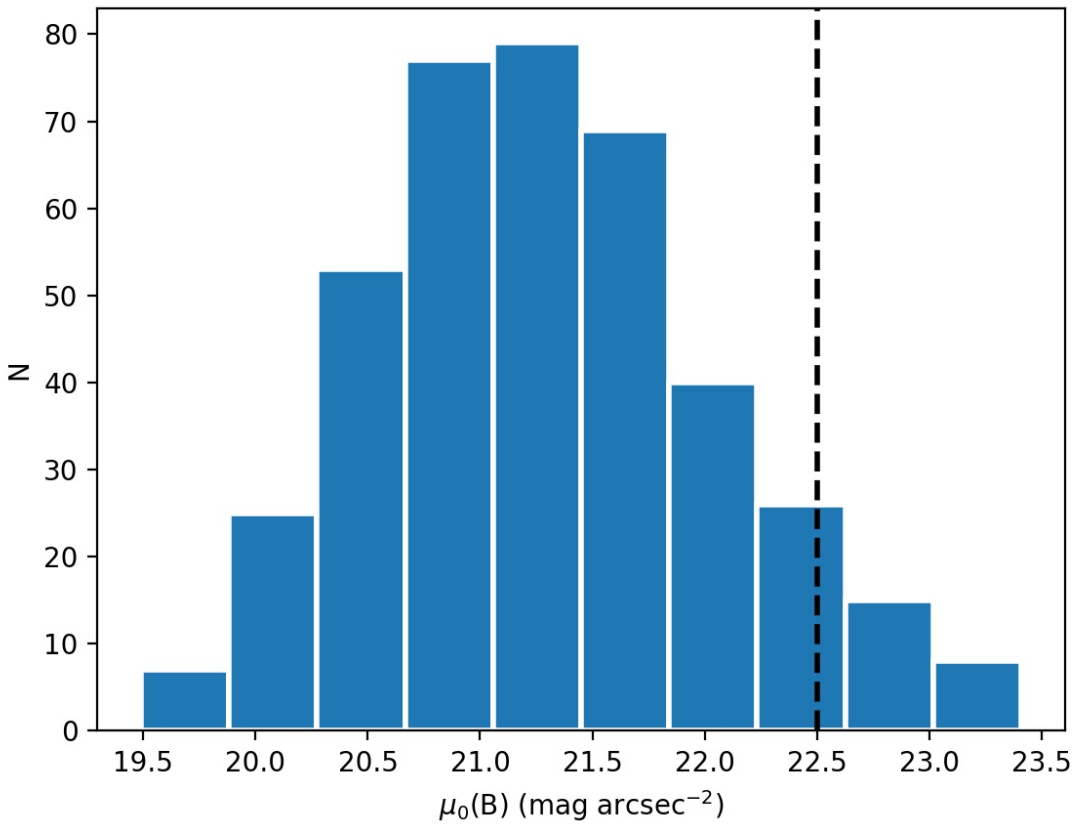

Figure 5.3: Estimated B-band central surface brightnesses for the observed disk galaxies in MaNGA. The vertical dashed line at $\mu_0(B) = 22.5$ mag arcsec^{-2} separates HSBs and LSBs.

data given the available data. In order to estimate the number of *barred* LSBs in MaNGA, we match the MaNGA galaxies to those classified in Galaxy Zoo 2 (Willett et al. 2013), specifically those with disk vote weights greater than 0.5. This leaves us with 1537 disk galaxies in MaNGA.

We show the estimated central surface brightnesses for these galaxies in Fig. 5.3. Here, the vertical dashed line at $\mu_0(B) = 22.5$ mag arcsec^{-2} separates HSBs and LSBs. Clearly, the observed MaNGA galaxies are heavily biased towards HSBs, with the distribution peaking close to $\mu_0 \sim 21$ mag arcsec^{-2} (roughly corresponding to the Freeman value of $\sim$21.65 mag arcsec^{-2}, Freeman 1970). However, we note that there do appear to be LSBs present in MaNGA (see to the right of the dashed line in Fig. 5.3).

Next, we further cut the sample to only include galaxies with Sérsic indices <1.5 (taken from the SDSS photometry) to exclude bulge dominated galaxies, as we want to avoid galaxies with only LSB disks (see Greco et al. 2018). **This leaves us with 29 possible LSBs in MaNGA.** Finally, to determine if a galaxy is barred or not, we insist that the bar vote weight from Galaxy Zoo is greater than 0.5, ***leaving us with 8 possible barred LSBs in MaNGA.*** We note that this is a heavily biased selection of LSBs, namely those with the largest stellar mass and those with the strongest bars. In addition, our Sérsic index cut has selected only the blue LSBs, even though a red population of LSBs exists (O'Neil et al. 1997).

In Fig. 5.4 we show $(g-r)$ vs. $(g-i)$ for the MaNGA galaxies, with open red stars being HSBs and filled blue circles being LSBs. The vertical dashed line at $(g-i)=0.64$ is the deliminator between blue and red LSBs from Greco et al. (2018), showing our selected LSBs are almost all blue. We list the `mangaid`, `plateifu`, coordinates, and estimated central surface brightnesses of the possible LSBs in MaNGA in Table 5.2, with the barred LSBs separated at the bottom by the horizontal line. `mangaid` and `plateifu` can be used to extract a given data cube through various means, most easily from the Marvin API[1].

When visually examining these galaxies in Marvin, it appears as though our selection cuts have appropriately selected barred LSBs. Even though we make no final cuts based on quality of the MaNGA data cubes, **that there are 8 possible barred LSBs in MaNGA is exciting and warrants further exploration.** By further applying a quality cut to the data cubes (requiring no quality flags to be raised by the data reduction pipeline), we are left with 4 barred LSBs and 11 remaining LSBs. In Fig. 5.5, we show the SDSS image (left panel), stellar velocity map (2nd panel), and Hα velocity map (third panel) for the 4 barred LSBs, and the same for the remaining LSBs in Fig. 5.6.

It is quite clear from theses figures that the quality of the LSB velocity maps is quite variable, with 1-166889 and 1-592984 probably unusable due to no rotation present (i.e. there are no clear red and blue shifted sides of the velocity fields), and the IFUs on 1-389503 and

[1]https://dr15.sdss.org/marvin/

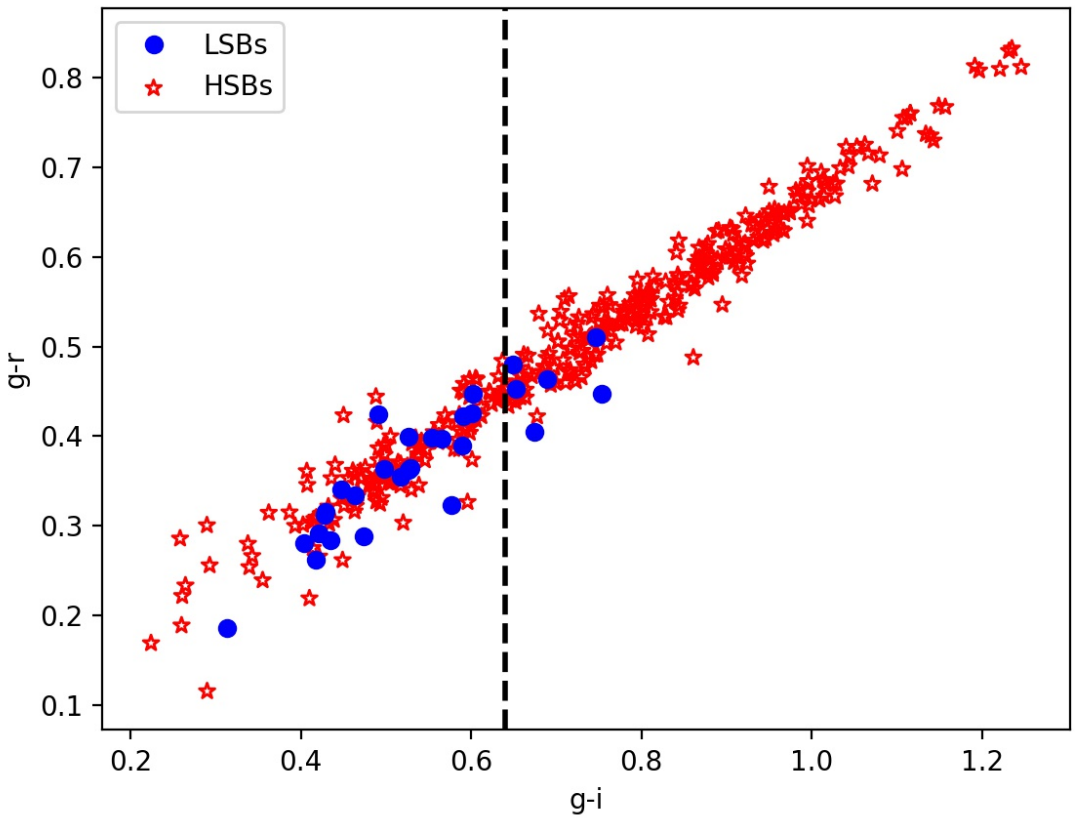

Figure 5.4: Color-color diagram for MaNGA disk galaxies. Open, red stars show HSBs, and filled blue circles show LSBs. The vertical dashed line at $(g-i)$ shows the deliminator between blue and red LSBs from Greco et al. (2018).

Table 5.2: Possible LSBs in MaNGA. `mangaid` (col. 1) and `plateifu` (col. 2) can be used to identify the galaxies for data cube retrieval. Col. 5 is our estimated B-band central surface brightness.

`mangaid`	`plateifu`	R.A. (degrees)	Dec. (degrees)	$\mu_0(B)$ (mag arcsec^{-2})
1-71124	8139-12703	114.047490	32.515147	22.95
1-604846	8936-3703	117.543780	30.685090	22.95
1-201602	8936-12703	118.053469	30.2557736	22.85
1-145669	8147-12704	118.675160	26.642730	23.06
1-121994	9485-9102	121.080505	37.709432	22.80
1-230171	8942-12705	124.670296	26.535564	23.08
1-460305	8241-12701	125.697648	17.330886	22.87
1-166889	8459-9101	147.277689	44.048681	23.24
1-389503	8944-1901	147.638800	34.098819	22.54
1-394390	8943-12703	157.255706	36.605077	22.84
1-148985	8999-12704	164.982122	50.408830	23.00
1-489927	8338-12703	172.023327	23.429241	22.53
1-188218	8995-12702	175.948649	54.707498	22.70
1-259001	8464-12705	187.789625	44.712842	22.87
1-419251	8322-12703	200.702318	31.324497	22.92
1-260783	8447-12703	207.483361	40.895076	23.07
1-286805	8329-12702	211.677261	44.431671	23.41
1-592984	8335-12704	215.718400	40.622597	23.40
1-594082	9036-12701	238.268460	43.683850	22.88
1-93598	8548-12703	245.601009	47.731729	22.53
1-177632	9883-12705	256.723850	32.169550	23.02
1-232722	8462-12704	144.419761	38.062816	23.01
1-232333	8462-12702	145.202128	36.455540	22.91
1-389244	8150-12702	146.991437	32.991546	23.39
1-167337	8456-12704	150.842878	45.763536	22.56
1-487293	8448-12705	166.755650	22.296210	22.69
1-488469	8449-12701	167.380591	22.428005	22.81
1-591308	8323-12703	195.416050	36.290100	22.61
1-295955	9048-12704	244.698658	25.188738	22.58

1-66889 not covering the entire galaxy. In addition when looking at the galaxy images in Fig. 5.6, the majority of the LSBs seem as though they could be barred. We note again that our barred LSB candidates are simply those with bar weight votes greater than 0.5. It is therefore necessary for one to obtain rotation curves and pattern speeds for *all* of the LSBs we have identified, and classify the galaxies as barred based on further analysis.

Successfully measuring the bar pattern speed, Ω_b, using these MaNGA data cubes would increase the number of kinematic measurements for barred LSBs from 1 to 5. While it is valuable to obtain additional measurements of a relatively unstudied galaxy parameter, we would be unable to draw conclusions about the barred LSB population as a whole from only 5 galaxies. It is therefore necessary that a large number of barred LSBs are observed in order to fully probe this important subset of the galaxy population. This would be a challenging endeavour, due to the faint nature of LSBs, but in order to understand the true galaxy population, barred LSBs must be properly understood. However, before undertaking such a survey, these MaNGA data cubes will allow us to know if the TW method is appropriate to apply to LSBs, as well as if these data are high enough quality and spatial/spectral resolution for LSBs. It will then be possible to determine what instrumentation is required to undertake a future LSB survey. Finally, it is important to note that there are other IFU surveys that have different sample definitions and that this exercise only applies to the MaNGA sample. A larger LSB sample could be found in these other surveys.

CALIFA (Sánchez et al. 2012) has been previously discussed in this work (see Chapter 4, but likely would not provide an LSB sample given that it is comprised of only ∼650 nearby galaxies. Another candidate survey would be the Sydney-AAO Multi-object Integral field spectrograph (SAMI Croom et al. 2012). SAMI is comprised of 13 fiber bundles, called hexabundles, each made up of 61 fibers and having a total field of view of 15 arcsec. Unlike MaNGA, there is no stellar mass limit imposed on the sample selection, and is able to probe down to $\sim 10^7\ M_\odot$ (Bryant et al. 2015). The current data release contains 1559 galaxies (Scott et al. 2018), which could allow one to assemble a sample of LSBs for future study.

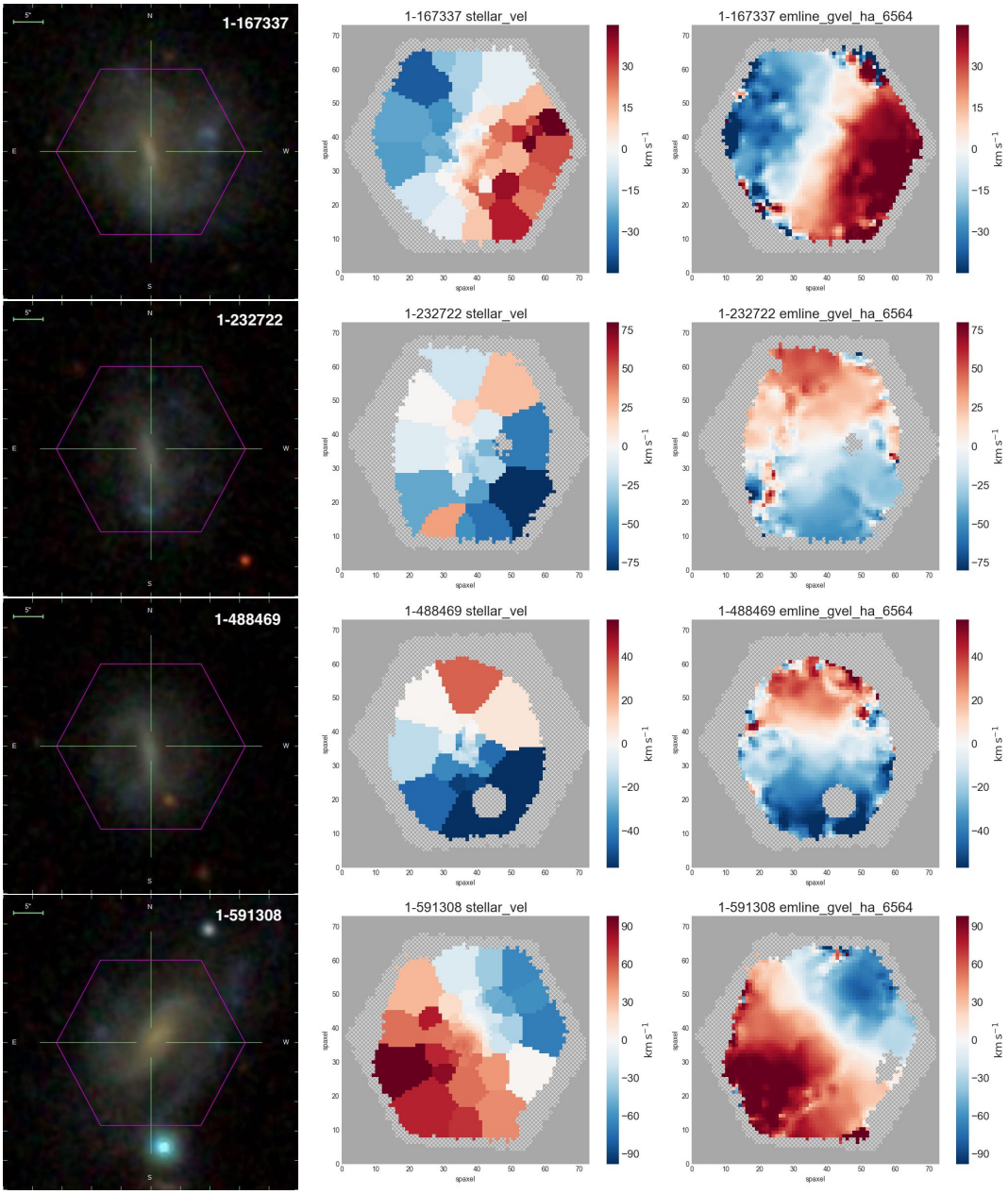

Figure 5.5: Barred LSBs in MaNGA with good quality data cubes. Here we show the SDSS image for each galaxy (left panel), as well as the stellar (2nd panel) and Hα (third panel) velocity maps. The velocity maps for each galaxy are all scaled to the same range.

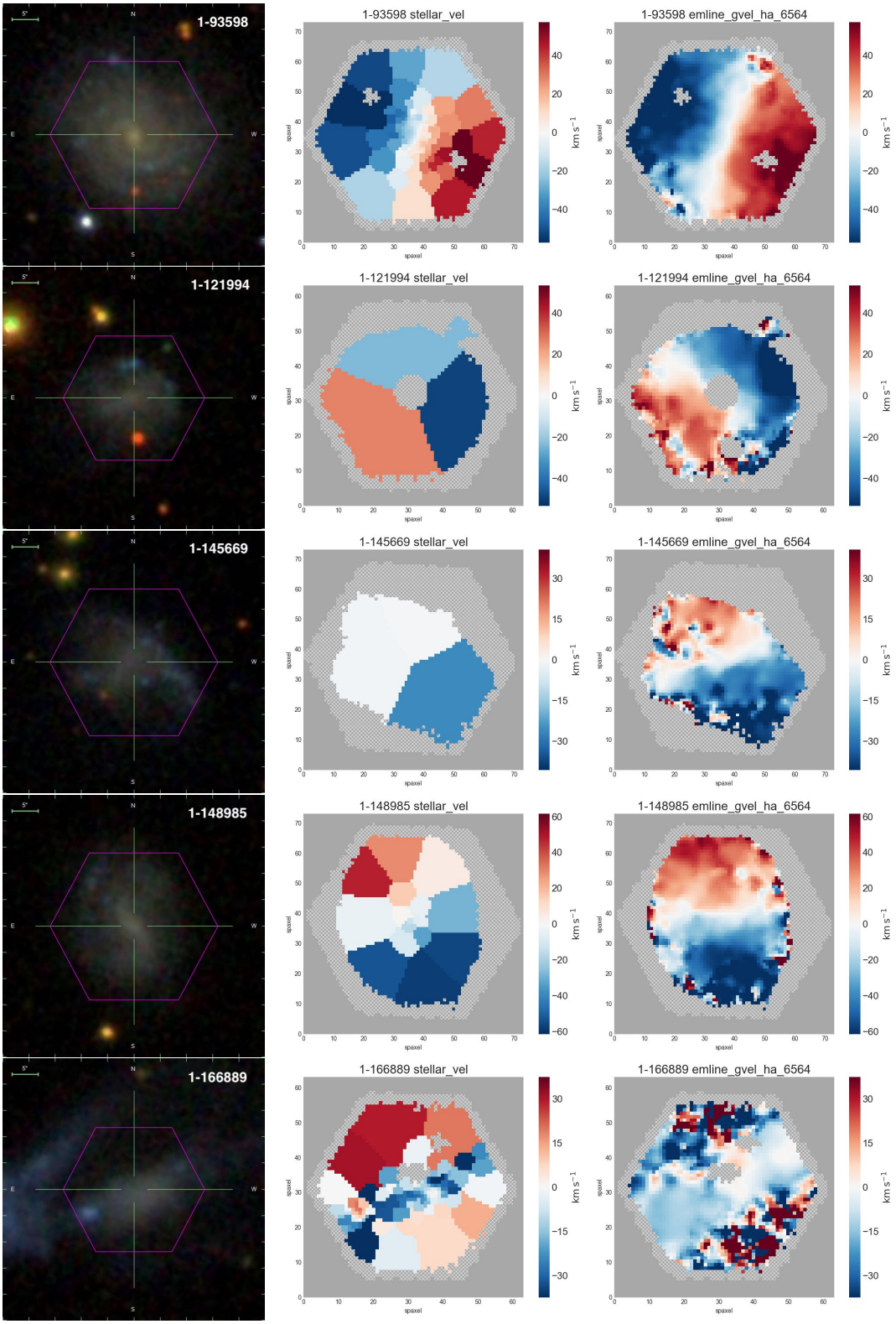

Figure 5.6: Remaining LSBs in MaNGA with good quality data cubes. Same as Fig. 5.5.

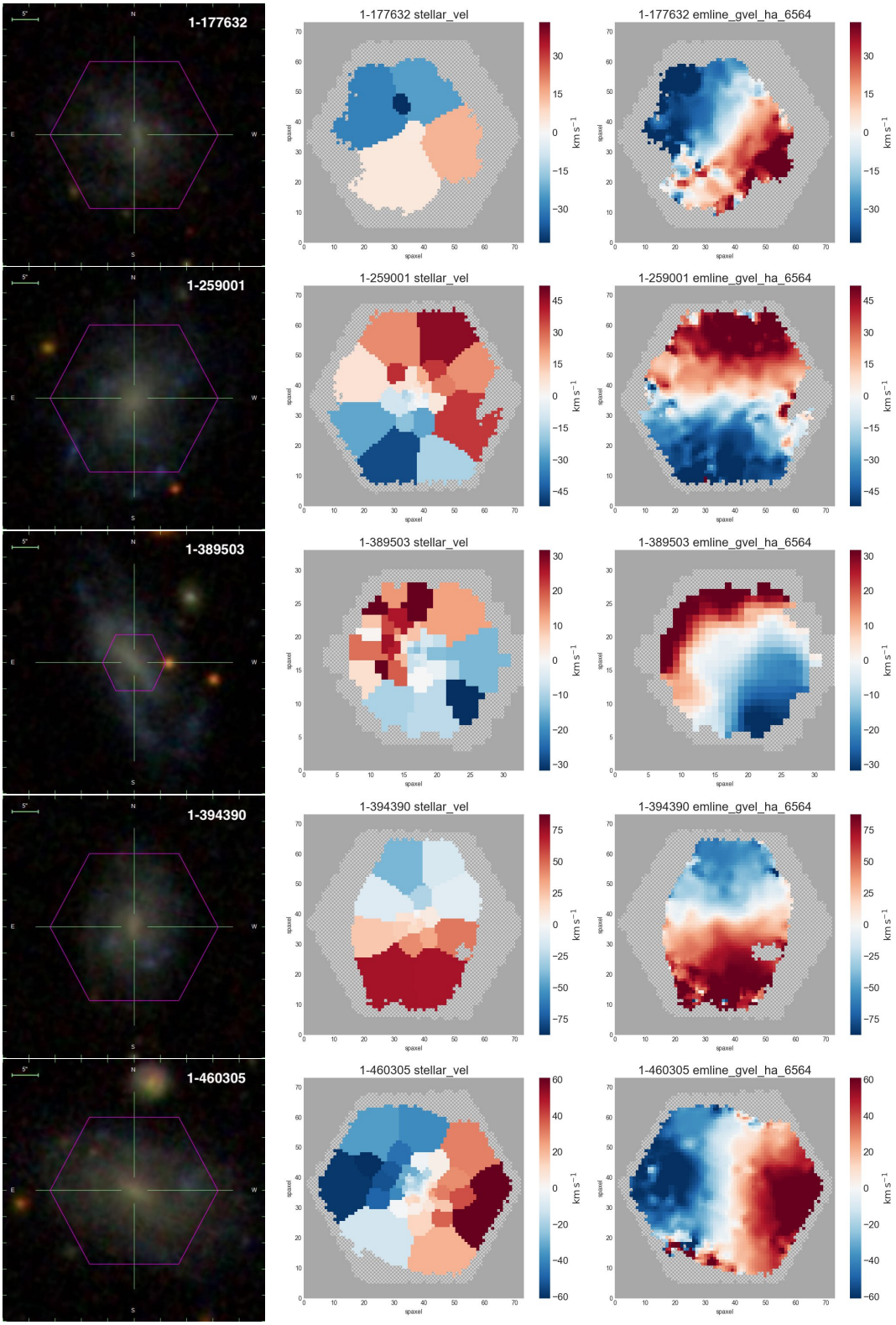

Figure 5.6: continued.

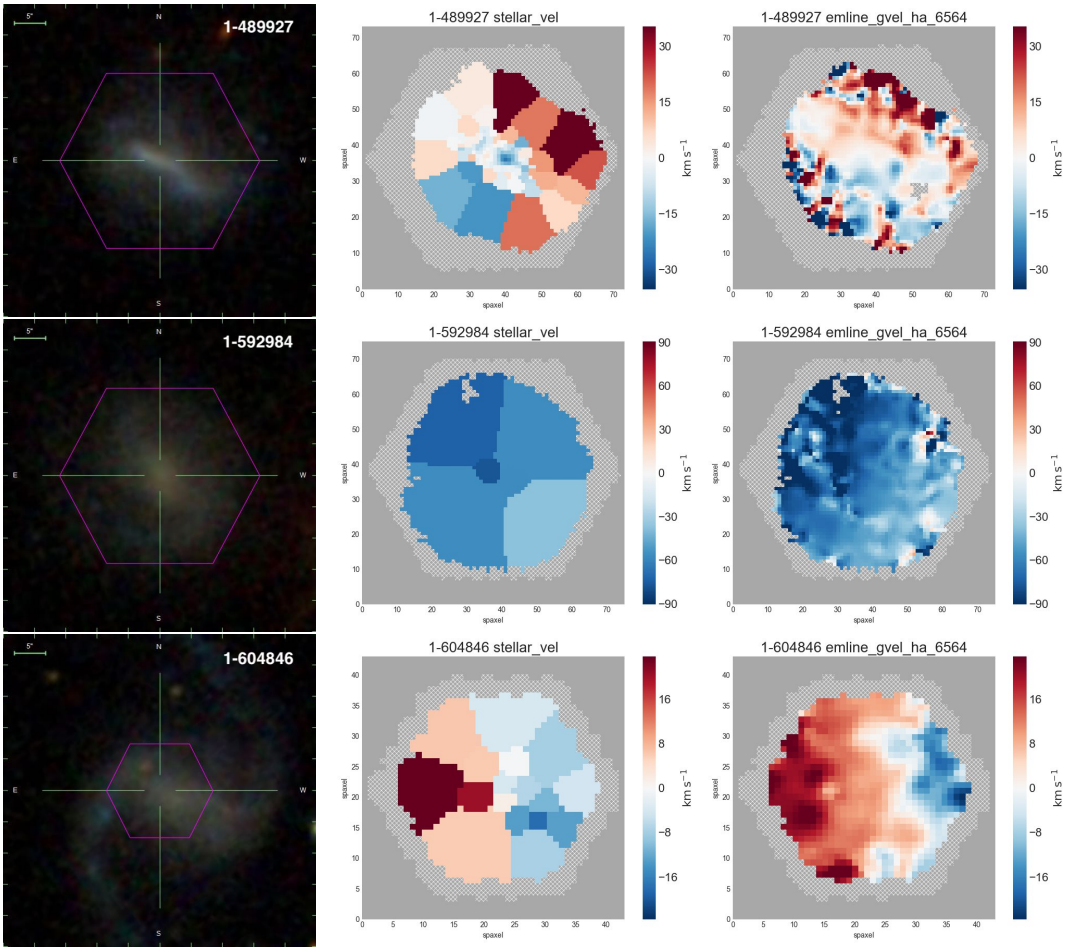

Figure 5.6: continued.

Chapter 6

Summary and Conclusions

6.1 Introduction

In this chapter, we summarize each preceding chapter in Sec. 6.2-6.5. We end with our main conclusions from this entire work in Sec. 6.6 and discuss outstanding questions and future work in Sec. 6.7.

6.2 Summary of Chapter 2

In Chapter 2, we measured the bar properties of four well studied LSBs: UGC 628, F563-V2, F568-1, and F568-3. We selected these galaxies as they had both existing photometry and mass modeling that confirmed they were low surface brightness galaxies. In addition, these four LSBs span very different morphologies, ranging from clear dual spiral structure in UGC 628 and F568-1, to lopsided spiral morphology in F568-3, to tenuous disk structure in F563-V2. We measured the bar lengths, strengths, and corotation radii of these galaxies, finding these bars to be roughly comparable to those in HSBs, albeit slightly shorter and weaker. In addition, we used the corotation radii to calculate the relative bar pattern speeds of these bars, finding that UGC 628, F568-1, and F568-3 were hosts to fast bars. This was intriguing, as UGC 628 previously had its bar pattern speed measured and was classified as a slow rotator. We attributed this discrepancy to a difference in bar length used when calculating the relative bar pattern speed, as when using the literature value for bar length we found UGC 628 to be host to a slow bar. We also developed a new means of measuring

the bar length in this chapter, based on analysis of azimuthal light profiles that performed the best out of the four methods tested.

6.3 Summary of Chapter 3

In Chapter 3, we applied the same methods used in Chapter 2 to 11 new barred LSBs identified from two large LSB catalogs. We found that when including the galaxies from Chapter 2, bars in LSBs were categorically shorter and weaker than those in HSBs, but had comparable relative bar pattern speeds. As determination of the relative bar pattern speed is directly dependent on the bar length, we created mock galaxy images with a disk and bar to apply the four bar length measures used to understand how accurate our bar lengths were. We found that our azimuthal bar length measure introduced in Chapter 2 performed the best and was the least biased measurement, leaving us to conclude that bars in LSBs were indeed fast. We also presented new B- and I-band magnitudes, colors, and surface brightnesses for the 11 additional barred LSBs in this chapter, as none existed in the literature. We found that all but one galaxy, UGC 2925, were clearly LSBs, with $\mu_0(B) > 22.5$ (mag arcsec^{-2}), and that barred LSBs were slightly brighter than unbarred LSBs. Finally, we obtained available HI fluxes and determined mass-to-light ratios from the $(B-I)$ colors to estimate gas and stellar masses. We found that barred LSBs were just as gas rich as their unbarred counterparts. In order to fully put these results into context with the general population of galaxies, we needed a more representative sample of HSBs. However, we noted that it was possible that a dark matter halo with a high spin could explain the short and weak bars in our LSBs.

6.4 Summary of Chapter 4

In Chapter 4, we identified a comparison sample of 24 HSBs and 2 LSBs from two large, representative surveys with available SDSS images. When applying our bar measures from the preceeding chapters to g- and i-band images, we found that bars in LSBs and HSBs formed a continuum across Hubble type, mass, and surface brightness. More specifically, we

found that the normalized bar length and bar strength formed clear trends as functions of these galaxy properties. However, we did not find any trends with the relative bar pattern speed, suggesting that bars were fast across Hubble type, mass, and surface brightness. Based on all three of these results, we interpreted this as evidence of barred LSBs existing in high spin dark matter halos. Together with the vast reserves of gas present in these galaxies, the high spin dark matter halos prevent bars from growing in length or strength. In addition, high spinning halos do not serve as good angular momentum sinks, preventing the bar from slowing down significantly over time. These conclusions were consistent with previous findings. However, we noted that based on recent findings regarding the reliability of the relative bar pattern speed, spectroscopic analysis of barred LSBs was required to fully probe the nature of the dark matter halos these galaxies are embedded in.

6.5 Summary of Chapter 5

In Chapter 5, we discussed the relevance and implications of our results, as well as exploring possible future work. We noted that bars in LSBs are still relatively poorly understood when compared to those in HSBs, but that recent work was shedding additional light. We also noted that while our results about bar length and strength were consistent with previous findings, we presented the currently largest number of relative bar pattern speed measurements for LSBs, finding almost all to be fast rotators. In order to explain our results, we estimated the spin of the underlying dark matter halos of both our LSB and HSB samples, finding that the previous trends with Hubble type, mass, and surface brightness were best explained by the halo spin. Thus, we concluded that the short, weak, and fast nature of the bars in LSBs are best explained by the fact that these galaxies have vast reserves of gas and are embedded in high spin dark matter halos. We ended this section by examining the MaNGA survey in order to identify any possible targets for future spectroscopic study. After a series of cuts to the sample, we found 29 possible LSBs and 8 possible barred LSBs out of roughly 1500 disk galaxies in MaNGA. As large scale surveys are biased against LSBs due to both sample

selection (e.g. only selecting galaxies with stellar masses greater than 10^9 $M_\odot$) as well as the large observational overhead, a dedicated spectroscopic survey of LSBs may be required in order to study the kinematics of barred LSBs en masse.

6.6 Conclusions

We list our main conclusions from this dissertation in terms of the four goals listed in Chapter 1:

1. **Characterize the bar properties for a large sample of barred LSBs.** We successfully measured the bar length, strength, and corotation radius of 15 barred LSBs. We employed the use of azimuthal light profiles in order to measure all three properties with only photometry, and developed a new bar length measure using these profiles. In conjunction with the bar length, our corotation radii measurements constitute the currently largest number of relative bar pattern speed measurements for LSBs, finding 13 to be hosts to fast bars.

2. **Obtain surface brightness profiles, magnitudes, and colors for barred LSBs.** We successfully obtained new B- and I-band photometry for 11 barred LSBs. We found barred LSBs were slightly brighter than the general LSB population, but had very similar blue colors and relatively long disk scale lengths.

3. **Obtain stellar and gas mass estimates for barred LSBs.** We successfully obtained mass estimates for 10 barred LSBs using our I-band photometry and available HI fluxes in the literature. We found that barred LSBs were just as gas rich as the unbarred LSB population, having $f_{gas} = M_{gas}/(M_{gas} + M_*) > 0.5$.

4. **Compare our results for barred LSBs with those from barred HSBs.** We applied the same measurement techniques to a sample of 26 HSB across various Hubble types, assembled from two large, statistically complete surveys to obtain bar lengths,

strengths, and corotation radii. We applied these techniques to SDSS fully reduced g- and i-band images and found bars in LSBs to be categorically shorter and weaker than those in HSBs. However, we found that bars in LSBs and HSBs are almost all fast rotators when examining the relative bar pattern speed, suggesting that bars in galaxies have not experienced significant slowdown due to dark matter halos.

6.7 Unanswered Questions and Next Steps

Based on our findings, it appears as though bars in LSBs have not been slowed down due to their dark matter halos. When estimating the halo spin parameter λ, we found that the barred LSBs were embedded in high spin halos ($\lambda > 0.03$), which, when also accounting for the large reserves of gas in these galaxies, can explain the short, weak, and fast nature of the bars in LSBs. However, we are unable to say more about the dark matter halos these galaxies are embedded in with our current data, and are therefore left with the following unanswered questions:

1. **What is the nature of the dark matter halos in barred LSBs?** We know that observations of non-barred LSBs suggest that the halo density profiles are cored, while numerical simulations predict cuspy halos. However, barred LSBs have been historically avoided in previous LSB studies. Therefore, this is still unexplored territory. Are barred LSBs embedded in similar halos to the general LSB population? Do they show more evidence of having cored halos, or do they show evidence of having cuspy halos? What does the high spin nature of the halos suggest about the evolution of the dark matter halos and its interaction with the disk?

2. **How are bars in LSBs formed, and how do they evolve?** While simulations have predicted that bars in LSBs, if they form, are shorter and weaker when compared to those in HSBs, we have shown that bars in LSBs are fast rotators. Cold dark matter numerical simulations must be able to reproduce or explain this facet of bars in LSBs.

In addition, as larger numbers of barred LSBs are being discovered, simulations must be able to predict the formation and evolution of these galaxies. Do bars in LSBs form at similar times to those in HSBs? Are fast bars in LSBs consistent with a centrally dense, cuspy dark matter halo? If not, is there some process that has changed the halo shape, or are the halos actually cored? How does the large reserve of gas affect the formation of a bar in a high spin halo?

In order to answer these questions, two different approaches must be taken, both of which are no easy task. Question 1 requires mass modeling of a large sample of barred LSBs in order to determine the shape of the dark matter halo in these galaxies. This poses two challenges, namely the observational overhead required, and the complications on deriving rotation curves from velocity fields when a bar is present. We have shown that even in a large IFU survey like MaNGA, barred LSBs are heavily biased against (we estimated there are 4 barred LSBs with good quality data out of the $\sim$1500 disk galaxies in MaNGA). Therefore, even if the available data from this and other surveys are adequate, the sample would not be large or representative enough to answer this question. However, given the recent advent of large LSB catalogs (there are 12282 LSBs alone in Zhong et al. 2008), it is possible to identify such a sample in order to undertake an IFU survey. However, another complication is selecting an appropriately sized IFU for such a survey, as the entire disk of the barred LSB would need to be observed. While this would obviously invoke a significant amount of observational time, it would help shed further light on a virtually unknown facet of the barred LSB population: their kinematics.

Question 2, on the other hand, requires high resolution, hydrodynamical simulations. We have shown that barred LSBs are just as gas rich as the general LSB population, so gas cannot be ignored in these simulations. In addition, various halo profiles must be considered in order to determine what is most consistent with observations, rather than simply invoking a centrally dense, cuspy halo. Collier et al. (2018), for example, explore bar formation and evolution for various halo spins ($0 < \lambda < 0.09$), but only consider a cuspy NFW halo ($\alpha = -2$)

and a disk with no gas. Again, a significant amount of time would be required to run such a suite of simulations, but it is necessary in order to fully explain the observations of bars in LSBs. Possibly fulfilling such a requirement is the Illustris simulation (Vogelsberger et al. 2014).

Illustris is an impressive hydrodynamical cosmological simulation that aims to explore the formation and evolution of our Universe, and broadly matches various galaxy scaling relations (Vogelsberger et al. 2014; Genel et al. 2014). However, there appear to be significant problems with 'low-mass' galaxies (defined as $M_* < 10^{11}\ M_\odot$) (Genel et al. 2014). Given that this stellar mass is quite high (eclipsing all of our LSBs, and most of the galaxy population as a whole), and that the baryonic resolution is still $\sim 10^6\ M_\odot$, it would be better if individual simulations of barred LSBs were run, rather than large-scale, cosmological simulations with the hopes of finding barred LSBs.

We have shown that barred LSBs are important to our understanding of the galaxy population as a whole. Future work will shed light on the nature of the interaction between dark matter halos and galaxy disks, and bars in LSBs will be vital in forming a complete picture.

Bibliography

Abraham, R. G., & Merrifield, M. R. 2000, AJ, 120, 2835

Aguado, D. S., Ahumada, R., Almeida, A., et al. 2019, The Astrophysical Journal Supplement Series, 240, 23.

Aguerri, J. A. L., Beckman, J. E., & Prieto, M. 1998, AJ, 116, 2136

Aguerri, J. A. L., Muñoz-Tuñón, C., Varela, A. M., & Prieto, M. 2000, A&A, 361, 841

Aguerri, J. A. L., Varela, A. M., Prieto, M., & Muñoz-Tuñón, C. 2000, AJ, 119, 1638

Aguerri, J. A. L., Méndez-Abreu, J., & Corsini, E. M. 2009, A&A, 495, 491

Aguerri, J. A. L., Méndez-Abreu, J., Falcón-Barroso, J., et al. 2015, A&A, 576, A102

Astropy Collaboration, Robitaille, T. P., Tollerud, E. J., et al. 2013, A&A, 558, A33

The Astropy Collaboration, Price-Whelan, A. M., Sipőcz, B. M., et al. 2018, arXiv:1801.02634

Athanassoula, E. 1980, A&A, 88, 184

Athanassoula, E., Morin, S., Wozniak, H., et al. 1990, MNRAS, 245, 130

Athanassoula, E. 1992, MNRAS, 259, 345

Bahcall, J. N., & Casertano, S. 1985, ApJ, 293, L7

Banerjee, A., Patra, N. N., Chengalur, J. N., & Begum, A. 2013, MNRAS, 434, 1257

Beckman, J. E., & Cepa, J. 1990, A&A, 229, 37

Beijersbergen, M., de Blok, W. J. G., & van der Hulst, J. M. 1999, A&A, 351, 903

Bell, E. F., Barnaby, D., Bower, R. G., et al. 2000, MNRAS, 312, 470

Bell, E. F., McIntosh, D. H., Katz, N., & Weinberg, M. D. 2003, ApJS, 149, 289

Binney, J., & Tremaine, S. 2008, Galactic Dynamics: Second Edition, by James Binney and Scott Tremaine. ISBN 978-0-691-13026-2 (HB). Published by Princeton University Press, Princeton, NJ USA, 2008.,

Blais-Ouellette, S., Amram, P., Carignan, C., & Swaters, R. 2004, A&A, 420, 147

Blanton, M. R., Bershady, M. A., Abolfathi, B., et al. 2017, AJ, 154, 28

Blumenthal, G. R., Pagels, H., & Primack, J. R. 1982, Nature, 299, 37

Blumenthal, G. R., Faber, S. M., Primack, J. R., & Rees, M. J. 1984, Nature, 311, 517

Boissier, S., Monnier Ragaigne, D., Prantzos, N., et al. 2003, MNRAS, 343, 653

Bond, J. R., Szalay, A. S., & Turner, M. S. 1982, Physical Review Letters, 48, 1636

Bosma, A. 1978, Ph.D. Thesis

Bothun, G. D., Schombert, J. M., Impey, C. D., Sprayberry, D., & McGaugh, S. S. 1993, AJ, 106, 530

Bothun, G., Impey, C., & McGaugh, S. 1997, PASP, 109, 745

Bottrell, C., Torrey, P., Simard, L., et al. 2017, MNRAS, 467, 2879

Bryant, J. J., Owers, M. S., Robotham, A. S. G., et al. 2015, MNRAS, 447, 2857

Bundy, K., Bershady, M. A., Law, D. R., et al. 2015, ApJ, 798, 7

Bureau, M., Freeman, K. C., Pfitzner, D. W., & Meurer, G. R. 1999, AJ, 118, 2158

Burkholder, V., Impey, C., & Sprayberry, D. 2001, AJ, 122, 2318

Buta, R. 1986, ApJS, 61, 609

Buta, R., & Block, D. L. 2001, ApJ, 550, 243

Buta, R. J., & Zhang, X. 2009, ApJS, 182, 559

Casteels, K. R. V., Bamford, S. P., Skibba, R. A., et al. 2013, MNRAS, 429, 1051

Cervantes-Sodi, B., Hernandez, X., Park, C., & Kim, J. 2008, MNRAS, 388, 863

Cervantes-Sodi, B., Li, C., Park, C., & Wang, L. 2013, ApJ, 775, 19

Cervantes Sodi, B., Li, C., & Park, C. 2015, ApJ, 807, 111

Cervantes Sodi, B. 2017, ApJ, 835, 80

Cervantes Sodi, B., & Sánchez García, O. 2017, ApJ, 847, 37

Chambers, K. C., Magnier, E. A., Metcalfe, N., et al. 2016, arXiv:1612.05560

Chemin, L., & Hernandez, O. 2009, A&A, 499, L25

Chequers, M. H., Spekkens, K., Widrow, L. M., & Gilhuly, C. 2016, MNRAS, 463, 1751

Collier, A., Shlosman, I., & Heller, C. 2018, MNRAS, 476, 1331

Combes, F., & Sanders, R. H. 1981, A&A, 96, 164

Contopoulos, G. 1980, A&A, 81, 198

Cook, D. O., Dale, D. A., Johnson, B. D., et al. 2014, MNRAS, 445, 890

Corsini, E. M., Aguerri, J. A. L., Debattista, V. P., et al. 2007, ApJ, 659, L121

Corsini, E. M. 2011, Memorie della Societa Astronomica Italiana Supplementi, 18, 23

Cousins, A. W. J. 1984, South African Astronomical Observatory Circular, 8, 59

Croom, S. M., Lawrence, J. S., Bland-Hawthorn, J., et al. 2012, MNRAS, 421, 872

Cowsik, R., & McClelland, J. 1973, ApJ, 180, 7

Dalcanton, J. J., Spergel, D. N., & Summers, F. J. 1997, ApJ, 482, 659

Davis, M., Efstathiou, G., Frenk, C. S., & White, S. D. M. 1985, ApJ, 292, 371

Debattista, V. P., & Sellwood, J. A. 2000, ApJ, 543, 704

Debattista, V. P. 2003, MNRAS, 342, 1194

Debattista, V. P., & Williams, T. B. 2004, ApJ, 605, 714

de Blok, W. J. G. 2005, ApJ, 634, 227

de Blok, W. J. G. 2010, Advances in Astronomy, 2010, 789293

de Blok, W. J. G., van der Hulst, J. M., & Bothun, G. D. 1995, MNRAS, 274, 235

de Blok, W. J. G., & McGaugh, S. S. 1996, ApJ, 469, L89

de Blok, W. J. G., McGaugh, S. S., & van der Hulst, J. M. 1996, MNRAS, 283, 18

de Blok, W. J. G., & McGaugh, S. S. 1997, MNRAS, 290, 533

de Blok, W. J. G., & van der Hulst, J. M. 1998, A&A, 335, 421

de Blok, W. J. G., McGaugh, S. S., Bosma, A., & Rubin, V. C. 2001a, ApJ, 552, L23

de Blok, W. J. G., McGaugh, S. S., & Rubin, V. C. 2001b, AJ, 122, 2396

de Blok, W. J. G., & Bosma, A. 2002, A&A, 385, 816

de Blok, W. J. G., Bosma, A., & McGaugh, S. 2003, MNRAS, 340, 657

de Vaucouleurs, G. 1959, Handbuch der Physik, 53, 275

Díaz-García, S., Salo, H., Laurikainen, E., & Herrera-Endoqui, M. 2016, A&A, 587, A160

Disney, M. J. 1976, Nature, 263, 573

Du, W., Wu, H., Lam, M. I., et al. 2015, AJ, 149, 199

Du, W., Cheng, C., Wu, H., Zhu, M., & Wang, Y. 2019, MNRAS, 483, 1754

Dubinski, J., & Carlberg, R. G. 1991, ApJ, 378, 496

Efstathiou, G., Lake, G., & Negroponte, J. 1982, MNRAS, 199, 1069

Elmegreen, B. G., & Elmegreen, D. M. 1985, ApJ, 288, 438

Elmegreen, B. G., Elmegreen, D. M., Chromey, F. R., Hasselbacher, D. A., & Bissell, B. A. 1996, AJ, 111, 2233

El-Zant, A., & Shlosman, I. 2002, ApJ, 577, 626

Erwin, P. 2005, MNRAS, 364, 283

Erwin, P. 2018, MNRAS, 474, 5372

Eskridge, P. B., Frogel, J. A., Pogge, R. W., et al. 2000, AJ, 119, 536

van Eymeren, J., Trachternach, C., Koribalski, B. S., & Dettmar, R.-J. 2009, A&A, 505, 1

Font, J., Beckman, J. E., Martínez-Valpuesta, I., et al. 2017, ApJ, 835, 279

Font, J., Beckman, J. E., James, P. A., & Patsis, P. A. 2019, MNRAS, 482, 5362

Freeman, K. C. 1970, ApJ, 160, 811

Fuchs, B. 2003, AP&SS, 284, 719

Fujii, M. S., Bédorf, J., Baba, J., & Portegies Zwart, S. 2019, MNRAS, 482, 1983

Genel, S., Vogelsberger, M., Springel, V., et al. 2014, MNRAS, 445, 175

Gerin, M., Combes, F., & Athanassoula, E. 1990, A&A, 230, 37

Gerssen, J., Kuijken, K., & Merrifield, M. R. 1999, MNRAS, 306, 926

Greco, J. P., Greene, J. E., Strauss, M. A., et al. 2018, ApJ, 857, 104

Guo, R., Mao, S., Athanassoula, E., et al. 2019, MNRAS, 482, 1733

Haghi, H., Khodadadi, A., Ghari, A., Zonoozi, A. H., & Kroupa, P. 2018, MNRAS, 477, 4187

Haynes, M. P., & Giovanelli, R. 1984, AJ, 89, 758

Hernandez, X., & Cervantes-Sodi, B. 2006, MNRAS, 368, 351

Hinz, J. L., Rieke, M. J., Rieke, G. H., et al. 2007, ApJ, 663, 895

Ho, L. C., Li, Z.-Y., Barth, A. J., Seigar, M. S., & Peng, C. Y. 2011, ApJS, 197, 21

Honey, M., Das, M., Ninan, J. P., & Manoj, P. 2016, MNRAS, 462, 2099

Honey, M., van Driel, W., Das, M., & Martin, J.-M. 2018, MNRAS, 476, 4488

Impey, C. D., Sprayberry, D., Irwin, M. J., & Bothun, G. D. 1996, ApJS, 105, 209

Impey, C., & Bothun, G. 1997, ARA&A, 35, 267

Into, T., & Portinari, L. 2013, MNRAS, 430, 2715

Jimenez, R., Padoan, P., Matteucci, F., & Heavens, A. F. 1998, MNRAS, 299, 123

Johnson, H. L., Mitchell, R. I., Iriarte, B., & Wisniewski, W. Z. 1966, Communications of the Lunar and Planetary Laboratory, 4, 99

Kent, S. M. 1987, AJ, 93, 816

Kent, S. M. 1987, AJ, 93, 1062

Kim, J.-h., & Lee, J. 2013, MNRAS, 432, 1701

Kuzio de Naray, R., McGaugh, S. S., & de Blok, W. J. G. 2004, MNRAS, 355, 887

Kuzio de Naray, R., McGaugh, S. S., de Blok, W. J. G., & Bosma, A. 2006, ApJS, 165, 461

Kuzio de Naray, R., McGaugh, S. S., & de Blok, W. J. G. 2008, ApJ, 676, 920-943

Kuzio de Naray, R., McGaugh, S. S., & Mihos, J. C. 2009, ApJ, 692, 1321

Kuzio de Naray, R., & Spekkens, K. 2011, ApJ, 741, L29

Kuzio de Naray, R., & Kaufmann, T. 2011, MNRAS, 414, 3617

Landolt, A. U. 1992, AJ, 104, 340

Laurikainen, E., & Salo, H. 2002, MNRAS, 337, 1118

Laurikainen, E., Salo, H., & Buta, R. 2005, MNRAS, 362, 1319

Lee, H.-c., Gibson, B. K., Flynn, C., Kawata, D., & Beasley, M. A. 2004, MNRAS, 353, 113

Lee, G.-H., Park, C., Lee, M. G., & Choi, Y.-Y. 2012, ApJ, 745, 125

Lelli, F., McGaugh, S. S., Schombert, J. M., Desmond, H., & Katz, H. 2019, MNRAS, 484, 3267

Li, Z.-Y., Ho, L. C., Barth, A. J., & Peng, C. Y. 2011, ApJS, 197, 22

Lin, C. C., & Shu, F. H. 1964, ApJ, 140, 646

Lin, Y., Cervantes Sodi, B., Li, C., Wang, L., & Wang, E. 2014, ApJ, 796, 98

Long, S., Shlosman, I., & Heller, C. 2014, ApJ, 783, L18

Makarov, D., Prugniel, P., Terekhova, N., Courtois, H., & Vauglin, I. 2014, A&A, 570, A13

Marinova, I., & Jogee, S. 2007, ApJ, 659, 1176

Martin, P. 1995, AJ, 109, 2428

Martínez-García, E. E., & Puerari, I. 2014, ApJ, 790, 118

Masters, K. L., Nichol, R. C., Haynes, M. P., et al. 2012, MNRAS, 424, 2180

Matthews, L. D., & Wood, K. 2001, ApJ, 548, 150

Mayer, L., & Wadsley, J. 2004, MNRAS, 347, 277

McGaugh, S. S., & Bothun, G. D. 1994, AJ, 107, 530

McGaugh, S. S., & de Blok, W. J. G. 1997, ApJ, 481, 689

McGaugh, S. S., Schombert, J. M., & Bothun, G. D. 1995a, AJ, 109, 2019

McGaugh, S. S., Bothun, G. D., & Schombert, J. M. 1995b, AJ, 110, 573

McGaugh, S. S. 1996, MNRAS, 280, 337

McGaugh, S. S., Schombert, J. M., Bothun, G. D., & de Blok, W. J. G. 2000, ApJ, 533, L99

McGaugh, S. S., Rubin, V. C., & de Blok, W. J. G. 2001, AJ, 122, 2381

McGaugh, S. S., & Schombert, J. M. 2014, AJ, 148, 77

Merrifield, M. R., & Kuijken, K. 1995, MNRAS, 274, 933

Menéndez-Delmestre, K., Sheth, K., Schinnerer, E., Jarrett, T. H., & Scoville, N. Z. 2007, ApJ, 657, 790

Michel-Dansac, L., & Wozniak, H. 2006, A&A, 452, 97

Mihos, J. C., McGaugh, S. S., & de Blok, W. J. G. 1997, ApJ, 477, L79

Mihos, J. C., Spaans, M., & McGaugh, S. S. 1999, ApJ, 515, 89

Mo, H. J., McGaugh, S. S., & Bothun, G. D. 1994, MNRAS, 267

Navarro, J. F., Frenk, C. S., & White, S. D. M. 1996, ApJ, 462, 563

Navarro, J. F., Eke, V. R., & Frenk, C. S. 1996, MNRAS, 283, L72

Navarro, J. F., Frenk, C. S., & White, S. D. M. 1997, ApJ, 490, 493

Ohta, K., Hamabe, M., & Wakamatsu, K.-I. 1990, ApJ, 357, 71

O'Neil, K., Bothun, G. D., Schombert, J., Cornell, M. E., & Impey, C. D. 1997, AJ, 114, 2448

O'Neil, K., Bothun, G. D., & Schombert, J. 2000, AJ, 119, 136

O'Neil, K., & Bothun, G. 2000, ApJ, 529, 811

Ostriker, J. P., & Peebles, P. J. E. 1973, ApJ, 186, 467

Pahwa, I., & Saha, K. 2018, MNRAS, 478, 4657

Pedani, M. 2009, PASP, 121, 778

Peebles, P. J. E. 1969, ApJ, 155, 393

Peebles, P. J. E. 1971, A&A, 11, 377

Peebles, P. J. E. 1982, ApJ, 263, L1

Pérez, I., Aguerri, J. A. L., & Méndez-Abreu, J. 2012, A&A, 540, A103

Peters, W., & Kuzio de Naray, R. 2018, MNRAS, 476, 2938

Peters, W., & Kuzio de Naray, R. 2019, MNRAS, 484, 850

Pineda, J. C. B., Hayward, C. C., Springel, V., & Mendes de Oliveira, C. 2017, MNRAS, 466, 63

Pizagno, J., Prada, F., Weinberg, D. H., et al. 2007, AJ, 134, 945

Pontzen, A., & Governato, F. 2012, MNRAS, 421, 3464

Puerari, I., & Dottori, H. 1997, ApJ, 476, L73

Rautiainen, P., Salo, H., & Buta, R. 2004, MNRAS, 349, 933

Rautiainen, P., Salo, H., & Laurikainen, E. 2005, ApJ, 631, L129

Rautiainen, P., Salo, H., & Laurikainen, E. 2008, MNRAS, 388, 1803

Reid, I. N., Brewer, C., Brucato, R. J., et al. 1991, PASP, 103, 661

Richmond, M. W., Droege, T. F., Gombert, G., et al. 2000, Publications of the Astronomical Society of the Pacific, 112, 397

Rosenbaum, S. D., & Bomans, D. J. 2004, A&A, 422, L5

Rubin, V. C., & Ford, W. K., Jr. 1970, ApJ, 159, 379

Rubin, V. C., Ford, W. K., Jr., & Thonnard, N. 1978, ApJ, 225, L107

Rubin, V. C., Ford, W. K., Jr., & Thonnard, N. 1980, ApJ, 238, 471

Rubin, V. C., Ford, W. K., Jr., Thonnard, N., & Burstein, D. 1982, ApJ, 261, 439

Rubin, V. C., Burstein, D., Ford, W. K., Jr., & Thonnard, N. 1985, ApJ, 289, 81

Salo, H., Rautiainen, P., Buta, R., et al. 1999, AJ, 117, 792

Sánchez, S. F., Kennicutt, R. C., Gil de Paz, A., et al. 2012, A&A, 538, A8

Schlafly, E. F., & Finkbeiner, D. P. 2011, ApJ, 737, 103

Schmidt, M. 1957, Bull. Astron. Inst. Netherlands, 14, 17

Schombert, J. M., Bothun, G. D., Schneider, S. E., & McGaugh, S. S. 1992, AJ, 103, 1107

Schombert, J., Maciel, T., & McGaugh, S. 2011, Advances in Astronomy, 2011, 143698

Schombert, J. M., & McGaugh, S. 2014, Publ. Astron. Soc. Australia, 31, e011

Schombert, J., McGaugh, S., & Lelli, F. 2019, MNRAS, 483, 1496

Scott, N., van de Sande, J., Croom, S. M., et al. 2018, MNRAS, 481, 2299

Sellwood, J. A., & Debattista, V. P. 2006, ApJ, 639, 868

Sellwood, J. A., & Sánchez, R. Z. 2010, MNRAS, 404, 1733

Sierra, A. D., Seigar, M. S., Treuthardt, P., & Puerari, I. 2015, MNRAS, 450, 1799

Spekkens, K., & Sellwood, J. A. 2007, ApJ, 664, 204

Spekkens, K., Giovanelli, R., & Haynes, M. P. 2005, AJ, 129, 2119

Swaters, R. A. 1999, Ph.D. Thesis,

Swaters, R. A., Madore, B. F., & Trewhella, M. 2000, ApJ, 531, L107

Swaters, R. A., Madore, B. F., van den Bosch, F. C., & Balcells, M. 2003, ApJ, 583, 732

Swaters, R. A., Sanders, R. H., & McGaugh, S. S. 2010, ApJ, 718, 380

Tollet, E., Macciò, A. V., Dutton, A. A., et al. 2016, MNRAS, 456, 3542

Trachternach, C., Bomans, D. J., Haberzettl, L., & Dettmar, R.-J. 2006, A&A, 458, 341

Tremaine, S., & Weinberg, M. D. 1984, ApJ, 282, L5

Trujillo, I., Aguerri, J. A. L., Cepa, J., & Gutiérrez, C. M. 2001, MNRAS, 328, 977

Tully, R. B., Courtois, H. M., & Sorce, J. G. 2016, AJ, 152, 50

Valenzuela, O., & Klypin, A. 2003, MNRAS, 345, 406

van Albada, T. S., & Sancisi, R. 1986, Philosophical Transactions of the Royal Society of London Series A, 320, 447

van den Bosch, F. C., Robertson, B. E., Dalcanton, J. J., & de Blok, W. J. G. 2000, AJ, 119, 1579

van den Bosch, F. C., & Swaters, R. A. 2001, MNRAS, 325, 1017

van den Hoek, L. B., de Blok, W. J. G., van der Hulst, J. M., & de Jong, T. 2000, A&A, 357, 397

van de Hulst, H. C., Raimond, E., & van Woerden, H. 1957, Bull. Astron. Inst. Netherlands, 14, 1

van der Hulst, J. M., Skillman, E. D., Smith, T. R., et al. 1993, AJ, 106, 548

Villa-Vargas, J., Shlosman, I., & Heller, C. 2010, ApJ, 719, 1470

van Zee, L., Haynes, M. P., Salzer, J. J., & Broeils, A. H. 1997, AJ, 113, 1618

van Zee, L., Haynes, M. P., & Salzer, J. J. 1997, AJ, 114, 2497

Vera-Villamizar, N., Dottori, H., Puerari, I., & de Carvalho, R. 2001, ApJ, 547, 187

Vogelsberger, M., Genel, S., Springel, V., et al. 2014, MNRAS, 444, 1518

Volders, L. M. J. S. 1959, Bull. Astron. Inst. Netherlands, 14, 323

Weinberg, M. D. 1985, MNRAS, 213, 451

Willett, K. W., Lintott, C. J., Bamford, S. P., et al. 2013, MNRAS, 435, 2835

Willmer, C. N. A. 2018, The Astrophysical Journal Supplement Series, 236, 47.

Wittmann, C., Lisker, T., Ambachew Tilahun, L., et al. 2017, MNRAS, 470, 1512

Wozniak, H., Friedli, D., Martinet, L., Martin, P., & Bratschi, P. 1995, A&AS, 111, 115

Wyder, T. K., Martin, D. C., Barlow, T. A., et al. 2009, ApJ, 696, 1834

York, D. G., Adelman, J., Anderson, J. E., Jr., et al. 2000, AJ, 120, 1579

Zana, T., Dotti, M., Capelo, P. R., et al. 2018, MNRAS, 473, 2608

Zhong, G. H., Liang, Y. C., Liu, F. S., et al. 2008, MNRAS, 391, 986

Zwicky, F. 1933, Helvetica Physica Acta, 6, 110

Zwicky, F. 1957, Berlin: Springer, 1957

Appendix A

Fringe Removal

The ARCTIC imager on the 3.5m telescope at Apache Point Observatory (APO) allows us to obtain high quality, high spatial resolution optical images of low surface brightness galaxies (LSBs). However, the I-band filter suffers from some severe fringing that must be removed before any analysis is done. Here, we detail the process we employed in order to obtain our clean I-band images.

In Fig. A.1 we show four I-band images of four different barred LSBs: LEDA 135682 (top left), LEDA 135684 (top right), LEDA 135693 (bottom left), and UGC 2925 (bottom right). The fringing is quite obvious in these images, often obscuring the galaxies significantly. In order to remove this fringing pattern, we followed the same approach for each night of observing: obtain enough I-band images in order to construct a master fringe pattern by averaging the images together. This was accomplished in the following way:

1. **Observe each target more than once.** Not only is this necessary to combat the sky noise, but also provides additional images for averaging.

2. **Dither significantly between each observation.** Our final master fringe image must only contain signal from the fringe patter itself, therefore our dithering pattern ensures that signal from the same galaxy field do not overlap when averaging.

3. **Observe additional dark regions of the sky as needed.** Ideally, one would be able to obtain all the data needed to construct a master fringe from the science images. However, if this is not possible, deep images (i.e. >100 seconds of exposure time) of

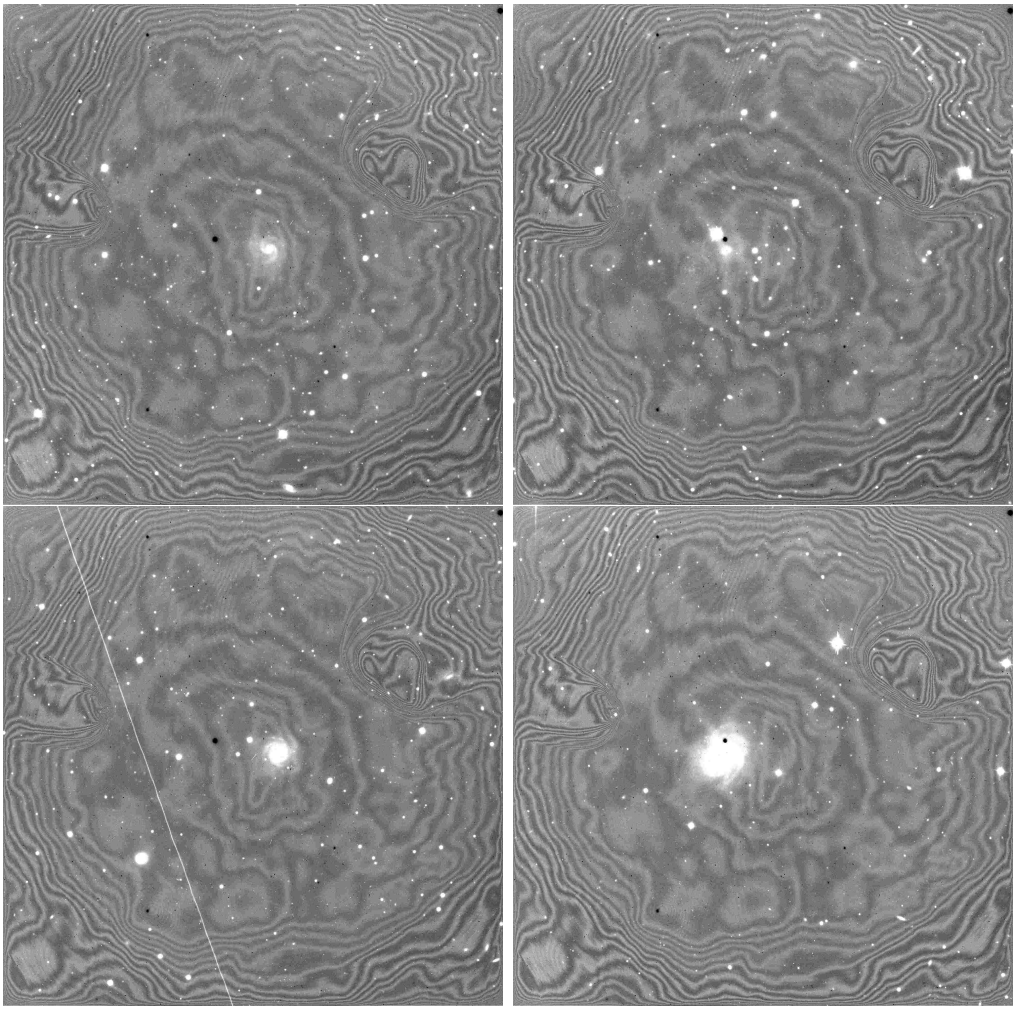

Figure A.1: Examples of bias subtracted, flat-fielded I-band ARCTIC images of four LSBs: LEDA 135682, LEDA 135684, LEDA 135693, UGC 2925. These four galaxies were all observed on the same night, with a total of three images per galaxy observed in the I-band. In total, we averaged twelve images together to create a master fringe image.

relatively dark regions of the sky should be observed in order to provide enough data to average.

The above procedure **must be done for each night of observing.** This is due to the fact that the fringing pattern depends on a wide range of things, such as observing conditions, and that the pattern evolves over time as the filter ages. We stress again that one should **not** create a master fringe pattern and apply it to observations not obtained on the same night. As long as the above procedure is followed, data for the master fringe image will be acquired as science images are taken, imposing no additional observational time.

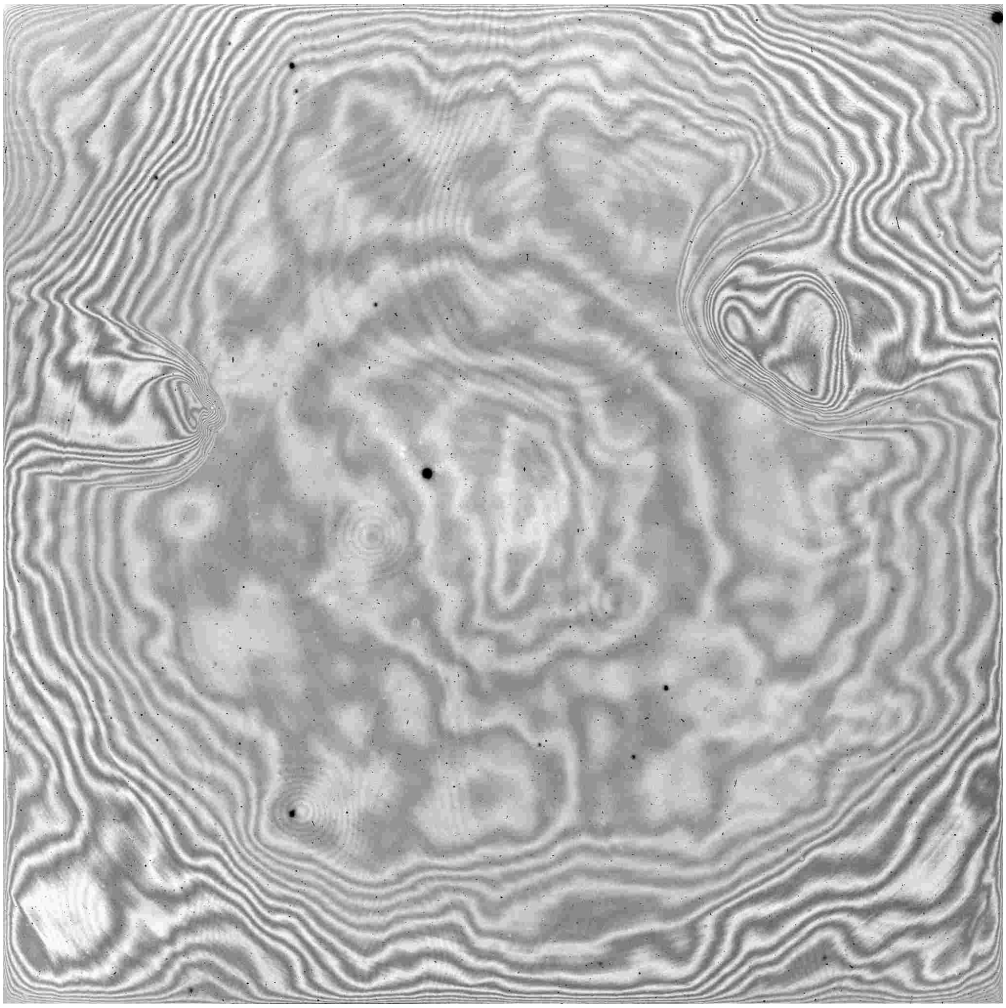

Figure A.2: Master fringe image created from images in Fig. A.1 and additional images obtained from the same night of observing.

Once it comes time to reduce the raw images, one should proceed as normal by subtracting the bias and flat-fielding. As a reminder, the science images will then appear similar to those in Fig. A.1. In order to construct the master fringe image, simply average the available science I-band images together. The procedure outlined above will ensure that the resulting average will consist of signal from the fringe pattern. Our master fringe image for the galaxies in Fig. A.1 is shown in Fig. A.2.

As this master fringe image has been created using images with various sky levels, the intensity must be scaled before applying it to any image. The simplest means of accomplishing this is to determine the average 'sky' value of the master fringe image (i.e. the average value

Figure A.3: Final, fringe corrected images for those images in Fig. A.1. Artifacts are still visible in these images, namely near the edges of the images and near the centers.

of the darker regions in the image) and subtract it. Finally, by dividing by the maximum value in the image, one now has a scalable image based on the sky value of any image taken that night. Once scaled to the sky value of an image, it can be simply subtracted. The result of this fringe correction for the images in Fig. A.1 is shown in Fig. A.3.

From these images, it is clear that while the fringe pattern has been removed, there are still artifacts present. Thankfully, these are all but removed when combining multiple images of the same galaxy. We show trimmed versions of our final, combined images in Fig. A.4.

However, it is worth pointing out means of further reducing these artifacts. For instance, one could make sure that I-band observations of galaxies are away from the center of the

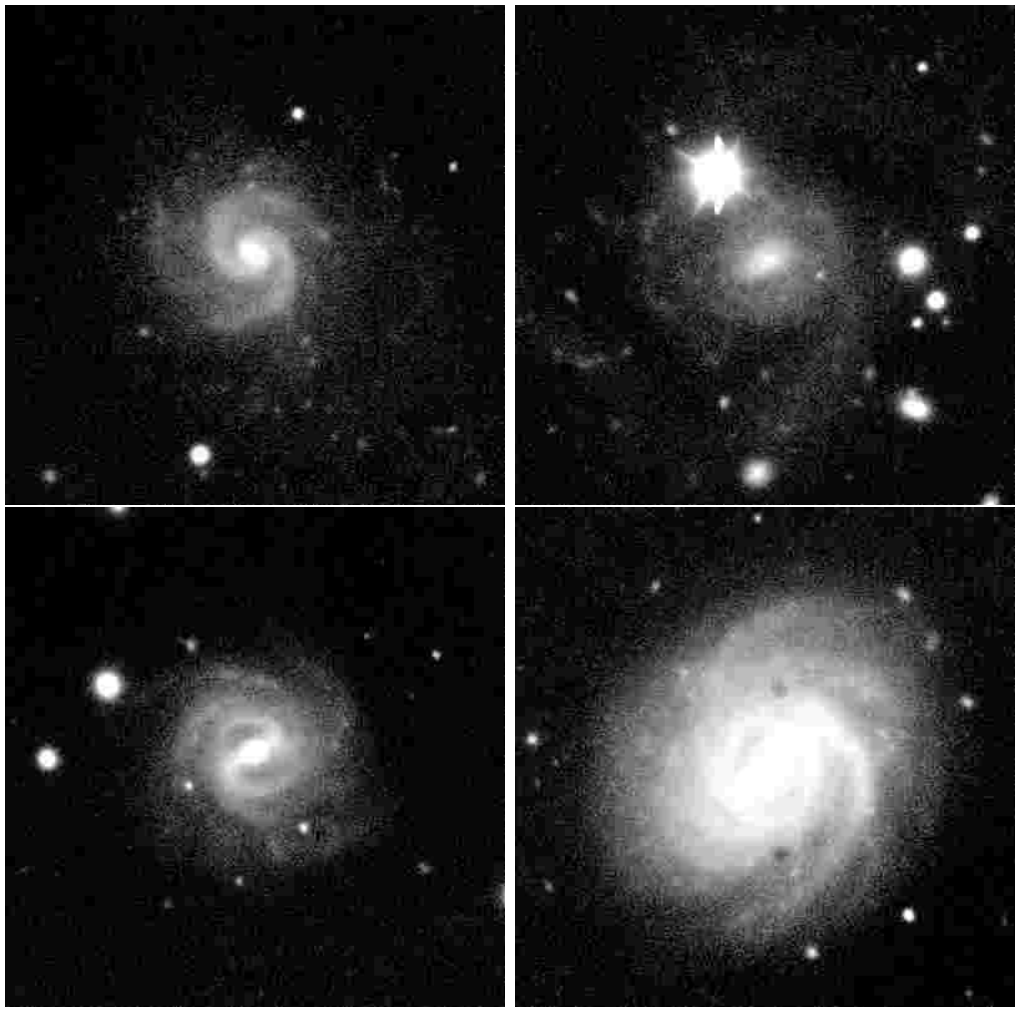

Figure A.4: Bias subtracted, flat fielded, fringe corrected, combined and trimmed I-band images for those galaxies in Fig. A.1.

CCD, where the fringing is more apparent. For large enough targets this could be unavoidable, however. Additionally, one could create master fringe images for each galaxy image, especially if targets are at significantly different airmasses. Again, this could prove to be difficult to accomplish if there are many science observations.

Appendix B

Comparison of Stellar Mass Estimates

Here we show a comparison of stellar mass estimates between using Υ_*^r, Υ_*^I, and Υ_*^V. In order to obtain Υ_I^*, we use the B- and I-band magnitudes in the `HYPERLEDA` database. We then use the stellar mass-to-light ratio equaiton from Into & Portinari (2013):

$$\log \Upsilon_*^I = -0.997 + 0.641(B - I). \tag{B.1}$$

As we are dealing with SDSS images, we can also obtain stellar mass estimates by using the r-band mass-to-light ratio from Bell et al. (2003):

$$\log \Upsilon_*^r = -0.306 + 1.097(g - r) \tag{B.2}$$

Finally, we have the V-band mass-to-light ratio equation based on $(B - V)$ colors from Schombert et al. (2019):

$$\log \Upsilon_*^V = -1.224(B - V)^2 + 3.120(B - V) - 1.271 \tag{B.3}$$

We determine $(B - V)$ colors via the transformation from Cook et al. (2014):

$$(B - V) = 0.89(g - r) + 0.16 \tag{B.4}$$

We obtain luminosities in the various bands in the same way: by using absolute magnitude values of the Sun in various filters from (Willmer 2018) and the distances from Chapter 3 and Chapter 4.

In Fig. B.1 we show a comparison of our I-band and r-band stellar masses to the V-band stellar masses. The dashed line in each panel shows unity. We can see that the I-band stellar masses produce quite a significant amount of scatter, while the r-band stellar masses agree quite well with the V-band masses. That we see the stellar masses are generally smaller for the Into & Portinari (2013) model, and generally larger (but very similar) for the Bell et al. (2003) model is consistent with Schombert et al. (2019) (see their Fig. 10).

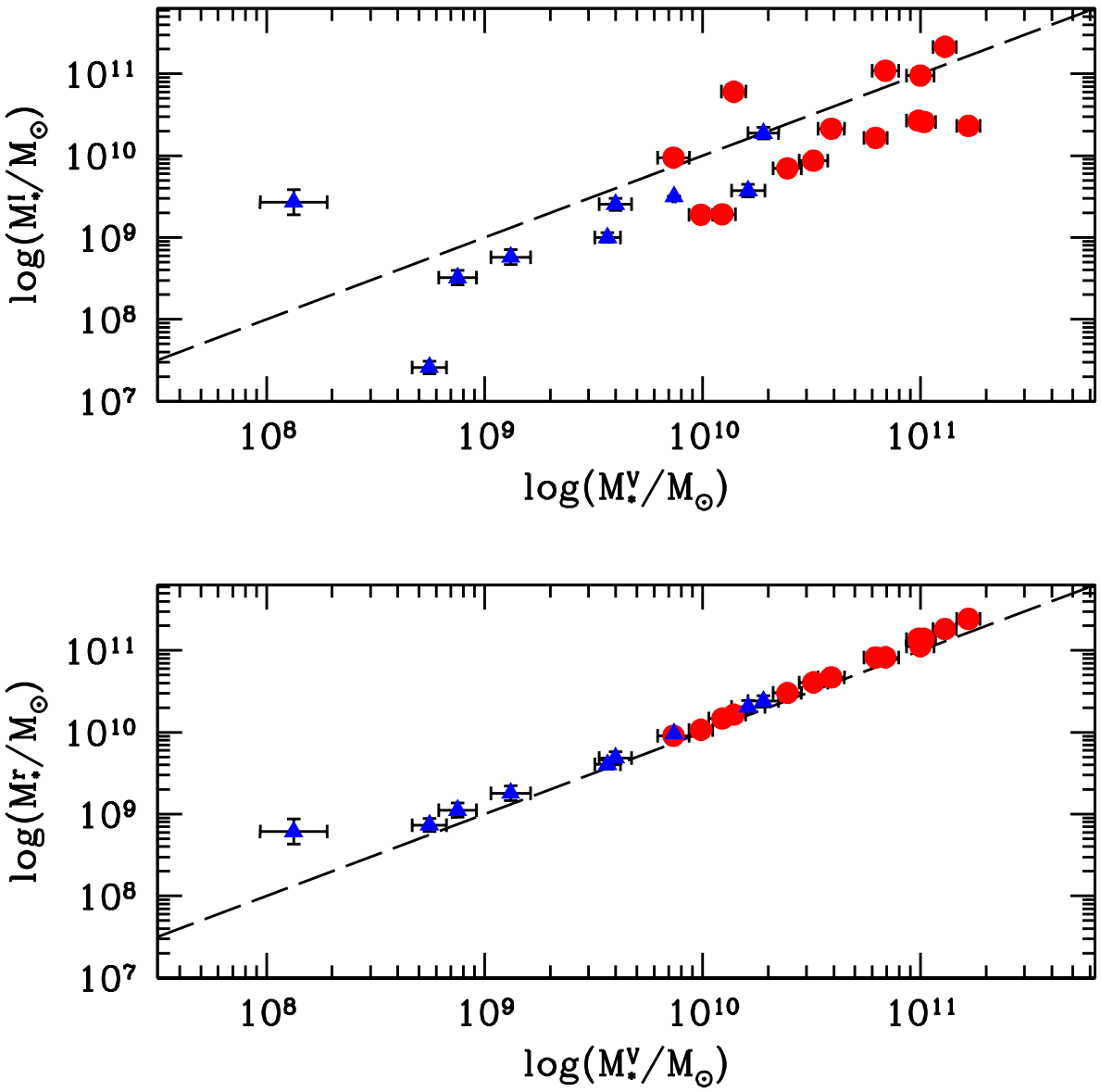

Figure B.1: Comparison of the Into & Portinari (2013) I- (top) and Bell et al. (2003) r-band (bottom) stellar mass estimates to the V-band mass estimates from Schombert et al. (2019). Blue triangles are LSBs and red circles are HSBs. The dashed lines in each panel show unity.